

For Reference

NOT TO BE TAKEN FROM THIS ROOM

Ex LIBRIS
UNIVERSITATIS
ALBERTAENSIS





Digitized by the Internet Archive
in 2022 with funding from
University of Alberta Libraries

<https://archive.org/details/Kisabeth1972>

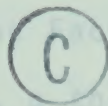
72A-542

THE UNIVERSITY OF ALBERTA

FACULTY OF GRADUATE STUDIES AND RESEARCH

THE DYNAMICAL DEVELOPMENT OF THE
POLAR ELECTROJETS

The undersigned certify that they have read, and
by



JERRY L. KISABETH

recommend to the Faculty of Graduate Studies and Research,
for acceptance, a thesis entitled THE DYNAMICAL DEVELOPMENT
OF THE POLAR ELECTROJETS submitted by Jerry L. Kisabeth

in partial fulfilment of the requirements for the degree
A THESIS
SUBMITTED TO THE FACULTY OF GRADUATE STUDIES AND RESEARCH
IN PARTIAL FULFILMENT OF THE REQUIREMENTS FOR THE DEGREE
OF DOCTOR OF PHILOSOPHY

DEPARTMENT OF PHYSICS

EDMONTON, ALBERTA

FALL, 1972

Thesis
72P-54D

THE UNIVERSITY OF ALBERTA

FACULTY OF GRADUATE STUDIES AND RESEARCH

The undersigned certify that they have read, and recommend to the Faculty of Graduate Studies and Research, for acceptance, a thesis entitled THE DYNAMICAL DEVELOPMENT OF THE POLAR ELECTROJETS submitted by Jerry L. Kisabeth in partial fulfilment of the requirements for the degree of Doctor of Philosophy.

ABSTRACT

During the summer and fall of 1970, a line of nine magnetic observatories was set up along a corrected geomagnetic meridian through western Canada. This thesis contains an analysis of polar magnetic substorms recorded at these stations and at a large number of standard observatories around the world. The research was directed toward the study of the dynamic development of the substorm current system, and the accurate modelling of the current system at various instants throughout the substorm. Data from all-sky cameras on the station line facilitated a study between substorm current system fluctuations and the variations in auroral arc structure.

It was found that the substorm current system develops through the growth of the westward electrojet in the midnight sector of the auroral oval. The substorm further develops through quasi-periodic intensifications of the northern border of the electrojet in conjunction with the generation of irregular loops and surges in the auroral arc structure. An intensification of the eastward electrojet in the evening sector accompanies the substorm onset, although the eastward electrojet may be active without accompanying substorm activity.

Model studies of the electrojet yielded several plausible three-dimensional current system configurations which could explain the substorm perturbation patterns. Distortions of the northern border of the electrojet were generally found to be represented by confined north-to-south current flow which was capable of explaining the large positive D-component perturbations in the region of the surges or loops. It was found to be extremely important to include the effects of induction in the modelling of the current systems, and excellent agreement between the perturbation patterns by the model current systems and the observed perturbation patterns resulted when induction was taken into account.

Several different methods of portraying the dynamic development of the auroral electrojets are employed, and it is found that no one presentation is completely adequate to transfer all the information involved.

ACKNOWLEDGEMENTS

I am grateful to Professor J. A. Jacobs and Dr. G. Rostoker for their encouragement and support throughout the course of this research. I also wish to thank Mr. W. Sherrard, Mr. D. B. Guptill, Mr. R. Mah and Mrs. E. Tooley for their help in the logistics of the experiment and the analysis of the data. Thanks are also due to Dr. J. V. Olson, Dr. A. J. Chen, Dr. J. C. Samson, Dr. C. H. Chapman, Dr. F. W. Jones, H. Lam and R. G. Wiens for useful discussions.

The Department of Energy, Mines and Resources [Earth Physics Branch] aided the project by supplying the fluxgate magnetometers and by granting permission for the installation of one system at the Meanook Magnetic Observatory. Thanks are also due to the University of Calgary, Alberta Government Telephones, Atmospheric Environment Service and Department of Transport for permission to set up observatories at many of their installations in western Canada. The standard magnetograms used in this study were supplied by the Department of Energy, Mines and Resources [Earth Physics Branch] and World Data Center A, Boulder, Colorado.

I am grateful to Mrs. L. Cech for her excellent work in the arrangement and typing of this thesis, and to Mrs. G. Dinwoodie and Mrs. H. Hawkes for their help and encouragement during my stay at this university. The encouragement and patience of my wife, Marilyn, was invaluable in helping me to complete this project.

Throughout the final part of this research I have received financial assistance from the University of Alberta in the form of a Dissertation Fellowship. This research has been supported by the National Research Council of Canada, in part by the Defense Research Board of Canada under grant number 9510-82, and in part by the Boreal Institute of the University of Alberta.

TABLE OF CONTENTS

	Page
CHAPTER I INTRODUCTION	
1.1 The magnetospheric substorm	1
1.2 The auroral and polar magnetic substorms	4
1.3 Current systems thought to be responsible for polar magnetic substorms	8
1.4 The problems studied in this thesis	11
CHAPTER II EVALUATION OF THE MAGNETIC FIELD DUE TO THREE-DIMENSIONAL CURRENT SYSTEMS	
2.1 Introduction	13
2.2 Evaluation of magnetic fields due to three- dimensional current systems using Biot- Savart's law	15
2.2.1 Arbitrary current loop	15
2.2.2 East-west (E-W) current system	16
2.2.3 North-south (N-S) current system	32
2.3 Induced currents in a conducting Earth	47
2.4 A model current system coincident with the auroral oval	58
2.5 N-S and E-W (latitudinal and longitudinal) current distributions associated with the E-W model current system	62
2.5.1 Latitudinal current distributions	62
2.5.2 Longitudinal current distributions	67

CHAPTER III INSTRUMENTATION, DATA PROCESSING AND ANALYSIS

3.1	Instrumentation	73
3.2	Data processing	76
3.3	Data analysis	78
3.3.1	Component magnetogram format	78
3.3.2	Component contour diagrams	79
3.3.3	Three-dimensional (3-D) diagrams	79
3.3.4	Polar plot	80
3.3.5	Latitude profile	85
3.4	Baselines and the orientation of HDZ coordinates in the C.G. coordinate system	91

CHAPTER IV DYNAMIC DEVELOPMENT OF THE POLAR ELECTROJETS

4.1	Introduction	95
4.2	Magnetic field associated with a model three-dimensional current system containing both an eastward and westward electrojet	96
4.3	Eastward electrojet and associated substorm events of July 5, 1970 (Day 186)	101
4.4	The dynamic development of the substorm event of June 15, 1970 (Day 166)	118
4.5	The dynamic development of the substorm event of July 14, 1970 (Day 195)	134

CHAPTER V THE POLAR MAGNETIC SUBSTORM AND THE ASSOCIATED SUBSTORM

5.1	Introduction	144
5.2	Substorm events of October 7, 1970 (Day 280)	145
5.2.1	Polar substorm (0659 UT)	148
5.2.2	Polar substorm (0748 UT)	161
5.2.3	Polar substorm (0814 UT)	164
5.3	Substorm event of September 1, 1970 (Day 244)	167
5.3.1	Expansion phase	171
5.3.2	Recovery phase	183

CHAPTER VI MODELLING OF THE CURRENT SYSTEM ASSOCIATED WITH THE POLAR MAGNETIC SUBSTORM

6.1	Introduction	196
6.2	Depth of the superconductive layer used in our modelling	197
6.3	Modelling of the polar electrojet	198
6.4	Model current system to explain the magnetic perturbations associated with E-W propagating auroral forms	210

CHAPTER VII DISCUSSION AND CONCLUSIONS

7.1	Morphology of polar magnetic substorms	217
7.2	The modelling of polar magnetic substorm current systems	222
7.3	Techniques of presentation of polar magnetic substorm data	224
REFERENCES		227
APPENDIX A1	METHODS OF EVALUATING THE MAGNETIC FIELD PERTURBATIONS OF MODEL CURRENT SYSTEMS	A1
APPENDIX A2	EVALUATION OF THE MAGNETIC FIELD DUE TO CURRENTS INDUCED IN AN INFINITELY CONDUCTING EARTH	A16
APPENDIX A3	THE METHOD OF GAUSSIAN INTEGRATION	A40
APPENDIX A4	INSTRUMENTATION	A44
APPENDIX A5	INTERPRETATION OF MODEL CURRENT SYSTEMS WITH A HYPOTHETICAL LINE OF STATIONS	A54
APPENDIX A6	THREE-DIMENSIONAL DIAGRAMS	A60
APPENDIX A7	MORE EXAMPLES OF MAGNETIC PERTURBATIONS ASSOCIATED WITH POLAR ELECTROJETS	A69

LIST OF TABLES

Table		Page
2.1	Ratio of internal to external field for different depths of the super-conductive layer	53
3.1	Locations and code names of the magnetometer stations	75
3.2	Locations and code names of magnetometer stations used in polar diagrams	83
3.3	Comparison of the magnetic declination and corrected magnetic declination for our line of stations	93
6.1	Geomagnetic coordinates of observatories used in this thesis	200
6.2	Parameters of model current systems	206
A3.1	Comparison of the total field intensities obtained by using the method developed in this thesis with that developed by Bonnevier et al. (1970) and Boström (1971).	A43
A7.1	Kp indices for the days represented in Appendix A7.	A70

LIST OF ILLUSTRATIONS

Figure		Page
1.1	Average configuration of the magnetosphere	2
1.2	Example of a polar magnetic substorm	5
1.3	Schematic diagram to show the development of the auroral substorm	6
2.1	Model of a three-dimensional E-W current system	17
2.2	(a) E-W primary current loop associated with the E-W current system (b) N-S primary current loop associated with the N-S current system	20
2.3	Diagram showing the ionospheric sheet current for an E-W current system	21
2.4	Latitude profile of the total field associated with an E-W three-dimensional current system	30
2.5	Series of latitude profiles for an E-W current system	33
2.6A	Contour plot of the H component for an E-W current system	34
2.6B	Contour plot of the D component for an E-W current system	35
2.6C	Contour plot of the Z component for an E-W current system	36
2.7	Model of a N-S three-dimensional current system	37
2.8	Diagram showing the ionospheric sheet current for the N-S current system	39

Figure		Page
2.9	Latitude profiles for a N-S current system	41
2.10	Series of latitude profiles at various longitudes for a W-S current system	42
2.11A	Contour plot of the H component for a N-S current system	44
2.11B	Contour plot of the D component for a N-S current system	45
2.11C	Contour plot of the Z component for a N-S current system	46
2.12	Total field and induced field for an E-W three-dimensional current system	51
2.13	Latitude profiles of the total field associated with an E-W three-dimensional current system	54
2.14A	Contour plot of the H component for an E-W three-dimensional current system including the induced field	55
2.14B	Same as Fig. 2.14A but for the D component	56
2.14C	Same as Fig. 2.14A but for the Z component	57
2.15	Diagram of four possible parabolas to represent the path of current flow in conjunction with the auroral oval	60
2.16	Diagram showing the relationship between the auroral oval ($Q=2$) and a parabola representation	61
2.17	Latitude profiles at various positions along the auroral oval	63
2.18	Latitude profiles associated with current systems having various latitudinal current distributions	65

Figure		Page
2.19	Latitude profiles associated with a current system having a longitudinal current distribution	68
2.20	Same as Fig. 2.19 but using the different technique to evaluate the magnetic field	70
2.21	Latitude profiles for a current system located at various ionospheric heights	72
3.1	Chain of magnetometers used in the present study	74
3.2	Distribution of magnetometer stations in the northern hemisphere used in the present study	82
3.3	Sample polar plot showing the distribution of horizontal magnetic perturbation vectors associated with a substorm	84
3.4	Polar plot of horizontal perturbation vectors associated with a three-dimensional E-W current system	86
4.1	Model three-dimensional current system containing an eastward and westward electrojet	98
4.2	Polar plot showing the distribution of horizontal magnetic perturbation vectors due to the current system in Fig. 4.1	100
4.3	Magnetograms for July 5, 1970	102
4.4	Pi 2 micropulsation activity for July 5, 1970	103
4.5	Magnetograms from eighteen observatories in the northern hemisphere for July 5, 1970	104

Figure		Page
4.6	Latitude profiles for July 5, 1970	108
4.7	Differential profile and polar plot of 0416 UT on July 5, 1970	109
4.8A	H component contour for July 5, 1970	111
4.8B	D component contour for July 5, 1970	112
4.8C	Z component contour for July 5, 1970	113
4.9	Some examples of eastward electrojets	117
4.10	Magnetograms for June 15, 1970	119
4.11	Pi 2 micropulsation activity for June 15, 1970	120
4.12	Magnetograms from 23 observatories in the northern hemisphere for June 15, 1970	122
4.13	Latitude profiles showing the development of the westward electrojet for June 15, 1970	124
4.14	Same as Fig. 4.13 but showing the continued development	126
4.15	Same as Fig. 4.13 but showing the continued development	129
4.16	Polar plots for June 15, 1970	130
4.17A	H component diagram for June 15, 1970	132
4.17B	Z component diagram for June 15, 1970	133
4.18	Magnetogram for July 14, 1970	135
4.19	Pi 2 micropulsation activity for July 14, 1970	136

Figure		Page
4.20	Magnetograms from 21 observatories in the northern hemisphere for July 14, 1970	137
4.21	Latitude profiles showing the development of the westward electrojet	139
4.22	H component contour for July 14, 1970	141
4.23	Latitude profile and polar plot for ~ 0831 UT	143
5.1	Magnetograms for October 7, 1970	146
5.2	Pi 2 micropulsation activity for October 7, 1970	147
5.3	Magnetograms from seventeen observatories in the northern hemisphere for October 7, 1970	149
5.4a	Development of a westward travelling surge and the associated latitude profiles	150
5.4b	Continuation of Fig. 5.4a	151
5.5a	H component contour for October 7, 1970	154
5.5b	D component contour for October 7, 1970	155
5.5c	Z component contour for October 7, 1970	156
5.6	Polar plot and latitude profile for ~ 0703 UT on October 7, 1970	159
5.7	Polar plot and latitude profile for ~ 0708 UT on October 7, 1970	160
5.8	Polar plot and latitude profile for ~ 0800 UT on October 7, 1970	163
5.9	Polar plot and latitude profile for ~ 0816 UT on October 7, 1970	165

Figure		Page
5.10	Magnetograms for September 1, 1970	168
5.11	Pi 2 micropulsation activity for September 1, 1970	169
5.12	Polar plot showing the distribution of perturbation vectors prior to the onset of the first substorm on September 1, 1970	170
5.13	Magnetograms from nineteen observatories in the northern hemisphere for September 1, 1970	172
5.14	Series of latitude profiles showing the poleward expansion of the current system on September 1, 1970	174
5.15	The Z component contour for the expansive phase of the first substorm on September 1, 1970	176
5.16	Latitude profiles associated with a westward travelling loop	177
5.17	Latitude profiles and the associated auroral diagrams	178
5.18	Latitude profiles depicting the poleward expansion of the electrojet	180
5.19	Three-dimensional plot of the H component for September 1, 1970	185
5.20	Polar plots for 0730 UT and 0809 UT on September 1, 1970	187
5.21	D component magnetogram band pass filtered (60-1000 sec)	188
5.22	Latitude profiles and associated auroral diagrams showing the enhancement of the northern border due to a westward propagating loop	190

Figure		Page
5.23	Differential profiles associated with a westward propagating loop	191
5.24	Differential profiles associated with an eastward propagating auroral form	193
6.1	The relationship between various coordinate systems	201
6.2	Comparison of theoretical and observed profiles for \sim 0715 UT on June 15, 1970	202
6.3	Same as Fig. 6.2 but for \sim 0743 UT	203
6.4	Same as Fig. 6.2 but for \sim 0704 UT on September 1, 1970	204
6.5	Comparison of theoretical and observed horizontal magnetic perturbations for \sim 0715 UT on June 15, 1970	207
6.6	Same as Fig. 6.5 but for \sim 0743 UT	208
6.7	Same as Fig. 6.5 but for \sim 0704 UT on September 1, 1970	209
6.8	Proposed model for the perturbation of the westward electrojet due to the propagating auroral form	211
6.9	Differential profiles for the proposed model shown in Fig. 6.8	213
6.10	Proposed shears of N-S three-dimensional current systems	215
6.11	Perturbations associated with the sheared current systems	216

Figure		Page
A1.1	Diagram defining vectors in spherical coordinates for magnetic field calculations	A2
A1.2	E-W and N-S current loops with associated infinitesimal magnetic dipoles	A11
A2.1	Diagram showing the spherical conductor at depth a-b and observation point where the total field is calculated	A19
A4.1	Block diagram of the basic magnetic recording system at each station	A45
A4.2	Block diagram of the fluxgate magnetometer	A46
A4.3	Theoretical frequency response curves for the magnetometer	A48
A4.4	Gain curve of the magnetometer	A49
A4.5	Block diagram of the digital recording system	A51
A4.6	Frequency response of the aliasing filters	A53
A5.1	Series of latitude profiles of observations from a hypothetical line of stations	A55
A5.2	Same as Fig. A5.1	A57
A5.3	Same as Fig. A5.1	A58
A6.1	The H component 3-D diagram for July 14, 1970	A61
A6.2	The D component 3-D diagram for July 14, 1970	A62
A6.3	The Z component 3-D diagram for July 14, 1970	A63

Figure		Page
A6.4	The H component 3-D diagram for October 7, 1970	A64
A6.5	The D component 3-D diagram for October 7, 1970	A65
A6.6	The Z component 3-D diagram for October 7, 1970	A66
A6.7	The D component diagram for September 1, 1970	A67
A6.8	The Z component diagram for September 1, 1970	A68
A7.1	Magnetograms for June 19, 1970 (0430-0800 UT)	A72
A7.2	Magnetograms for June 19, 1970 (0830-1200 UT)	A73
A7.3	Latitude profiles for the events shown in Fig. A7.1 and A7.2	A74
A7.4	Magnetograms for June 30, 1970 (0500-1000 UT)	A75
A7.5	Magnetograms for September 18, 1970 (0600-1000 UT)	A77
A7.6	Latitude profiles for the events shown in Fig. A7.4 and A7.5	A78
A7.7	Magnetograms for July 2, 1970 (0615-0915 UT)	A79
A7.8	Magnetograms for July 2, 1970 (0930-1300 UT)	A80
A7.9	Latitude profiles for the events shown in Fig. A7.7 and A7.8	A81

Figure		Page
A7.10	Magnetograms for July 15, 1970 (0830-1200 UT)	A83
A7.11	Magnetograms for July 12, 1970 (0600-1100 UT)	A84
A7.12	Latitude profiles for the events shown in Fig. A7.10 and A7.11	A85
A7.13	Magnetograms for September 19, 1970 (0440-1140 UT)	A86
A7.14	Latitude profiles for the events shown in Fig. A7.13	A87
A7.15	Magnetograms for July 8-9, 1970 (2300-0230 UT)	A89
A7.16	Magnetograms for July 9, 1970 (0230-0630 UT)	A90
A7.17	Latitude profiles for the events shown in Fig. A7.15 and A7.16	A91

CHAPTER I INTRODUCTION

1.1 The magnetospheric substorm

It has long been realized that the energy which is dissipated in high latitude auroral and electromagnetic disturbances is derived from the interplanetary medium through the interaction of the solar wind with the outer regions of the Earth's magnetic field configuration. In this interaction, the Earth's dipole magnetic field is highly distorted, assuming a configuration as shown in Fig. 1.1. The magnetic field configuration, known as the magnetosphere, features a compression of the dipole lines on the dayside and a distention of the magnetic lines of force on the nightside forming the magnetotail. The magnetic field pattern shown in Fig. 1.1 is representative of steady state conditions, and the action of the solar wind on this configuration results in a flow of energy into the inner magnetosphere. While there are conflicting theories regarding the exact fashion in which energy may penetrate into the inner magnetosphere (eg. Axford and Hines, 1961; Dungey, 1961; Frank, 1971), it has become apparent that the rate of energy transfer is highly dependent on the parameters of the interplanetary plasma, and in particular

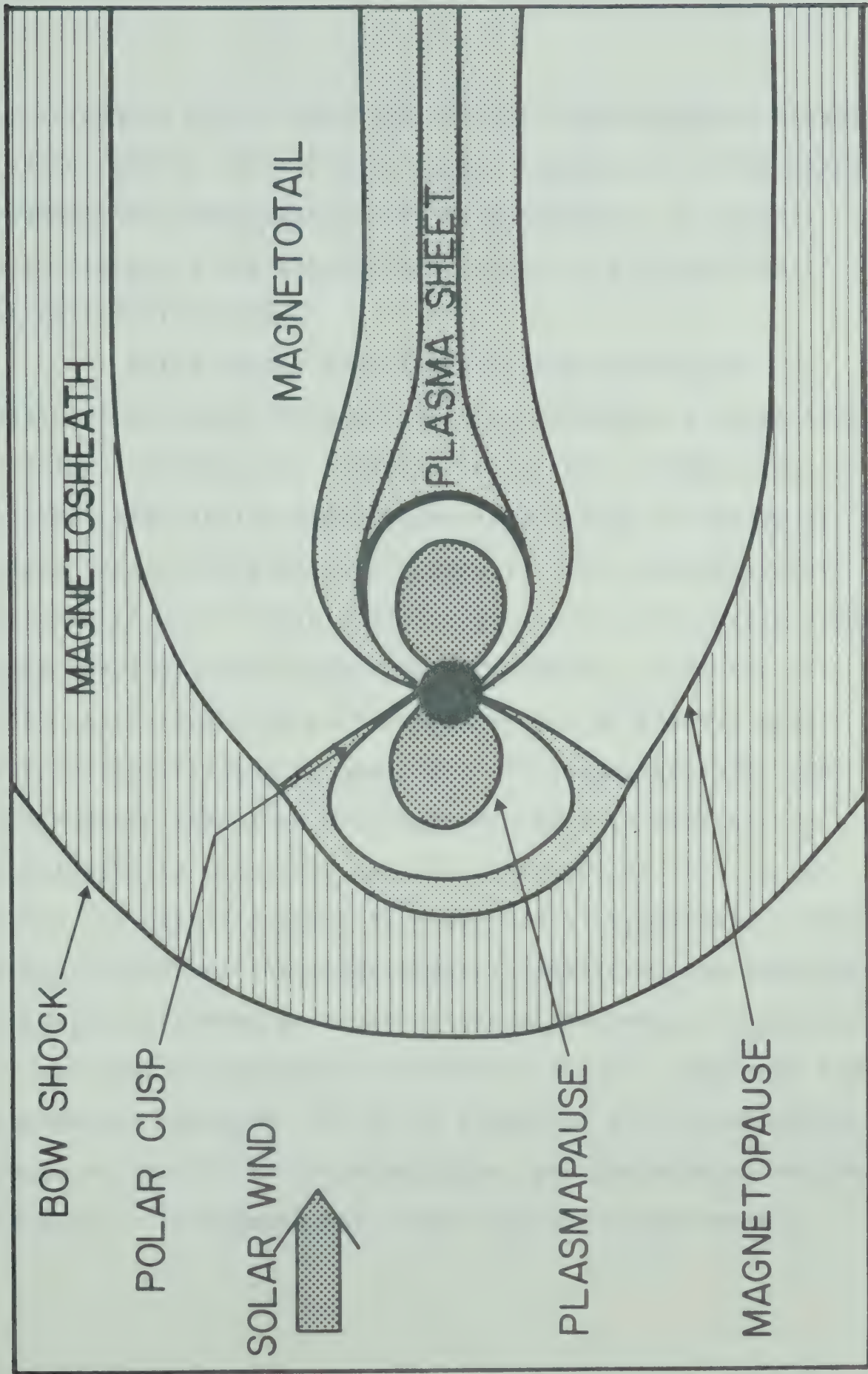


Fig. 1.1 Average configuration of the magnetosphere in the solar magnetospheric noon-midnight meridional plane.

the direction of the component of the interplanetary magnetic field normal to the ecliptic plane. Regardless of the means by which the energy enters the magnetosphere, it appears to be stored in the magnetotail through the distention of the tail field lines.

While energy may be dissipated slowly and continually within the magnetosphere through the generation of quiet auroral arcs, ionospheric current systems etc., the most outstanding magnetospheric activity is caused by sudden impulsive releases of energy. It is generally felt that the energy is released through explosive magnetic field lines merging in the magnetotail (Atkinson, 1966; Dessler, 1968) and during such periods of release of energy, many diverse electromagnetic phenomena are generated. The sum of all these impulsive phenomena has been termed the magnetospheric substorm, and the character of this perturbation has been discussed in great detail by Akasofu (1968). He has subdivided the magnetospheric substorm into substorms involving different portions of the electromagnetic spectrum, viz. the auroral substorm, the polar magnetic substorm, the ionospheric substorm, the X-ray substorm, the proton aurora substorm, the VLF emission substorm, and the micropulsation substorm. Throughout this thesis we will be primarily

interested in the auroral and polar magnetic substorms. For a comprehensive review of all the various substorm phenomena, the reader is referred to Akasofu (1968).

1.2 The auroral and polar magnetic substorms

As we have stated in the previous section, the auroral and magnetic signatures of the magnetospheric substorm are termed the auroral substorm and polar magnetic substorm respectively. At present the development of these two substorms is best described in the framework developed for the auroral substorm by Akasofu (1964) with some modifications involving more recent observations.

The development of the auroral substorm has been subdivided into the expansive phase and the recovery phase, and each of the phases has been divided into three stages as follows (see Fig. 1.2 and 1.3).

(i) Expansive Phase Stage I: The auroral arcs near midnight brighten suddenly, at which time the magnetic field changes sharply in the vicinity of the arc and a Pi 2 micropulsation burst is initiated.

Stage II: The auroral arcs become distorted and move poleward, during which time the magnetic field perturbation tends to intensify.

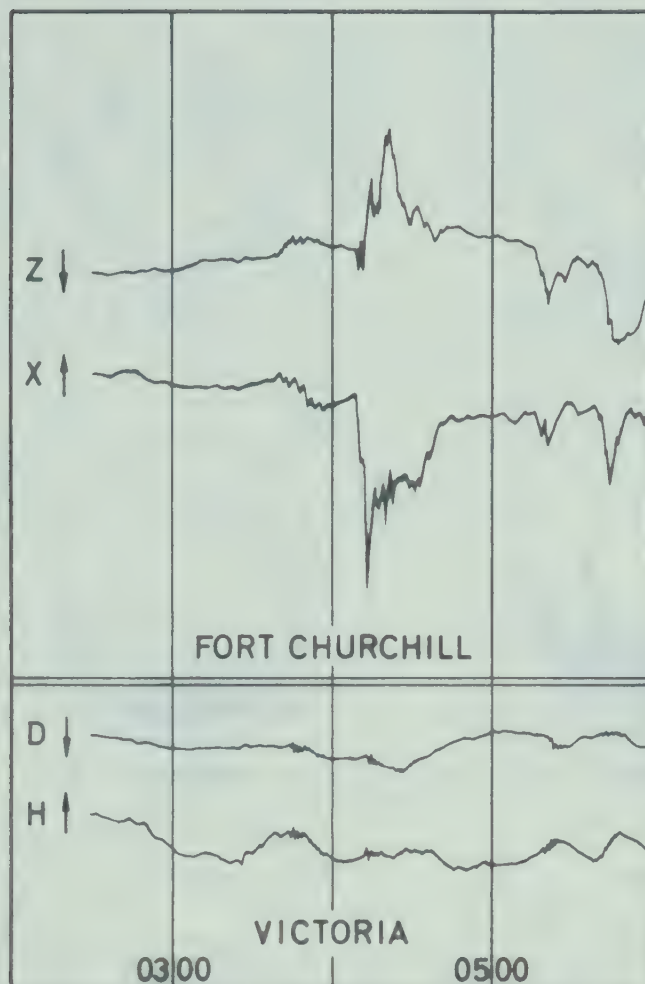


Fig. 1.2 Examples of a polar magnetic substorm recorded at a high-latitude station (Fort Churchill) and a mid-latitude station (Victoria). Note the burst of Pi 2 micropulsation activity associated with the substorm onset. A typical polar magnetic substorm in the high-latitude regions has an amplitude on the order of a couple hundred gammas (one gamma equals 10^{-5} Gauss).

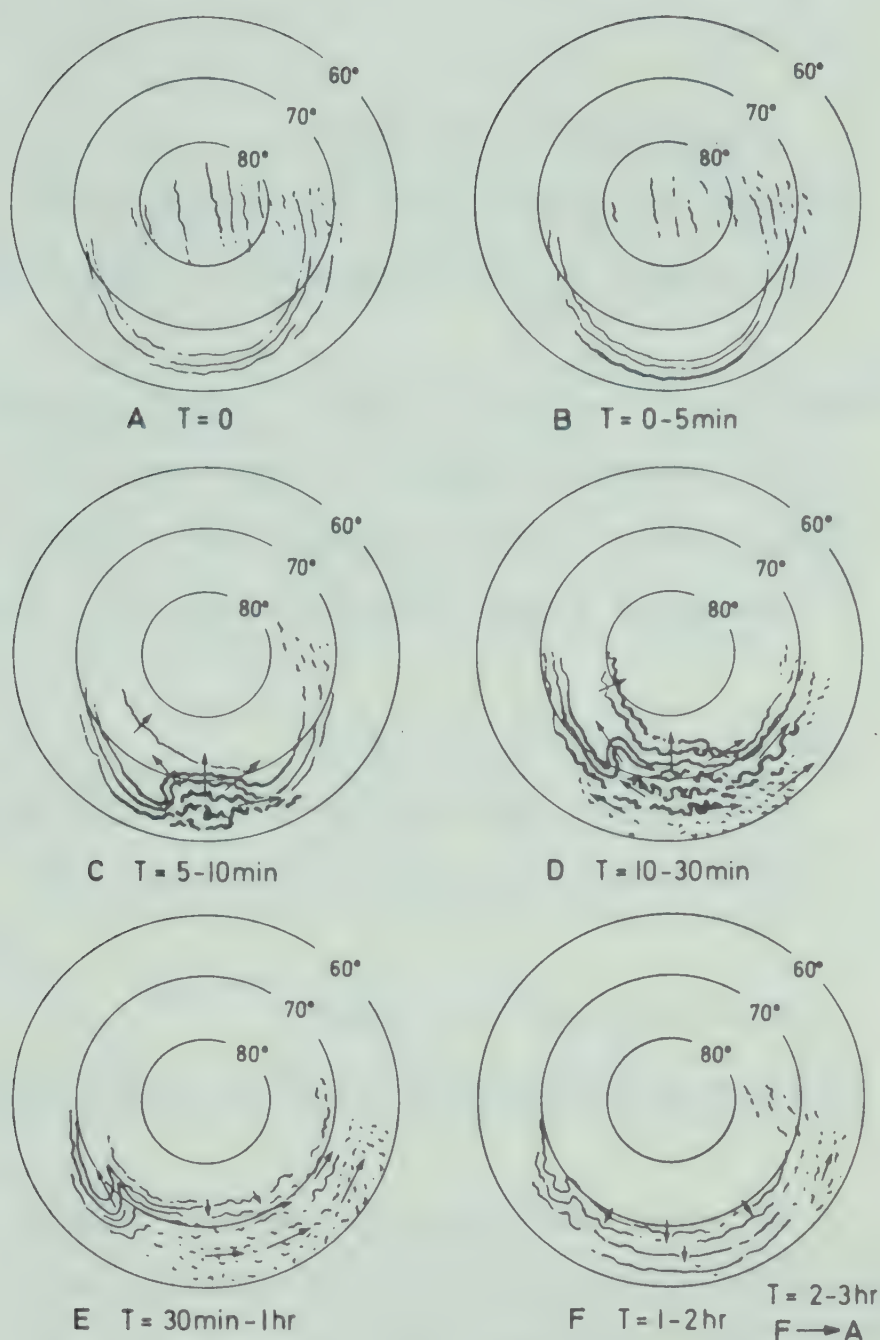


Fig. 1.3 Schematic diagram to illustrate the development of the auroral substorm. The center of the concentric circles in each stage is the north geomagnetic pole, and the Sun is toward the top of the diagram (after Akasofu, 1964).

Stage III: The westward travelling surge and eastward drifting patches are formed, at which time the magnetic field perturbation intensifies strongly.

(ii) Recovery Phase Stage I: The arcs reach their northernmost position and start to recede southward, while surges and loops distort the northern border. During this time, the magnetic field perturbations remain large and irregular.

Stage II: The arcs continue to drift equatorward and the drifting loops change into irregular bands. The magnetic perturbations start to die down at this time.

Stage III: The arcs slowly complete their equatorward drift, and the magnetic activity ceases.

It has recently become apparent that there is a period of distinctive activity in the magnetosphere prior to the onset of the expansive phase of the substorm. This pre-substorm activity has been termed the growth phase (McPherron, 1970), and is thought to represent the period of time during which there is an enhanced flow of energy from the solar wind into the magnetosphere. At the present time there is consider-

able controversy regarding the auroral and ground-based magnetic signatures of the growth phase. While McPherron (1970) claims that a slowly deepening H-component trace at auroral zone observatories is typical of the growth phase, this particular perturbation is also the signature of a substorm expansive phase seen some distance from the intensified portion of the auroral electrojet. In addition Feldstein (1972) and Mozer (1971) have suggested that equatorward drifting arcs signify the development of the growth phase, while Akasofu and Snyder (1972) and Subbarao and Rostoker (1972) claim that this is not the case. In this thesis we will comment in more detail on the magnetic signatures of the various phases of substorm activity.

1.3 Current systems believed to be responsible for polar magnetic substorms

For some time it has been known that current systems in the Earth's upper atmosphere are responsible for the large magnetic variations observed during auroral displays (see Chapman, 1967). The first definitive study of such current systems was done by Birkeland (1908, 1913), who concluded that the current system associated with, what he termed 'polar elementary storm', was three-dimensional in nature with current

flowing down along magnetic fields to the ionosphere, westward through the ionosphere and back up the field lines into space. He also introduced the equivalent current concept for the purpose of data presentation. Chapman (1935) disagreed with Birkeland's model and suggested that all currents responsible for the observed magnetic perturbations were confined to the ionosphere. Vestine and Chapman (1938) modelled the auroral electrojet with this idea in mind.

The next important study of polar substorms was made by Fukushima (1953) in which he effectively used the equivalent current system to analyze the development of geomagnetic bays. In his model studies he used distributions of electric doublets confined to the ionosphere. Heppner (1954) discussed the possible ionospheric current systems which could explain the diurnal patterns of geomagnetic bays observed at College, Alaska. He concluded that a two jet system, an eastward electrojet in the evening sector and a westward electrojet in the morning sector, could explain these observations.

Akasofu et al. (1965) introduced a new model current system that included a strong westward electrojet flowing along the auroral oval with return currents flowing across the polar cap and also at lower latitudes below the auroral

oval. They believed this return current to be responsible for the positive H bays in the evening sector as observed by Heppner.

About this time the concept of field-aligned current as originally proposed by Birkeland was again considered (Boström, 1964). This followed from the realization that certain regions of the magnetosphere were not subject to perfect frozen field conditions as proposed by Alfvén and Fälthammar (1963) (also see Block, 1967). More recent studies by Armstrong and Zmuda (1970), Cloutier et al. (1970), Vondrak et al. (1971), and Park and Cloutier (1971) have confirmed the existence of Birkeland (field-aligned) currents (see Cloutier (1971) for a recent review of such currents).

Model studies of three-dimensional current systems which include field-aligned current linkage of the westward electrojet to the outer magnetosphere, have been used recently to model substorm perturbations by Akasofu and Meng (1969) and Bonnevier et al. (1970). Despite the ability of these three-dimensional current systems to generate positive H regimes at high and low latitudes, the positive bays in the evening sector suggest the existence of an eastward electrojet (Langel and Cain, 1967; Feldstein and Zaitzev, 1968) and from the work of Cummings (1966), Cummings and Dessler (1967),

and Kamide and Fukushima (1971), this electrojet would appear to be associated with the asymmetric ring current in the evening sector (see Rostoker (1972) for a comprehensive review of polar magnetic substorms).

1.4 The problems studied in this thesis

Previous studies of polar magnetic substorms were made using magnetic data from a distribution of magnetic observatories which, in most cases, were sparsely scattered over the surface of the Earth (eg. Birkeland, 1908; Vestine and Chapman, 1938; Silsbee and Vestine, 1942; Fukushima, 1953; Akasofu and Meng, 1969). Since the ionospheric portion of the current system responsible for the polar magnetic substorm is limited in both latitudinal and longitudinal extent, a detailed analysis of the dynamic development of polar magnetic substorms was not possible. This fact prompted us to install a line of magnetometer stations along a common geomagnetic meridian through Western Canada. This thesis pertains to the acquisition and analysis of data obtained from this line of stations during the summer of 1970.

In the following chapters we will present a detailed analysis of several polar magnetic substorms, outlining the development of the polar electrojets and the associated auroral

activity. We will use three-dimensional equivalent current systems to model the substorm current system. We will show that when induction and asymmetric current distributions are taken into account, excellent agreement between the observed magnetic perturbation pattern and the theoretically calculated pattern is obtained.

CHAPTER II EVALUATION OF THE MAGNETIC FIELD DUE TO THREE-DIMENSIONAL CURRENT SYSTEMS

2.1 Introduction

In this chapter we present a convenient method of evaluating the magnetic field associated with three-dimensional current systems using Biot-Savart's law. The advantages we find in using this particular method over other methods presented in the literature are: (1) the ease with which this method can be applied to arbitrary current systems in the magnetosphere (the assumption being made that the geometries of these current systems can be expressed in polar coordinates with the origin located at the center of the Earth), (2) the ability to include effects of induction due to a conducting Earth (although we assume infinite conductivity, the finite conductivity case can also be included using this method), and (3) the small amount of computer time required to integrate over current systems with large spatial dimensions.

Other methods for obtaining the magnetic effects associated with various three-dimensional model current systems have been reported in the literature. These magnetic effects may be evaluated either by performing numerical computations or by using wire models and a search coil (see

Boström (1968) for a review of this subject). Recently Meng and Akasofu (1969) revised Kirkpatrick's model system (Kirkpatrick, 1952) in order to explain magnetic perturbations associated with polar magnetic substorms. Kawasaki and Akasofu (1971) computed the magnetic effects associated with this revised model. Bonnevier et al. (1970) (also see Boström, 1968) used a distribution of infinitesimal magnetic dipoles along dipole field lines to obtain the scalar magnetic potential and thus the magnetic field associated with field-aligned currents. We also use this method in conjunction with some specific model current systems (see section 2.5 and Appendix A1). Kamide and Fukushima (1971) used Biot-Savart's law to calculate the magnetic perturbations associated with a three-dimensional eastward electrojet. Although we also use Biot-Savart's law, our mathematical formulation presented in this chapter and Appendix A1 is such that the differential form of Biot-Savart's law can be represented by a single matrix which includes all the necessary coordinate transformations. In so doing, a large number of terms either cancel or become greatly simplified, thereby allowing more accurate computations to be made with a significant decrease in computer time. Such a formulation also lends itself to a solution of the induction problem for three-dimensional current systems (see Appendix A2).

2.2 Evaluation of magnetic fields due to three-dimensional current systems using Biot-Savart's law

2.2.1 Arbitrary current loop

The application of Biot-Savart's law to an arbitrary current loop external to the earth's surface is presented in Appendix A.1. We showed that for a current loop (C) (see Fig. A1.1) the total contribution to the j^{th} field component at (r_0, θ_0, ϕ_0) is

$$B_j(r_0, \theta_0, \phi_0) = k J \int_C \sum_i dc_{ij} \quad (j = 1, 2, 3) \quad (2.1)$$

where J is the current flowing in the loop, k is a proportionality factor dependent upon the system of units used and dc_{ij} is an element of the matrix

$$\tilde{dc} = \frac{1}{R^3} \begin{bmatrix} 0 & r_0 A_{31} ds_1 & -r_0 A_{21} ds_1 \\ rA_{13} ds_2 & (rA_{23} + r_0 A_{32}) ds_2 & (rA_{33} - r_0 A_{22}) ds_2 \\ -rA_{12} ds_3 & (r_0 A_{33} - rA_{22}) ds_3 & -(r_0 A_{23} + rA_{32}) ds_3 \end{bmatrix} \quad (2.2)$$

All variables in \sim dc are defined in Appendix A1. The field components given by equation 2.1 are related to the total magnetic field at (r_0, θ_0, ϕ_0) by

$$\vec{B} = B_1 \hat{r}_0 + B_2 \hat{\theta}_0 + B_3 \hat{\phi}_0 \quad (2.3)$$

Equation 2.1 is indeed very simple to use for evaluating the field due to three-dimensional current systems provided, of course, an analytic expression for the current path C exists. This equation also lends itself to the problem of determining the field due to induced currents in a uniformly conducting earth (see section 2.3 and Appendix A2, section A2.3).

2.2.2 East-west (E-W) current system

A model of a three-dimensional E-W current system is illustrated in Fig. 2.1. In this system, field-aligned (Birkeland) currents flow from the magnetospheric equatorial plane down the field lines to the eastern edge of the ionospheric westward electrojet. After flowing westward to the western edge of the ionospheric electrojet, they flow back up the field lines to the magnetospheric equatorial plane. The path of current flow is completed by eastward

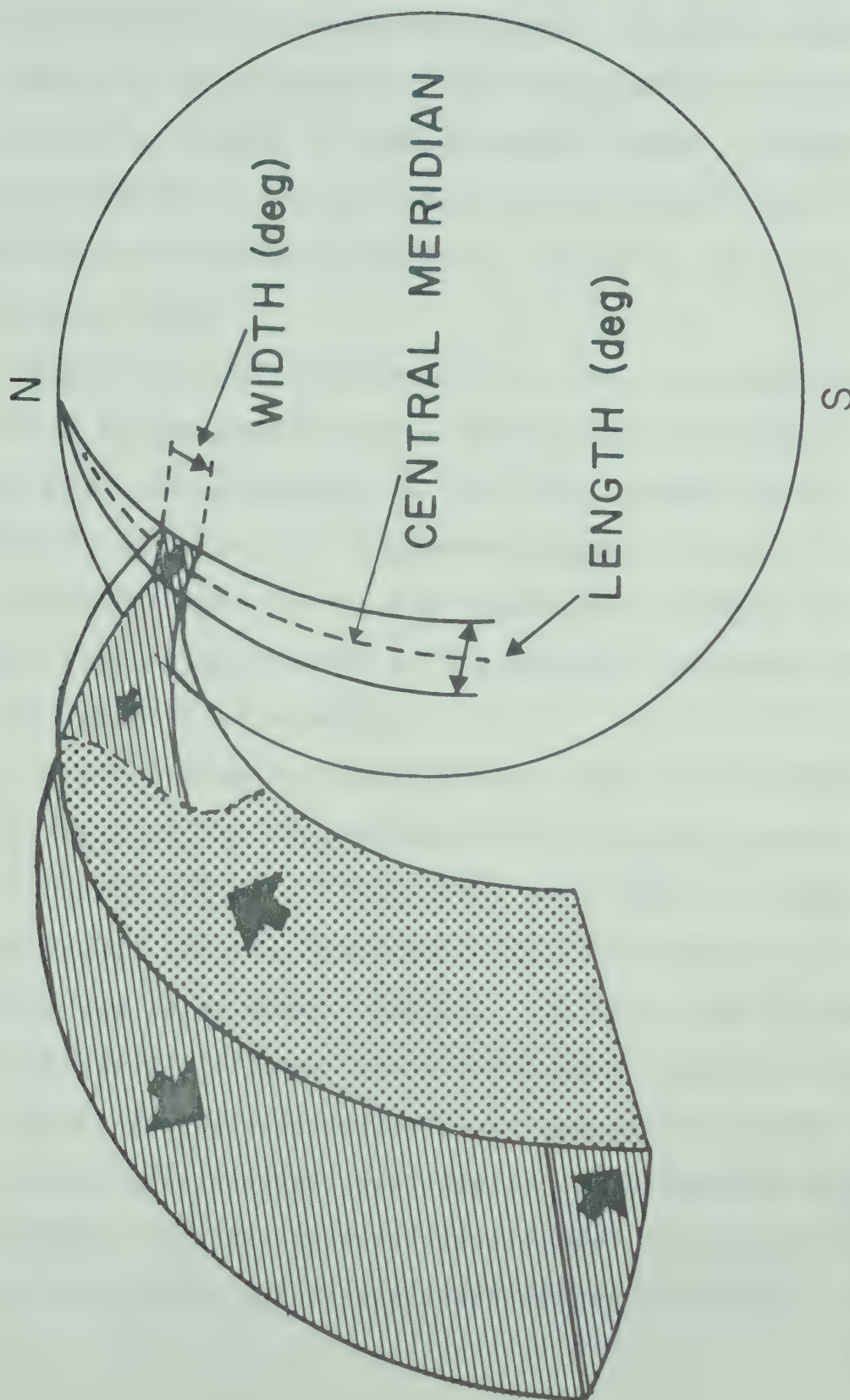


Fig. 2.1 Model of a three-dimensional E-W current system with finite longitudinal and latitudinal extent.

directed currents in the equatorial plane. In model studies this is analogous to a decrease in the ring current intensity in this particular sector of the equatorial plane. A model system with eastward directed ionospheric currents (eastward electrojet) is obtained merely by reversing the direction of current flow.

Since the configuration of the total current system is controlled by the configuration of the magnetic dipole field, the physical parameters of the total system can be represented by those of the ionospheric segment alone. This proves to be very useful since the ionospheric segment provides the largest contribution to the magnetic perturbations observed by our line of stations.

In the following discussion we refer to Birkeland currents at each end of the westward electrojet as eastern and western sheet currents. This does not, however, suggest that such current flow is confined to a narrow region in longitude as the term 'sheet' implies. In fact such current flow is probably distributed along the entire length of the westward (or eastward) electrojet. An example of a model with this particular current distribution is presented later in this chapter. For the present development we assume any longitudinal distribution of Birkeland currents can be

approximated by sheet currents at both ends of the electrojet. We also refer to the ionospheric segment as a sheet current. Here, we assume the height-integrated ionospheric segment can be approximated by a horizontal sheet current at a height h above the surface of the earth.

To facilitate the following mathematical development we use a series of primary current loops such as those shown in Fig. 2.2 to represent an integral part of the total current system. The two examples (a) and (b) are primary loops with ionospheric current flowing E-W and N-S along lines of constant latitude and longitude respectively. In general, however, the ionospheric segment and thus the complete primary loop can have any orientation and shape necessary to coincide with the geometry of the total current system.

The latitudinal and longitudinal extent ('width' and 'length' in degrees) of the ionospheric sheet current for the model in Fig. 2.1 is shown in Fig. 2.3. The lines of x's and dots designate incoming and outgoing Birkeland currents respectively. The angles ϕ_C (central meridian) and θ_C represent the centers of the current system with respect to longitude and to latitude. Both parameters prove to be very useful when comparing observations of magnetic perturbations with those of model current systems.

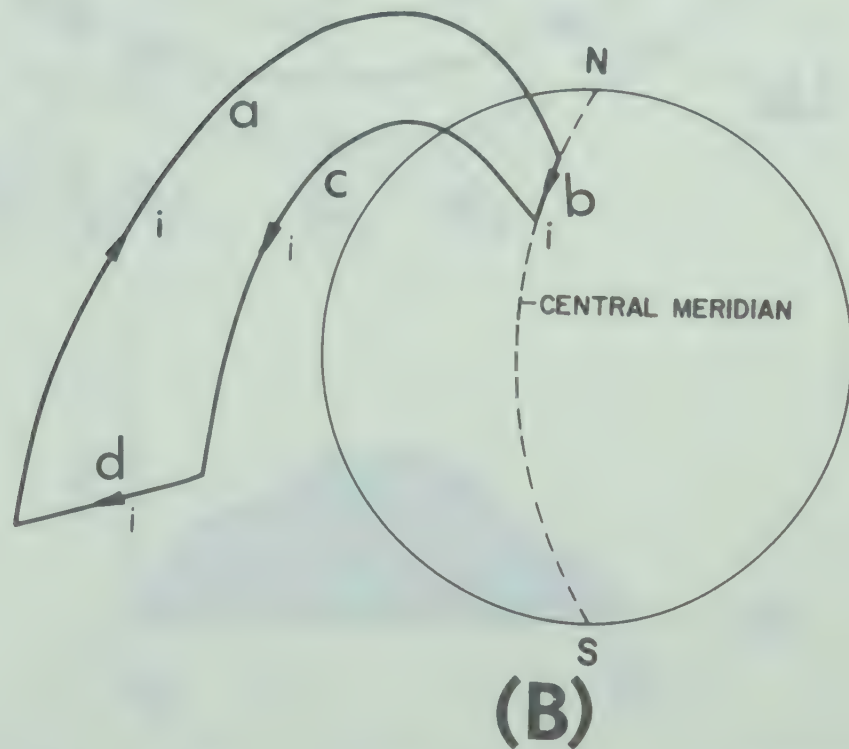
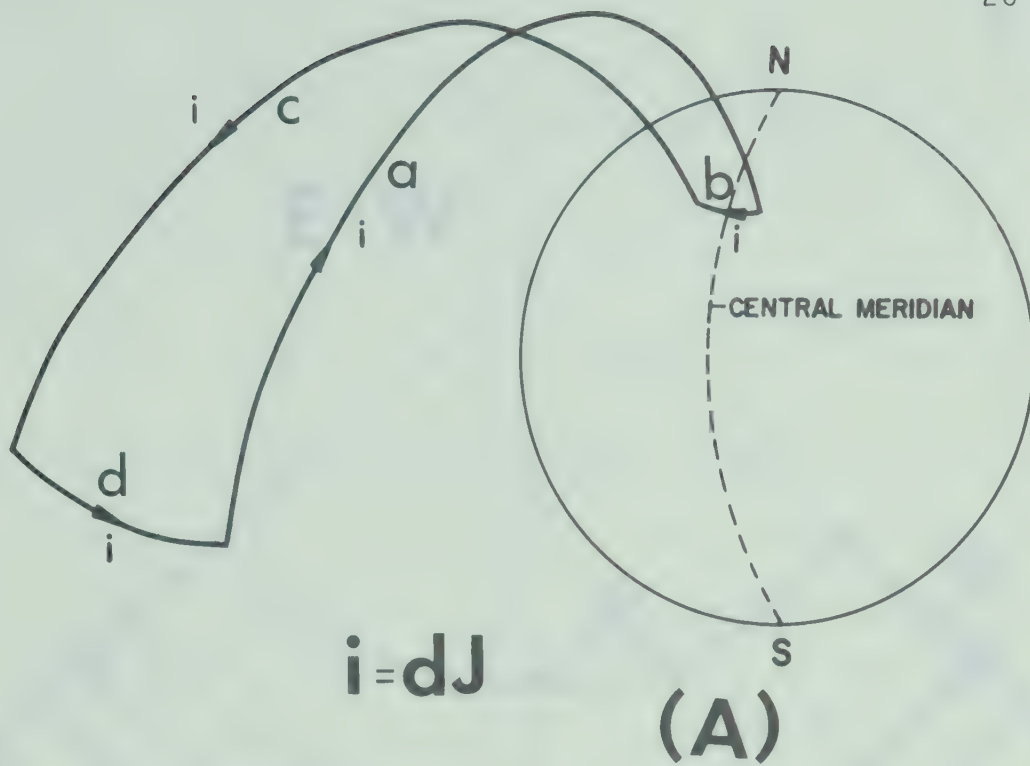


Fig. 2.2 (a) E-W primary current loop associated with the model current system illustrated in Fig. 2.1. (b) N-S primary current loop associated with the model current system presented later in this section (see Fig. 2.7).

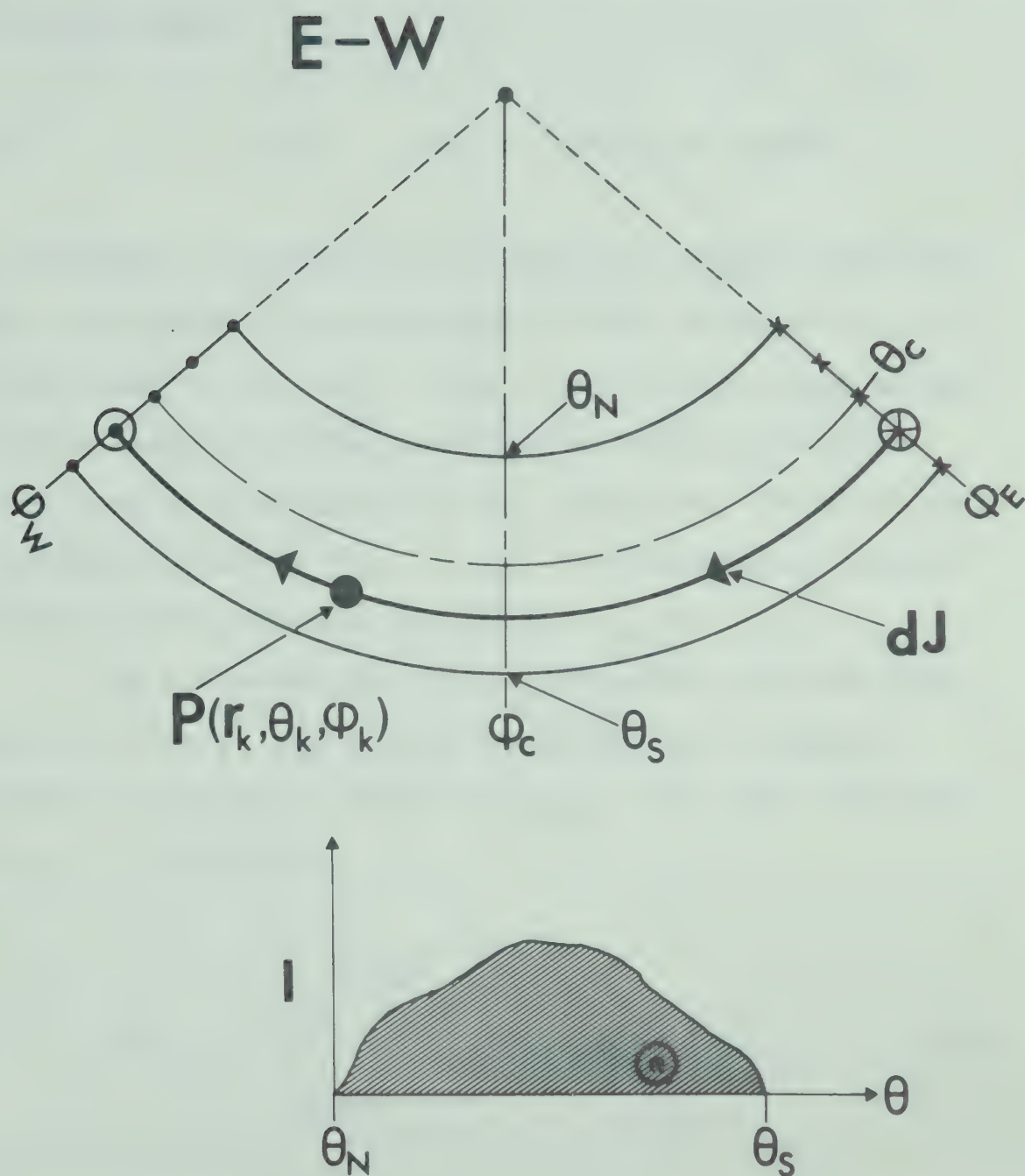


Fig. 2.3 Diagram showing the ionospheric sheet current for an E-W current system. Also shown is an arbitrary distribution of current across the electrojet (see section 2.5).

Any point P on the ionospheric sheet current is $P(r_k, \theta_k, \phi_k)$ where

$$r_k = a + h \quad (a = \text{radius of earth}).$$

The ionospheric element of the particular primary loop used in the evaluation of the field due to the model in Fig. 2.1 is also shown in Fig. 2.3. Thus, once we have obtained an analytical expression for the field of this particular primary loop as a function of θ_k , the total field due to the current system in Fig. 2.1 can be evaluated by integrating this expression over the width θ_N to θ_S .

To allow for arbitrary latitudinal distributions of current flow in the system, we define a latitudinal current distribution function $I(\theta_k, \phi_k)$ such that the total current J is given by

$$J(\phi_k) = \int_{\theta_N(\phi_k)}^{\theta_S(\phi_k)} I(\theta_k, \phi_k) r_k d\theta_k \quad (2.5)$$

where we have allowed for a variable width by denoting θ_S and θ_N as functions of ϕ_k . Since the total current

$J(\phi_k)$ flowing across any meridian between ϕ_E and ϕ_W is constant and therefore independent of ϕ_k , we can arbitrarily define both $I(\theta_k)$ and width of the current system as

$$I(\theta_k) = I(\theta_k, \phi_C)$$

and

$$\text{width} = \theta_S(\phi_C) - \theta_N(\phi_C)$$

Thus, the total current J is

$$J = \int_{\theta_N(\phi_C)}^{\theta_S(\phi_C)} I(\theta_k) r_k d\theta_k \quad (2.6)$$

These definitions for width and J are important, especially for model current systems containing ionospheric sheet currents oriented along the auroral oval, in which case neither the width or latitudinal current distribution are necessarily constant with respect to longitude.

Writing equation 2.6 in differential form

$$dJ = I(\theta_k) r_k d\theta_k \quad (2.7)$$

(dJ is the current flowing in the primary loop located at θ_k) and using eq. 2.3 and 2.6, the total contribution to each field component can be expressed as

$$B_j(r_o, \theta_o, \phi_o) = k \int_{\theta_N}^{\theta_S} I(\theta_k) \left[\int_{\text{loop}(\theta_k)} \sum_i dc_{ij} \right] r_k d\theta_k \quad (2.8)$$

where $\int_{\text{loop}(\theta_k)}$ is the line integral over the primary loop located at θ_k .

To evaluate the line integral in eq. 2.8 the $d\vec{s}$ element at any point on the loop must be known. Therefore, to accomplish this, we separate the E-W loop into elements a, b, c and d (see Fig. 2.2a) and derive an expression for $d\vec{s}$ on each element. First we derive an expression for $d\vec{s}$ along the field line passing through point $P(r_k, \theta_k, \phi_k)$ in the ionosphere. This expression is then substituted into eq. 2.2 for \tilde{dc} , thus enabling us to obtain the contribution to the line integral in eq. 2.8 due to field-aligned elements a and c.

The equation for a field line through $P(r_k, \theta_k, \phi_k)$ in the ionosphere is

$$r = \frac{r_k}{\sin^2 \theta_k} \sin^2 \theta \quad ; \quad \phi = \phi_k \quad (2.9)$$

One method of obtaining the $d\vec{s}$ element along this particular field line is by setting

$$\begin{aligned} d\vec{s} &= |d\vec{s}| \hat{i}_{||} \\ &= ds \hat{i}_{||} \end{aligned} \quad (2.10)$$

where $\hat{i}_{||}$ is the unit vector parallel to the field line and the magnitude $|d\vec{s}|$ is given by the equation

$$ds = \frac{r}{\sin \theta} (3 \cos^2 \theta + 1)^{\frac{1}{2}} d\theta \quad (2.11)$$

(ds can be derived using eq. 2.9). The unit vector \hat{i} can be found from the relationship

$$\hat{i}_{||} = \hat{i}_{\perp} \times \hat{\phi} \quad (2.12)$$

where

$$\hat{i}_{\perp} = \frac{\nabla (\sin^2 \theta / r)}{|\nabla (\sin^2 \theta / r)|} \quad (2.13)$$

Thus,

$$\hat{i}_{||} = \frac{1}{(3 \cos^2 \theta + 1)^{\frac{1}{2}}} (2 \cos \theta \hat{r} + \sin \theta \hat{\theta}) \quad (2.14)$$

Substituting eq. 2.11 and 2.14 into eq. 2.10 we find

$$d\vec{s} = ds_1 \hat{r} + ds_2 \hat{\theta} + ds_3 \hat{\phi}$$

where

$$\begin{aligned} ds_1 &= 2 r \cot \theta d\theta \\ ds_2 &= r d\theta \end{aligned} \quad (2.15)$$

and

$$ds_3 = 0$$

Since we have expressions for ds_1 , ds_2 and ds_3 , \tilde{dc} (see eq. 2.2) is completely specified and hence, the contributions to the line integral in eq. 2.8 from elements a , and c are

$$\int \sum_i dc_{i1} = \mp \int_{\theta_k}^{\pi/2} \left[\frac{r^2 A_{13}}{R^3} \right] d\theta$$

$$\int \sum_i dc_{i2} = \mp \int_{\theta_k}^{\pi/2} \left[\frac{r}{R^3} (2r_o A_{31} \operatorname{ctn} \theta + r A_{23} + r_o A_{32}) \right] d\theta$$

and

$$\int \sum_i dc_{i3} = \mp \int_{\theta_k}^{\pi/2} \left[\frac{r}{R^3} (-2r_o A_{21} \operatorname{ctn} \theta + r A_{33} - r_o A_{22}) \right] d\theta$$

$$\phi = \begin{Bmatrix} \phi_E \\ \phi_W \end{Bmatrix} \quad (2.16)$$

where the minus sign and $\phi = \phi_E$ pertain to element a , plus sign and $\phi = \phi_W$ to element c , and r (see eq. 2.9) and elements of matrix \tilde{A} (see eq. A1.12) are functions of θ .

The solutions for $d\vec{s}$ along the ionospheric (b) and equatorial elements (d) are much simpler since the flow is along a constant latitude line in both cases. The components of $d\vec{s}$ are

$$ds_1 = 0$$

$$ds_2 = 0$$

$$ds_3 = r \sin \theta d\phi \quad (2.17)$$

where

$$r = r_k$$

and

$$\theta = \theta_k$$

for the element b and

$$r = R_E = \frac{r_k}{\sin^2 \theta_k}$$

$$\theta = \frac{\pi}{2}$$

for element d. Therefore, the contributions to the line integral from elements b and d are

$$\int \sum_i dc_{i1} = \mp \int_{\phi_W}^{\phi_E} \left[\frac{r^2}{R^3} (-\sin \theta A_{12}) \right] d\phi$$

$$\int \sum_i dc_{i2} = \mp \int_{\phi_W}^{\phi_E} \left[\frac{r}{R^3} (r_0 A_{33} - r A_{22}) \sin \theta \right] d\phi$$

and

$$\int \sum_i dc_{i3} = \mp \int_{\phi_W}^{\phi_E} \left[-\frac{r}{R^3} (r_0 A_{23} + r A_{32}) \sin \theta \right] d\phi$$

$$r = \begin{cases} r_k \\ R_E \end{cases}$$

$$\theta = \begin{cases} \theta_k \\ \pi/2 \end{cases}$$

(2.18)

where the minus sign, $r = r_k$ and $\theta = \theta_k$ pertain to element b ; the plus sign, $r = R_E$ and $\theta = \pi/2$ to element d . Substituting eq. 2.16 and 2.18 into eq. 2.8, we obtain a solution for the magnetic field associated with an E-W three-dimensional current system as shown in Fig. 2.1.

In the following numerical results H , D and Z are used to represent $-B_3$, B_2 and $-B_1$ respectively. The numerical method we used in evaluating integrals such as those in eq. 2.8 is discussed in appendix A3.

Fig. 2.4A shows the latitude profile which would be observed on a meridian 4° east of ϕ_c for an E-W current system 20° long and 5° wide evaluated using eq. 2.8. Fig. 2.4B, C and D show the individual contributions to the magnetic field from the ionospheric, western and eastern Birkeland sheet currents respectively. Since the contribution from the equatorial sheet current for this particular system is only

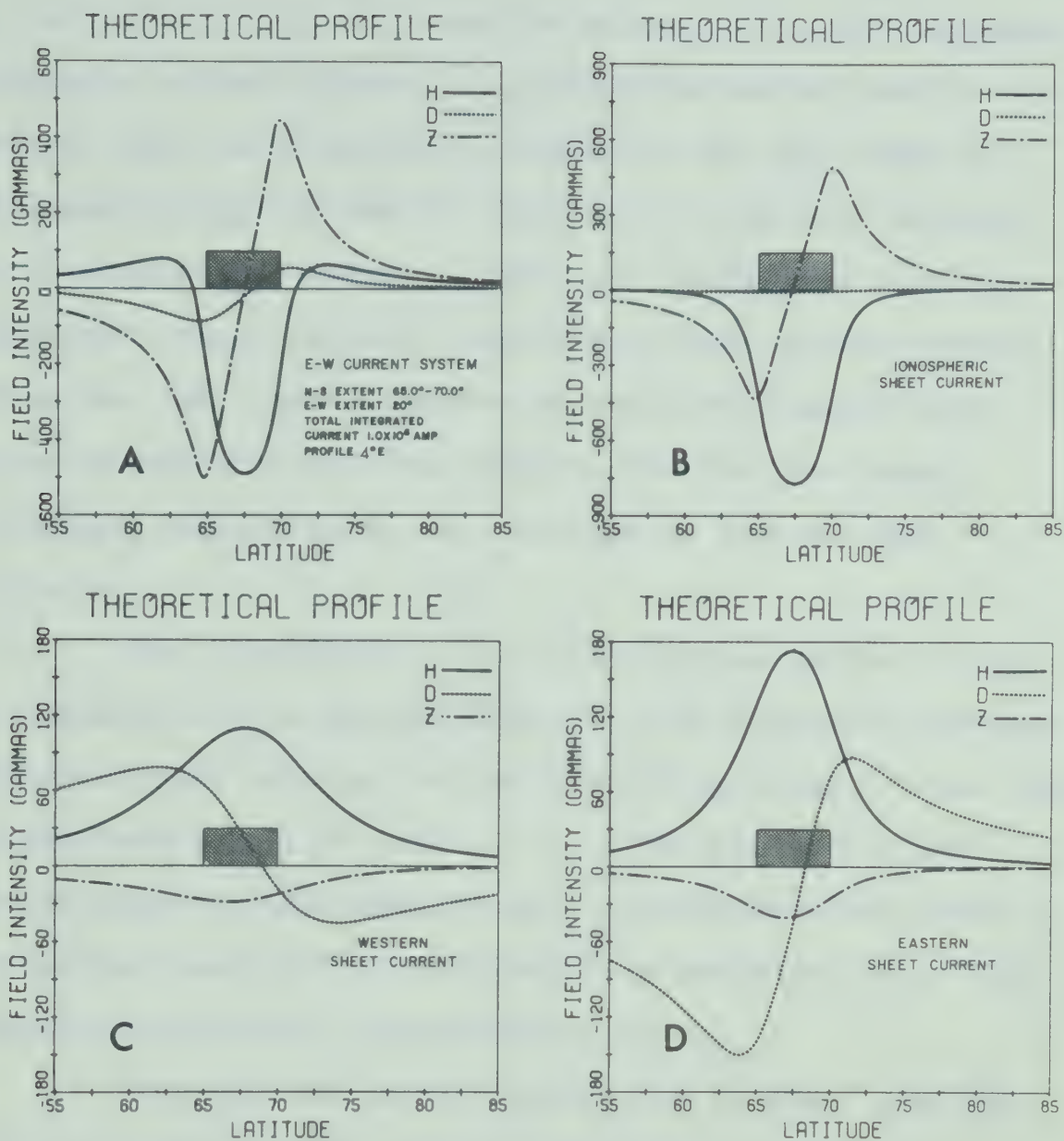


Fig. 2.4 Latitude profile of the total field associated with an E-W three dimensional current along with profiles attributed to each individual sheet current.

of the order of 1γ at these latitudes, it is not included separately in this figure. The contribution to the H profile from the Birkeland currents can be very large as evidenced in Fig. 2C and D ($\sim 300\gamma$ at θ_c) and thus substantially reduces the effect of the $-H$ regime due to the ionospheric sheet current. North and south of the current system the $+H$ contribution from the Birkeland currents dominates over the $-H$ contribution of the ionospheric electrojet, resulting in $+H$ regimes at low and high latitudes.

The D profile in Fig. 2.4A represents the difference between two large contributions from Birkeland currents positioned east and west of the central meridian. Since the latitude profile is 4° east of ϕ_c , the field from the eastern sheet is the dominant one. Therefore the D profile is negative south of θ_c and positive north of θ_c . The opposite is true for a profile west of ϕ_c .

Although the main contribution to the Z profile is due primarily to the ionospheric sheet current, a significant contribution is caused by Birkeland currents ($\sim 70\gamma$ at θ_c). The effects of Birkeland currents on the Z profile are discussed later in this chapter in conjunction with E-W asymmetries in the flow of Birkeland currents into and out of the auroral zone.

Fig. 2.5 shows a series of profiles at various longitudes east and west of ϕ_c for the same current system as shown in Fig. 2.4. Figs. 2.5D and 2.5E illustrate the N-S asymmetry introduced in the Z profile east (or west) of the end of the ionospheric portion of the current system. This proves to be useful in the analysis of magnetic observations. In Fig. 2.5F we show an example of a profile west of ϕ_c to illustrate the reversal of the sign of the D profile.

Contour plots of the H , D and Z components as a function of latitude and longitude are shown in Fig. 2.6. We have found that such plots as these are very useful for mapping the positive and negative regimes of each component for various current systems. They are also useful in allowing easy visual comparison of the magnetic perturbation pattern of theoretical current systems with and without Earth induction effects taken into account.

2.2.3 North-South (N-S) current system

A model of a N-S three-dimensional current system is illustrated in Fig. 2.7. In this system the Birkeland currents flow from the magnetospheric equatorial plane to the northern edge of the southward directed ionospheric sheet

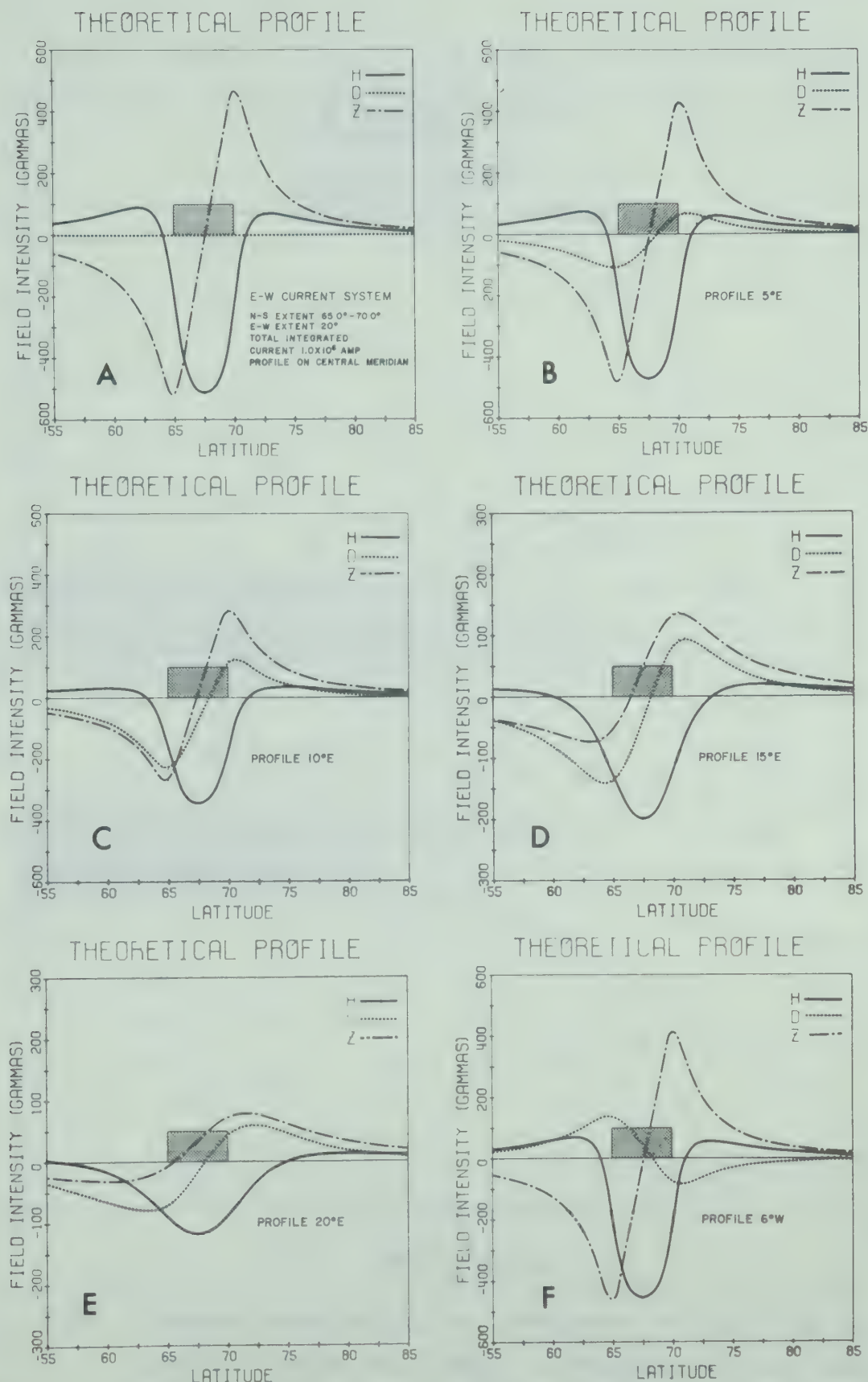


Fig. 2.5 Series of latitude profiles at various longitudes east and west of the central meridian.

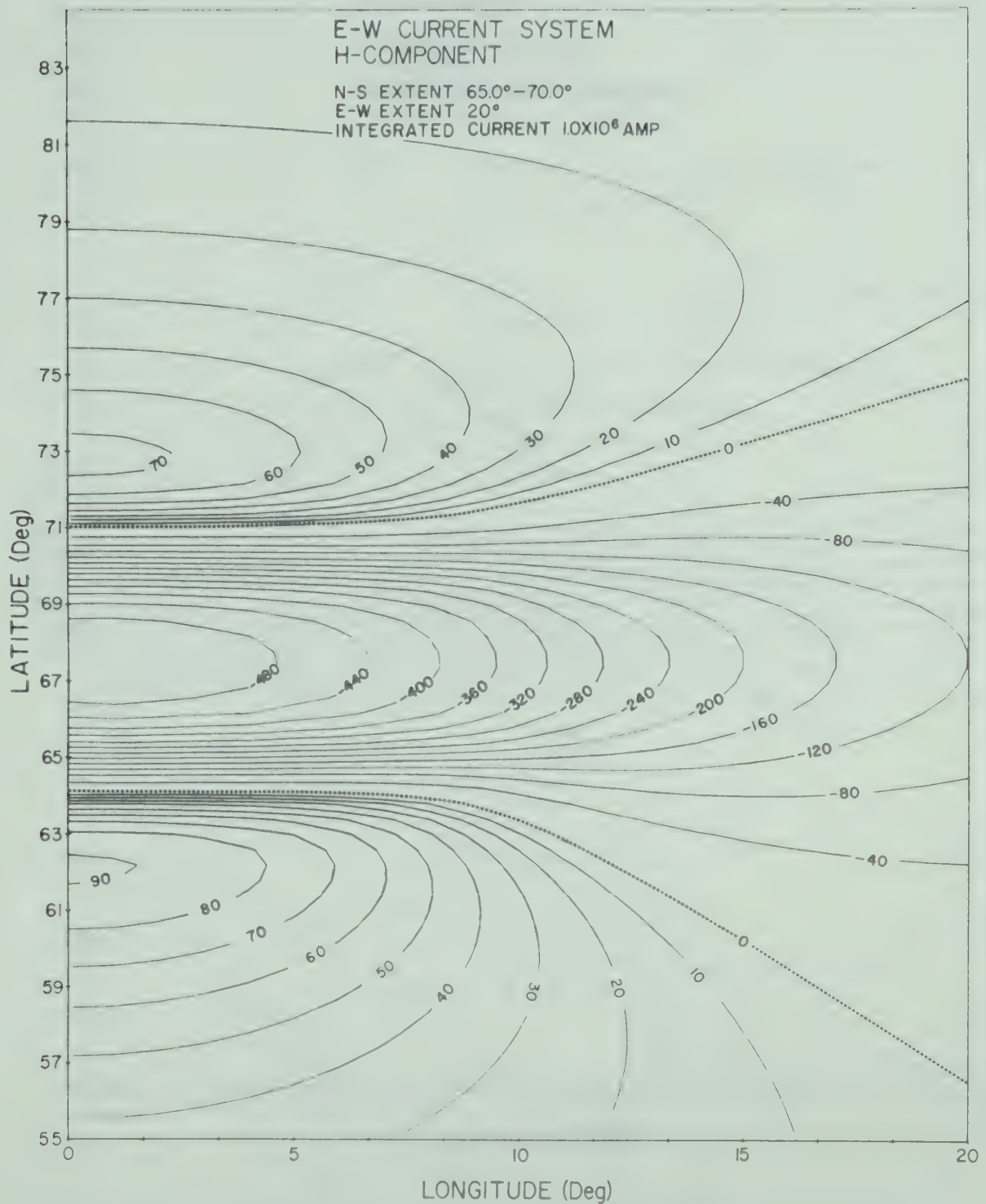


Fig. 2.6A Contour plot of the H component for an E-W current system. Note the large $-H$ regime off the ends of the current system (longitude $> 10^0$) even though there is no overhead ionospheric current.

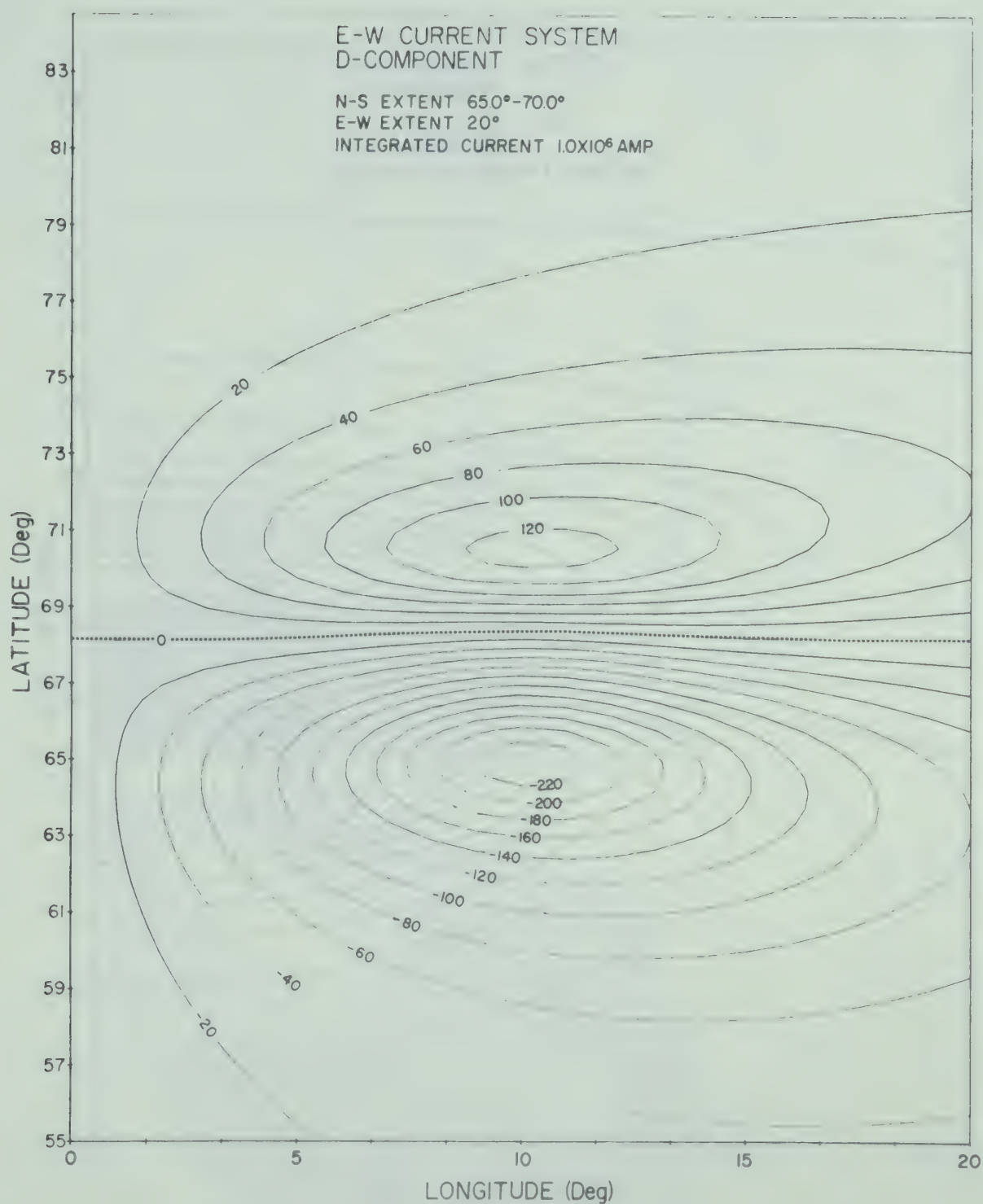


Fig. 2.6B Contour plot of the D component for an E-W current system.

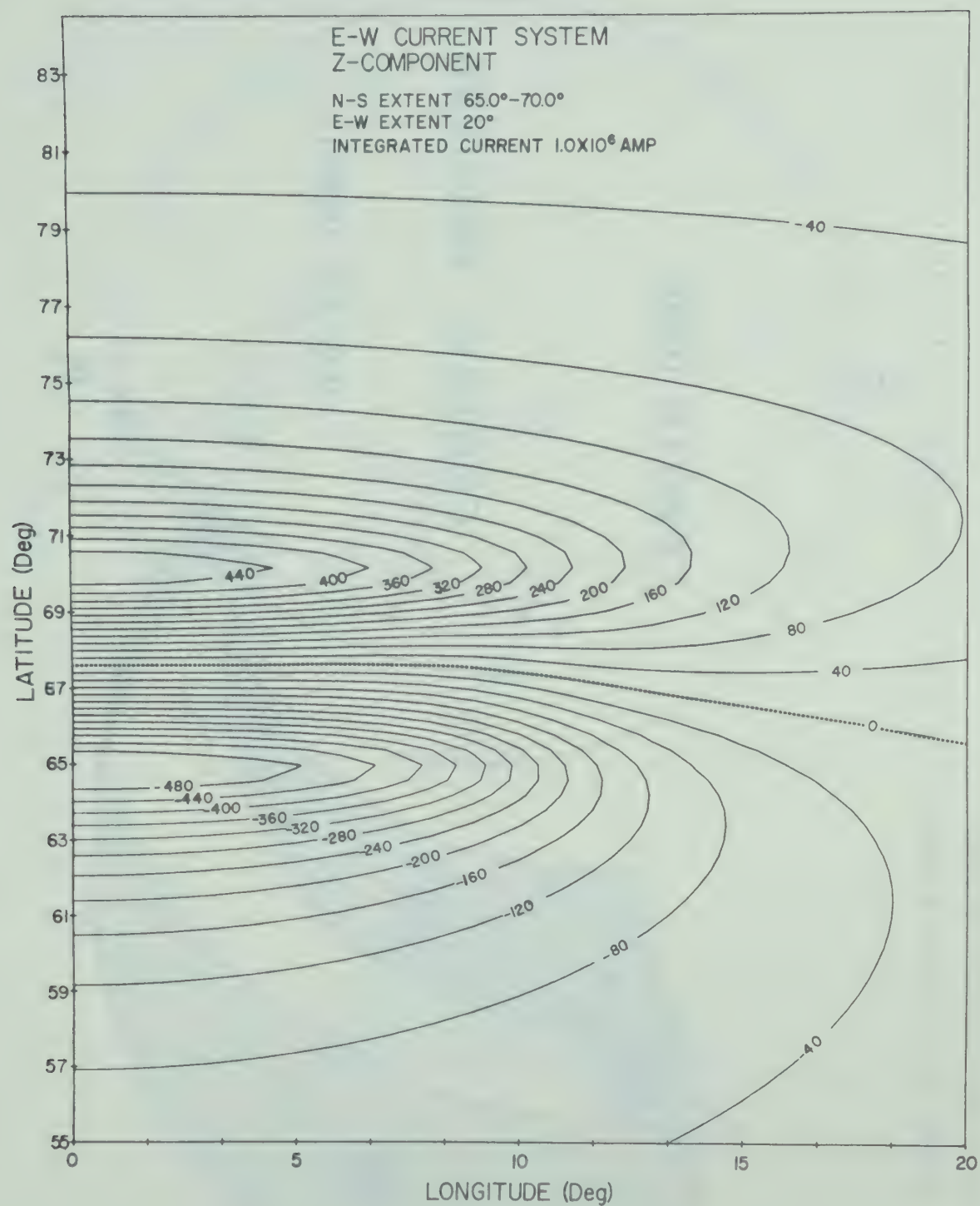


Fig. 2.6C Contour plot of the Z component for an E-W current system.

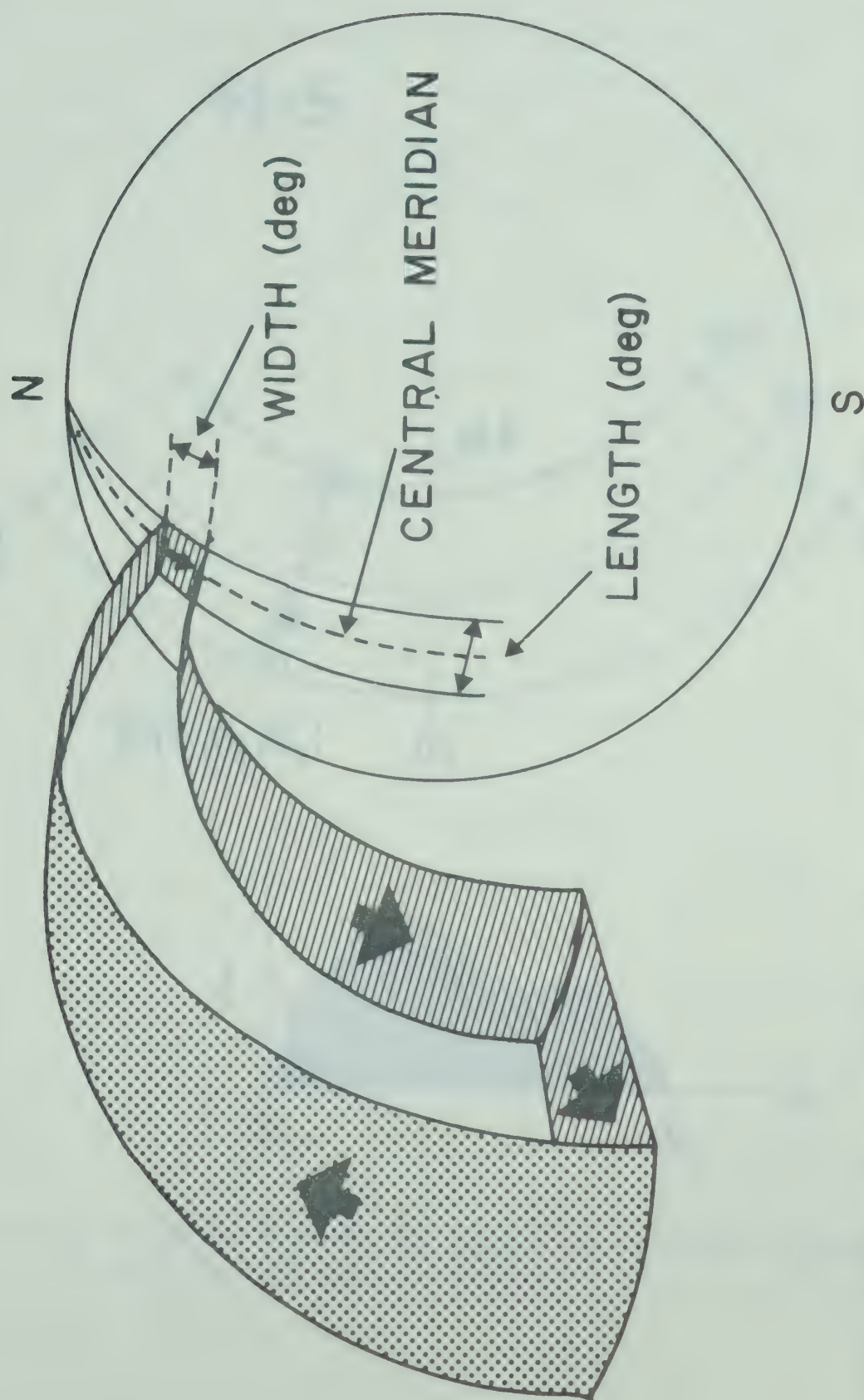


Fig. 2.7 Model of a three-dimensional N-S current system with finite longitudinal and latitudinal extent.

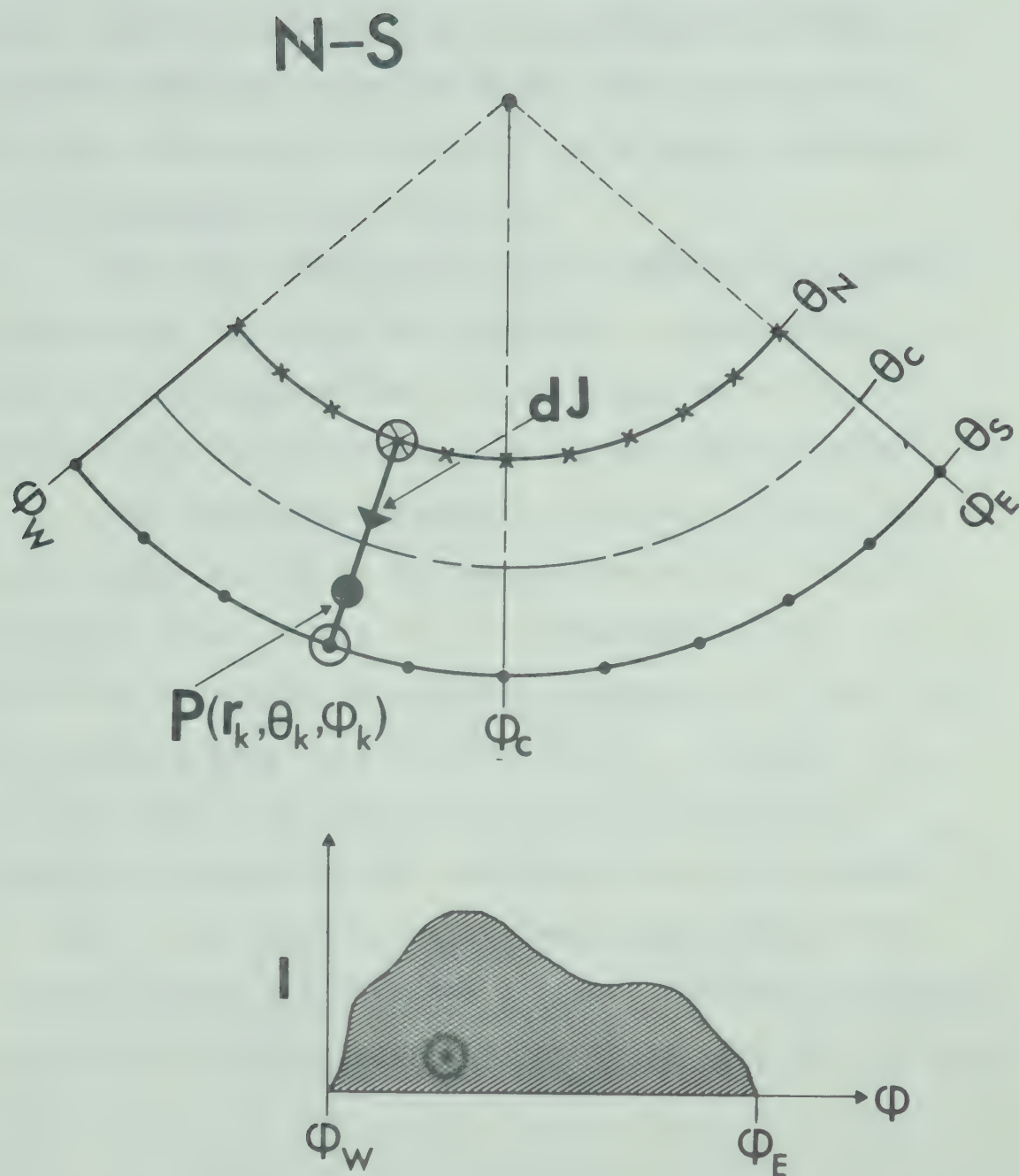


Fig. 2.8 Diagram showing the ionospheric sheet current for the N-S current system.

current and out at the southern edge to the equatorial plane where the path of current flow is completed by a sheet current directed away from the earth. We can obviously reverse the direction of current flow to give a northward directed ionospheric sheet current.

Since the mathematical development we presented for calculating the field due to an E-W current system is similar to that required for a N-S system, we will only present a brief discussion concerning the latter system.

The ionospheric element of the N-S primary loop (see Fig. 2.2b) we use in the evaluation of the field due to the model shown in Fig. 2.7 is presented in Fig. 2.8. In this case we obtain an analytic expression for the field of this primary loop as a function of ϕ_k . Hence, the total field due to an entire N-S current system can be evaluated by integrating this expression over the length ϕ_W to ϕ_E . The definitions of length and width of the N-S current system are the same as those for the E-W system. We also define an expression similar to eq. 3.6 for the total current J as

$$J = \int_{\phi_W(\theta_c)}^{\phi_E(\theta_c)} I(\phi_k) r_k \sin \theta_k d\phi_k \quad (2.19)$$

where $I(\phi_k)$ is the longitudinal current distribution function. Therefore we can write an expression for the total field similar to eq. 2.8 as follows:

$$B_j(r_o, \theta_o, \phi_o) = k \int_{\phi_w}^{\phi_E} I(\phi_k) \left[\int_{\text{loop}(\phi_k)} \sum_i dc_{ij} \right] r_k \sin \theta_k d\phi_k \quad (2.20)$$

where $\int_{\text{loop}(\phi_k)}$ is the line integral over the N-S primary loop located at ϕ_k .

Since we have already calculated the line integral over an E-W primary loop (see eq. 2.16 and 2.18), we do not believe that a similar calculation for the N-S primary loop is warranted here.

Fig. 2.9 shows the latitude profile 2°E of ϕ_c for a N-S current system 4° long and 4° wide. Again we show the individual contributions to the magnetic field from the separate portions of the current system. Fig. 2.10 shows latitude profiles east and west of ϕ_c . The D profile is symmetric in longitude with respect to ϕ_c while the H and Z profiles change sign from one side of the central meridian

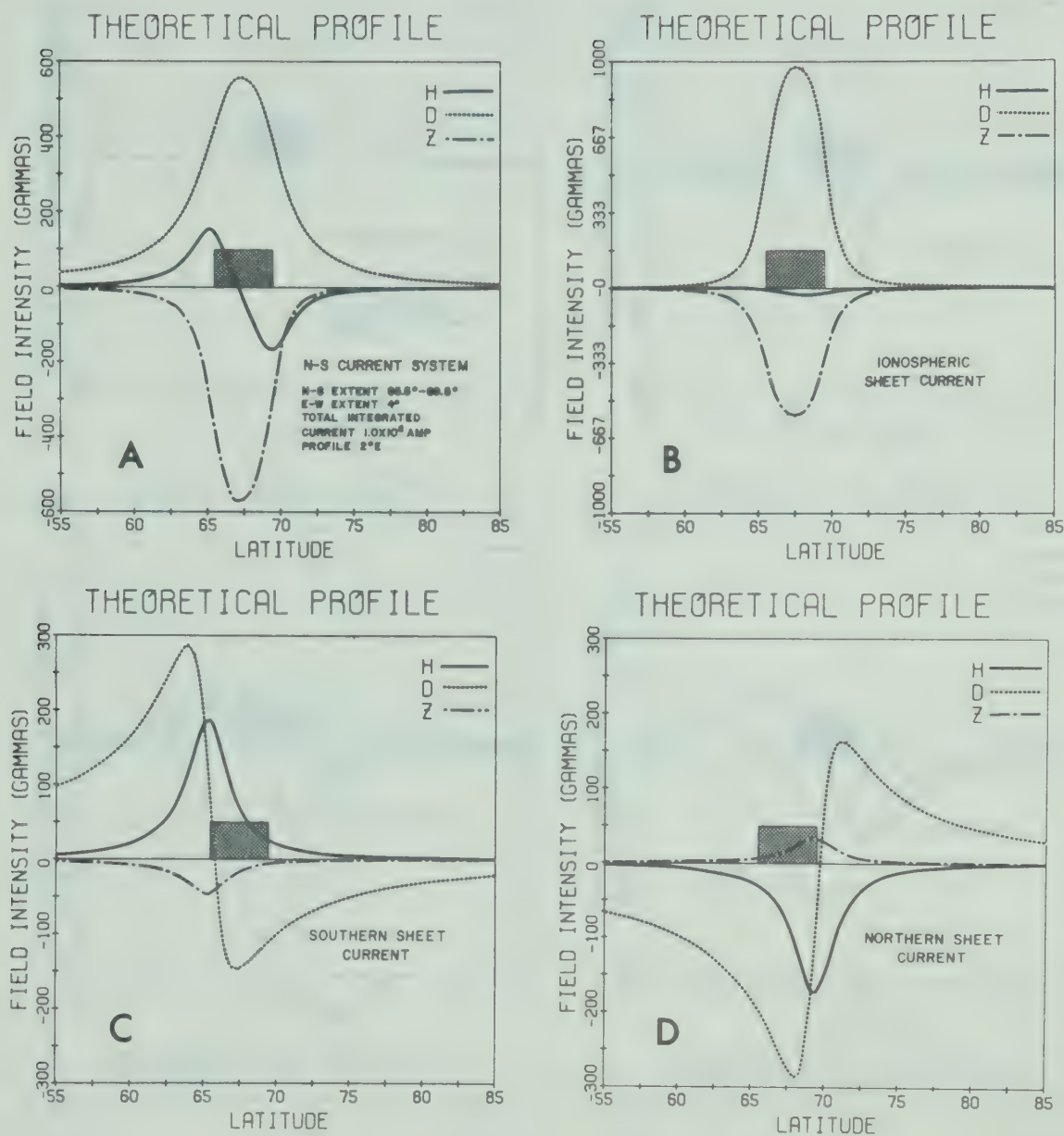


Fig. 2.9 Latitude profile of the total field associated with the N-S three-dimensional current system along with latitude profiles attributed to each individual sheet current.

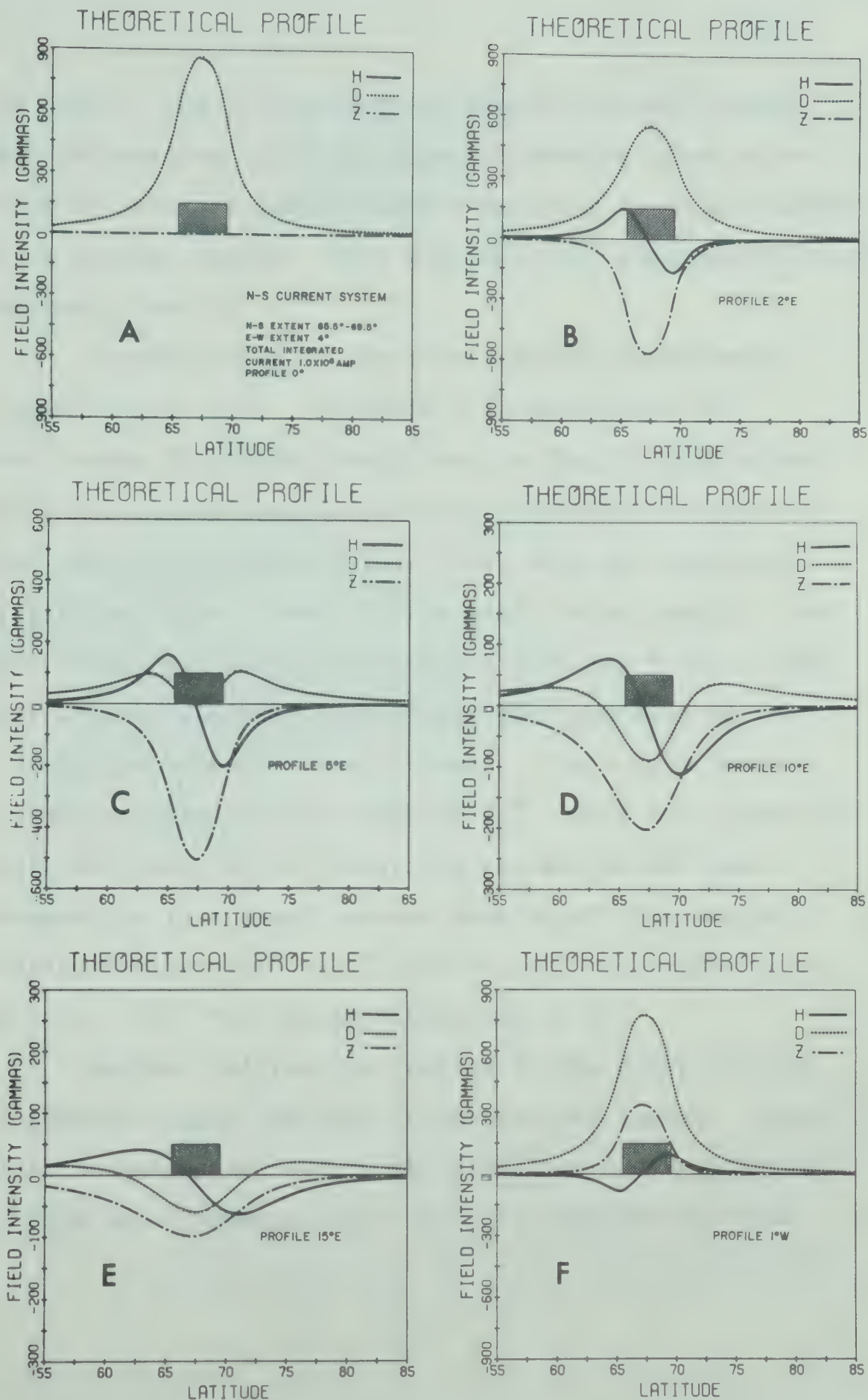


Fig. 2.10 Series of latitude profiles at various longitudes east and west of the central meridian.

to the other. The D component for the N-S current system is most interesting since the magnetic perturbations associated with eastward and westward travelling loops and surges are of a similar nature. This similarity is discussed further in Chapters V and VI.

Contour plots of the three separate components are shown in Fig. 2.11. Although this particular N-S current system is probably much less in longitudinal extent (length) than those observed in the ionosphere and magnetosphere, these particular contour plots show the important aspects of any such current system with finite length. For example, from Fig. 2.10C and D we see that the Z and H components are the dominant ones to the east and west of the ends of the ionospheric sheet current. For a much longer N-S current system with a length of 60° (~ 2550 km), width of 4° (~ 450 km) and a total integrated current of 10^6 amps (corresponding to a sheet current density of ~ 0.4 amp/m), the maximum value of Z at 30° east of ϕ_c is $\sim -106\gamma$ compared with $\sim 13\gamma$ for the maximum value of D.

Another interesting feature is the depression of the D component east and west of the current system. These negative D regions are due to the fact that the D component field from the Birkeland sheet currents dominate over the

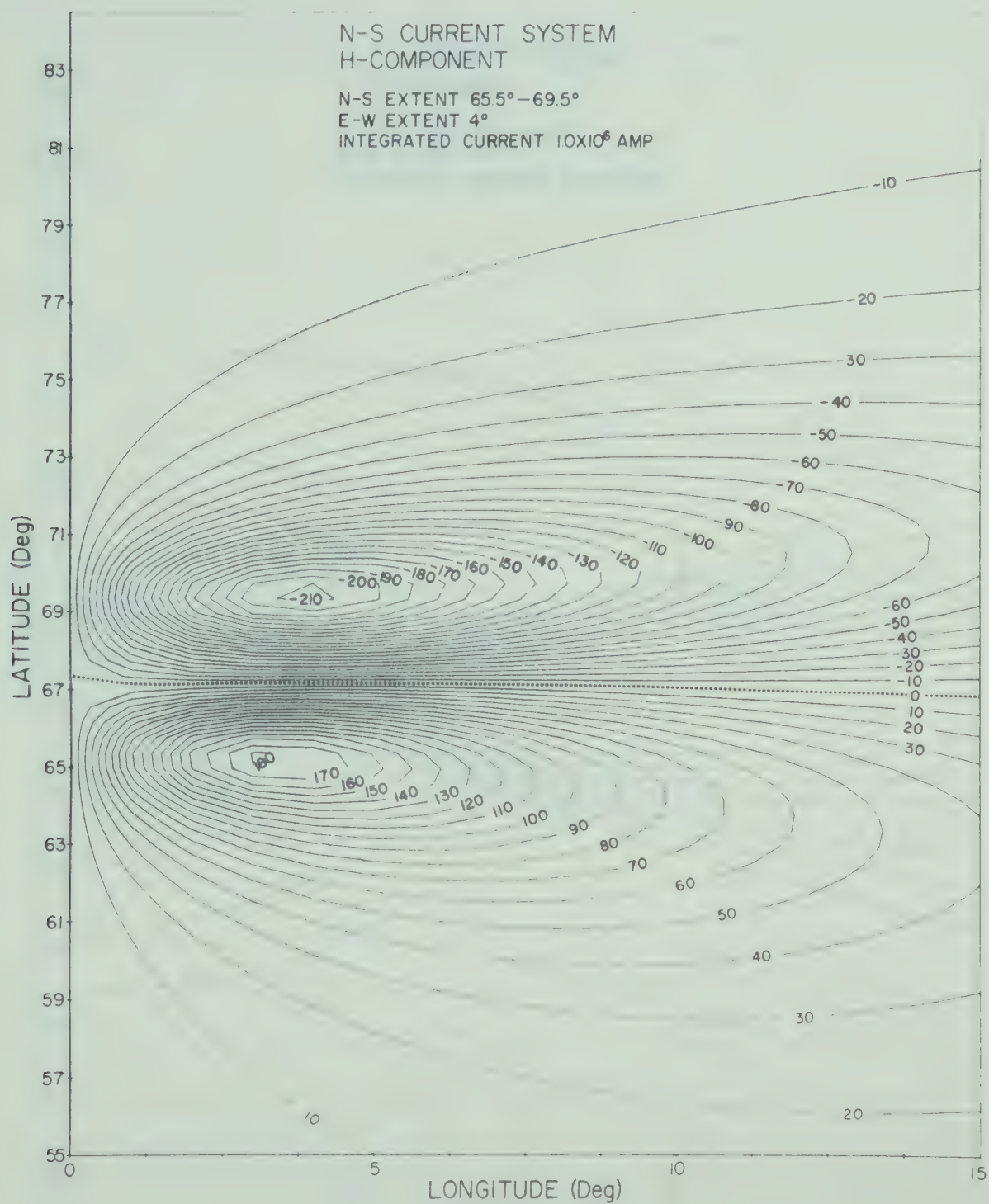


Fig. 2.11A Contour plot of the H component for a N-S current system. Note the similarity between this contour and the one shown in Fig. 2.6B.

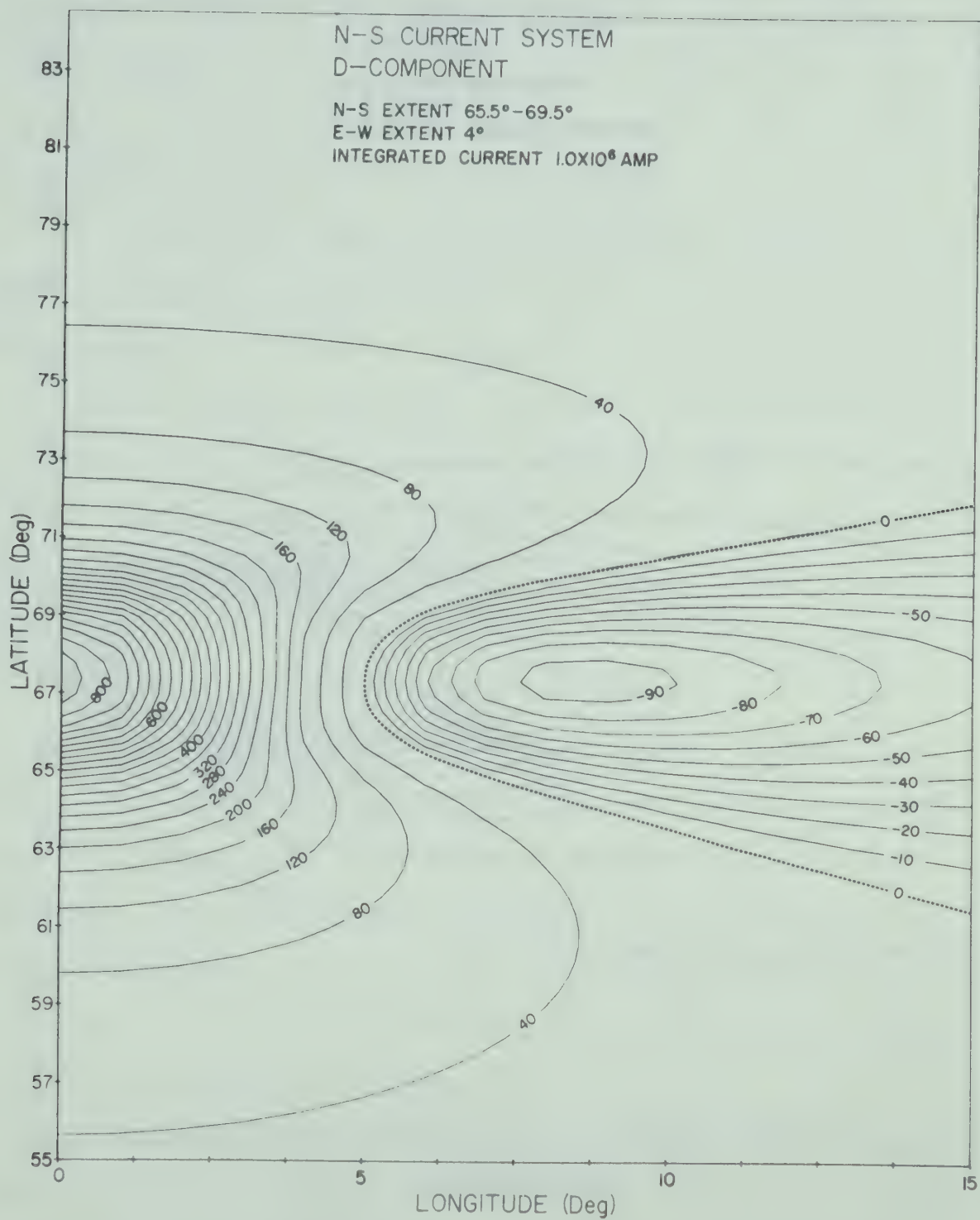


Fig. 2.11B Contour plot of the D component for a N-S current system.

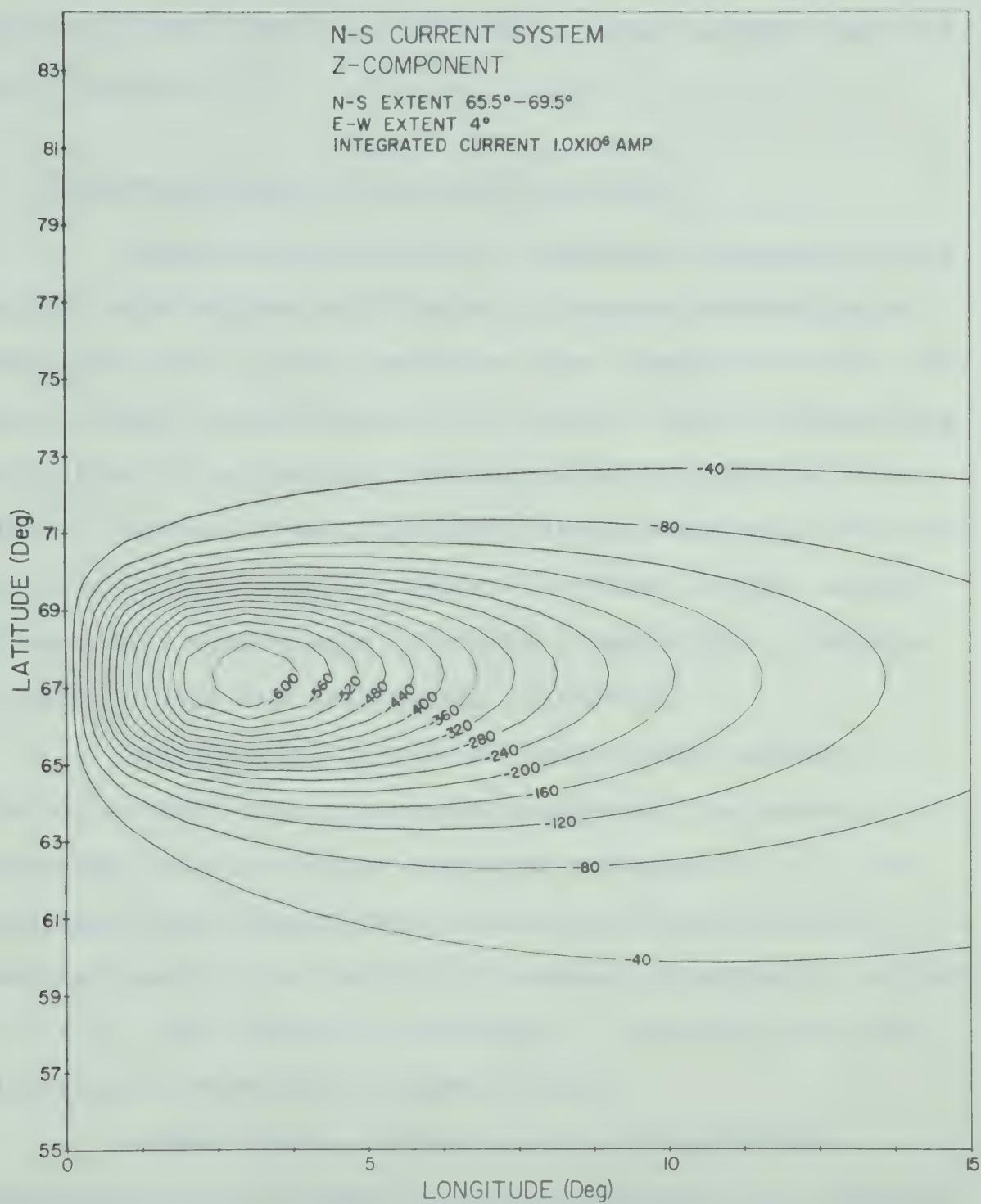


Fig. 2.11C Contour plot of the Z component for a N-S current system.

positive D field from the ionospheric sheet current (see Fig. 2.9B, C and D).

2.3 Induced currents in a conducting Earth

Since the variations of the Earth's magnetic field contain contributions attributed to induced currents in a conducting Earth as well as those from external currents, any model current system necessary to explain these observations should contain an induced current system in addition to an external current system. Although the conductivity structure of the Earth is extremely complex (Rikitake, 1966), we must assume a very simple model for this conductivity structure in order to make the mathematics tractable.

Boström (1971) used the image dipole method to obtain the field due to currents induced by the three-dimensional current system discussed in Appendix A1.2. He represented the conductivity structure of the Earth by a spherical shell of an infinitely conducting medium of radius b ($b < a$, the radius of the Earth). The results of this solution are presented in Appendix A2.4.

Ashour (1971) derived a set of relationships between the field produced by currents induced in a uniformly finite conducting spherical shell and the field of an arbi-

trary external current system provided the external field is known numerically. We have presented a much simpler derivation of Ashour's results in Appendix A2.2 for the case of infinite conductivity. The relationships between the internal (induced) and external (inducing) components of the magnetic field (equations A2.18, A2.30 and A2.31 in appendix A2.2) are

$$B_1^i(a, \theta_0, \phi_0) = - \left(\frac{b}{a}\right)^3 B_1^e(r'_0, \theta_0, \phi_0) \quad (2.21)$$

$$B_{2,3}^i(a, \theta_0, \phi_0) = \left(\frac{b}{a}\right)^3 B_{2,3}^e(r'_0, \theta_0, \phi_0) - \frac{1}{ab} \int_0^{r'_0} r_0 \cdot B_{2,3}^e(r_0, \theta_0, \phi_0) dr_0 \quad (2.22)$$

where (a, θ_0, ϕ_0) represents the observation position on the surface of the Earth ($r_0 = a$) and

$$r'_0 = \frac{b^2}{a}$$

b being the radius of the spherical shell (see Fig. A2.1) in Appendix A2.2).

The vertical component of the induced field given by eq. 2.21 can be evaluated by evaluating the vertical component of the external field at r_0' . This is also true for the horizontal components with regard to the first term in eq. 2.22. We see however, that the evaluation of the second term in eq. 2.22 is more difficult because of the integration with respect to r_0 . If an analytical expression for the external field exists such that the integration can be performed analytically, then eq. 2.22 becomes readily applicable. If this integration cannot be accomplished analytically, numerical methods would then have to be used. Since the evaluation of the external horizontal components normally requires numerical integration, the additional integration over r_0 would probably necessitate the use of large amounts of computer time. We have found that the horizontal components of the external field given by eq. 2.1 can be integrated analytically with respect to r_0 , thus allowing us to obtain a solution for the induced field due to an arbitrary current system external to the conducting shell. The complete solution for the three components of the induced field can be expressed as

$$B_j^i(a, \theta_0, \phi_0) = kJ \int_C \sum_i \left[\epsilon_j \left(\frac{b}{a}\right)^3 dc_{ij}' - \left(\frac{1}{ab}\right) dc_{ij}'' \right] \\ (\epsilon_1 = -1, \epsilon_{2,3} = 1) \quad (2.23)$$

where dc'_{ij} and dc''_{ij} are elements of matrices \tilde{dc}' and \tilde{dc}'' respectively and are defined in Appendix A2.3 (see Appendix A2.3 for the derivation of eq. 2.23). Since most of the variables in \tilde{dc} are also common to \tilde{dc}' and \tilde{dc}'' , the inclusion of induction effects in the model current system discussed in the previous section increases the computer time required by less than a factor of 1/10.

The induced field and total field (sum of both the induced and external fields) for various depths (a-b) of the superconductive shell below the surface of the Earth are presented in Fig. 2.12. The physical parameters of the E-W external current system are the same as those for the system described in section 2.2.2. The latitude profiles in Fig. 2.12 pertain to a meridian 5° east of ϕ_c and thus can be compared with the profile (representing the field due to the external system) shown in Fig. 2.5B. The main feature readily apparent in this series of profiles is the large value of the induced Z component at both high and low latitudes. As a result of this effect the total Z component is highly attenuated at these latitudes. This effect was reported previously by Boström (1971).

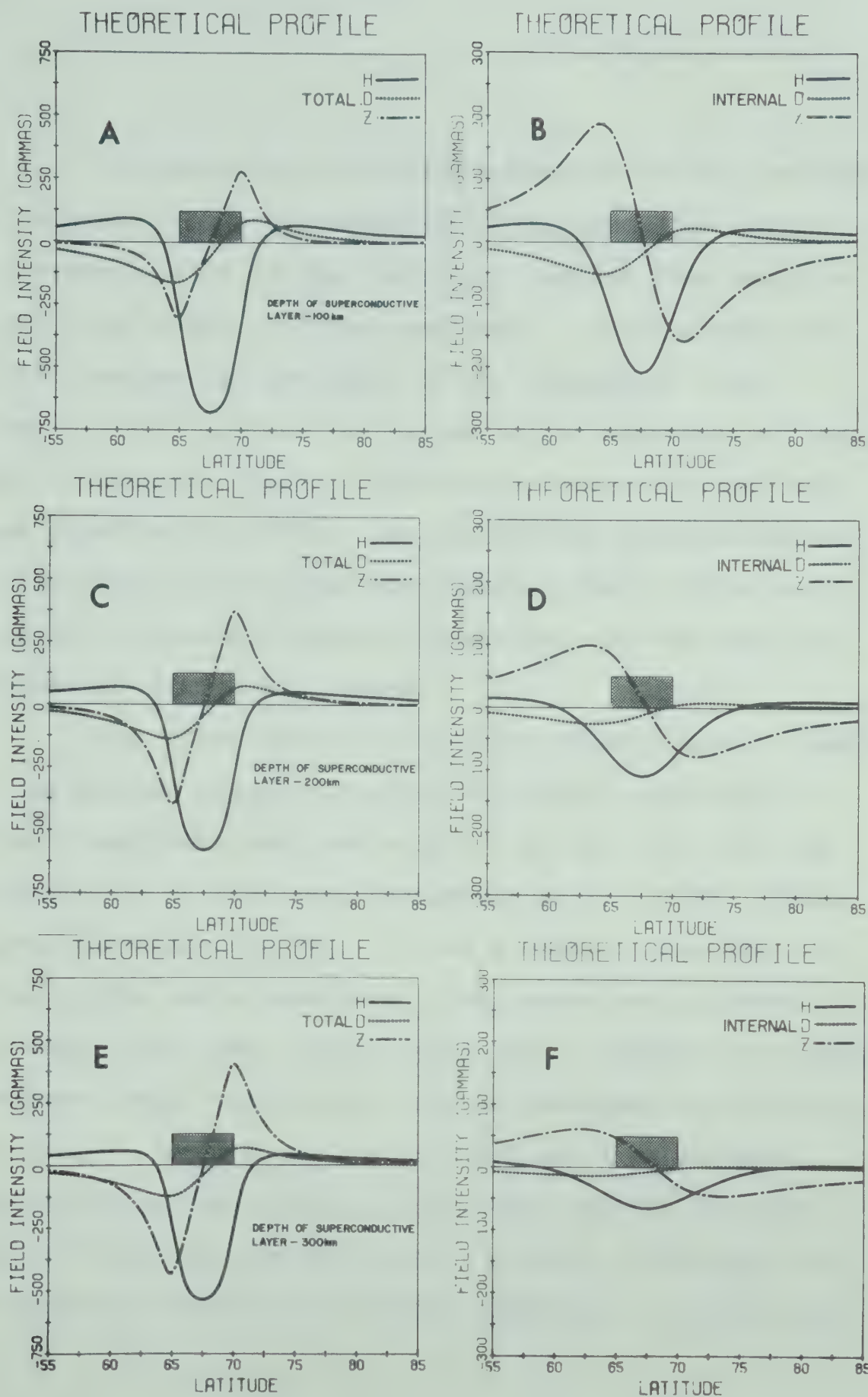


Fig. 2.12 Total field (sum of both the induced and external fields) and induced field for various depths of the superconductive shell below the surface of the Earth computed for an E-W current loop.

Although the horizontal components of the internal and external fields are normally of the same sign, this is not, however, true in the transition regions from negative to positive values of these components. This becomes more evident the greater the depth of the conductive layer. Listed in Table 2.1 are the ratios of the magnitude of induced field to external field at various latitudes for the three cases shown in Fig. 2.12. The interesting feature apparent in this table is the large variation in these ratios with respect to latitude, the smaller ratios occurring near the latitude of the current system.

To illustrate the effects of induction as a function of longitude we present a series of latitude profiles at various longitudes east and west of ϕ_c in Fig. 2.13 and contour plots of the three components in Fig. 2.14. These figures correspond to Fig. 2.5 and 2.6 which show similar contour plots where induction is not taken into account. It is evident from these figures that the Z component is highly attenuated away from the ends of the ionospheric portion of the current system as well as at high and low latitudes. Another interesting feature is the small effect that the induced field has upon the spatial extents of the positive and negative regimes of all three components. We also see

Table 2.1 Ratio of internal to external field

$$(F^i/F^e ; F = (H^2 + D^2 + Z^2)^{\frac{1}{2}}).$$

Depth of Superconductive Layer (a-b)

Latitude	100 km	200 km	300 km
55 ⁰	0.836	0.691	0.560
60	0.736	0.526	0.375
65	0.416	0.221	0.133
67.5	0.452	0.238	0.142
70	0.400	0.210	0.127
75	0.751	0.532	0.377
80	0.874	0.725	0.590
84.5	0.924	0.816	0.709

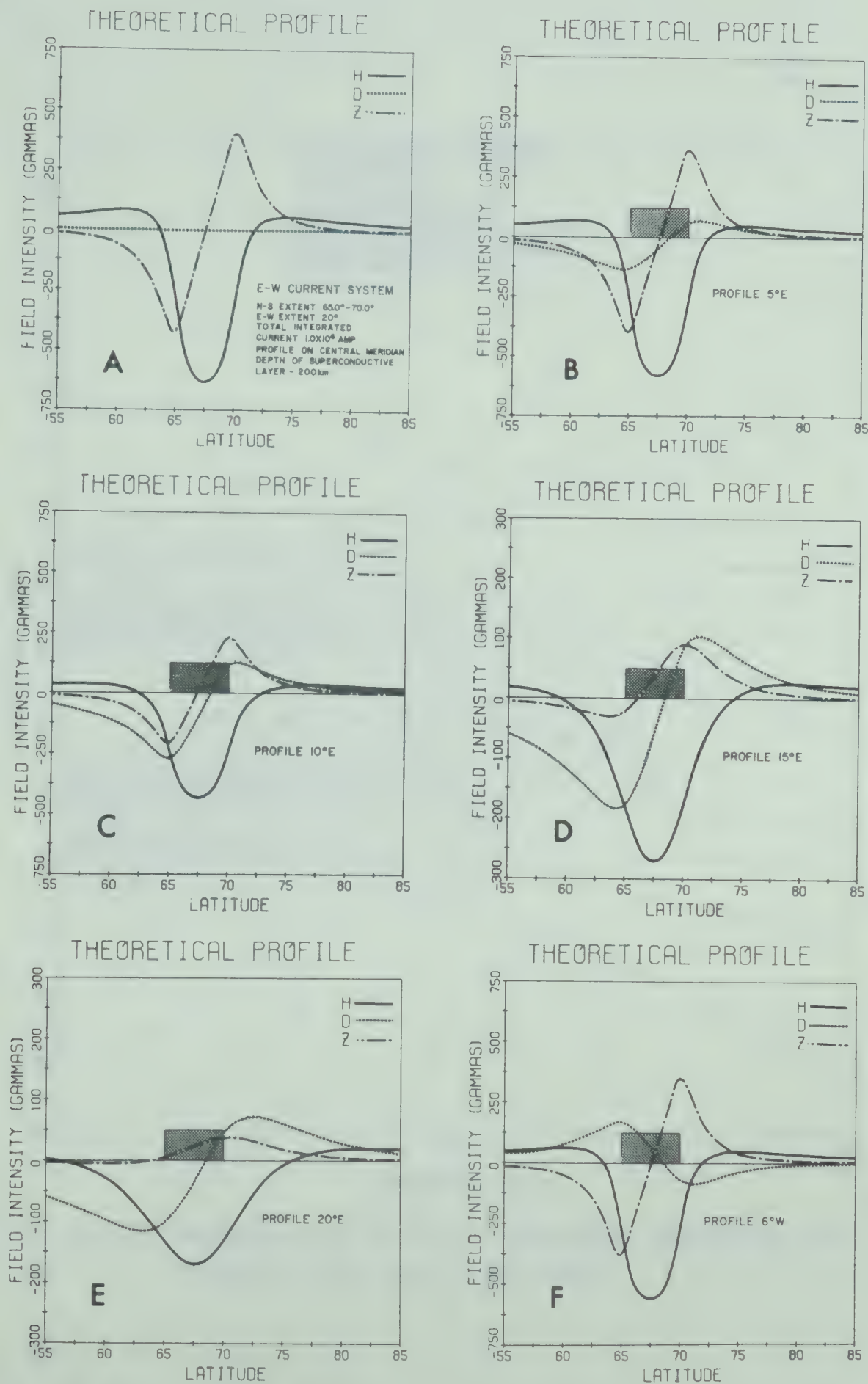


Fig. 2.13 Latitude profiles of the total field associated with an E-W three-dimensional current system (see Fig. 2.4 for the external field).

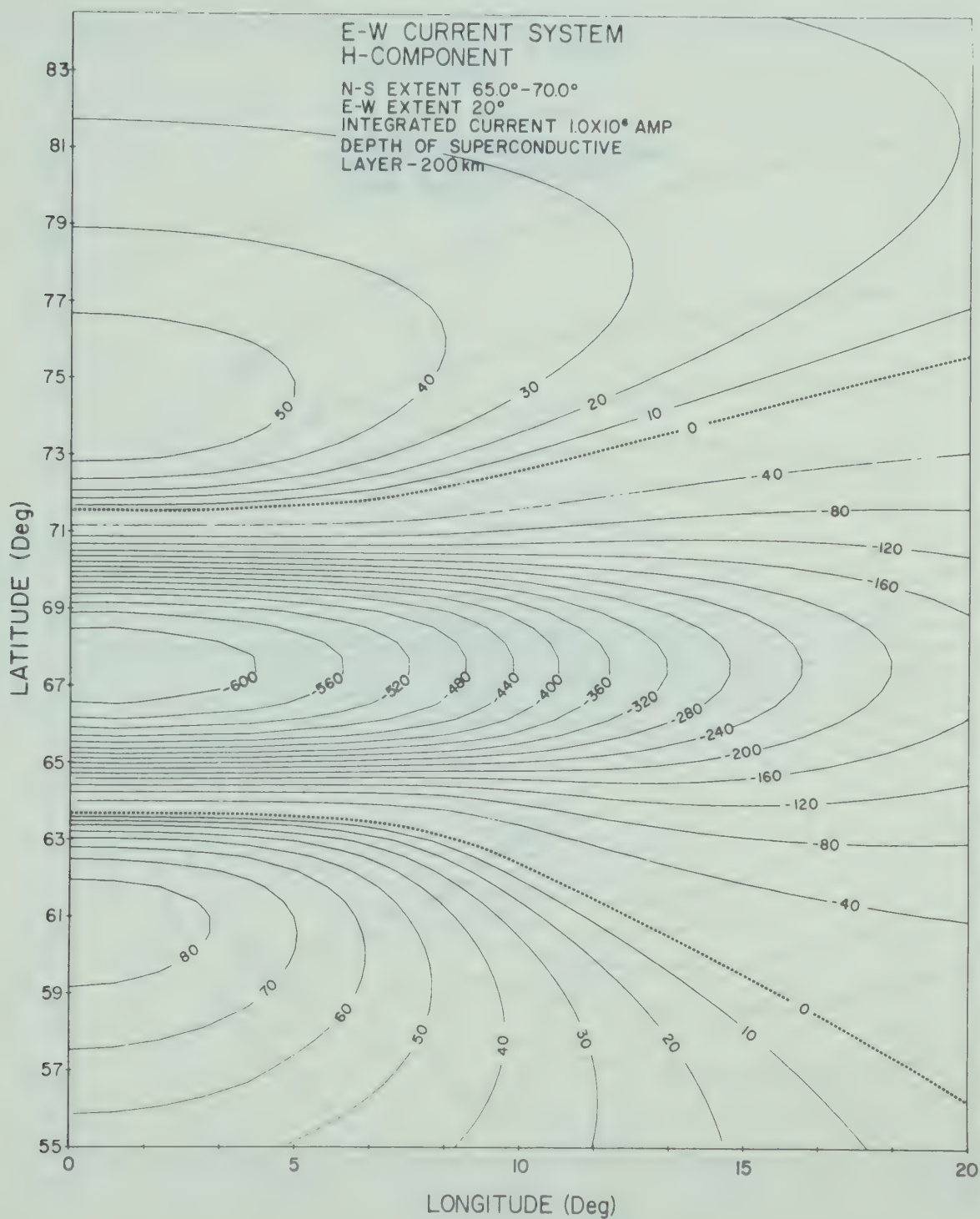


Fig. 2.14A Contour plot of the H component including the induced field (see Fig. 2.6A).

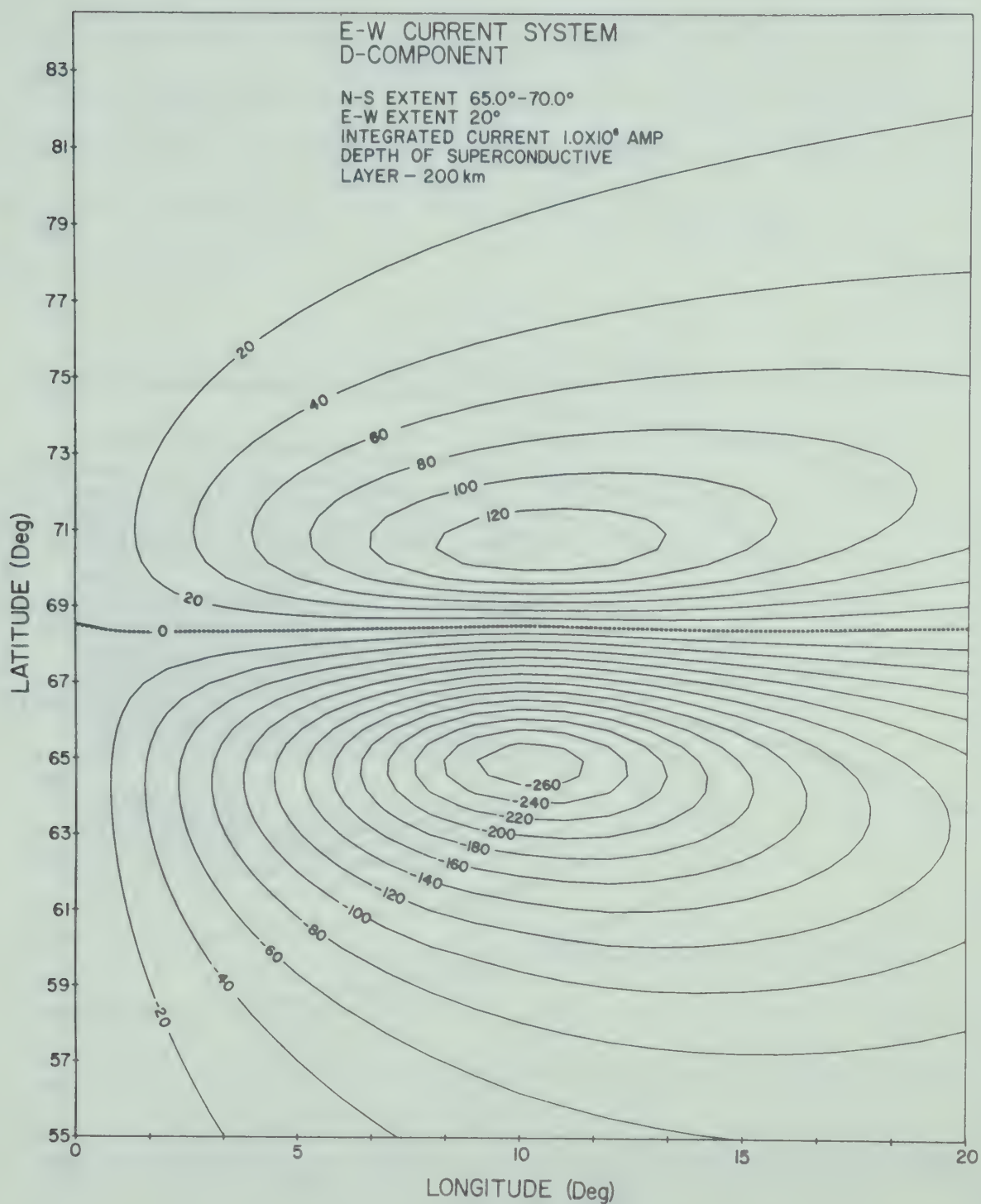


Fig. 2.14B Contour plot of the D component including the induced field (see Fig. 2.6B).

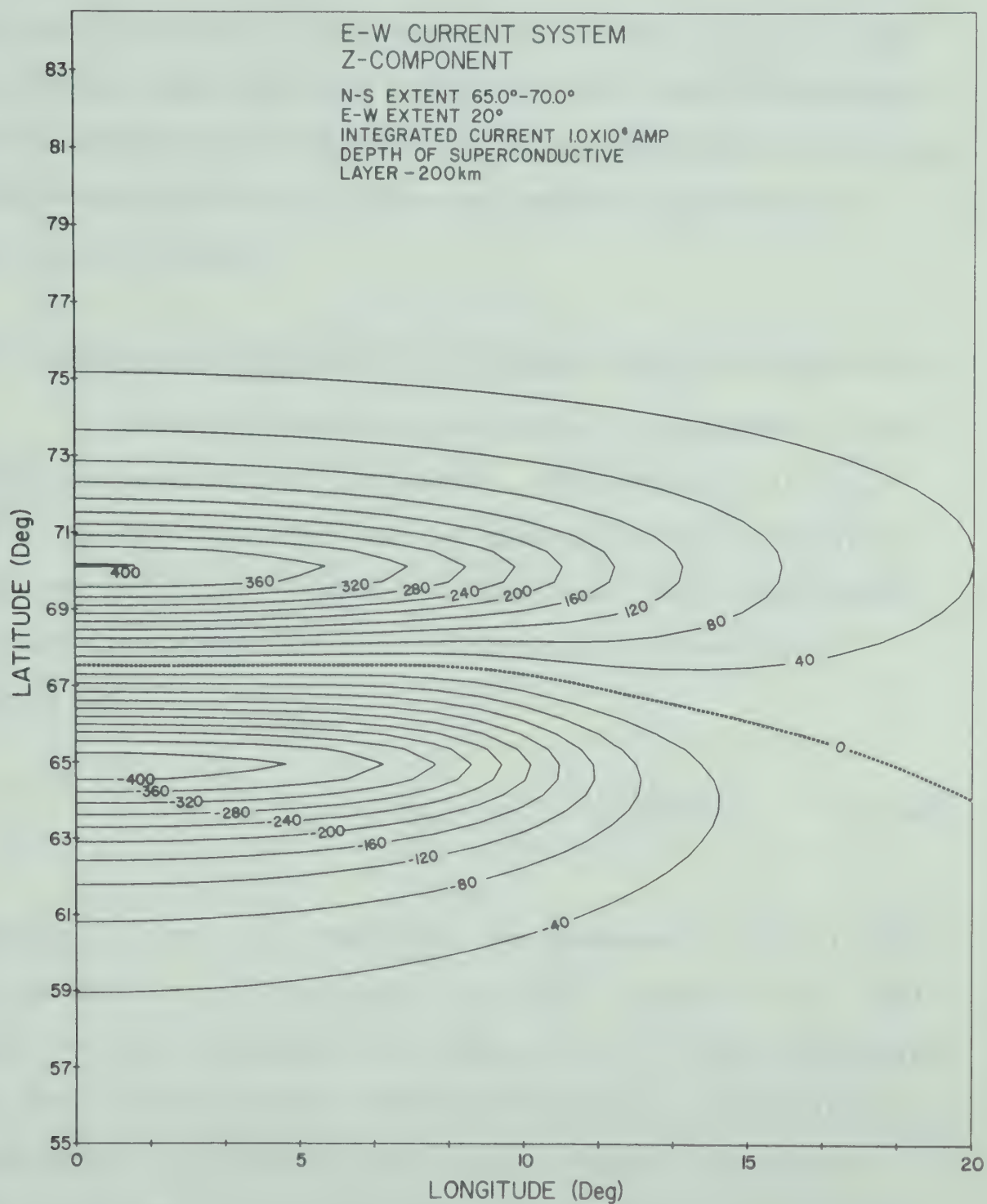


Fig. 2.14C Contour plot of the Z component including the induced field (see Fig. 2.6C). Note the high attenuation of the Z component away from the current system.

that the locations of the maxima and minima for each component remain approximately the same. This fact is important in our discussion in Chapter III in conjunction with the use of latitude profiles to infer the physical parameters of the current system.

2.4 A model current system coincident with the auroral oval

Since the westward electrojet is observed to flow along the auroral oval (Feldstein, 1963; Akasofu et al., 1965), we have modified the E-W current system to include such current flow. Kamide and Fukushima (1970) considered current flow along the model auroral oval given by the expression

$$\theta = \theta_1 + (\theta_2 - \theta_1) \frac{1 + \cos \phi}{2} \quad (2.24)$$

wherein θ_1 and θ_2 represent the geomagnetic colatitudes at midnight ($\phi = 0$) and noon ($\phi = 180^\circ$) respectively. Their model current system was confined entirely to the ionosphere and thus did not contain Birkeland currents. Although we developed a three-dimensional current system using their model oval, we prefer a parabola representation of the oval instead. The advantages of such a representation will

become apparent in the ensuing discussion.

Since we are mainly interested in modelling the nightside portion of the oval, the following expression is used:

$$\theta = \frac{a b}{[b^2 \cos^2 \phi + a^2 \sin^2 \phi]^{\frac{1}{2}}} \quad (2.25)$$

where a is the midnight ($\phi = 0$) colatitude and b the dawn or dusk ($\phi = 90^\circ$ or 270°) colatitude of the auroral oval. Four different parabolas are illustrated in Fig. 2.15. The different arrows show possible paths of current flow. For example we may wish to have the current flowing along parabola #3 in both the morning and evening sectors or possibly along #2 in the morning sector and #4 in the evening sector. By utilizing configurations such as these we have thus greatly enhanced our ability to model observed magnetic perturbations. Fig. 2.16 shows a parabola ($a = 22.5^\circ$ and $b = 17.5^\circ$) superimposed upon an auroral oval ($Q = 2$). The dayside portion of the oval can also be modelled using a parabola that maintains continuity with the nightside portion at $\phi = 90^\circ$ and 270° .

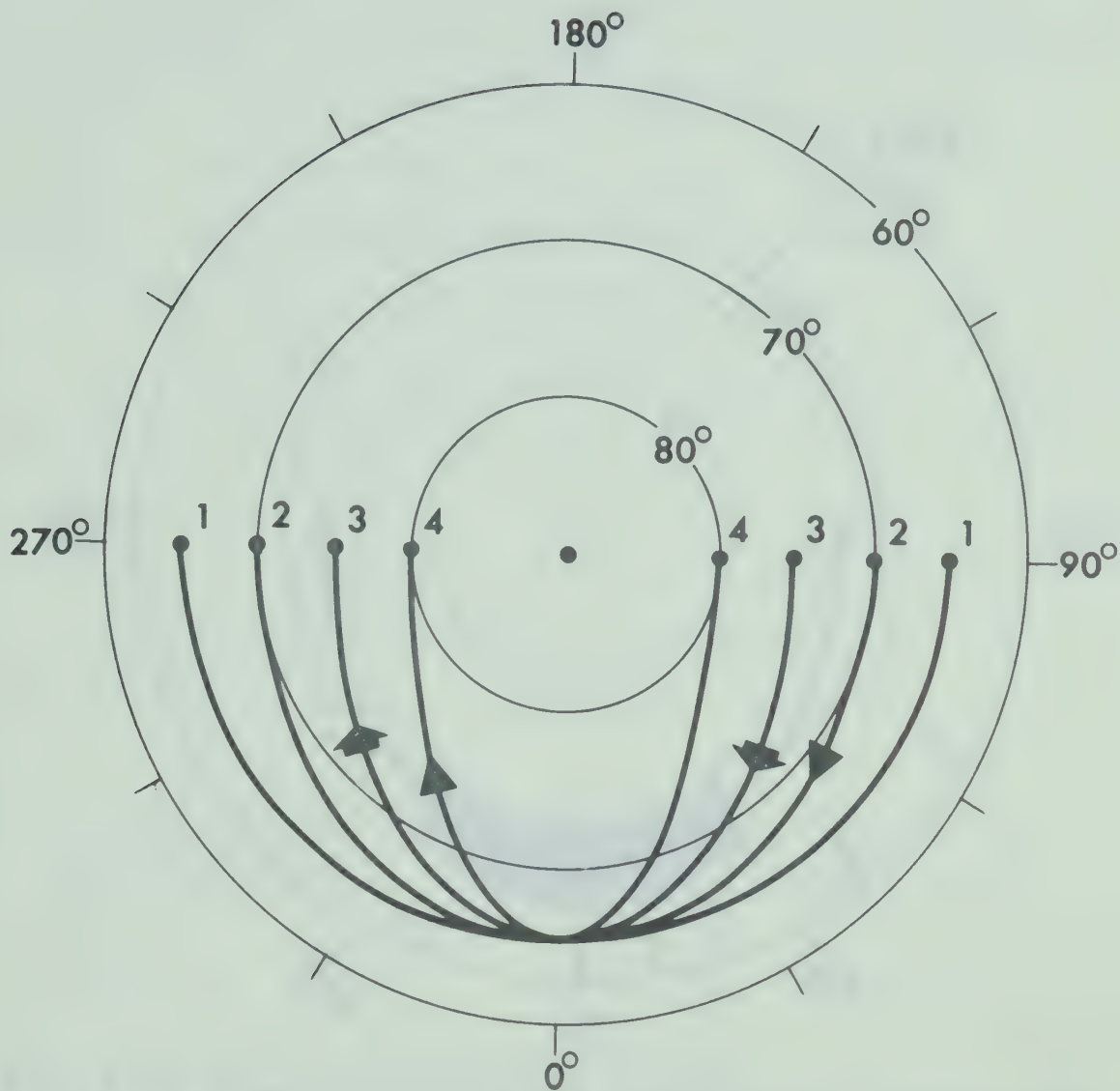


Fig. 2.15 Diagram of four possible parabolas to represent the path of current flow in conjunction with the auroral oval. The two sets of arrows represent possible paths of current for a single current system.

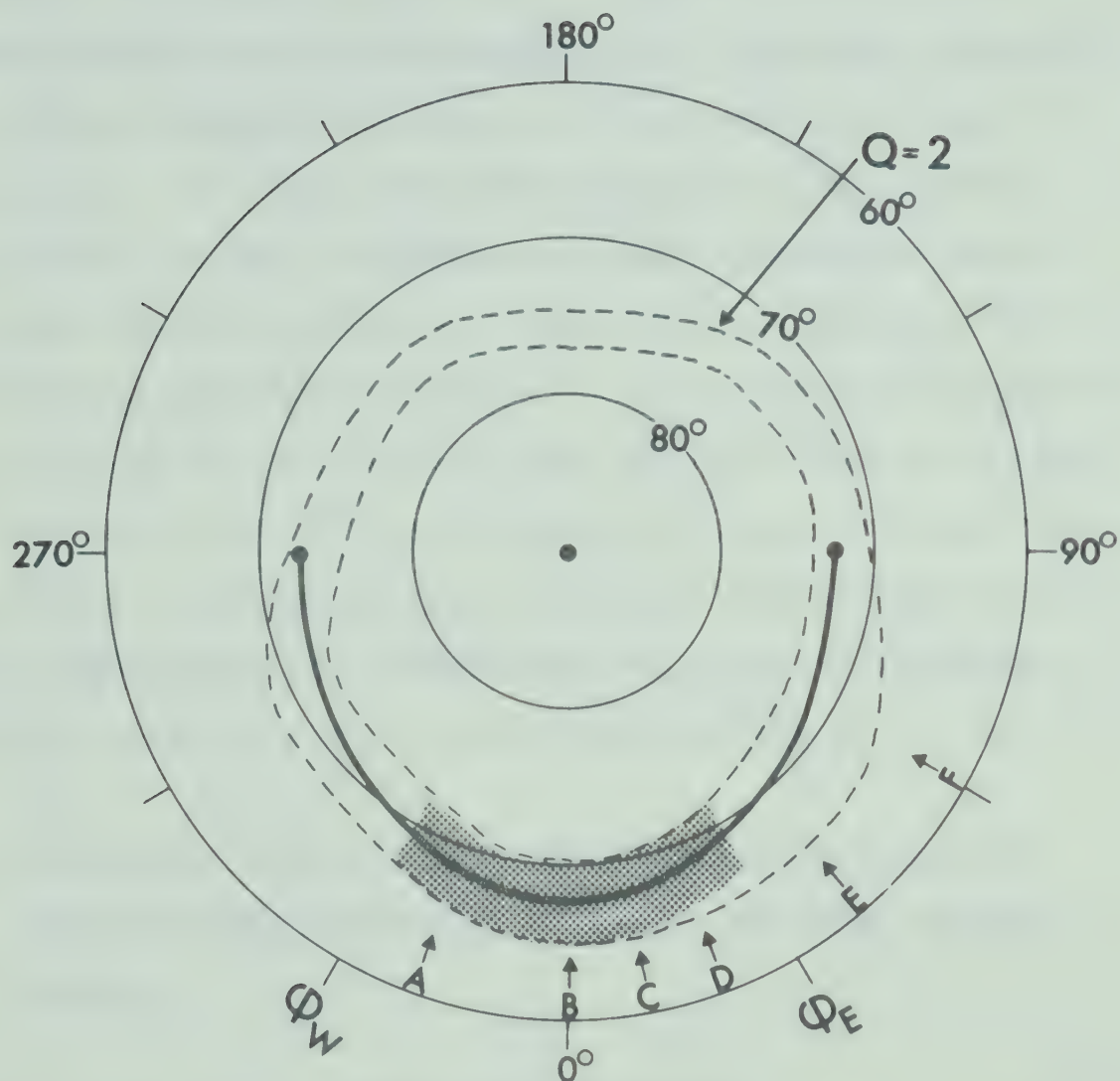


Fig. 2.16 Diagram showing the relationship between the auroral oval ($Q = 2$; see Whalen, 1970 and Feldstein, 1967) and the parabola corresponding to $a = 22.5^\circ$ and $b = 17.5^\circ$ (see eq. 2.25). The shaded area represents the ionospheric sheet current associated with an E-W three-dimensional current system modified to flow along this particular parabola.

The shaded portion centered about $\phi = 0^0$ represents the ionospheric portion of a modified E-W current system coincident with the model oval. Latitude profiles at various longitudes denoted by A through F are shown in Fig. 2.17. The important effect evident in this series of profiles is the deformation of the D component profile for profiles east and west of the central meridian. This deformation (southward movement of the D component crossover) is caused by the ionospheric sheet current flowing at some angle (other than 90^0) with respect to the profile meridian. This effect has been observed with our line of magnetometers and in most cases can be explained in terms of currents flowing along the auroral oval (see Chapters IV, V, and VI).

2.5 N-S and E-W (latitudinal and longitudinal) current distributions associated with the E-W model current system

2.5.1 Latitudinal current distributions

To obtain the numerical results presented in section 2.2.2 we represented the latitudinal current distribution function by a constant. From preliminary analysis of magnetic perturbations associated with polar electrojets

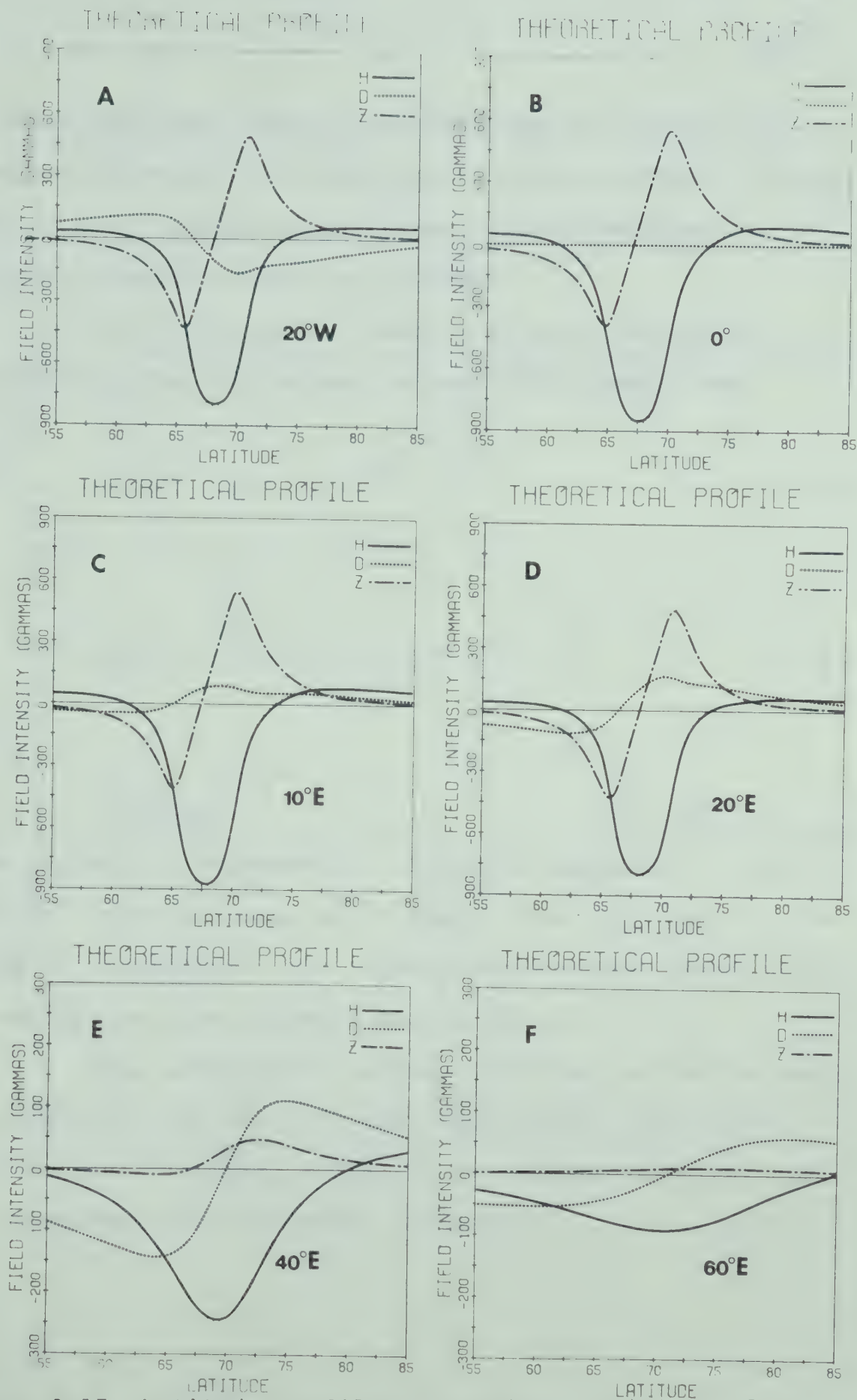


Fig. 2.17 Latitude profiles at various positions along the auroral oval (The letters on these profiles coincide with the letters in Fig. 2.16).

we found that more complex distributions of current are necessary to explain the observed latitude profiles. Therefore, we modified our model current system programs to include various current distributions.

The functions we found to be most useful for representing the latitudinal current distribution are

$$I(x) = I_1 + I_2 e^{-ax^2} \quad (2.26)$$

and

$$I(\pm x) = I_1 + I_2 (1 \pm x)^a e^{-b(1 \pm x)} \quad (2.27)$$

$$(-1 \leq x \leq 1)$$

where variable x represents a change in variable θ such that the limits of integration change from θ_N and θ_S to -1 and $+1$ respectively for integration over the width of the current system (see Appendix A3, eq. A3.3).

Some examples of various distributions of currents utilizing eq. 2.26 and 2.27 are illustrated in Fig. 2.18.

The first profile (Fig. 2.18A) is an example using eq. 2.26.

The parameters for this model system are $I_1 = 0$, $I_2 = 1$,

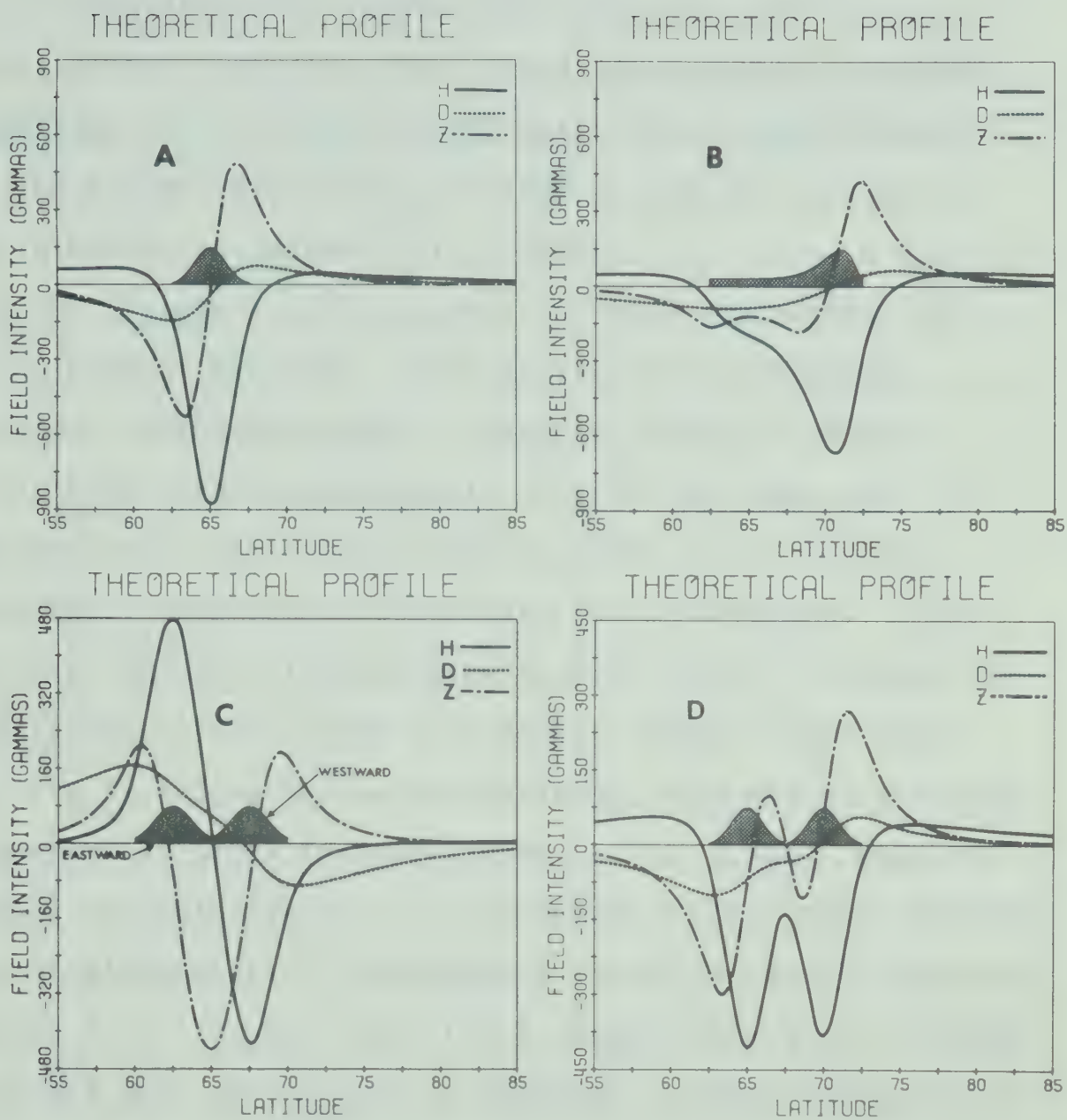


Fig. 2.18 Latitudinal profiles associated with current systems having various latitudinal current distributions.

$a = 3$, length = 20° , width = 5° , and the profile 5° E of the central meridian (the current distribution is always normalized to give the required total integrated current). For the second profile (Fig. 2.18B) we used eq. 2.27 with the following parameters: $I_1 = 0.003$, $I_2 = 1.0$, $a = 2.0$, $b = 7.0$, length = 40° , width = 10° and the profile 10° E of the central meridian. This particular distribution function can thus be used to represent either a northern or southern border enhancement. Fig. 2.18C shows the magnetic effect associated with an eastward and westward electrojet, each having different central meridians. This system of currents is discussed in more detail in Chapter IV. Illustrated in Fig. 2.18D is a double westward electrojet obtained by adding two current systems, each having the same parameters as those for the system in Fig. 2.18A. Note the partial cancellation of the Z component in the region between the two electrojets. The opposite effect is readily apparent in Fig. 2.18C in which case the Z components are of the same sense and thus add to give an enhanced -Z regime between the two electrojets. Both compound current systems are very common in the auroral zone.

2.5.2 Longitudinal current distributions

In section 3.2.1 we represented Birkeland currents associated with the E-W three-dimensional current system as sheet currents located at the eastern and western ends of the ionospheric electrojet. Since, if such currents exist, they are probably distributed all along the electrojet, we have modelled various distributions of field-aligned current flow using both the method developed by Bonnevier et al. (1970) (see Appendix A1.3) and the Biot-Savart method presented in this chapter. Eq. 2.26 and 2.27 were also used to represent the longitudinal current distribution function.

Fig. 2.19 shows the results obtained using the Bonnevier et al. method. Eq. 2.27 was used with $I_1 = 0.003$, $I_2 = 1.0$, $a = 2.0$ and $b = 5.0$. No induction effects were included in the numerical evaluations. The shape of the distribution function is shown in Fig. 2.19A with the location of the various profiles designated by arrows labelled A through F. The latitudinal current distribution is uniform but could also have been of the forms discussed previously. From Fig. 2.19C and D we see that the sense of D changes somewhere between 5° W and 0° ($\phi_C = 0^\circ$ is normally defined as the central meridian). The longitude at which D cancels completely can be determined from the moment of the current

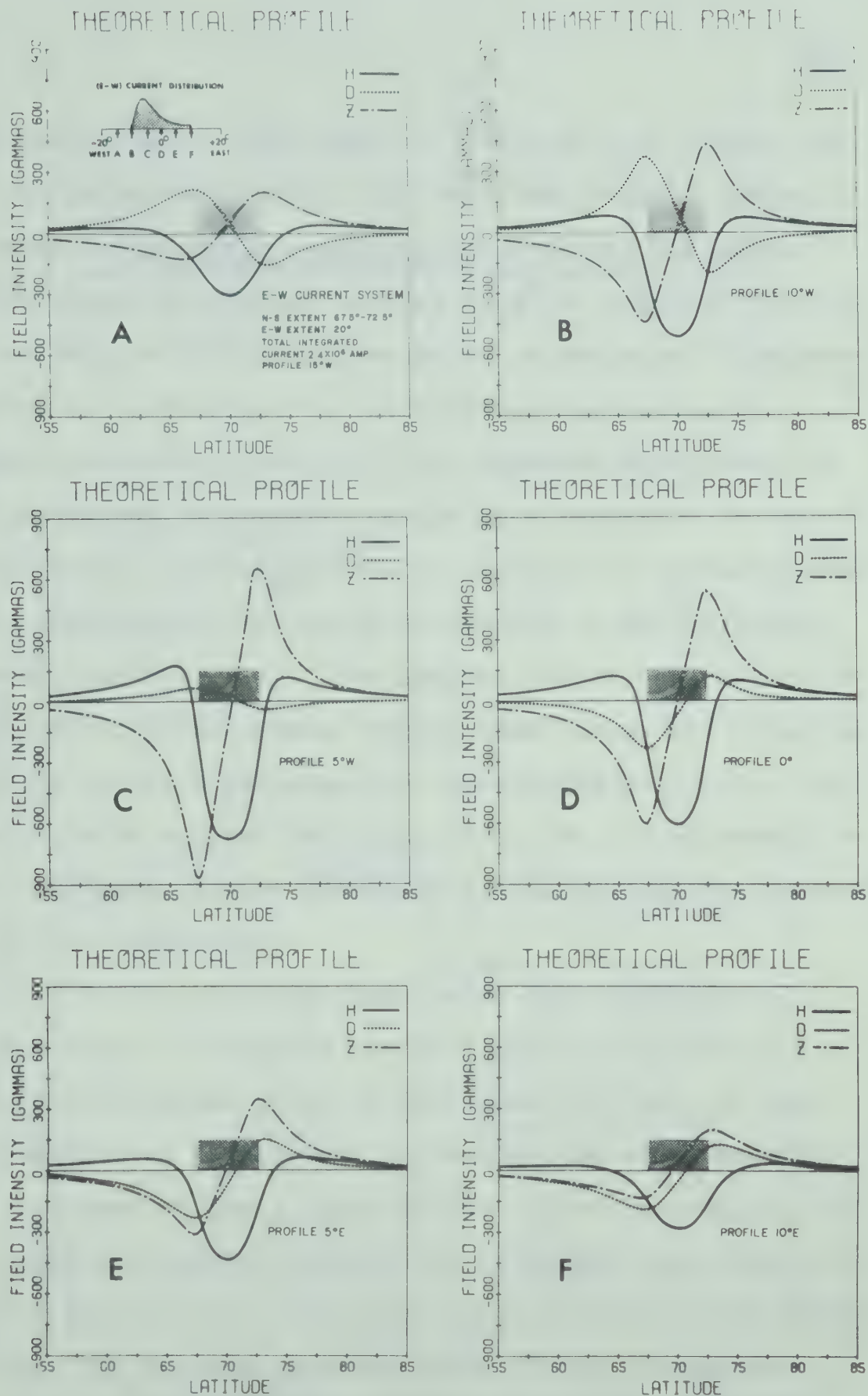


Fig. 2.19 Latitude profiles at various longitudes associated with a current system having a longitudinal current distribution as shown above in profile A.

distribution and in this case is $\sim 4^\circ$ W of ϕ_C . Hence, in this particular model 2.4×10^6 amp flow into the auroral zone along much of the eastern portion of the electrojet and out along the western portion ($\sim 6^\circ$ in length). We can also see what at first appears to be an enhanced Z component south of the electrojet in the longitudinal region of enhanced Birkeland currents. This apparent enhancement of the Z component is actually caused by a reduction in the -H regime beneath the ionospheric portion of the current system due to the enhanced +H regime attributed to the Birkeland currents (see Fig. 2.4). The possibility of having such an effect occur in the auroral region complicates the interpretation of magnetic perturbations associated with polar electrojets. Also evident in Fig. 2.19 is the E-W asymmetry in the D component (larger values of D occurring at the western end of the electrojet).

In Fig. 2.20 we demonstrate how longitudinal distributions of Birkeland currents can be included in a model current system by using Biot-Savart's law. Various distributions of E-W current systems can be added together as illustrated in the diagram at the top of the figure. In this example induction effects are included, thus making the negative peak in the Z component south of the current system less than the maximum negative value of the H component.

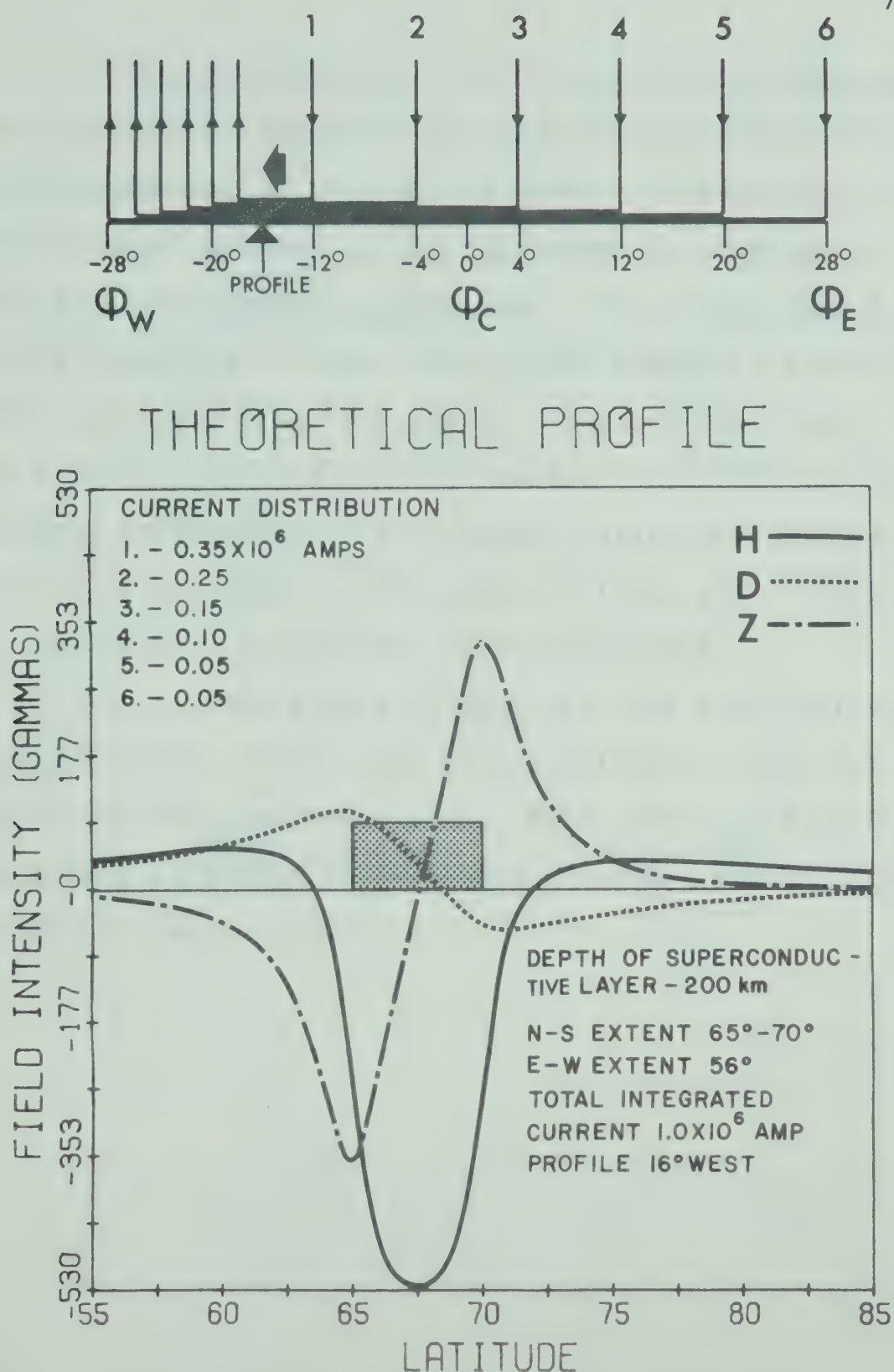


Fig. 2.20 Latitude profiles associated with the longitudinal current distribution illustrated at the top of the figure.

Since the ionospheric portion of three-dimensional current systems is dependent on the various conductivities in the ionosphere, we studied the effects of variations in height on model current systems to ascertain whether an integration over height is warranted. Fig. 2.21 shows a series of profiles for the same current system at various heights above the Earth's surface. It is evident from these profiles that the overall shape of the profiles remains relatively unchanged over this height interval with only a variation in magnitude on the order of 15 to 20% . Thus we feel that such an integration is not warranted.

It is interesting to note that the distributions discussed in this section are also applicable to the N-S three-dimensional current system. More complicated distributions such as shears in E-W and N-S current systems are discussed in later chapters.

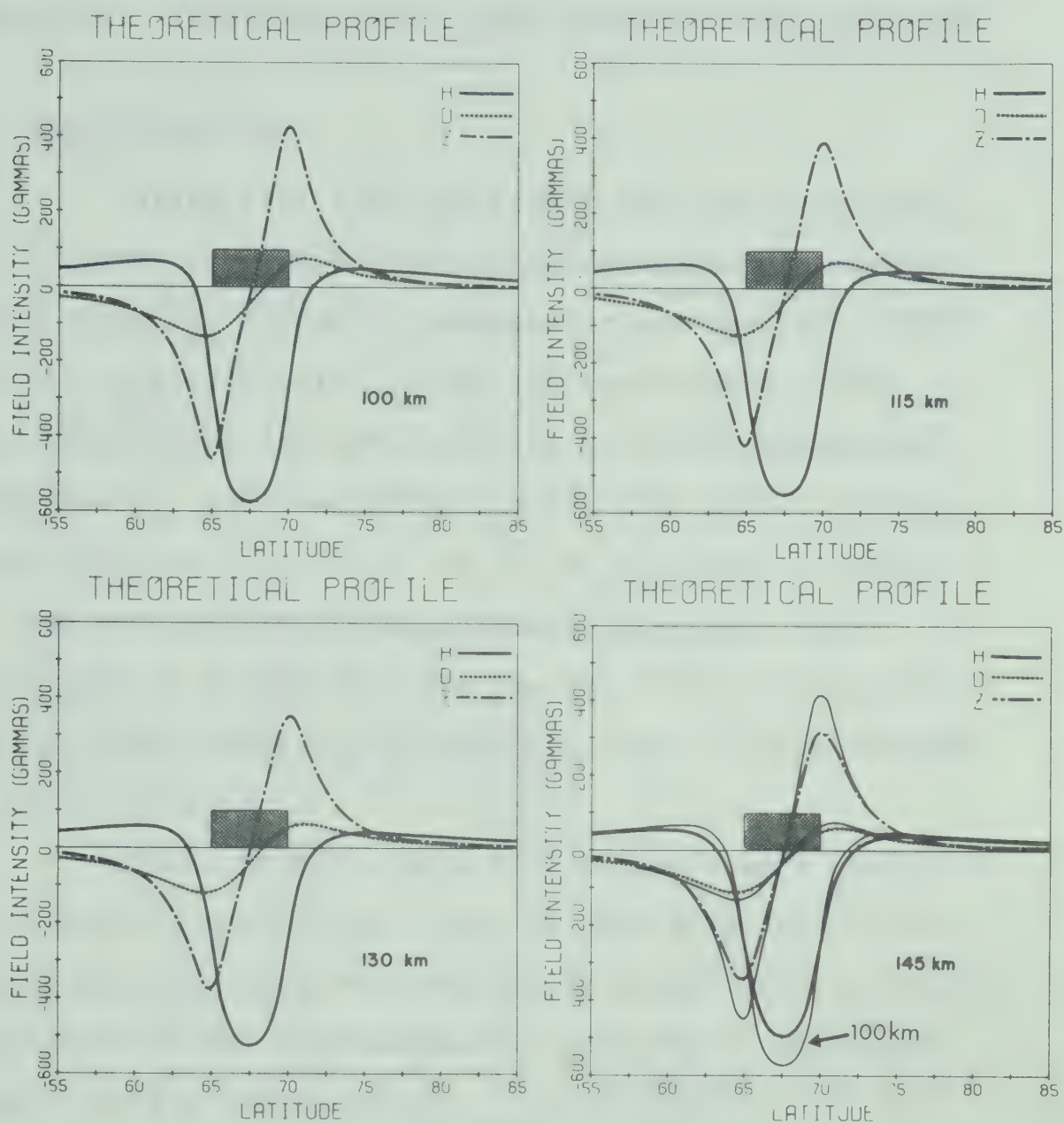


Fig. 2.21 Latitude profiles for a current system located at various ionospheric heights.

CHAPTER III INSTRUMENTATION, DATA PROCESSING AND ANALYSIS

3.1 Instrumentation

During fall 1969 and summer 1970 we installed a line of three-component fluxgate magnetometers in western Canada along the corrected geomagnetic meridian of $\sim 301^{\circ}\text{E}$ (see Fig. 3.1 and Table 3.1 for the coordinates of the observatories and the definition of corrected geomagnetic coordinates). The nine observatories were closely spaced in the latitude range 58.7° to 77° N, and data to extend our line were obtained from standard observatories at Newport (55.3° N) and Resolute Bay (84.3° N). The coordinates and code names of the complete line of observatories are given in Table 3.1.

Since, at most, only five stations were operative simultaneously during fall 1969, all the data used in the present analysis were obtained during summer 1970. Thus the description of the instrumentation pertains to that used during the 1970 field season.

Eight of the nine stations recorded three components (H, D, Z) of the magnetic field variations in digital form on magnetic tape while a paper chart recorder was used at Crow Lake (sample rate of one data point for each component every 9 seconds). The sample rate for the digital system was one data point for each component every two

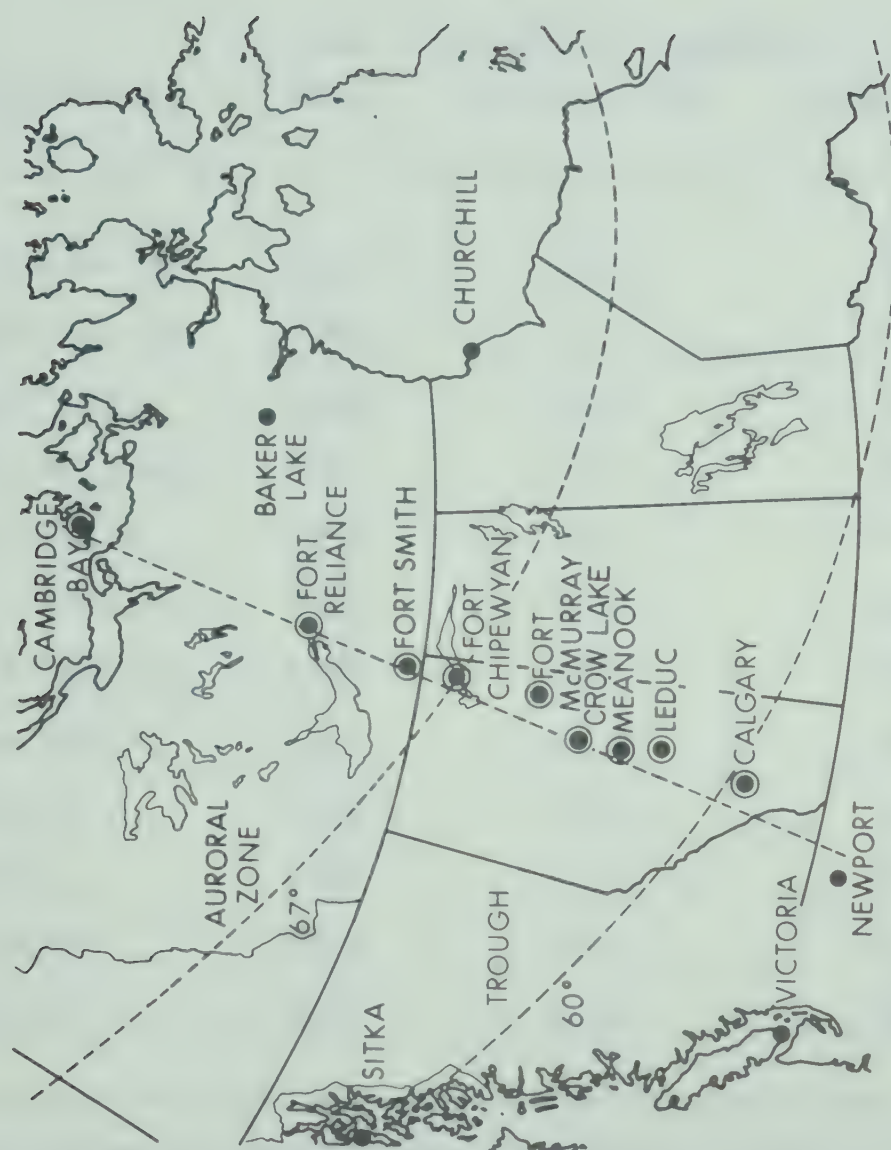


Fig. 3.1 Chain of magnetometer stations used in the present study. Digital recording systems were operative at Calgary, Leduc, Meanook, Fort McMurray, Fort Chipewyan, Fort Smith, Fort Reliance, and Cambridge Bay.

Table 3.1 Locations and code names of the magnetometer stations.

Observatory	Code Name	Corrected Geomagnetic Coordinates*	
		Latitude($^{\circ}$ N)	Longitude($^{\circ}$ E)
Resolute Bay	RSLT	84.3	306.0
Cambridge Bay	CAMB	77.7	300.3
Baker Lake	BAKE	75.1	320.4
Fort Reliance	FTRL	71.4	300.0
Fort Smith	FTSM	68.1	299.8
Fort Chipewyan	FTCH	67.0	301.3
Fort McMurray	FTMU	65.0	302.7
Crow Lake	CRLK	63.8	301.7
Meanook	MEAN	62.5	301.2
Leduc	LEDU	61.2	301.5
Calgary	CALG	58.7	302.0
Newport	NWPT	55.3	299.5

*The corrected geomagnetic coordinate system is a non-orthogonal system derived using the first five terms of the spherical harmonic expansion of the Earth's magnetic field (see Hakura, 1965).

seconds, and timing was accurate to within ± 2 sec. The dynamic range of the system was $\pm 1000\gamma$ with a sensitivity of $\pm 1\gamma$. The response was flat in the frequency range 0 to 0.3 Hz, with the high frequency end of the spectrum being set by the characteristics of the aliasing filters. A more complete description of the instrumentation is given in Appendix A4.

To complement our line of stations we installed all-sky cameras (on loan from the University of Alaska) at Meanook and Fort Smith. Photographs were taken at 1 min intervals with an exposure time of 8 sec on 16 mm Kodak Tri-X Reversal film.

3.2 Data processing

The process of transferring data from field tapes (7 track) to nine track tapes for use on the computer proved at times to be a long and tedious task. When the data was rewritten on nine track tapes the WWVB time blocks (see Appendix A4) were interpreted using a special WWVB read subroutine. This allowed the beginning time along with the station code name and reference number to be included in a label before each block of data. Reference numbers '1970' and '1111' were used to designate whether the block of data

was complete ('1970') or incomplete ('1111'). Short or incomplete blocks were usually attributed to power or equipment failures. When two or more bad blocks occurred between successive WWVB blocks, the good data blocks in between these bad blocks could not be timed automatically on the computer. If it became desirable to use such data, an attempt was made to correlate micropulsations occurring in this time interval with those recorded at adjacent stations. In most cases this method proved to be satisfactory. When the WWVB signal was too noisy to be interpreted on the computer, a Cal Comp plot was made to allow for a possible interpretation manually.

After the data from all stations were transferred to nine track station tapes, a series of event tapes was created with each tape containing a series of files. In each file all available data from the line of stations for a specified period of time (event) were written using the same format as was used for the nine track station tapes. This allowed the study of a specific event such as a polar magnetic substorm or micropulsation train by only utilizing one file rather than eight station tapes.

Most of the D component magnetic data recorded at Meanook were in error due to a faulty D component amplifier. The gain of the amplifier changed erratically during the

summer and thus the output had to be compared with standard magnetograms from Meanook. Fortunately during most of the events studied the gain remained at a constant (larger than normal) value and therefore was easily corrected.

3.3 Data analysis

In the study of spatial and temporal development of polar electrojets we used five different methods of presentation of data from our line of stations and supporting stations in the middle and high latitudes of the northern hemisphere. To complement the discussion of these methods examples of each can be found in Chapters IV, V and VI. In the ensuing chapters we used H, D and Z to represent the perturbation field.

3.3.1 Component magnetogram format

In this method the H, D or Z components of the magnetic data from our line of stations for a specified period of time are plotted with the northernmost station at the top of each plot. The magnetograms from supporting stations (NEWP, RSLT and CRLK) were hand digitized and, if desired, could be included in these component magnetograms. This method of data presentation is used mainly to give a

qualitative interpretation of the specific event being studied.

3.3.2 Component contour diagrams

A more quantitative method of presenting the data from our line of stations is accomplished by plotting equal intensity contours of each magnetic perturbation component with universal time and latitude as coordinates (see Zaitzev and Boström, 1971). The Z contour diagram is especially important since the approximate latitude and width of the electrojet can be obtained from the $Z = 0$ contour and the distance between lines of maximum and minimum Z respectively.

3.3.3 Three-dimensional (3-D) diagrams

Another method of presenting the same data contained in contour diagrams is drawing perspective views of three-dimensional surfaces. This is accomplished with the use of a perspective plotting subroutine written by H. Jespersen (Iowa State University) and modified by R. J. Beebe (Stanford University). Although there is a loss of quantitative information as compared with that available from a contour diagram, we feel that such 3-D diagrams are useful especially for complex spatial and temporal developments of current systems. A

good analogy would be the comparison between a map of equal elevation contours of a mountainous region and a photograph of the same region.

3.3.4 Polar plot

The most widely used method of displaying magnetic data from stations distributed both in latitude and longitude is that of plotting a vector representing the total horizontal component of the perturbation field for each station on a polar plot. Since there are numerous coordinate systems which can be represented with a polar plot, a choice had to be made as to what particular coordinate system would be best suited for ordering magnetic data at high latitudes. Whalen (1970) (also see Comfort, 1970) has discussed the advantages of using the corrected geomagnetic (C.G.) coordinate system (see Hakura, 1965) over other coordinate systems (i.e. centered dipole, eccentric dipole and geographic coordinate systems). Although some difficulties could possibly arise with the coordinate system (see section 3.4), we have displayed our data in the C.G. system of coordinates for all polar plots in Chapters IV and V.

Whalen (1970) has also presented a very useful nomograph for plotting auroral ovals in the C.G. coordinate

system and for converting from geographic to C.G. coordinates. Another valuable aspect of this nomograph is the ease with which the C.G. local midnight meridian (defined as the meridian which passes through the anti-subsolar point) can be obtained for any season of the year. Thus, rather than representing the azimuth of the polar plot as C.G. longitude, C.G. time can be used instead (C.G. time being computed on the basis of one hour equals 15° of C.G. longitude). To allow for a constant format for all polar plots with the position of stations remaining the same, we chose to represent the azimuth as C.G. longitude with C.G. noon being indicated by a large dot which rotates around the polar plot as a function of universal time. The size of the polar plots are such that they can be used in conjunction with Whalen's nomograph.

Fig. 3.2 shows the distribution of magnetic stations used in the present analysis (see Table 3.2). The C.G. coordinates for these stations were obtained using tables calculated by Hakura (1965). An example of a polar plot displaying actual magnetic data is shown in Fig. 3.3. The position of the auroral oval ($Q = 1$) was determined using the auroral oval plotter. Although the distribution of available stations is rather sparse in many areas, we are still able to obtain valuable information in order to infer

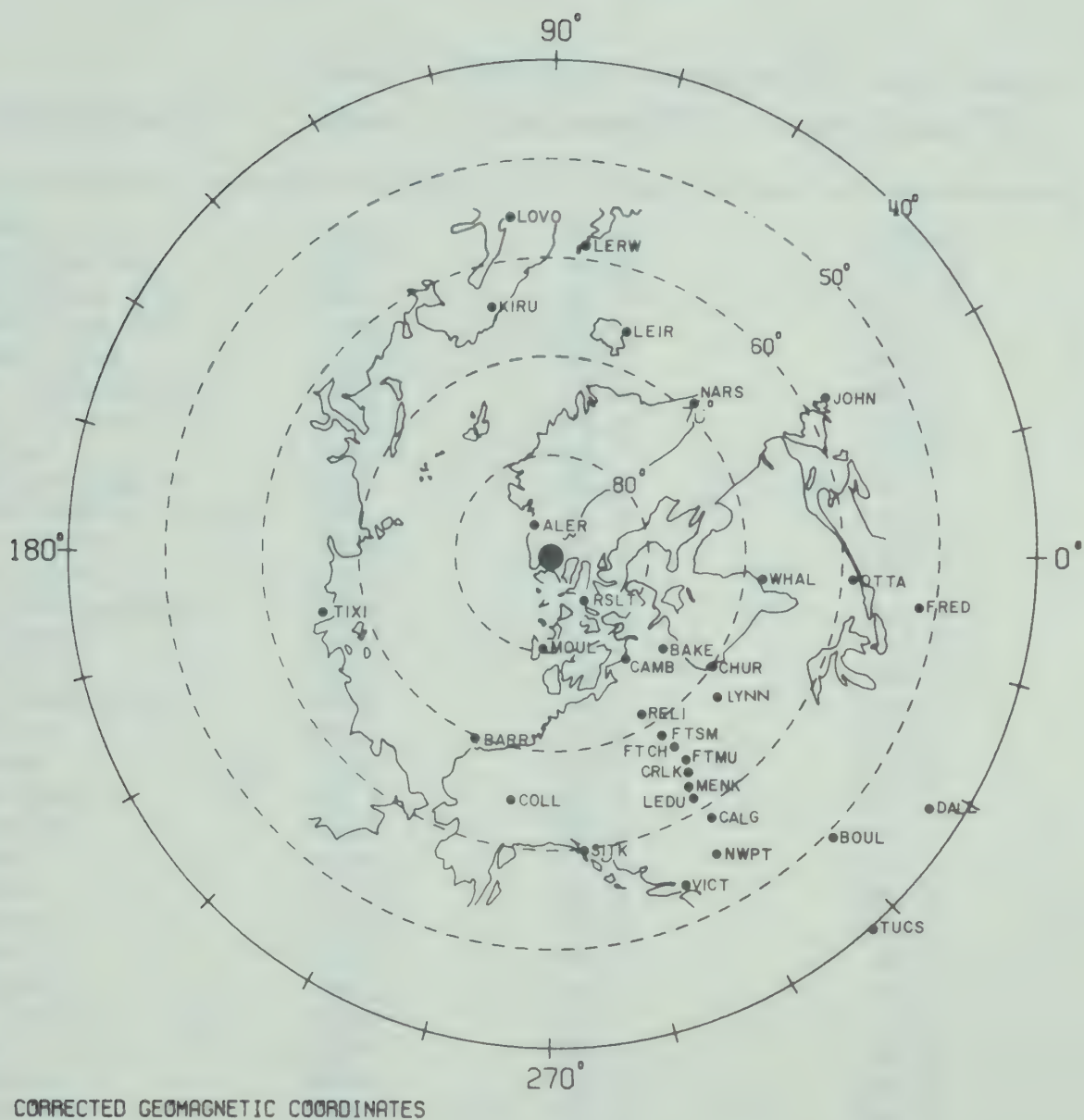


Fig. 3.2 Distribution of magnetometer stations in the northern hemisphere that are used in the present study. The outline of the continents is in corrected geomagnetic coordinates after Whalen (1970).

Table 3.2 Locations and code names of magnetometer stations used in polar diagrams.

Observatory	Code Name	Corrected Geomagnetic Coordinates	
		Latitude($^{\circ}$ N)	Longitude($^{\circ}$ E)
Alert	ALER	86.5	122.6
Resolute Bay	RSLT	84.3	306.0
Mould Bay	MOUL	80.5	264.3
Cambridge Bay	CAMB	77.9	300.3
Baker Lake	BAKE	75.1	320.4
Fort Reliance	FTRL	71.4	300.0
Fort Churchill	CHUR	70.0	326.0
Barrow	BARR	69.7	247.0
Narsarssuak	NARS	69.0	45.6
Great Whale River	WHAL	68.2	353.8
Fort Smith	FTSM	68.2	299.8
Lynn Lake	LYNN	67.3	316.1
Fort Chipewyan	FTCH	67.0	301.3
Leirvogur	LEIR	66.3	72.0
Tixie	TIXI	65.6	194.9
Fort McMurray	FTMU	65.0	302.7
College	COLL	64.9	260.3
Kiruna	KIRU	64.3	104.8
Crow Lake	CRLK	63.8	301.7
Meanook	MEAN	62.5	301.2
Leduc	LEDU	61.2	301.5
Sitka	SITK	59.8	276.6
Ottawa	OTTA	58.9	355.7
Lerwick	LERW	58.9	84.3
Calgary	CALG	58.7	302.0
St. John's	JOHN	57.7	29.8
Lövo	LOVO	55.9	97.9
Newport	NEWP	55.3	299.5
Victoria	VICT	53.9	292.6
Fredericksburg	FRED	51.8	352.2
Boulder	BOUL	49.3	315.7
Dallas	DALL	43.4	326.9
Tucson	TUCS	39.7	311.4
San Juan*	JAUN	29.6	3.1
Honolulu*	HOLU	21.1	266.5
Guam*	GUAM	4.0	212.9
Huancayo*	HUAN	-0.6	353.8

*Geomagnetic Coordinates

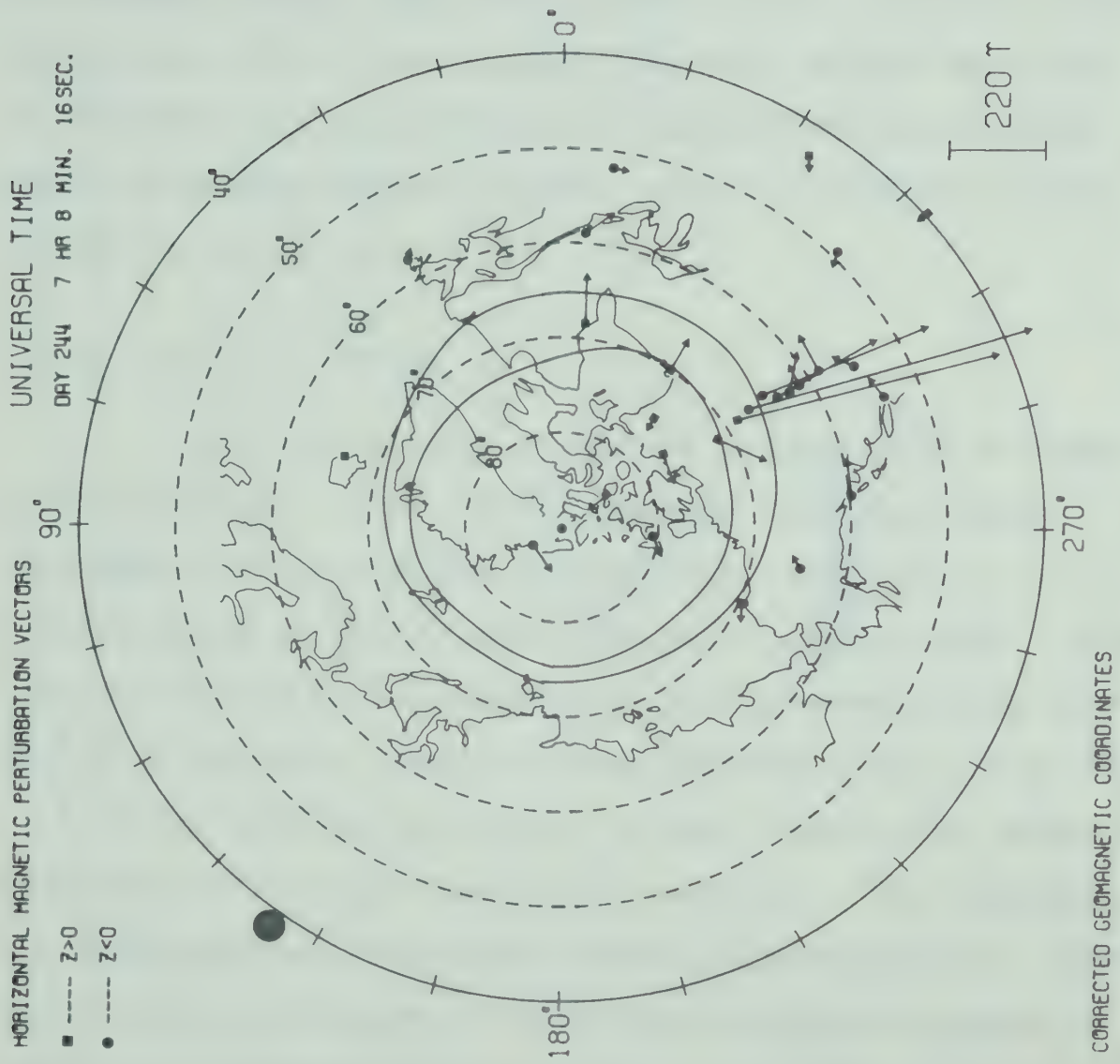


Fig. 3.3 Sample polar plot showing the distribution of horizontal magnetic perturbation vectors associated with a substorm. The auroral oval ($Q=1$) and continents are plotted in corrected geomagnetic coordinates. The solid circle represents C.G. noon.

some of the necessary parameters for determining an equivalent three-dimensional current system necessary to explain the observed perturbations. For example when we compare these disturbance vectors with those shown in Fig. 3.4 for a three-dimensional E-W current system (10^6 amp), we are thus able to determine the approximate latitudinal and longitudinal position of the current system. This is discussed in more detail in Chapter VI.

3.3.5 Latitude profile

From the results presented in Chapter II on model current systems, it is readily apparent that the use of latitude profiles provides an excellent technique for displaying magnetic fields associated with those systems. Since our line of stations is positioned approximately along the 301° C.G. meridian, displaying the magnetic data in the form of latitude profiles allowed us to make comparisons between observed profiles and theoretical profiles. This technique was used previously by Walker (1964), Bonnevier et al. (1970) and Kisabeth and Rostoker (1971) and has been discussed in detail by Kisabeth and Rostoker in conjunction with inferring three-dimensional current systems from data recorded with our line of stations.

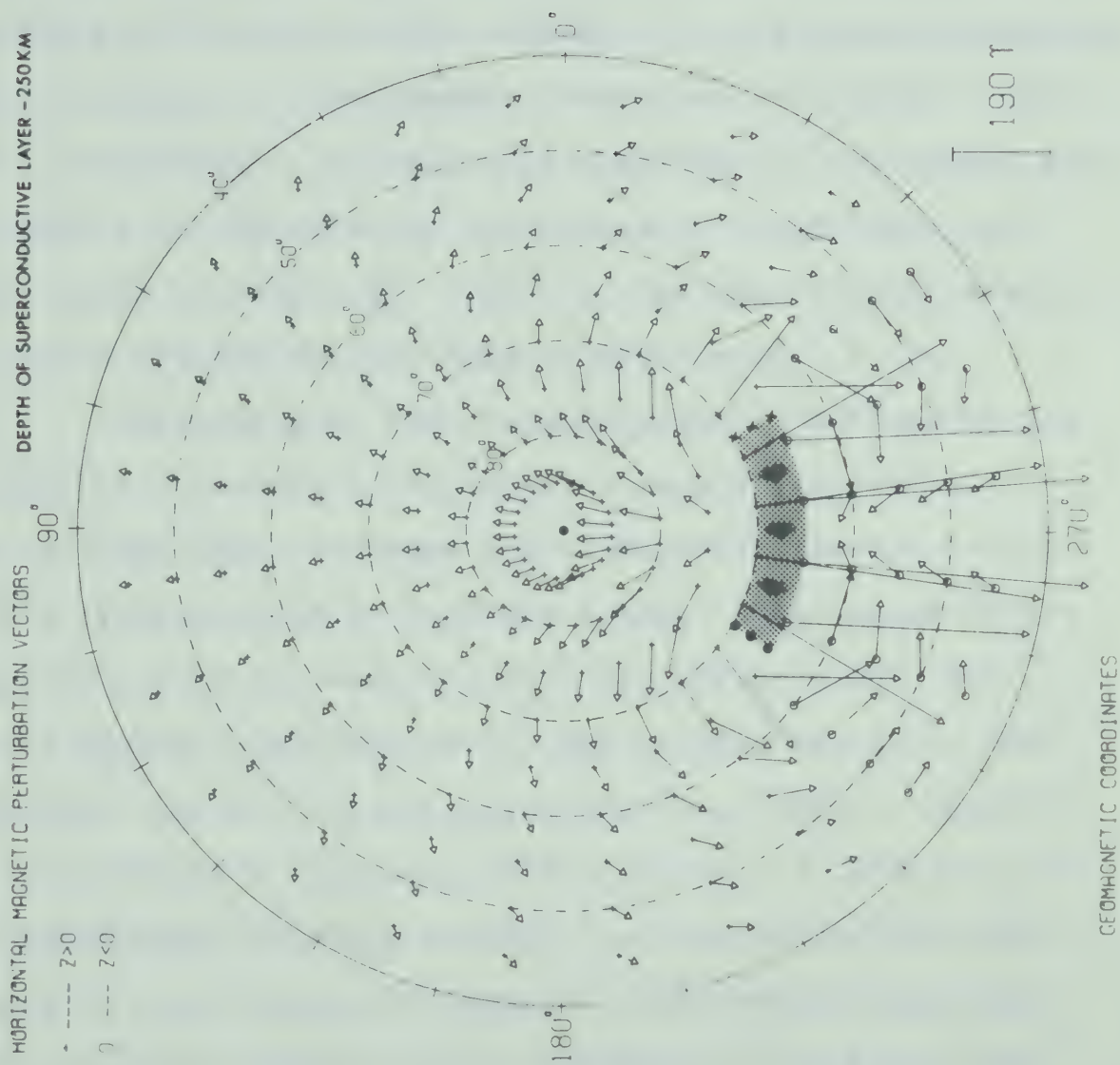


Fig. 3.4 Polar plot of horizontal distribution vectors associated with a three-dimensional E-W current system.

Throughout the discussion of the spatial and temporal development of current systems, some characteristics of latitude profiles are used to infer the physical parameters of these systems. In the following discussion the physical parameters of interest (with reference to E-W three-dimensional current systems) are the moment, width and latitudinal distribution of current. In Chapter II (section 2.3) we showed that the effects of induction do not seriously alter these parameters (also see Boström, 1969). All of the figures referred to in this discussion are found in Chapter II.

The moment of the current system is defined as the latitude at which the Z component is zero for meridional station lines that lie under the ionospheric portion of the current system (see Fig. 2.5A and 2.18B). The moment cannot always be easily defined, however, particularly when the Z profile becomes distorted due to two or more maxima in the latitudinal current distribution (see Fig. 2.18D). Another physical situation that will affect the $Z = 0$ crossover is the longitudinal distance between the line of stations and the end of the ionospheric segment of the three-dimensional current system. If the line of stations should lie to the east or west of the ionospheric portion of the current system, the $Z = 0$ crossover will be located slightly south of the

actual moment of the current system (see Fig. 2.5D,E and Fig. 2.6C). The location of the peak in H (negative for westward and positive for eastward electrojets) should coincide with the moment of the current system. Since this peak can be adjusted easily and still fit the observed data, it does not serve as a very accurate indicator of the location of the moment of the current system, whereas the $Z = 0$ crossover is usually well defined by our observed data.

The width of the current system is approximated by the separation between the maximum and minimum in the Z profile. Again this is true only for single current systems. The width measurements should be representative of the actual width of the current system if the line of stations is near or under the ionospheric segment of the current system. If the profile is obtained for a current system far to the east or west of the line of stations, the separation of the peaks in the Z profile will be greater than the width of the actual current system (see Fig. 2.6C). One important factor to look for in the Z profile is the shape of the Z peaks. If the line of stations is located far from either end of the ionospheric segment of the current system, both peaks will be very broad and thus the maximum will not be well defined (see Fig. 2.5E). The shape of these peaks can also be affected by the latitu-

dinal distribution of current as illustrated in Fig. 2.18B. Qualitatively, then, the shape of the peaks may give some indication of the distance of the line of stations from the end of the current system. Also the shape of the peaks (along with the H profile) may indicate asymmetries in the latitudinal current distribution.

The width of the negative H regime can also be used to infer the relative width of the current system; however, the inferred width is also dependent on the distance of the line of stations from the end of the current system (see Fig. 2.6A). Therefore we must be cautious in using the width of the negative H regime as a quantitative measure of the width of the ionospheric electrojet.

The D perturbation is positive to the south and negative to the north of the ionospheric portion of the three-dimensional current system for latitude profiles west of the central meridian. For profiles east of the central meridian the sign of the D perturbation is just the opposite of that discussed above (see Fig. 2.5B and F). Along the central meridian the D perturbation from field-aligned currents will be cancelled. Therefore we can use the D profile to determine whether the station line lies along the central meridian of the ionospheric portion of the current system. The D profile

can become highly distorted at times due to the presence of eastward and westward travelling surges and loops (see Chapter V).

In summary the Z profile appears to be the most important of the three profiles for inferring the physical parameters of the current system or systems responsible for the observed magnetic perturbations, although all three are necessary to infer the most probable model. Also, all three components are necessary to study the effects of induction that are included in the observed magnetic perturbations (see Chapter II, section 2.3 and Chapter VI). The D component appears to be the most important for detecting disruptions of the auroral arc systems and also flow of current along the auroral oval (see Chapter II, section 2.4).

The longitudinal distribution of current (and length of the current system) is more difficult to ascertain from observations of magnetic perturbations. A discussion of this problem is included in Chapter VI.

The resolution of our line of stations is very difficult to determine since the interpolation between two stations for one component may be accomplished with the aid of all components north and south of this particular regime. A discussion of this problem is presented in Appendix A5.

Since the arc spacings are of the order of 30 to 40 km (Akasofu et al., 1966) with arc thicknesses varying from a few hundred meters to 10 km with an average thickness of 1 km (Magge and Davis, 1968), our line of stations definitely does not have the necessary spacing to resolve individual arcs within a group of arcs having this average spatial distribution.

3.4 Baselines and the orientation of HDZ coordinates in the C.G. coordinate system

Since we cannot, at the present time, define an absolute baseline from which to measure magnetic perturbations associated with current systems, we set the baseline (sometimes referred to as the DC level) at each station just before the onset of the particular disturbance we are interested in analysing. To determine the DC level we usually used magnetograms from observatories positioned both east and west of our line of stations to allow for possible spatial effects such as westward travelling surges. We also used this method of setting the DC level to examine perturbations of existing current systems. Latitude profiles with such baselines are referred to in the text as differential profiles and prove to be invaluable in the study of magnetic

disturbances due to the passage of auroral forms such as travelling loops and surges.

Since the magnetometers along our line of stations are oriented in HDZ coordinates (H being the horizontal component of the field in the local magnetic meridian plane), we related this frame of reference at each station with lines of constant C.G. latitude and longitude. This is necessary since we wanted to compare the orientation of current systems with that of auroral ovals plotted in C.G. coordinates (Whalen, 1970). Comfort (1970) represented lines of constant C.G. latitude by a family of concentric ellipses (eccentricity = 0.5914) centered about a point on the Earth's surface with geographic coordinates 80°N and 280°E . To relate the orientation of the magnetometer at each station to the C.G. coordinate system we defined a C.G. declination at each station as the angle between the direction of the North geographic pole and the normal to the constant C.G. latitude line. The C.G. declination was determined by calculating the gradient (in spherical coordinates) of the function given by Comfort (1970) to represent the ellipses. Table 3.3 shows how closely the values for magnetic declination and C.G. declination correspond along our line of stations. Thus we should be able to compare the orientation of the current system

Table 3.3 Comparison of the magnetic declination and corrected magnetic declination (defined in text) for our line of stations.

Observatory	Magnetic Declination ($^{\circ}$ E)	Corrected Magnetic Declination ($^{\circ}$ E)	Difference ($^{\circ}$)
CAMB	33.0	31.9	-1.1
FTRL	29.8	27.2	-2.6
FTSM	28.0	26.4	-1.6
FTCH	27.0	25.6	-1.4
FTMU	25.0	24.7	-0.3
MEAN	24.4	24.4	0.0
LEDU	23.6	24.1	0.5
CALG	22.3	23.7	1.4
NWPT	21.3	23.4	2.1

as measured in the HDZ system with the auroral oval in C.G. coordinates.

Since constant C.G. latitude lines can be represented by ellipses on the surface of the Earth, we can expect to have variations in lengths of arc measured in degrees of C.G. latitude. This variation is dependent upon the location at which the measurement is made due to the orientation of the major and minor axes of this family of ellipses. Such errors could be serious when using the latitude profile techniques to infer actual widths of current systems. We were fortunate to have our line of stations located in a C.G. longitudinal regime such that this error is negligible. This would not, however, have been the case had our line of stations been positioned in Eastern Canada or in the Alaskan sector.

CHAPTER IV DYNAMIC DEVELOPMENT OF THE POLAR ELECTROJETS

4.1 Introduction

The dynamic development of two polar magnetic substorms are included in this chapter. Before we present these two substorms, the results of our study of the eastward electrojet in the evening sector are discussed with emphasis on the response of this electrojet to substorm activity in the midnight sector. Heppner (1954) has claimed that positive H component bays in the evening sector are associated with the development of an eastward electrojet at auroral zone latitudes, while Akasofu et al. (1965) contended that these positive H bays are caused by the return current from a westward electrojet flowing far to the north. We hope that the results presented in this chapter will help to cast some additional light on this controversy.

In section 4.2 the magnetic field due to a combination model current system including both an eastward and westward electrojet in the auroral zone is discussed in detail. We feel this presentation is necessary to better understand the magnetic perturbations observed in the evening sector as discussed in section 4.3. In sections 4.4 and 4.5 the dynamic development of the substorm events that occurred on June 15, 1970 and July 14, 1970 respectively are presented.

4.2 Magnetic field associated with a model three-dimensional current system containing both an eastward and westward electrojet

To better understand the magnetic observations discussed in the following sections of this chapter, we present a further discussion of magnetic fields associated with a model current system containing both an eastward and westward electrojet as shown in Fig. 4.1A (see Chapter II, section 2.5). Represented in this figure are the ionospheric portions of two three dimensional E-W current systems with oppositely flowing current. The central meridian of this combination current system is represented by the 0° meridian. The center (θ_c and ϕ_c) of the eastward current system is (62.5° , -15°), while the center of the westward current system is located to the north and east (67.5° , $+15^{\circ}$) of the eastward system (see Chapter II, section 2.2). Both electrojets are 40° in length and 5° in width. The latitudinal current distributions shown in Fig. 4.1B, C and D for each system are of the form given by eq. 2.26 in Chapter II. The effects of induction were also included by assuming a superconductive layer at a depth of 250 km. The total integrated current in the system is 2×10^6 amp (10^6 amp for each electrojet).

The latitude profiles shown in Fig. 4.1B, C and D are for meridians -15° , 0° and $+15^{\circ}$ respectively. In Fig. 4.1B the effect of the westward electrojet appears as a slight enhancement of the $-H$ regime north of the eastward electrojet. Since this profile is coincident with the central meridian of the eastward electrojet, the contribution to the D profile is solely from the Birkeland currents associated with the current system containing the westward electrojet and vice versa in the vicinity of the central meridian of the westward electrojet (see Fig. 4.1D). The Z component in Fig. 4.1B is almost completely due to the eastward electrojet, although the small $+Z$ regime to the north of the $-Z$ regime is due to the $+Z$ regime off the end of the westward electrojet (see Chapter II, Fig. 2.14C).

Fig. 4.1C shows the profile on the 0° meridian of the overall system. In this example the $-H$ and $+H$ regimes resemble one another very closely. The Z profile shows a pronounced enhancement between the two electrojets due to the addition of the $-Z$ fields from both electrojets. The D profile is greatly enhanced (both the negative and positive regimes) and is caused by the fact that the Birkeland currents associated with both current systems near this particular meridian are flowing out of the ionosphere (see Fig. 4.1A).

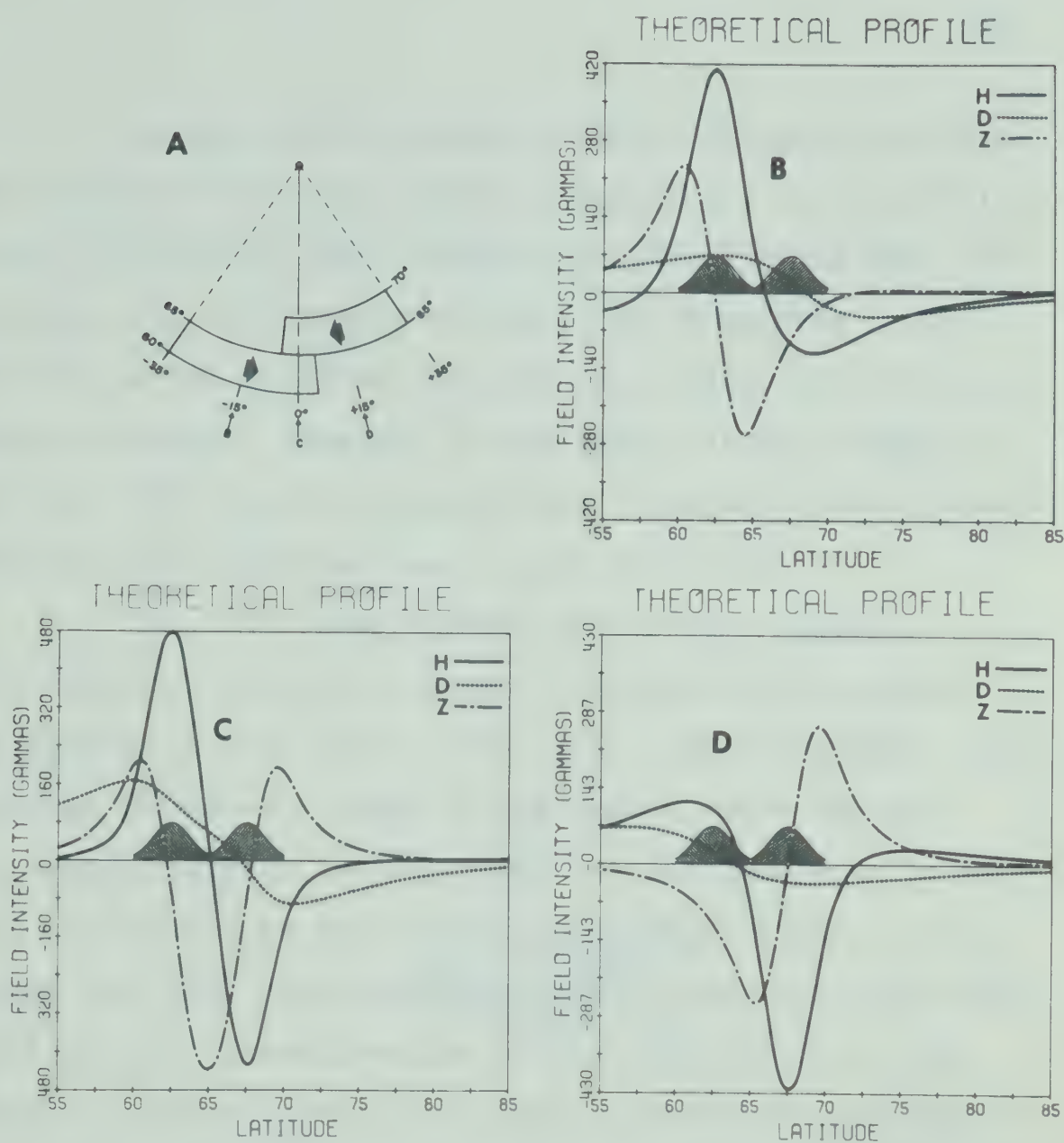


Fig. 4.1 Model three-dimensional current system containing an eastward and westward electrojet. The latitude profiles show the magnetic field along the -15° , 0° and $+15^\circ$ meridian.

In the profile shown in Fig. 4.1D the field from the westward electrojet dominates both the H and Z profiles as was the case for the eastward electrojet along the -15° meridian. As mentioned previously, the D profile is due entirely to the Birkeland currents associated with the eastward electrojet, however, in the longitudinal regimes of -35° and $+35^{\circ}$ the Birkeland currents located in these areas determine the relative shape of the D profiles.

Fig. 4.2 shows a polar plot of the magnetic perturbation vectors associated with the current system illustrated in Fig. 4.1A. This figure clearly depicts the enhanced +D and -D regimes in the region where the two electrojets overlap in longitude (the 270° meridian in this plot corresponds to the 0° meridian in Fig. 4.1A). If we assume that 270° represents the midnight meridian, then the total current system produces a substantial dawn to dusk magnetic field perturbation on the nightside of the polar cap. Also note the almost complete cancellation of the horizontal perturbation field on the dayside (see Chapter III, Fig. 3.4 for the distribution of horizontal field vectors associated with a single E-W three-dimensional current system).

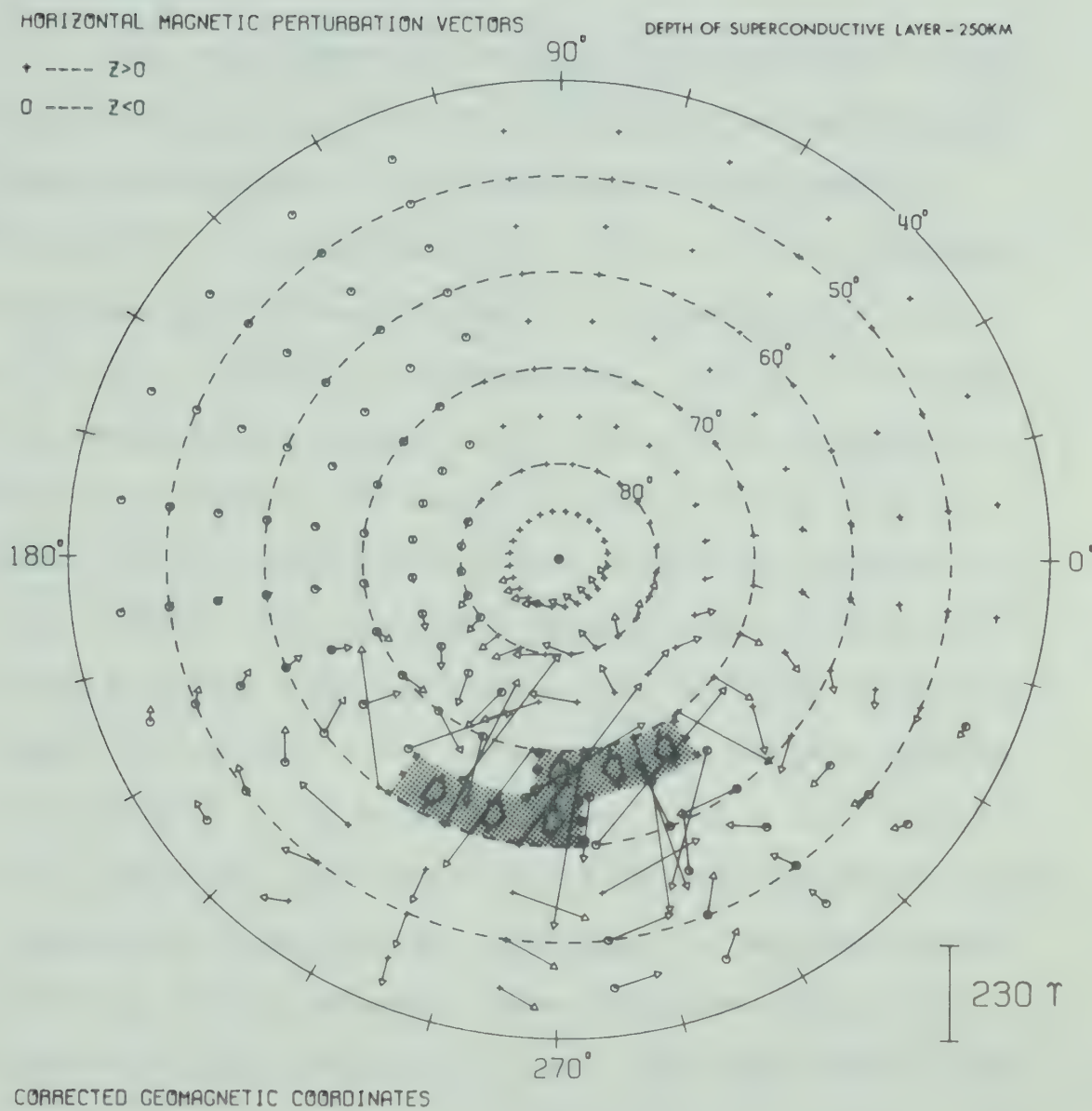


Fig. 4.2 Polar plot showing the distribution of horizontal magnetic perturbation vectors due to the current system in Fig. 4.1.

4.3 Eastward electrojet and associated substorm events of July 5, 1970 (Day 186)

The development of an eastward electrojet in the evening sector on July 5, 1970 afforded us the opportunity to study the response of this particular electrojet to polar magnetic substorm activity. The H, D and Z component magnetograms and the associated Pi 2 micropulsations are shown in Fig. 4.3 and 4.4 respectively. The Pi 2 micropulsations presented throughout this thesis were obtained by numerically filtering the magnetic data from our line of stations using a Butterworth filter subroutine written by Alpaslan (1968). The component magnetograms representing data from eighteen observatories in the northern hemisphere are shown in Fig. 4.5. The letters on the various magnetograms allow each trace to be followed. The + and - signs on the Z component magnetogram for SITK were necessary since this particular component was accidentally reversed during the plotting of this diagram. Also note the change in amplitude scale as indicated on the right hand side of this diagram.

The purpose of the following discussion is not to give a detailed dynamic development of the eastward electrojet, but rather to show the response of the eastward electro-

DAY 186

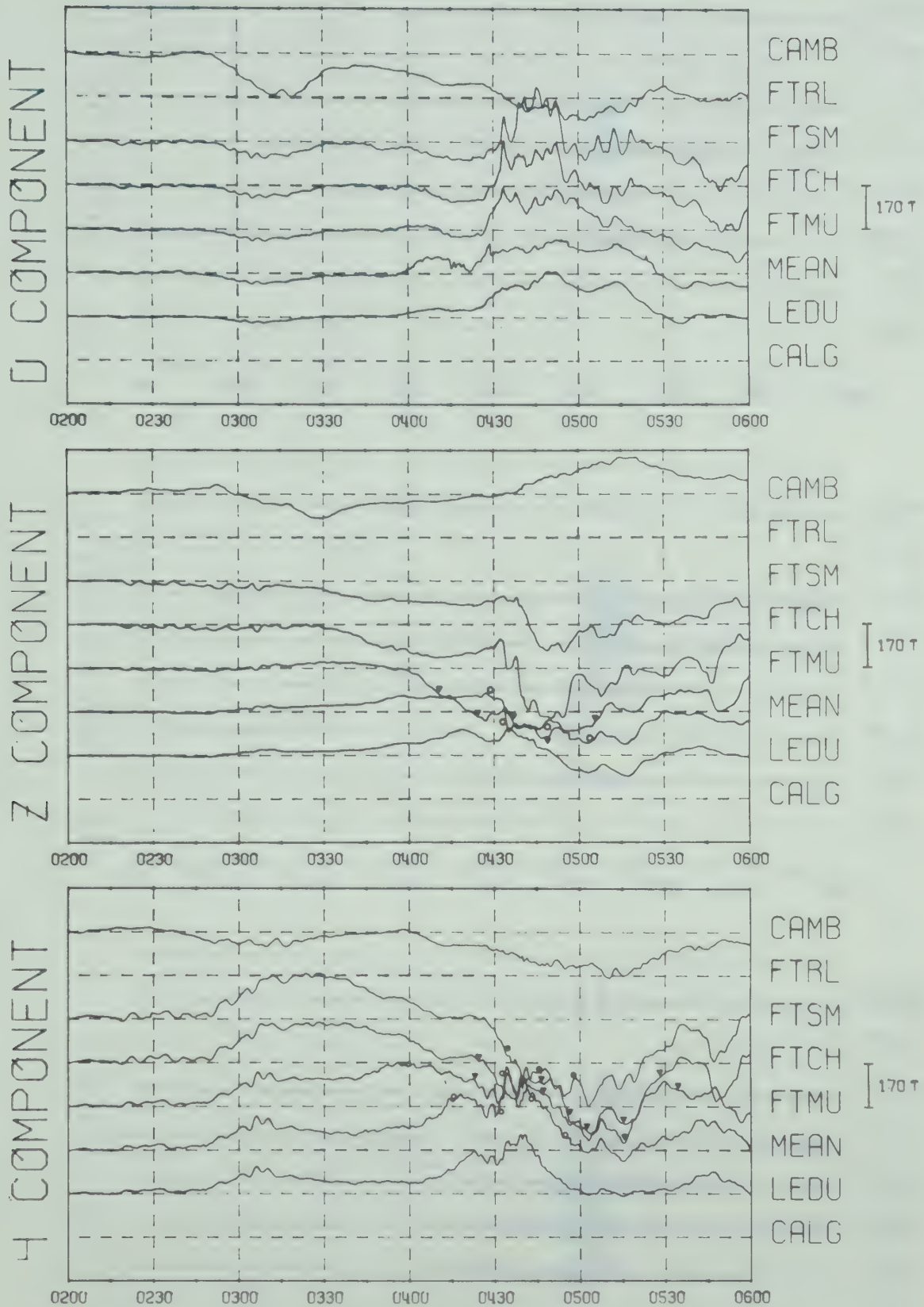


Fig. 4.3 Magnetograms showing the development of an eastward electrojet in the evening sector on July 5, 1970.

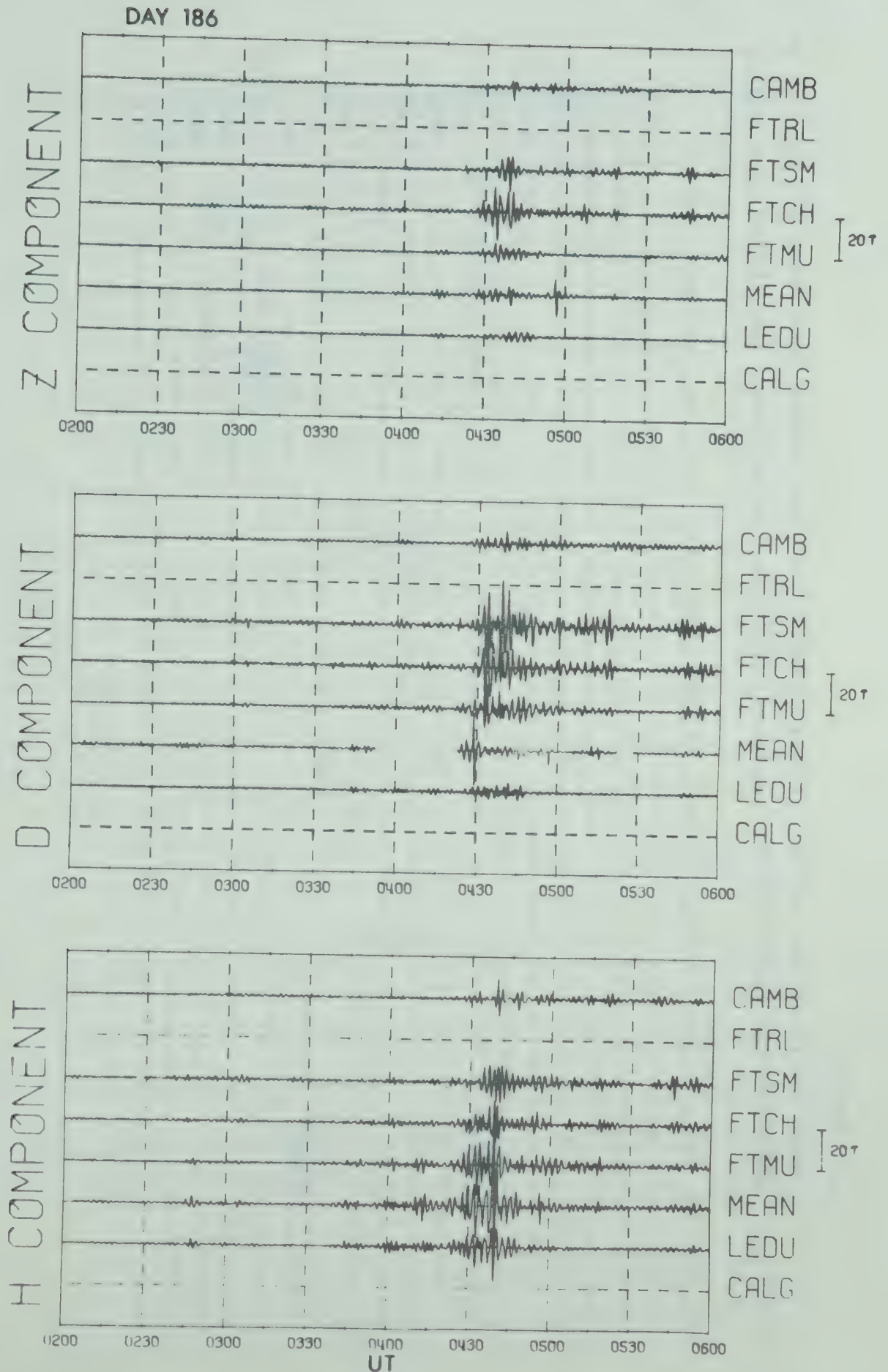


Fig. 4.4 Pi 2 micropulsation activity (40-150 sec) associated with the event shown in Fig. 4.3.

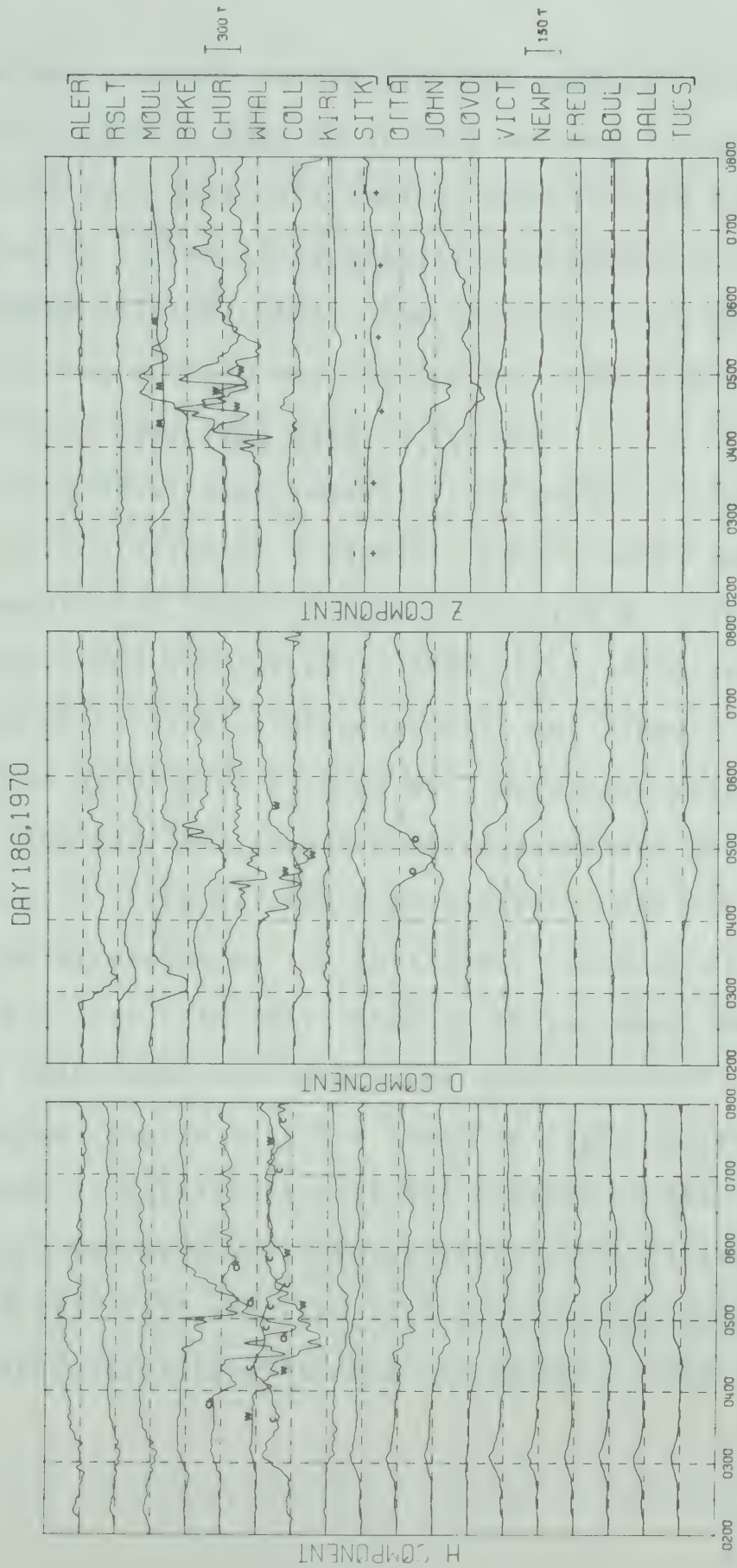


Fig. 4.5 Magnetograms from eighteen observatories in the northern hemisphere for July 5, 1970. The letters on the magnetograms allow the traces from each station to be followed.

jet to substorm activity in the midnight sector. Although the magnetic recording station at FTRL was not in operation at the time of this particular event, BAKE (75.1°) proved to be invaluable for the interpretation of magnetic perturbations between FTSM and CAMB. The Kp indices for this day were (3-, 4+, 4-, 2-, 3+, 3o, 2+, 3-; $\Sigma Kp = 23$) and for the previous 9 hours (Day 185) were 1o or less.

The gradual development of the eastward electrojet shown in Fig. 4.3 began at ~ 0245 UT, nearly coincident with the development of a large -D regime observed at high latitude stations (most pronounced at ALER, RSLT, MOUL and BAKE). The eastward electrojet as observed with our line of stations was very broad at 0300 UT with no well developed peaks in the Z profile. The latitude at which the Z component changed sign was $\sim 66.0^{\circ}$. The maximum H perturbation was $\sim 60\gamma$ with the +H regime extending to low latitudes. This is clearly evident in Fig. 4.3. In fact, similar +H perturbations were observed at HUAN, GUAM and HOLU. The development of this broad +H regime coupled with the large -D field observed at high latitudes is consistent with the pattern of the DP 2 current system (Nishida and Kokubun, 1971). It is interesting to note also that KIRU recorded a -H perturbation while LOVO recorded a very small transition H (+H to -H). This may be

indicative of the current cell in the dawn sector associated with the DP 2 system.

Immediately after 0300 UT the H profiles from our line of stations showed the development of a well defined eastward electrojet. At 0310 UT the electrojet showed a maximum H perturbation of $+152\gamma$ at FTSM. A meaningful width determination of the electrojet at this time was not possible. By 0322 UT (see Fig. 4.6A) the eastward electrojet was well defined with a maximum peak of $\sim 160\gamma$ and a width of $10-15^\circ$. Also, by this time the $+H$ perturbation field at lower latitudes had decayed substantially. Coincident with this decay the $-D$ perturbation at higher latitudes subsided with the large -300γ bay at MOUL having almost completely disappeared by ~ 0330 UT. As the low latitude $+H$ field disappeared, the southern ($+Z$) peak in the Z profile became more well defined. This is what we would expect to observe as was shown in our model studies presented in Chapter II. For example in Fig. 2.18B we showed how the Z component peak at the equatorward side of the electrojet is not well defined due to the particular latitudinal current distribution used. If the distribution were to gradually change to the form shown in Fig. 2.18A, the Z peak would experience an enhancement along with becoming more well defined. Thus, we feel that

the observed profiles can be explained by the decay of the DP 2 system along with an enhancement of the eastward electrojet in the auroral zone. This is clearly shown in Fig. 4.6A and B. At ~ 0419 UT the eastward electrojet was $\sim 6-8^\circ$ wide with a maximum H perturbation of $\sim -200\gamma$.

In the sequence of latitude profiles shown in Fig. 4.6, the development of a westward electrojet is evident to the north of the pre-existing eastward electrojet. This development, in fact, was associated with the onset of substorm activity in the late evening and midnight sectors. The onset of a substorm just prior to 0400 UT is evident from the H component magnetograms for WHAL and CHUR. The increased micropulsation activity at this time is also indicative of a substorm onset. To determine the magnetic response to this substorm activity as observed in the evening sector, we set the DC level at 0357 UT and analyzed the ensuing development. Fig. 4.7 shows the differential profile and differential polar plot for ~ 0416 UT. (The length of the perturbation vectors in the polar plot is measured to the base of the arrow head.) To illustrate the approximate orientation of our line of stations with respect to the auroral oval, a $Q = 2$ oval was drawn on the plot. In Fig. 4.6A and B the eastward electrojet cannot be explained in terms of

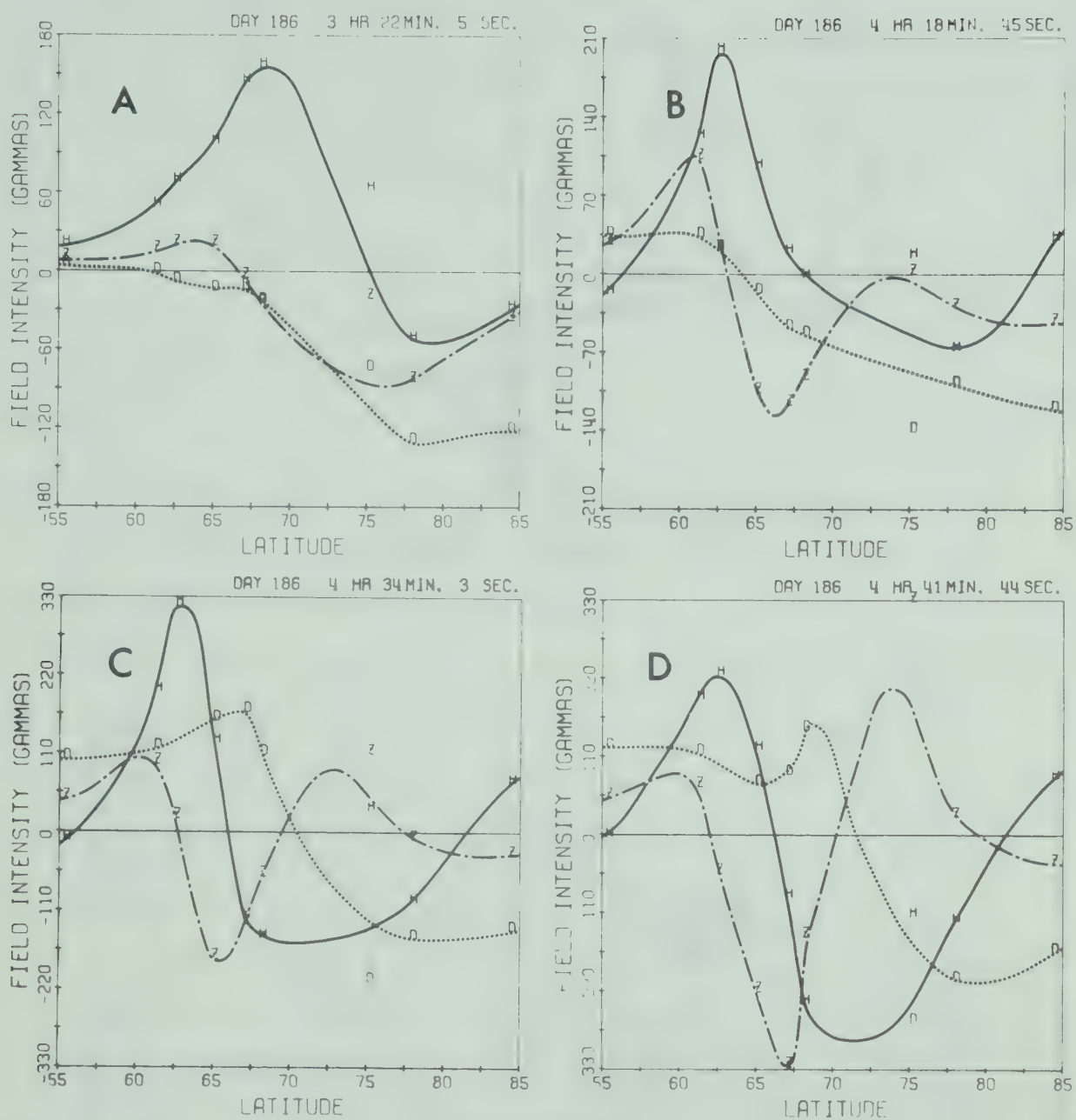


Fig. 4.6 The development of both electrojets is depicted here. Note the enhancement of the D component. See Appendix A5 for a discussion of the technique of fitting curves to the data points.

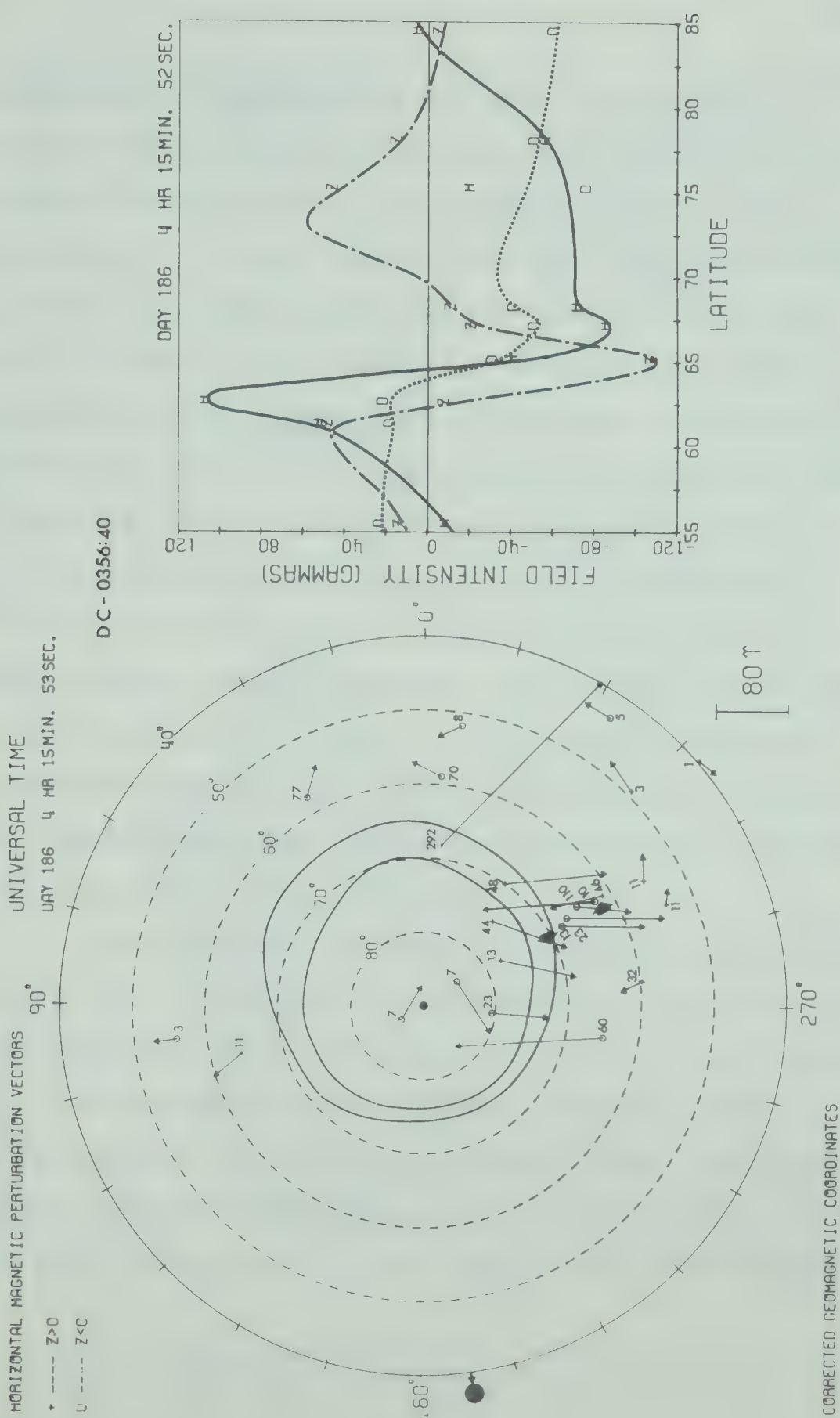


Fig. 4.7 Differential profile and polar plot ($0 = 2$ oval) for 0416 UT. Note the buildup of the two electrojets in the evening sector associated with a substorm in the midnight sector.

a return current associated with a much larger westward electrojet flowing along the auroral oval, especially since the eastward electrojet was the dominant system in the evening sector. In fact the existence of a westward electrojet flowing along the auroral oval at 0322 UT is unlikely. However, in Fig. 4.7 the eastward electrojet (representing the perturbation of the pre-existing eastward electrojet) was associated with a much larger westward electrojet (that had developed since \sim 0357 UT) flowing along the auroral oval. The approximate location of the two electrojets is depicted by the large arrows on the polar plot (the size of these arrows does not represent the relative size of the inferred electrojets). Similar results were obtained for other perturbations of the eastward and westward electrojets in the evening sector which occurred during this event and events recorded on other days as well.

The development of both electrojets in the evening sector for this particular event is portrayed with the use of the component contour diagrams presented in Fig. 4.8A, B and C. The dominance of the eastward electrojet over a possible westward electrojet to the north from \sim 0245-0430 UT is clearly demonstrated by the large +H regime in Fig. 5.8A. During this interval of time the location of the maximum +H

DAY 186

H COMP.

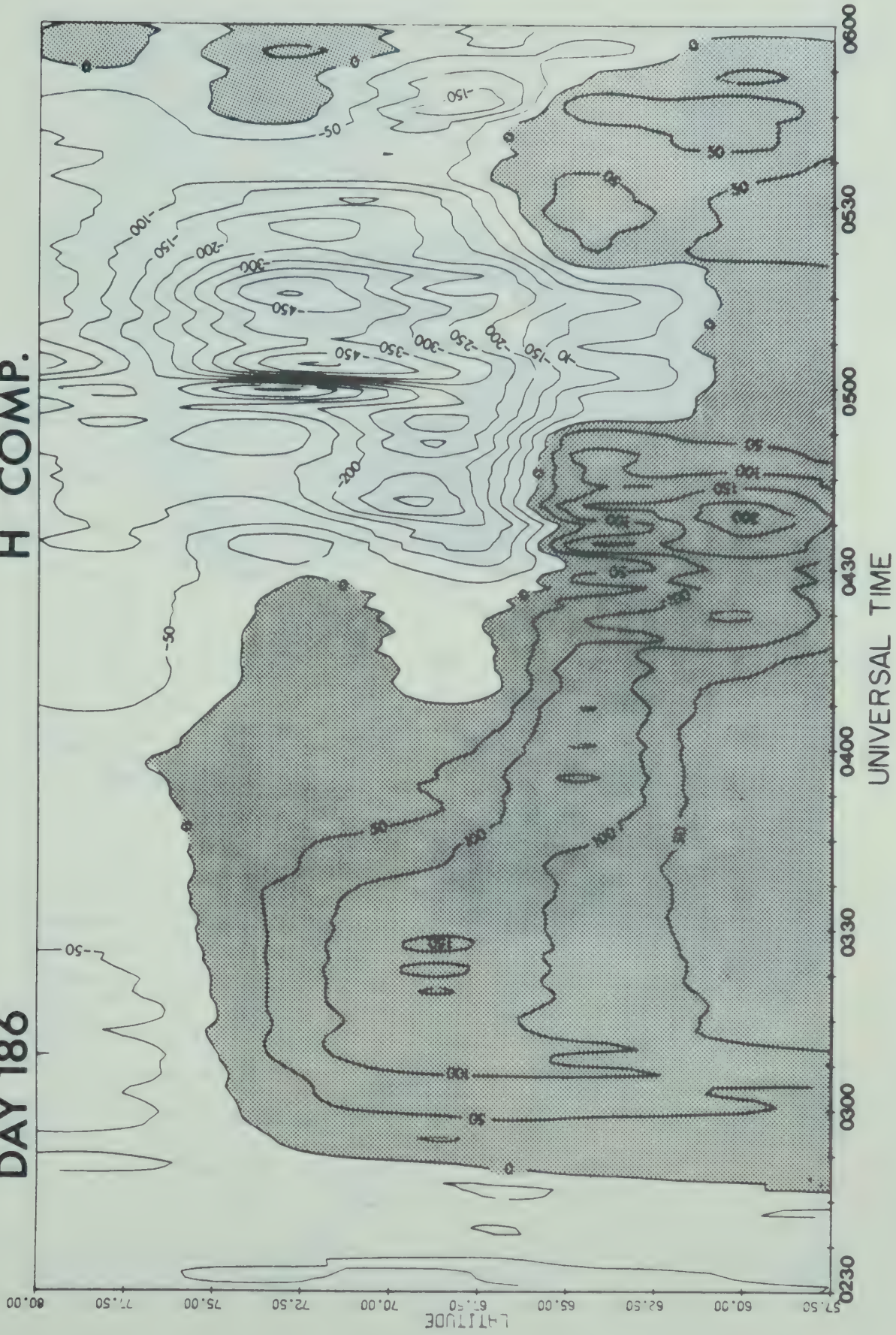


Fig. 4.8A H component contour diagram for July 5, 1970.

DAY 186

D-COMP.

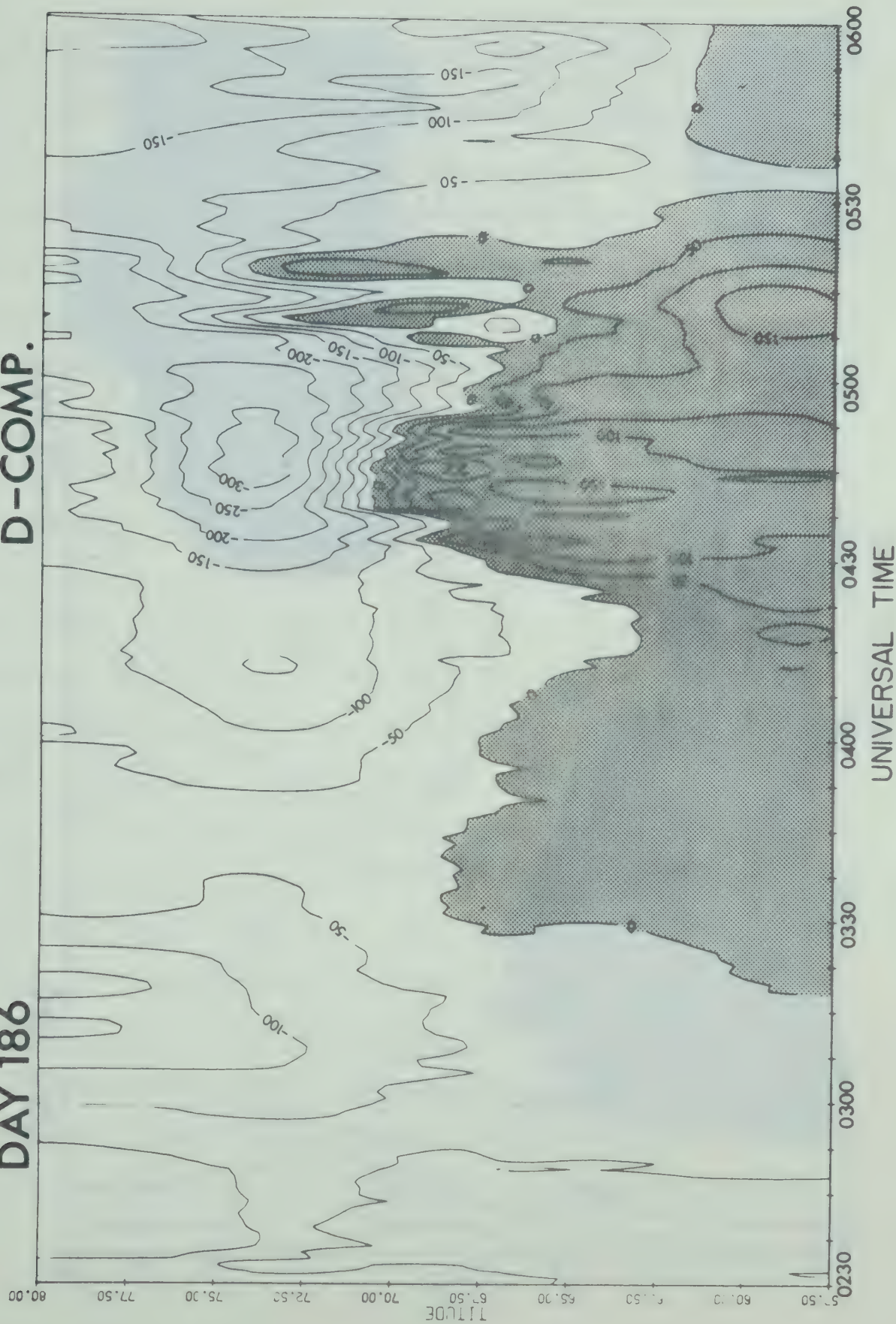


Fig. 4.8B Same as Fig. 4.8A but for the D component.

DAY 186

Z-COMP.

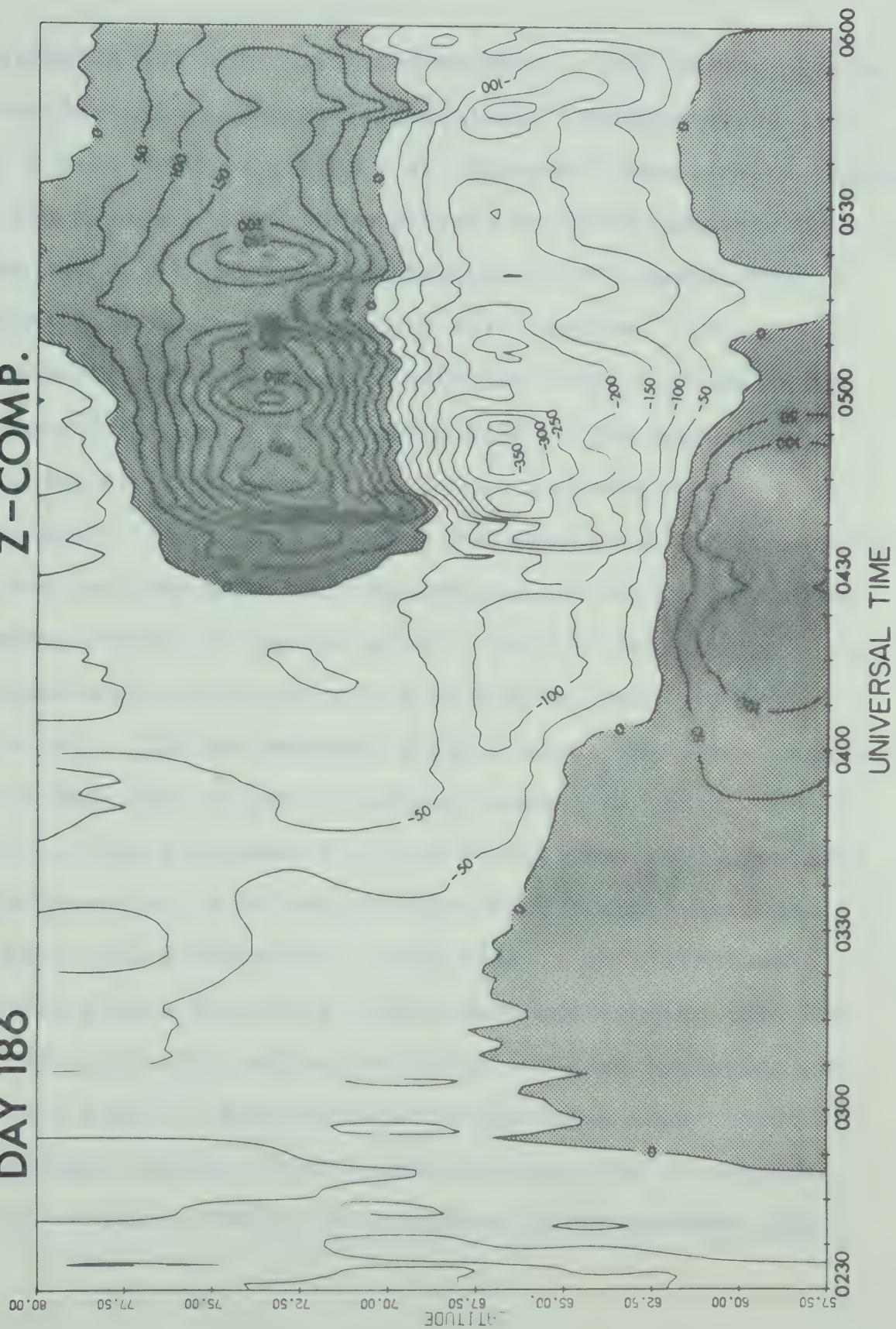


Fig. 4.8C Same as Fig. 4.8A but for the Z component.

perturbation shifted slowly equatorward. This motion is also observable in the Z component diagram. From the slope of the $Z = 0$ contour we obtained an 'apparent' equatorward velocity of ~ 150 m/sec, similar in magnitude to those obtained by Kamide and Fukushima (1971). The reason for emphasizing 'apparent' is discussed later in this section. The rapid development of the westward electrojet is also shown in the H component diagram. From ~ 0450 - 0520 UT the westward electrojet was the dominant system as observed by our line of stations. The development of two regimes of $+Z$ at both high and low latitudes and the enhancement of the $-Z$ regime in between these $+Z$ regimes after ~ 0425 UT was due to the development of two oppositely directed and well defined electrojets. The D component diagram shows the large enhancement of both the $+D$ and $-D$ regimes commencing just prior to 0430 UT. This enhancement of the D component could possibly be attributed to outflowing Birkeland current associated with these two electrojets. This idea is consistent with the model system discussed in the previous section (see Fig. 4.1C and 4.2). This effect was also reported by Kamide and Fukushima (1971). Associated with the large enhancement of the westward electrojet at ~ 0500 UT (the time of onset of a large $-H$ bay at CHUR), the southern $+Z$ perturbation de-

creased in amplitude and became negative even south of CALG. The +H perturbation associated with the eastward electrojet also decreased in amplitude. As the westward electrojet along the auroral oval decayed, both the +Z and +H regimes increased in amplitude and advanced poleward. From latitude profile analysis and the H and Z component diagrams, it is obvious that the strength of the eastward electrojet appeared to decrease significantly between 0440 and 0600 UT. However, the spatial and temporal changes observed may only be apparent changes due to the increased strength of the -H and -Z perturbations associated with the enhancement of the westward electrojet to the north. If this were the case for the event shown here, then this example demonstrates the fact that the dynamics of the eastward electrojet are not easily studied, especially when only a sparse distribution of stations is used. Also, it should be noted that the equatorward (or poleward) velocities obtained using the $Z = 0$ crossover motion may be meaningless when obtained during the development of a westward electrojet. This is best illustrated in Fig. 4.1B, C and D in the previous section. As the westward electrojet enhances (or the line of stations rotates beneath the current system shown in Fig. 4.1A, the $Z = 0$ crossover associated with the eastward

electrojet moves southward even though the eastward electrojet remains stationary. Therefore, we feel that such velocity measurements (including our previous measurement of ~ 150 m/sec) should be treated with care and referred to only as 'apparent' velocities. If, however, the density of stations is such that the development of both electrojets can be ascertained, then (possibly through the use of modelling techniques described in Chapter II and VI) the true velocity and other important aspects of the dynamic development could be extracted from the observed data. For an isolated electrojet (eastward or westward) the use of $Z = 0$ crossover for velocity calculations is probably warranted (see Chapter III, section 3.3).

Fig. 4.9 shows some other examples of eastward electrojets. Fig. 4.9A and B depict the development of first an eastward electrojet (0504 UT profile) and then an enhancement of the westward electrojet positioned along the auroral oval (0603 UT profile). Fig. 4.9C and D demonstrate the stability of the shape and strength of a larger eastward electrojet associated with a large SD current system. Other examples of eastward electrojets are shown in Appendix A7.

In summary, from the analysis of magnetic perturbations observed by our line of stations in the evening

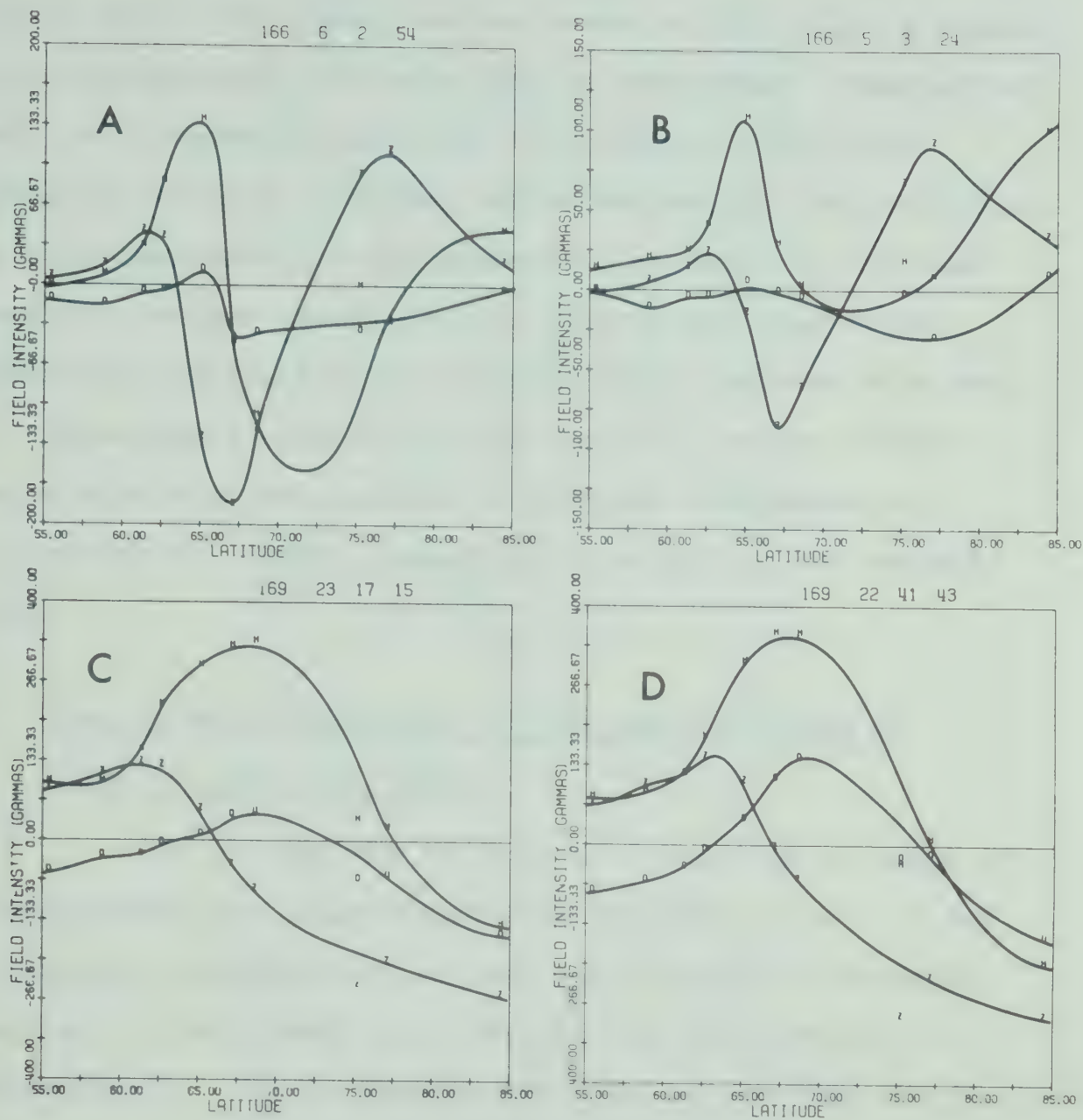


Fig. 4.9 Some examples of eastward electrojets. The two profiles for Day 166 are in reverse order.

sector and by the observatories shown in Fig. 3.2, we suggest that the eastward electrojet has an independent component as well as a dependent component in relation to the polar magnetic substorm. Whether the mechanism for the excitation of both components of the eastward electrojet is the same requires further investigation. Due to the size of the dependent component of the electrojet as compared with that of the westward electrojet, the idea of a return current associated with the westward electrojet as proposed by Akasofu et al. (1965), cannot be ruled out at the present time.

4.4 The dynamic development of the substorm event of June 15, 1970 (Day 166)

In this section we present a detailed analysis of the substorm that occurred on June 15, 1970. The H, D and Z component magnetograms and the associated Pi 2 micropulsations for this event are shown in Fig. 4.10 and 4.11 respectively. The Kp indices for this day are (4-, 3+, 4, 3+, 4-, 3+, 3, 4+; $\Sigma Kp = 29-$). The Dst indices for the interval 0500-1200 UT are (-9, -6, -2, -1, -3, -0, 2, -2) indicating a lack of response of the symmetric component of the ring current during the time of this substorm.

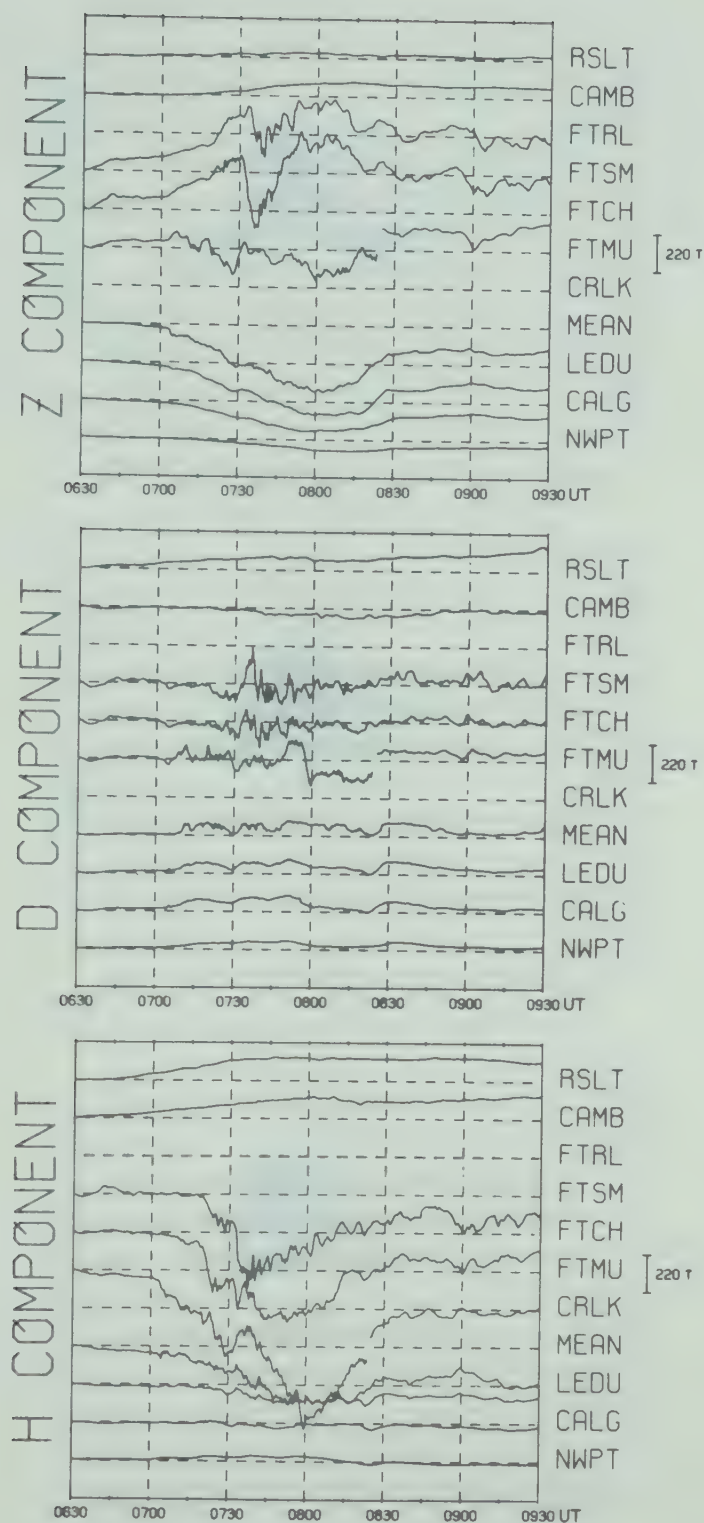


Fig. 4.10 Magnetograms for the substorm that occurred on June 15, 1970 (Day 166).

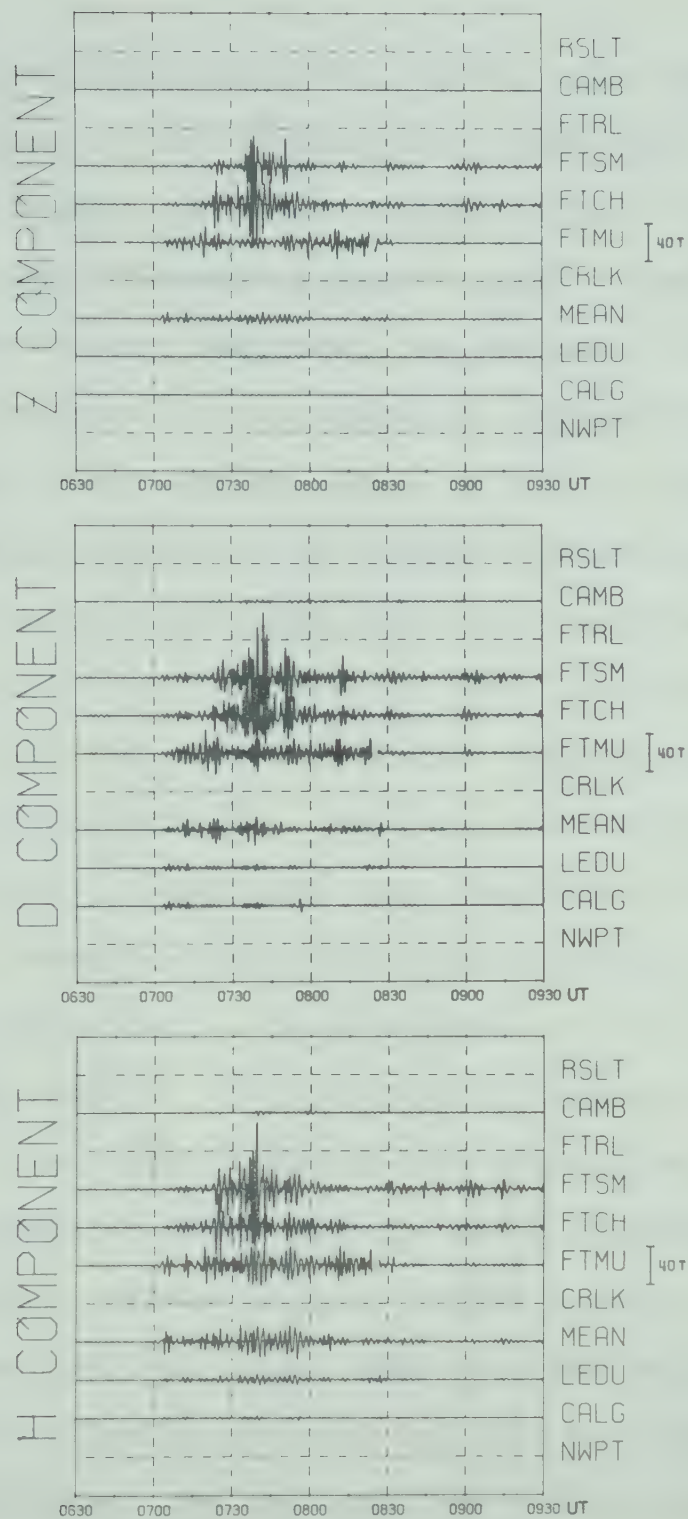


Fig. 4.11 Pi 2 micropulsation activity (40-150 sec) associated with the substorm shown in Fig. 4.10.

From the micropulsation activity, the onset of the expansive phase of the substorm was identified at ~ 0702 UT. This estimate was confirmed by the analysis of latitude profiles before and after the substorm onset. Before the onset of this particular substorm, the magnetic activity was relatively high as seen in the component magnetograms shown in Fig. 4.12 and from the high values of the Kp indices prior to 0700 UT. The existence of an eastward electrojet and the subsequent buildup of a westward electrojet north of the eastward electrojet prior to the onset of this substorm was shown previously in Fig. 4.9. In fact a substorm was observed at CHUR around 0600 UT. Also the observation at NARS, WHAL and COLL of what might have been the buildup of a large convective type current system (SD current system), commencing between 0400 UT and 0500 UT, is noticeable. It is interesting to note that the onset of this particular substorm at 0702 UT was hardly discernible at any of the observatories shown in Fig. 4.12 except for WHAL (only in the Z component). There does, however, appear to be a slight positive response of the H component at COLL associated with the onset.

In the following analysis we feel confident that we were able to extract the perturbation field associated with the 0702 UT substorm by setting the DC level just before

DAY 166, 1970

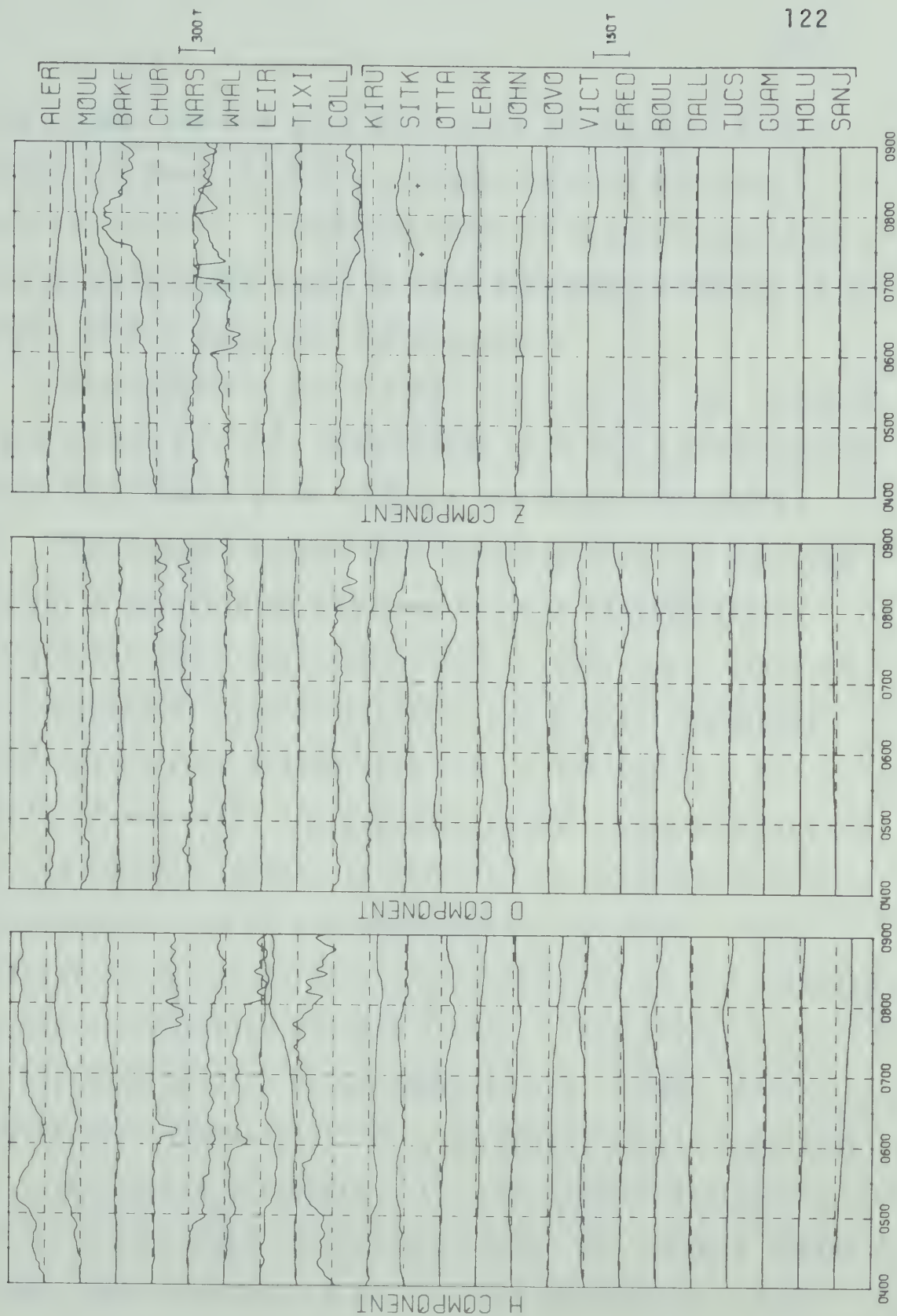


Fig. 4.12 Magnetograms from 23 observatories in the northern hemisphere for June 15, 1970.

the onset time. We are also well aware of the fact that the growth and decay of other systems may possibly have affected our results. Since the level of magnetic activity was so high before the onset of this substorm, evidence of a possible growth phase was not obtainable.

Approximately 4 min after the onset of the substorm, a current system was well established with the H perturbation reaching -140γ (see Fig. 4.13A) and the moment located at $\sim 64.0^\circ$. The current system grew steadily over the next few minutes while maintaining the same profile configuration, attaining a maximum H perturbation of $\sim -200\gamma$ and a width of $\sim 3.5^\circ$. Associated with this growth was a small northward motion of the current system (see Fig. 4.13A and B). At 0719 UT (~ 17 min after the substorm onset) an intensification of the current system was observed in conjunction with an enhancement of the Pi 2 micropulsation activity. The intensification of the current system occurred on the northern edge of the pre-existing current system. This effect was clearly apparent by 0723 UT as shown in Fig. 4.13C. Associated with this intensification, the moment of the resulting current system moved northward $\sim 1^\circ$. By 0728 UT the amplitude of the H component perturbation under the current system was $\sim -450\gamma$ and the width of the current system was $\sim 4.5^\circ$.

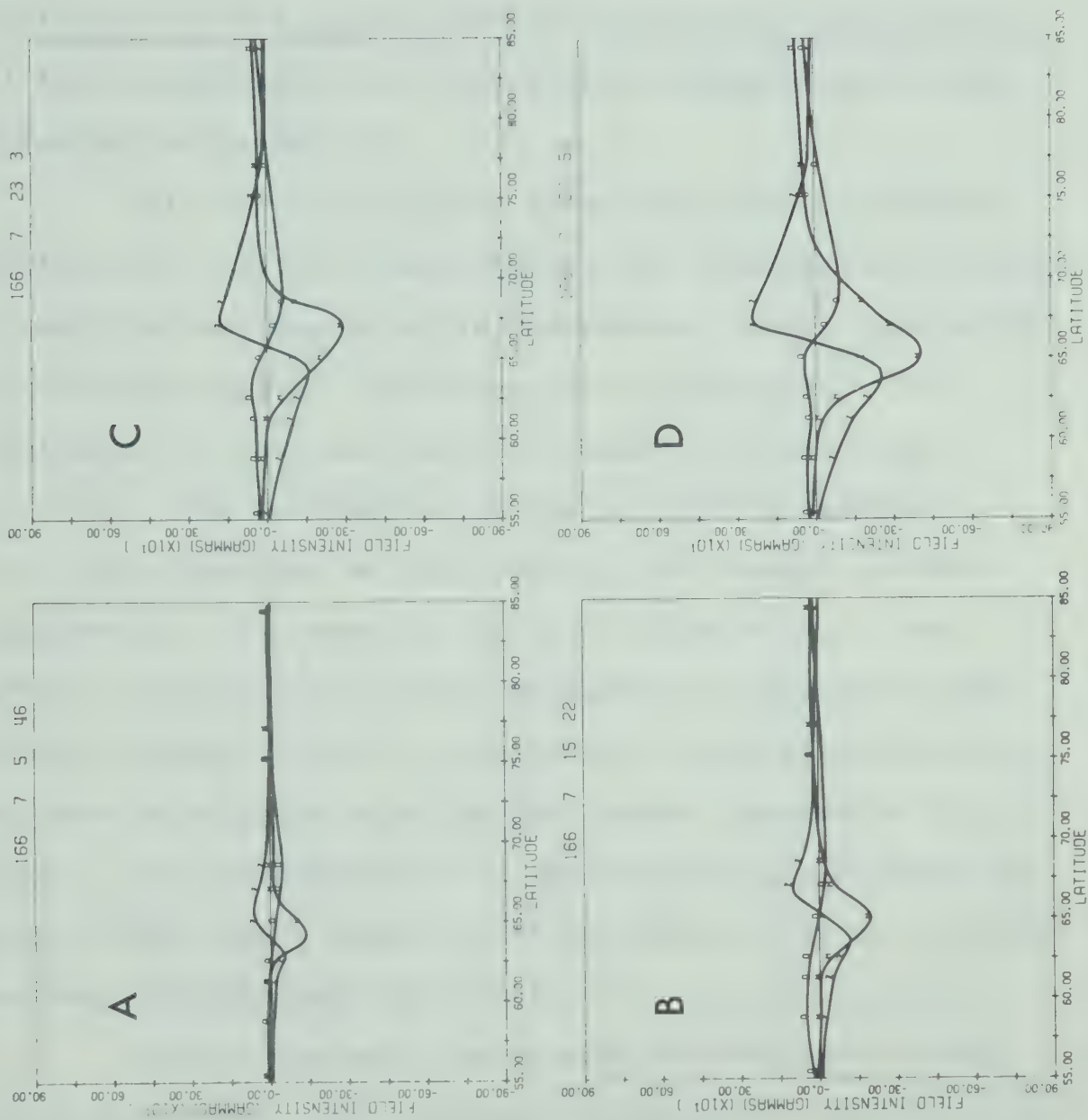


Fig. 4.13 Latitude profiles showing the development of the westward electrojet for Day 166.

(see Fig. 4.13D). It is interesting to note that the D profile is representative of a three-dimensional E-W current system with a central meridian east of our line of stations. In fact, up to 0729 UT the latitude profiles of all three components are in excellent agreement with those presented in Chapter II.

At 0732 UT (~ 13 min after the previous intensification) the substorm perturbation was dramatically altered through the development of an independent current system at the northern edge of the pre-existing electrojet. The development of this new current system is illustrated in Fig. 4.14. The deformation of the profiles presented in this figure can best be explained by two current systems separated by $\sim 5^\circ$ (see Fig. 2.18D in Chapter II). The partial cancellation of the Z perturbation between the two current systems is due to the opposite sense of the vertical component associated with the two current systems in this region. This development of a new current system caused an onset of what would appear at first glance to be an isolated substorm at CHUR (see Fig. 4.12).

During the next few minutes the northern current system grew (with the H component perturbation reaching -460γ) while the southern current system decayed substantially so

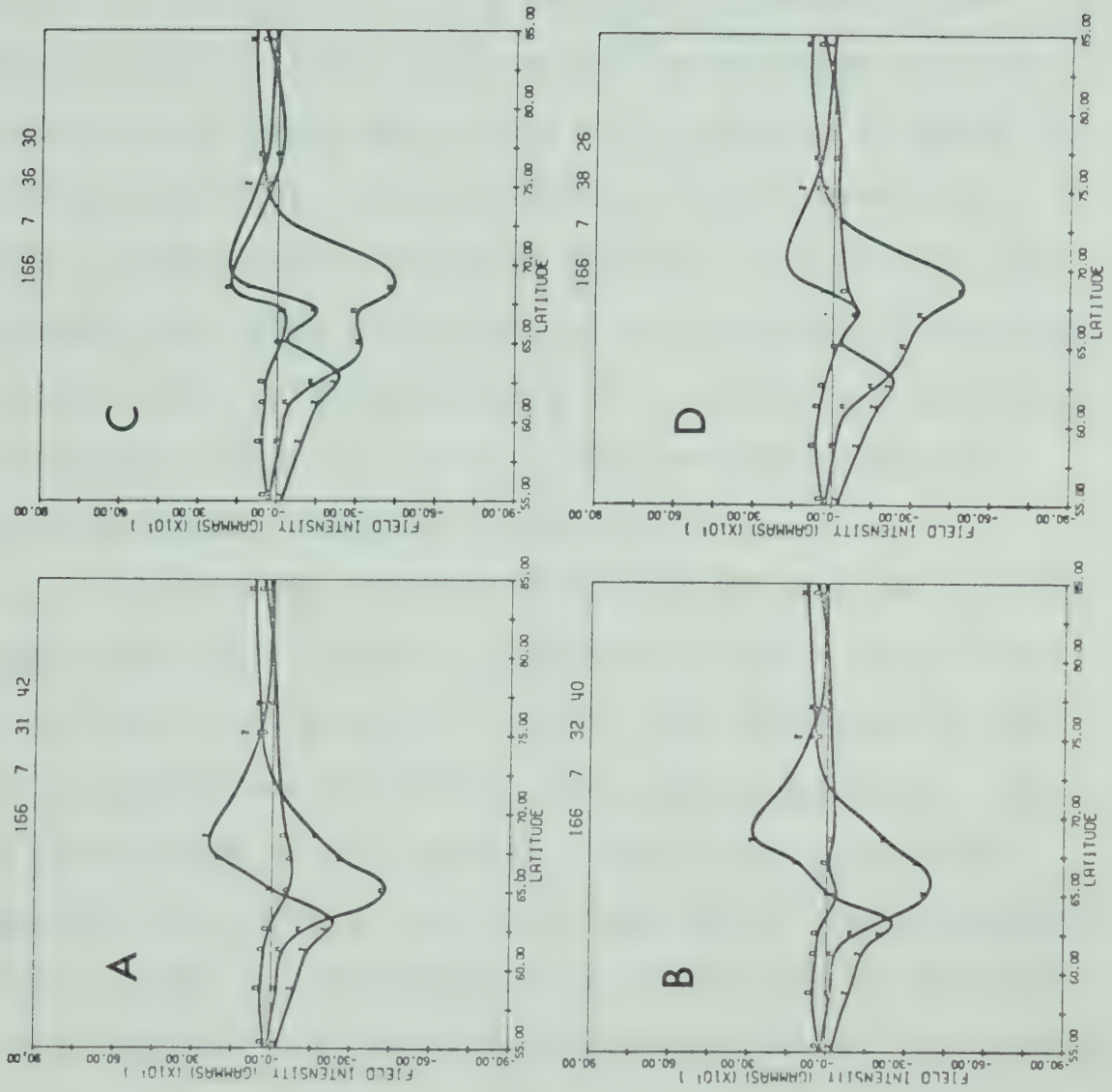


Fig. 4.14 Same as Fig. 4.13 but showing the continued development of the electrojet.

that by 0734 UT the northern system was the larger of the two. It is interesting to note the deformation (at FTSM) of the D profile exhibited in Fig. 4.14C. Such +D perturbations are indicative of E-W propagating auroral forms possessing N-S aligned segments such as eastward and westward travelling loops and surges. An analysis of these +D perturbations along with available all-sky camera photographs is presented in the next chapter. Although no all-sky camera data were available for this particular substorm, we believe that this development of a new current system at the northern border of the pre-existing electrojet was associated with a westward travelling surge.

During the interval 0734-0739 UT, the two current systems were well defined. It should be noted that if we had not had a station at 67° (FTCH), the existence of two current systems would probably have gone undetected. In fact the buildup of the northern edge of the electrojet commencing at ~ 0719 UT may have been due to an independent current system, but the resolution of our line of stations was not sufficient to determine whether this was the case or not.

By 0704 UT, the two current systems were blended together forming a resultant system having a width of $\sim 7^{\circ}$.

and a moment located at $\sim 66.5^{\circ}$ (see Fig. 4.15A). The distribution of horizontal perturbation vectors before 0731 UT and after ~ 0744 UT showing the buildup of the second current system is illustrated in Fig. 4.16. The only notable changes in the overall pattern were the dramatic enhancements of the horizontal perturbation vectors at FTCH, FTSM and CHUR and a slight increase in the magnitude of these vectors at all other stations. The stability of the directions of these perturbation vectors is interesting in light of the development of a new current at the northern border. There was definitely an enhancement of the eastward electrojet in the afternoon and evening sectors. The horizontal vectors in both plots (except for the influence of the eastward electrojet as discussed in section 4.2) are remarkably similar to those shown in Fig. 3.4 for an E-W three-dimensional current system. The central meridian of the current system in these two plots is placed at $\sim 10^{\circ}$ east of our line of stations. The $Q = 3$ oval is included in both plots for orientation purposes.

The latitude profile pattern remained stable from 0740 UT to 0748 UT after which it underwent one final alteration. Associated with a further enhancement of Pi 2 micro-pulsation activity, the southern border of the current system

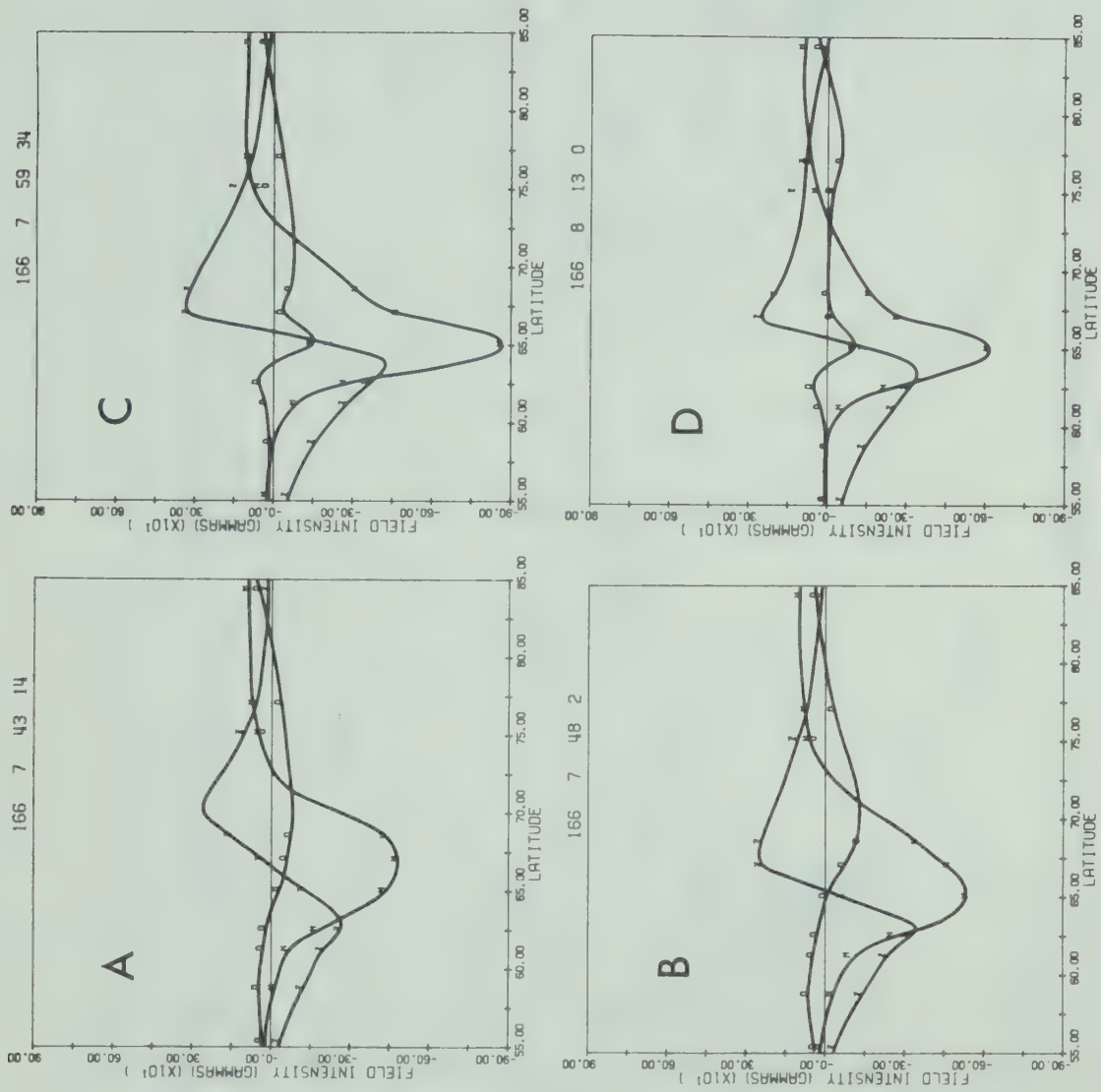


Fig. 4.15 Same as Fig. 4.13 but showing the continued development of the electrojet.

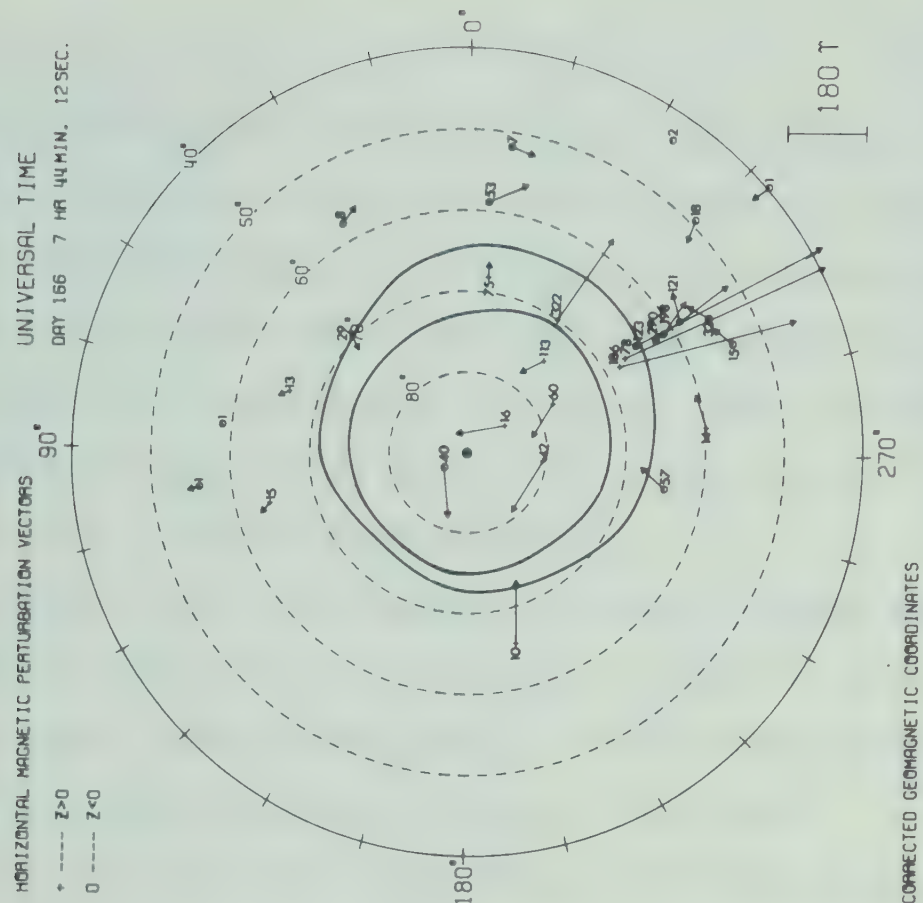
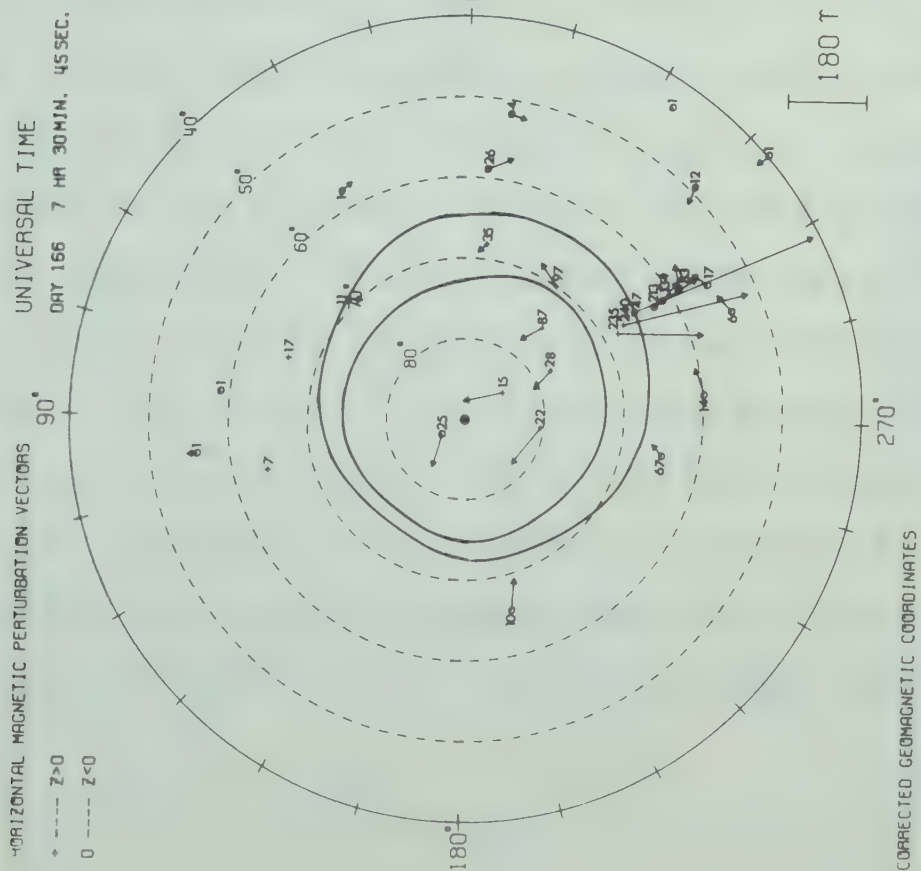


Fig. 4.16 Polar plots showing the distribution of horizontal perturbation vectors before and after the enhancement of the northern border.

drastically intensified with the maximum H perturbation reaching an amplitude of -870γ by 0759 UT (see Fig. 4.15B and C). During this period of development, the width of the current system decreased to $\sim 4.5^\circ$ while the moment of the current system moved equatorward to $\sim 65.5^\circ$ (the location of the moment of the current system before the initial intensification at the northern border).

About 0800 UT the substorm started to decay and it disappeared after roughly 2 to 3 hours (see Fig. 4.15D). During this decay phase, the moment of the current system moved progressively equatorward from 65.5° to 64.0° .

The overall dynamic development of this particular substorm as observed with our line of stations is best illustrated in the H and Z component contour diagrams shown in Fig. 4.17A and B. In the H component diagram, the perturbations of the system at 0719 UT, 0732 UT and 0748 UT are clearly distinguishable. The development of the new current system is evident from the two maxima in $-H$ perturbation between 0735 UT and 0740 UT. The final intensification of the southern border is also well defined in this contour diagram. The Z component diagram shows the motions of the $Z = 0$ crossover along with the approximate width of the total system (designated by the dashed lines) throughout the

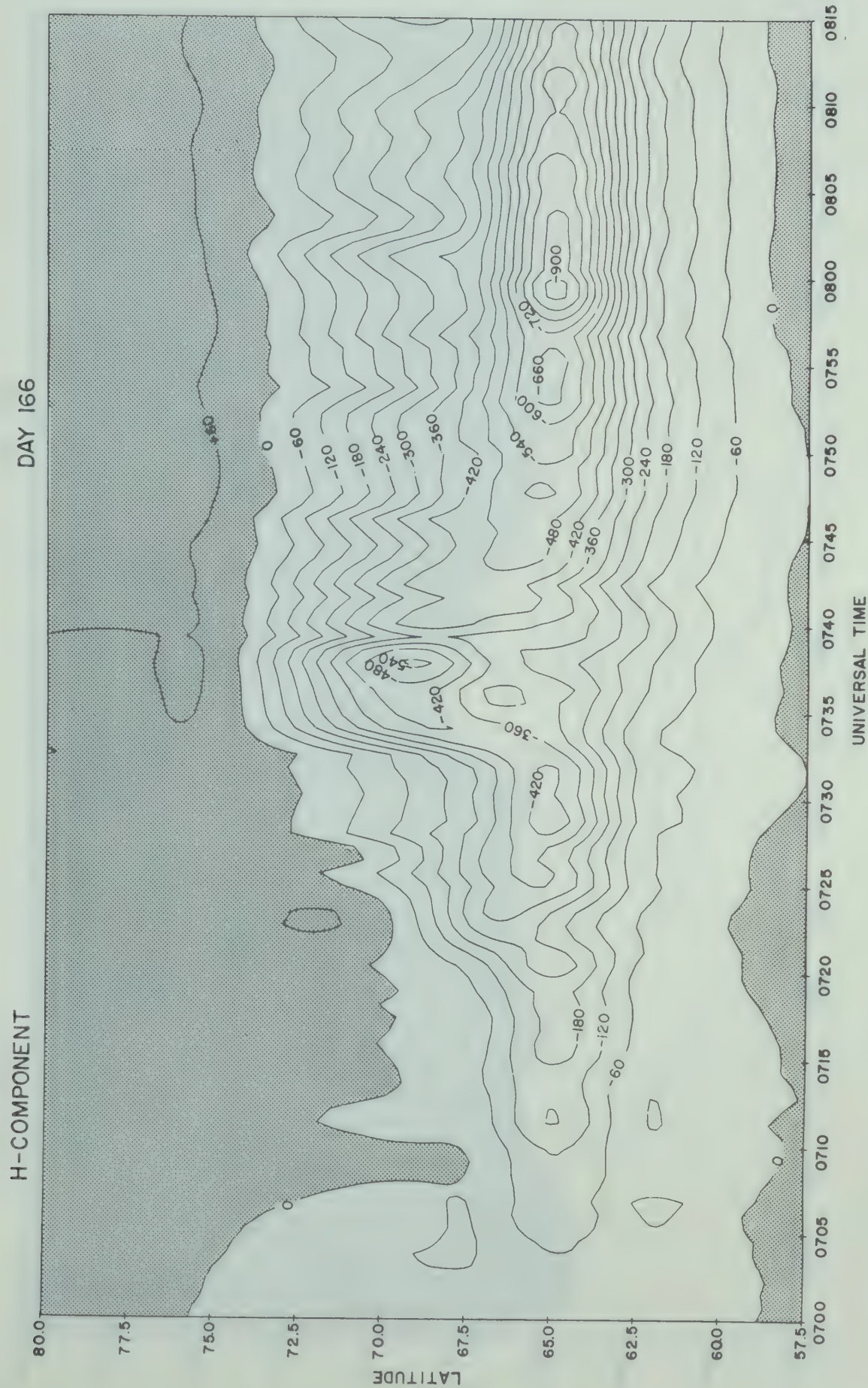
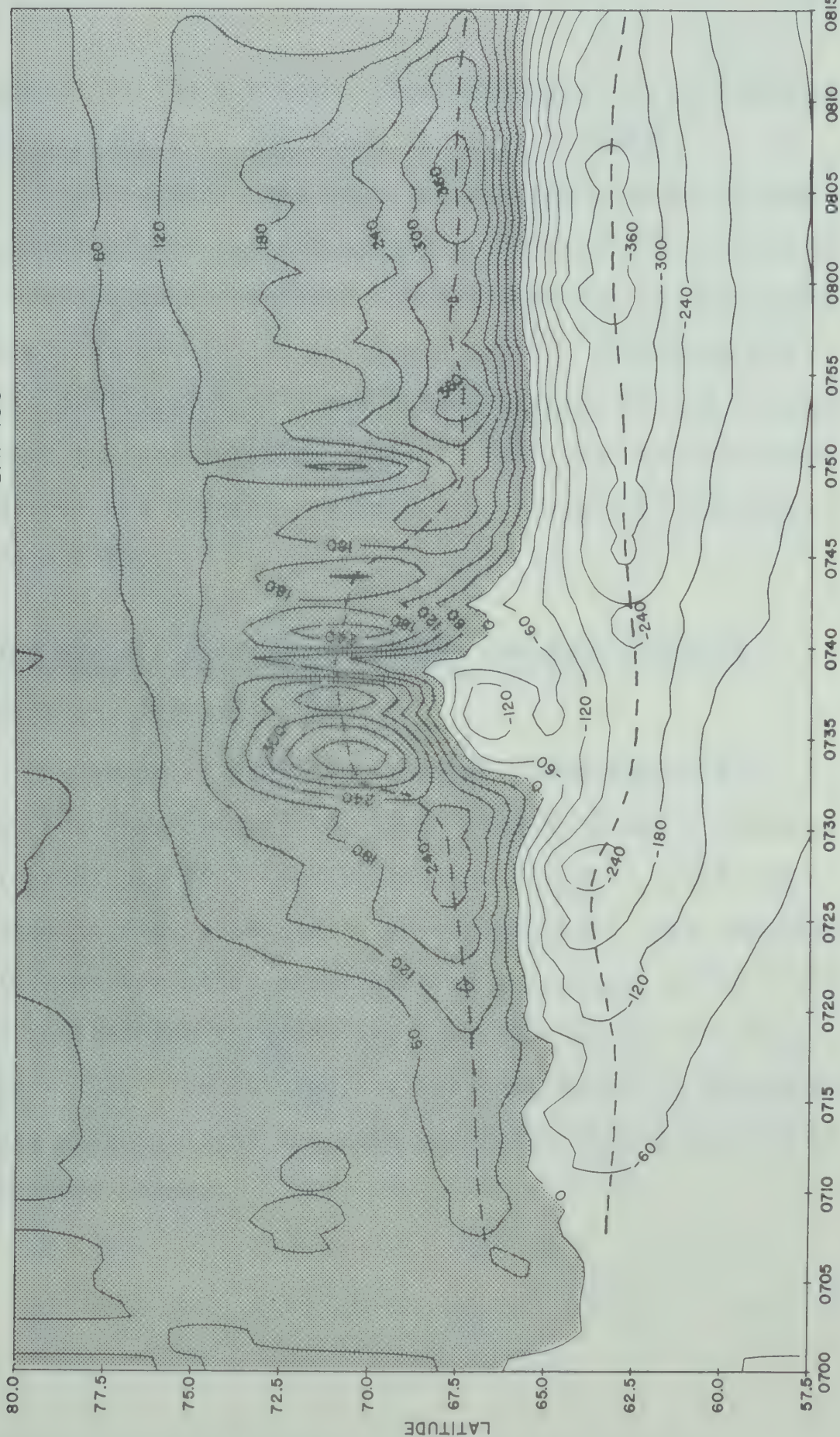


Fig. 4.17A H component contour diagram for the substorm that occurred on June 15, 1970.

DAY 166

Z-COMPONENT



UNIVERSAL TIME

Fig. 4.17B Same as Fig. 4.17A but for the Z component. The dashed lines represent the width of the westward electrojet.

development of the substorm. The major portion of the decay or recovery phase is not shown in these diagrams.

In summary, the most interesting aspects of the development of the current system associated with this substorm are the quasi-periodic intensifications of the northern border of the electrojet (~ 15 min apart), including the dramatic development of a new current system at the northern border of the pre-existing system. Also the relative stability of the southern current system during the entire substorm is most noteworthy.

4.5 The dynamic development of the substorm event of July 14, 1970 (Day 195)

The polar magnetic substorm presented in this section occurred on July 14, 1970. The H, D and Z component magnetograms and Pi 2 micropulsations for this event are presented in Fig. 4.18 and 4.19 respectively. The component magnetograms for other observatories are shown in Fig. 4.20. The Kp indices for this day are (3-, 2+, 3-, 2-, 1+, 2o, 3-, 3-; $\Sigma Kp = 18$). The Dst indices averaged about +5 during this substorm with a slight decrease occurring toward the end of the recovery phase.

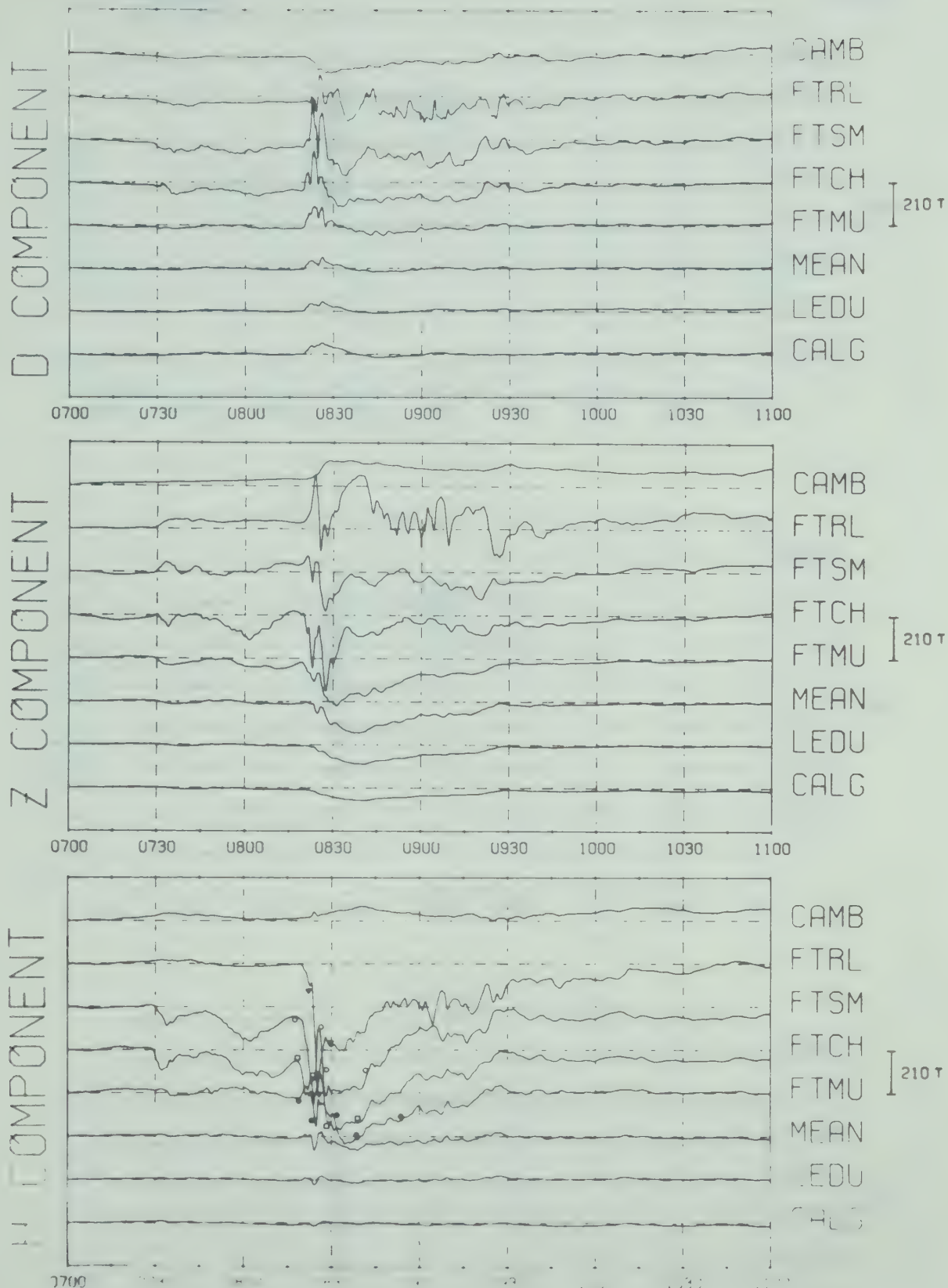


Fig. 4.18 Magnetograms for the substorm that occurred on July 14, 1970 (Day 195).

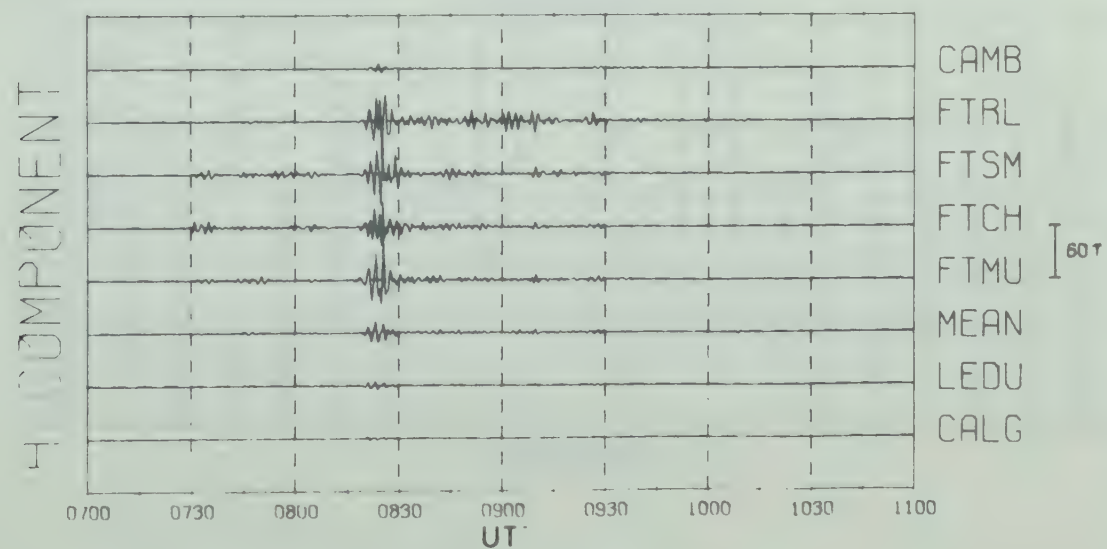
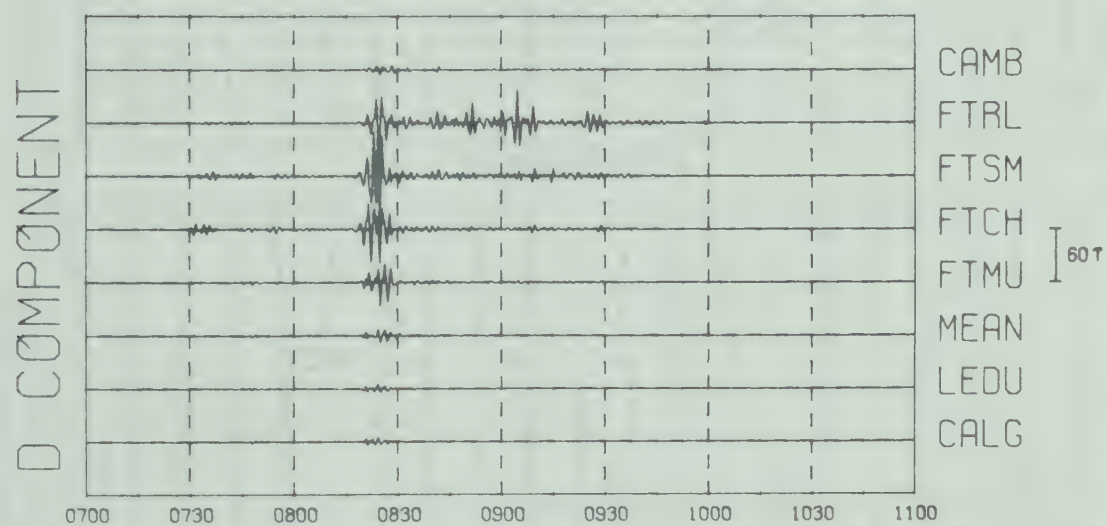
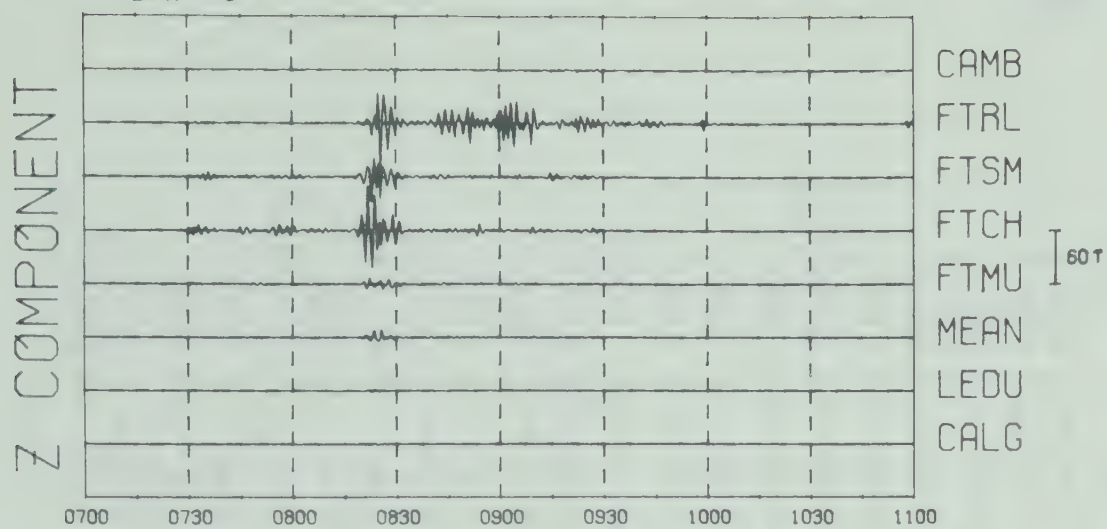


Fig. 4.19 Pi 2 micropulsation activity (40-150 sec) for the substorm shown in Fig. 4.18.

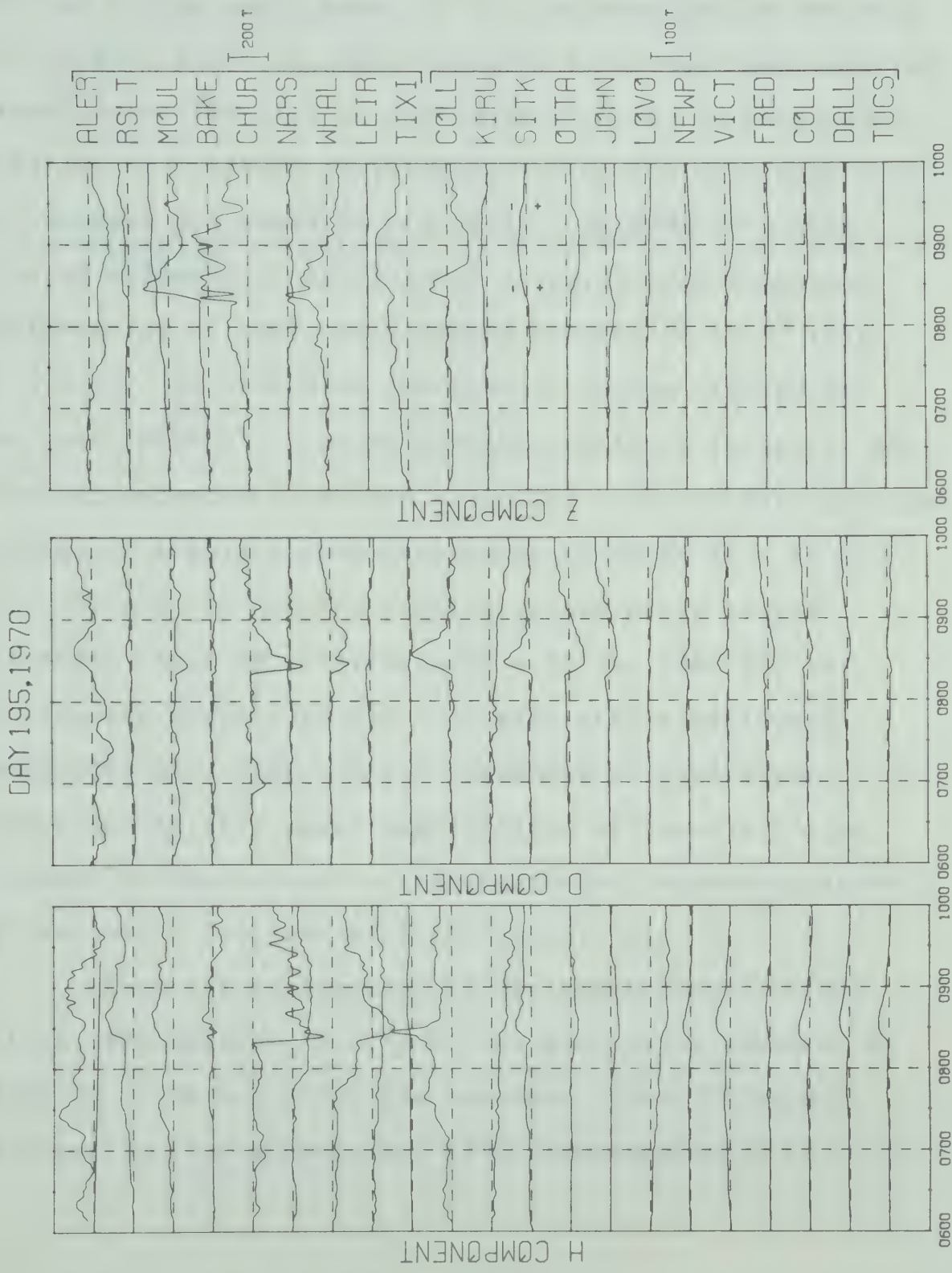


Fig. 4.20 Magnetograms from 21 observatories in the northern hemisphere for July 14, 1970.

The onset of this substorm was ~ 0730 UT as indicated by the small burst of Pi 2 micropulsation activity. Prior to this onset, a small eastward electrojet was observed centered over FTMU with an amplitude of $\sim 20\gamma$ (H component). The series of latitude profiles depicting the development of this substorm are shown in Fig. 4.21. By 0733 UT a well developed westward electrojet was observed with a maximum H perturbation of -90γ and a moment located at 67.5° (see Fig. 4.21A). At this time the current system started to decay until 0745 UT at which time the northern border of this electrojet enhanced (~ 15 min after the onset of the substorm) resulting in a well formed electrojet centered at $\sim 69.0^\circ$. During the next 15 min the current system moved slowly equatorward reaching a latitude of $\sim 68^\circ$ by 0800 UT. At this time the electrojet was $\sim 4^\circ$ wide with a maximum H perturbation of $\sim 156\gamma$. The H component at FTMU became positive during this equatorward motion of the electrojet. The moment of the current system continued to move equatorward reaching a latitude of 67.0° by 0818 UT.

From the analysis of 10 sec resolution latitude profiles, the southern border of the electrojet enhanced at 0818:50 UT (~ 34 min after the previous intensification). This onset is also accompanied by an enhancement of Pi 2

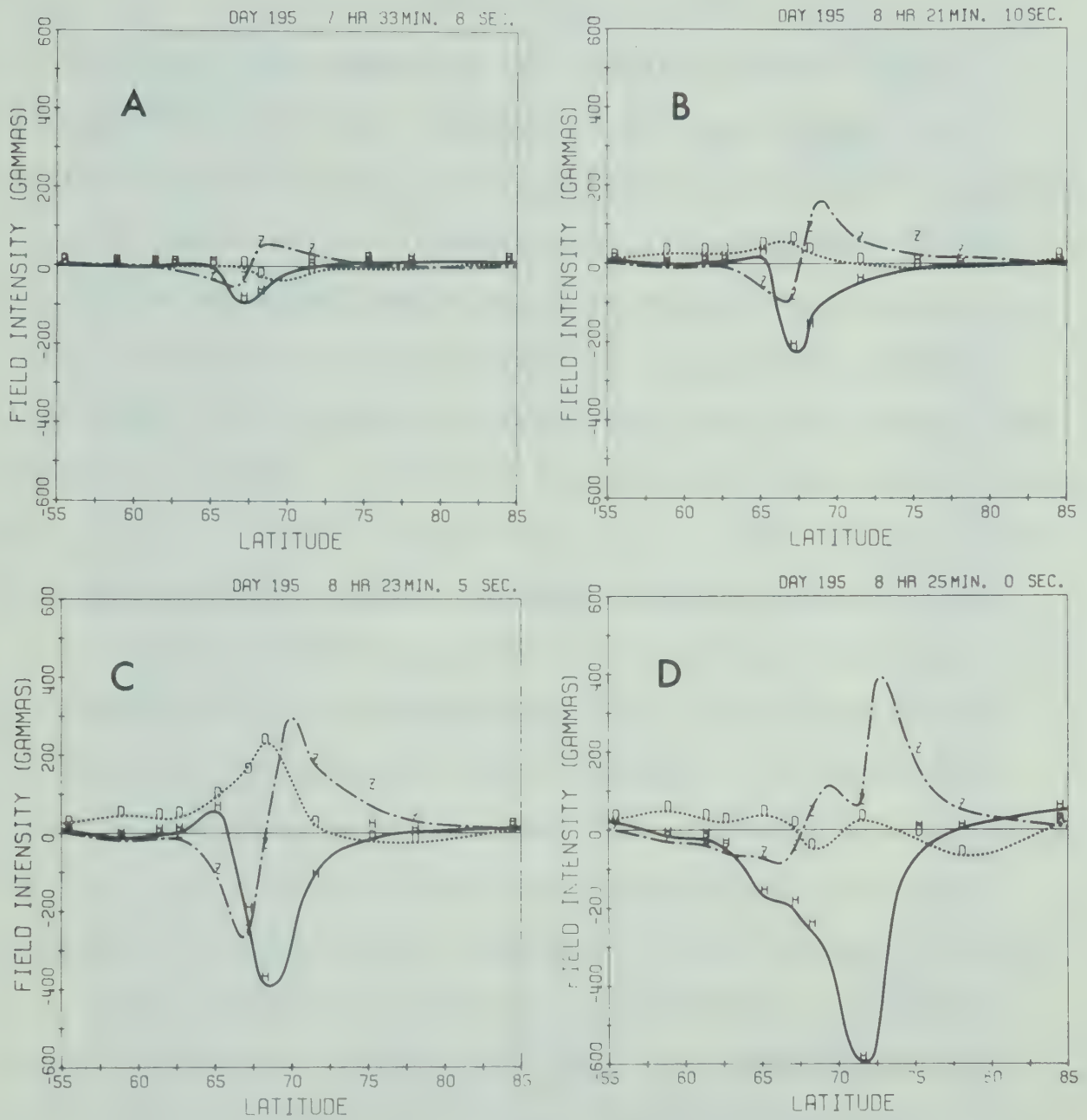


Fig. 4.21 Latitude profiles showing the development of the westward electrojet.

activity and an increase in the +H bay at COLL. By 0821 UT (see Fig. 4.21B) the H perturbation at FTCH reached a value of -218γ with the moment of the current system located between FTCH and FTSM. During the next two minutes the northern border of the electrojet rapidly developed resulting in a northward motion of the moment of the current system. Associated with this enhancement of the northern border, a large +D perturbation developed (as shown in Fig. 4.21C) indicating that a westward travelling surge was located over our station line. By 0823 UT the maximum H perturbation along our line of stations reached a value of -374γ and the moment of the current system was located slightly north of FTSM.

Between 0823 UT and 0825 UT (see Fig. 4.21D) the H component at FTRL strengthened indicating an enhancement of the northern border of the electrojet. In addition, a negative H regime developed from FTMU southward as illustrated in Fig. 4.22. The +H regime that existed prior to this enhanced -H regime is also depicted in this contour diagram.

The latitude profile for 0825 UT shows an example of the latitudinal asymmetries that occur in conjunction with the polar electrojet. It is interesting to note

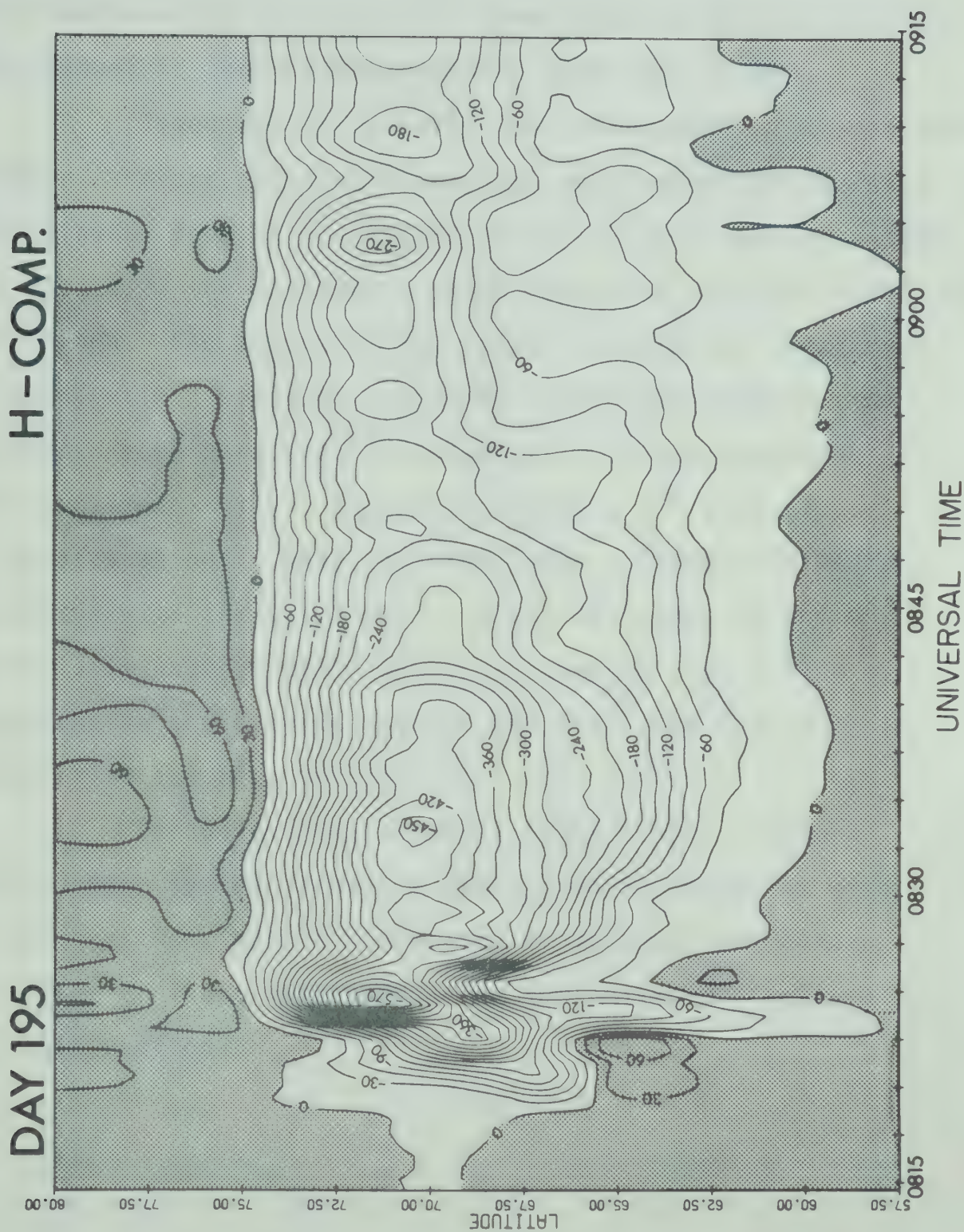


Fig. 4.22 H component contour for the substorm that occurred on Day 195.

the shape of the Z component south of the $Z = 0$ crossover. This deformation is similar to that shown in Chapter II for an asymmetric current distribution (see Fig. 2.18B).

Immediately following the enhancement of the northern border, the pre-existing electrojet developed over the next few minutes forming a wide and fairly uniform current system. In Fig. 4.23 the latitude profile and polar plot for ~ 0831 UT are shown. The moment of the current system was located at $\sim 70.5^\circ$ with a width of $\sim 9^\circ$. The horizontal perturbation vectors shown here are indicative of a three-dimensional current system with a central meridian $\sim 15^\circ$ east of our line of stations. Note that the large perturbation vectors coincide with the $Q = 2$ oval. Also, the shape of the D profile is what we would expect to observe with a line of stations on the evening side of the oval (see Fig. 2.17 in Chapter II and also Chapter VI).

Throughout the recovery phase of the substorm the current system gradually diminished in intensity with minor quasi-periodic enhancements at the northern border (similar to those observed during the substorm discussed in this section).

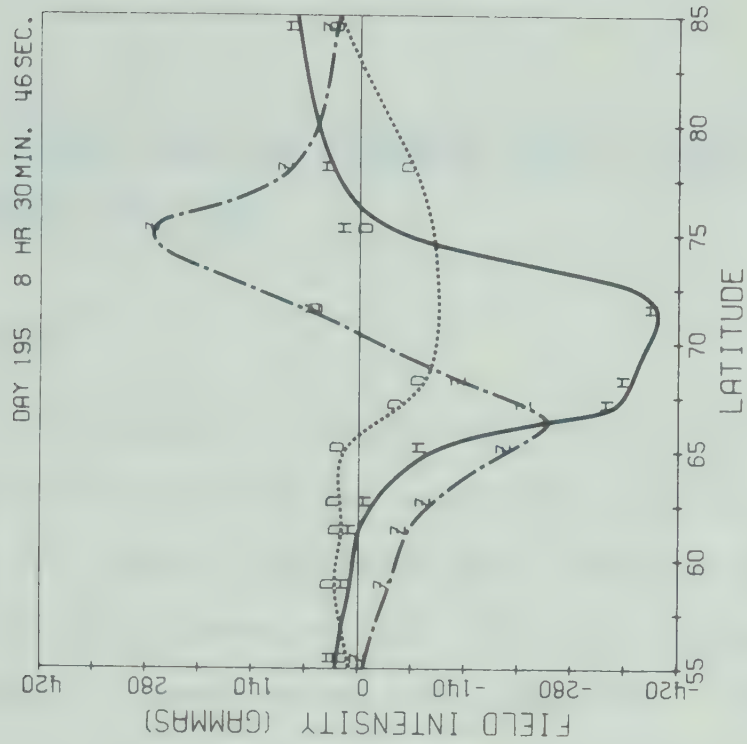
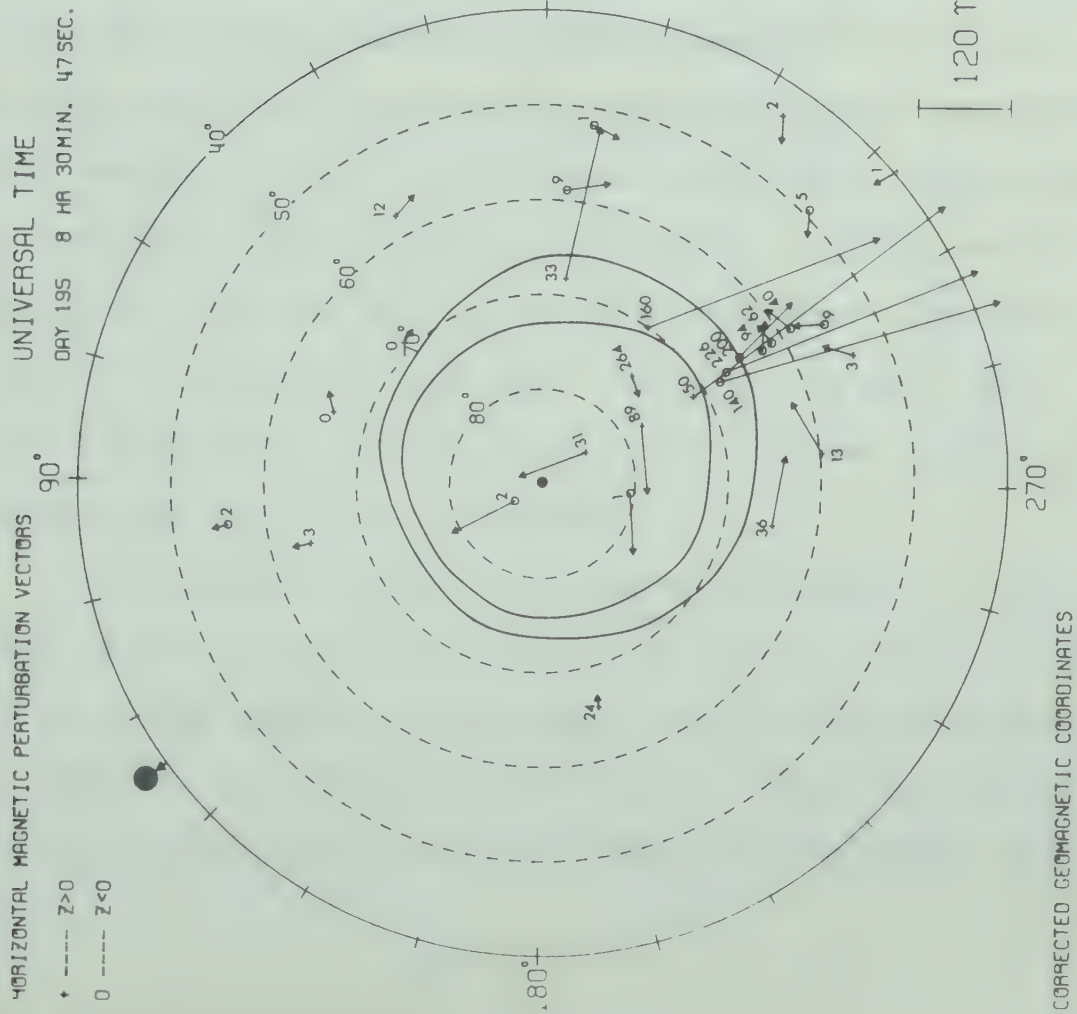


Fig. 4.23 Latitude profile and polar plot ($Q = 2$ oval) for ~ 0831 UT.

CHAPTER V THE POLAR MAGNETIC SUBSTORM AND THE ASSOCIATED AURORAL SUBSTORM

5.1 Introduction

In this chapter we present the analysis of four polar magnetic substorms with the associated auroral substorms. Since the auroral substorms were studied using data from only one all-sky camera, a full correlation between auroral and magnetic substorms was not possible. However, we were able to obtain very interesting results due to the fact that the all-sky camera at FTSM happened to be in an appropriate position to observe a major portion of the auroral activity during at least two of these substorms. During one of the substorms, that occurred on October 7, 1970, the all-sky camera was located west of the position where the westward travelling surge originated. Therefore we were able to study the magnetic effects associated with the passage of this surge over our line of stations.

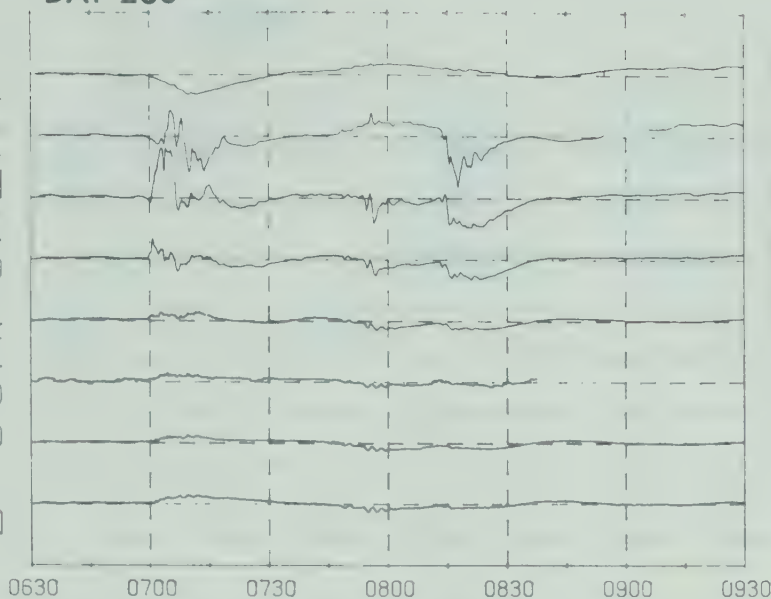
The substorm that occurred on September 1, 1970 afforded us the opportunity to study in detail the latitudinal expansion of the westward electrojet within and probably close to the western edge of the auroral bulge. Also, during this particular substorm the position of the all-sky camera was

centered latitudinally with respect to the region of the major auroral activity associated with the recovery phase (see Akasofu, 1964). Recently the results of a study of the auroral substorm using a meridional line of stations in the Alaskan sector were reported by Snyder and Akasofu (1972) (also see Akasofu et al., 1971). It is quite obvious from the results of their study that analyzing an auroral substorm with data from several all-sky camera stations is necessary in order to minimize the possibility of producing erroneous interpretations. With this limitation in mind we present the following results of our study.

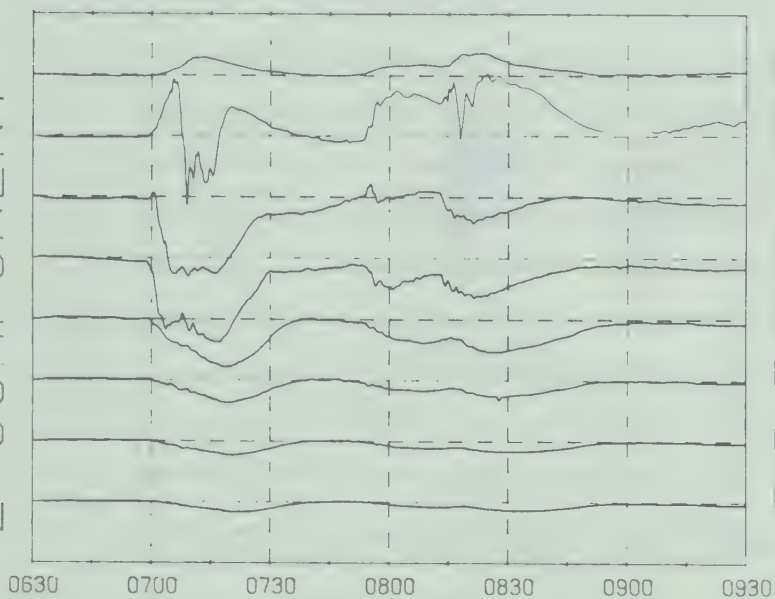
5.2 Substorm events of October 7, 1970 (Day 280)

Even though October 7, 1970 appears as an international quiet day (QQ) with Kp indices of (0+, 1-, 1+, 1o, 1o, 1-, 0+, 1+; $\Sigma Kp = 7-$), a series of four substorms was observed in the Canadian sector between 0600 and 0900 UT. The H, D and Z components of the magnetic perturbations and Pi 2 micro-pulsations associated with three of these substorms are shown in Fig. 5.1 and 5.2 respectively. The symbols on the H component magnetogram allow the traces from each station to be followed. Prior to the first substorm shown in Fig. 5.1, the development of a small eastward electrojet was observed flowing over our line of stations and centered between FTCH and FTSM.

D COMPONENT



Z COMPONENT



H COMPONENT

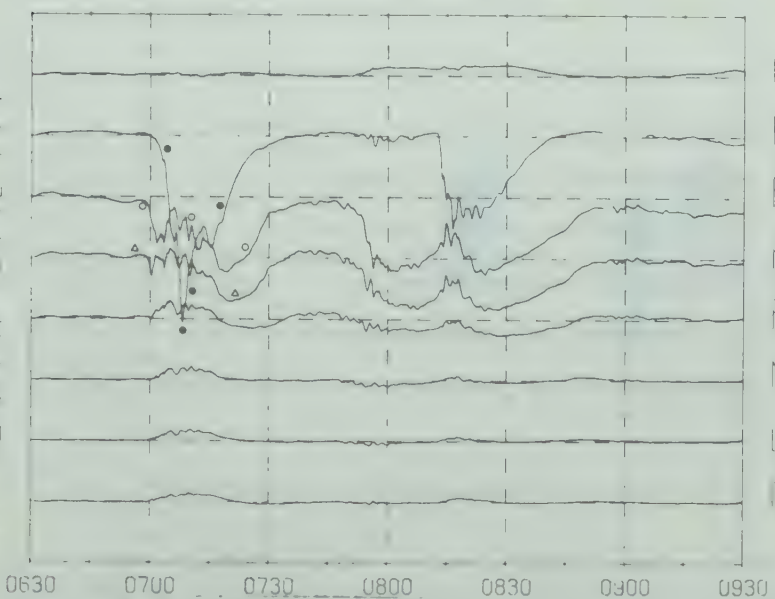


Fig. 5.1 Magnetograms for the series of substorms that occurred on October 7, 1970.

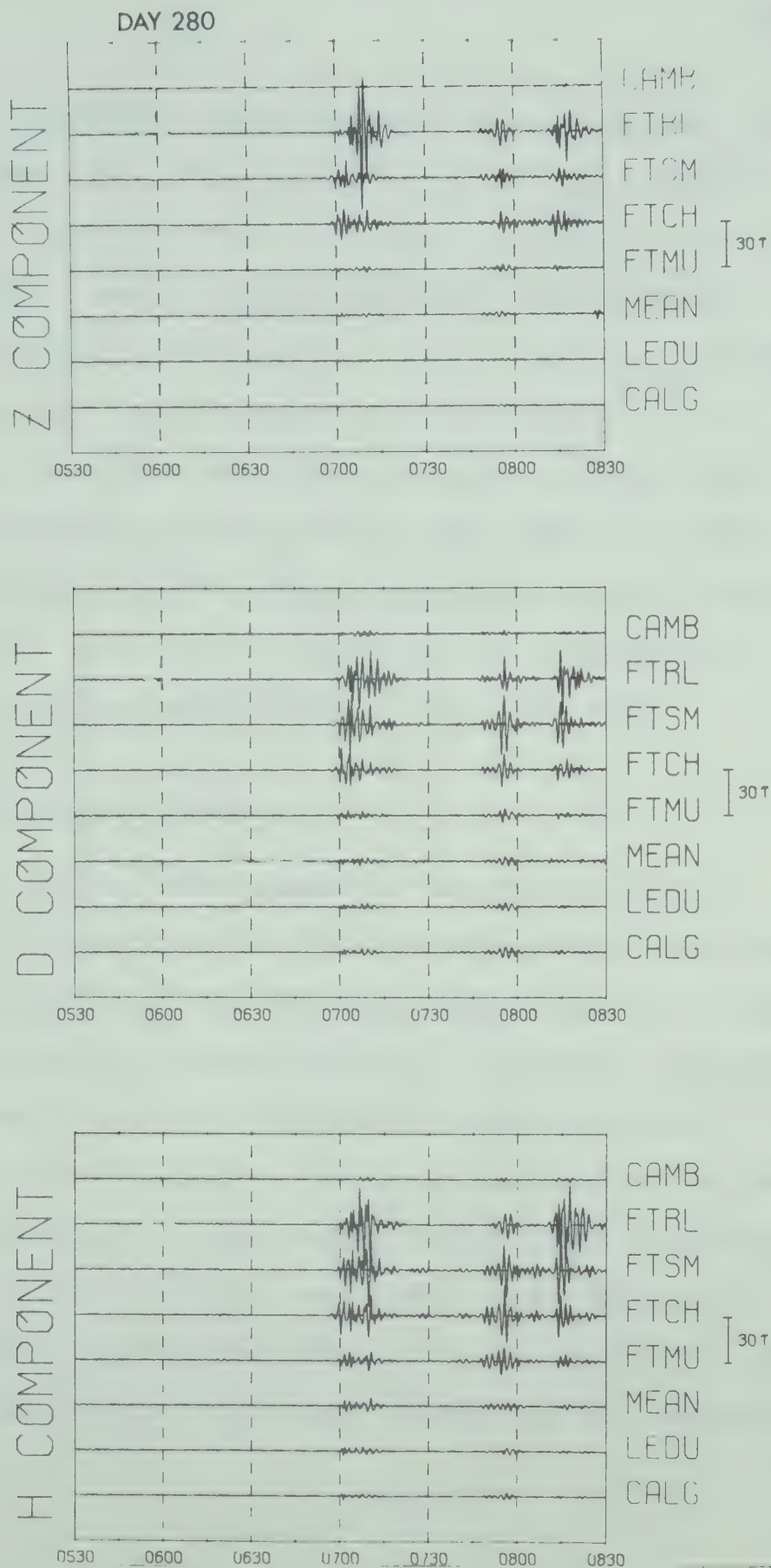


Fig. 5.2 Pi 2 micropulsation activity (40-150 sec) associated with the series of substorms shown in Fig. 5.1.

At first we thought the development of this particular current system was indicative of a growth phase for the substorm that occurred at ~ 0659 UT. This was quickly ruled out when we discovered that a very isolated substorm (onset time of ~ 0615 UT) was recorded at CHUR (see Fig. 5.3). Positive deviations of the H component (with respect to the baselines in Fig. 5.3) commencing at about the onset time of this isolated substorm are also discernable at ALER, RSLT, MOUL, BAKE, and BARR. The all-sky camera at FTSM did not show any auroral activity before 0659 UT. Also no Pi 2 activity was recorded with our line of stations before 0659 UT (see Fig. 5.2).

5.2.1 Polar substorm (0659 UT)

The initial development of the first substorm presented in this section is illustrated in Fig. 5.4a and b. The plane projection of the all-sky camera data is included with each successive latitude profile. It should be noted that north (north being in the same direction as the H component of the perturbation field) is to the left in these diagrams. At 0659 UT a weak westward electrojet developed slightly south of FTSM with a maximum H perturbation of $\sim -20\gamma$ (see Fig. 5.2 for the onset of Pi 2 activity). Associated with the onset of this weak electrojet was the appearance

DAY 280, 1970

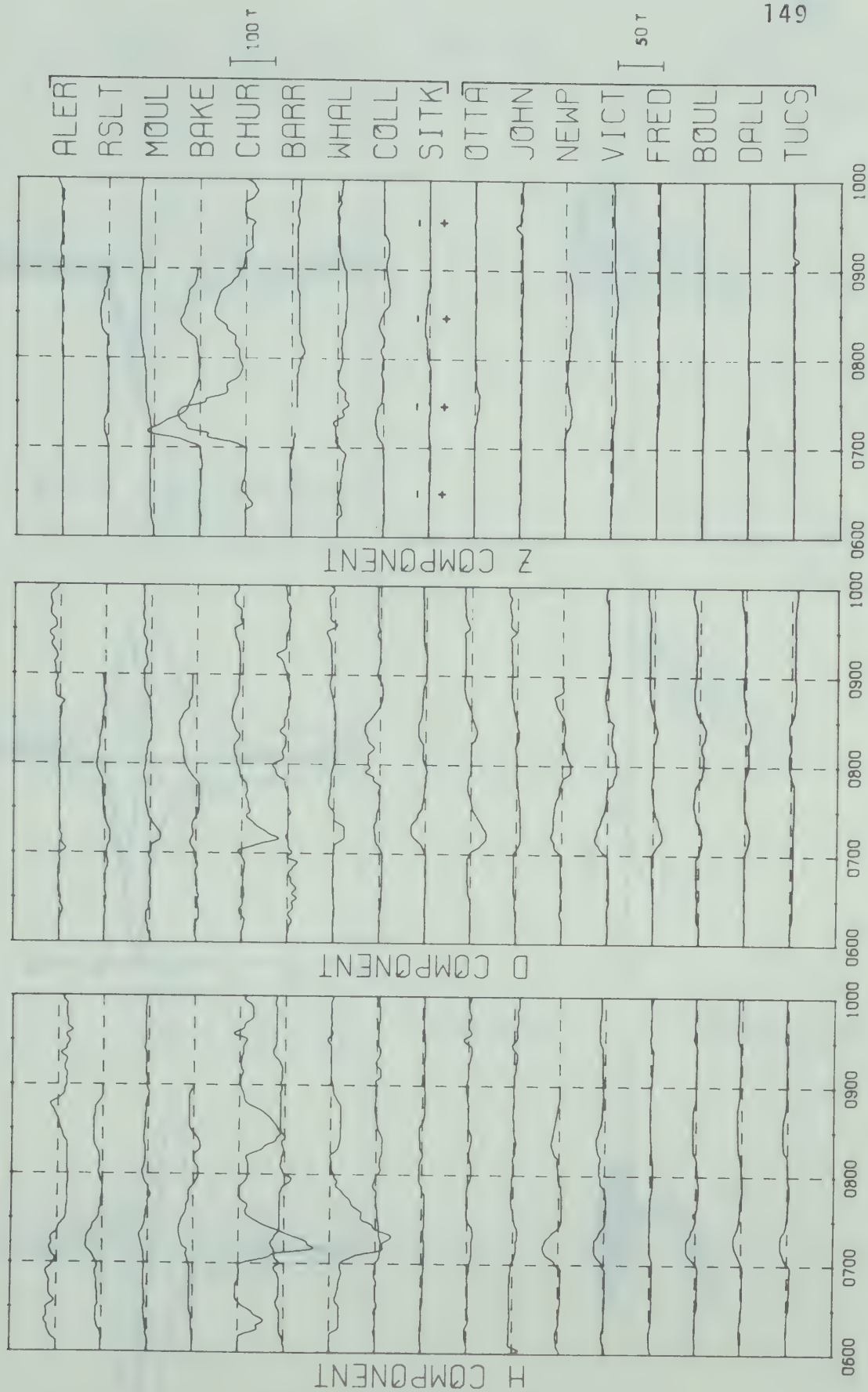


Fig. 5.3 Magnetograms from seventeen observatories in the northern hemisphere for October 7, 1970.

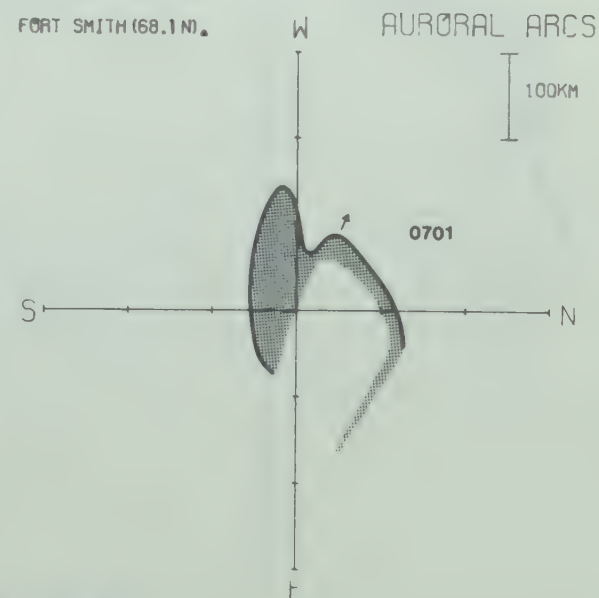
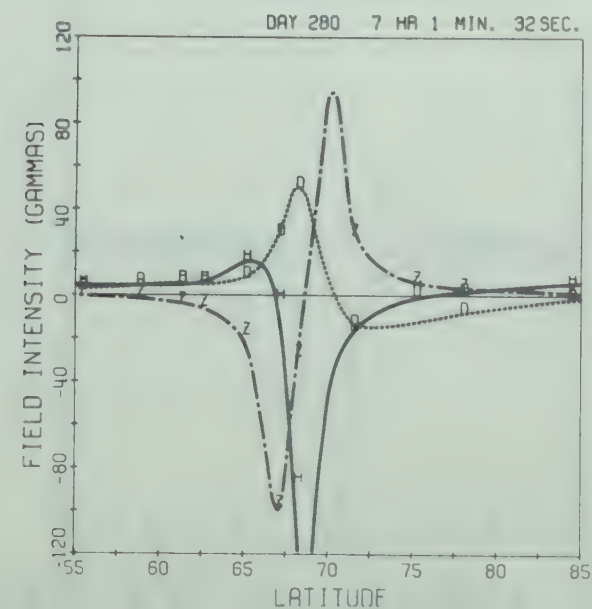
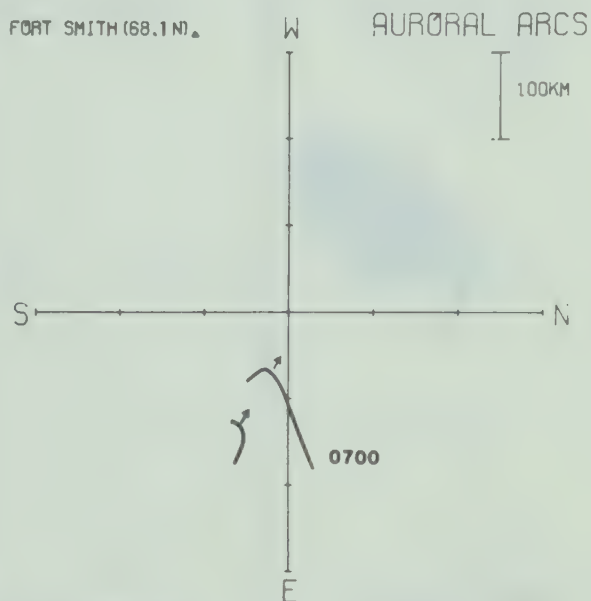
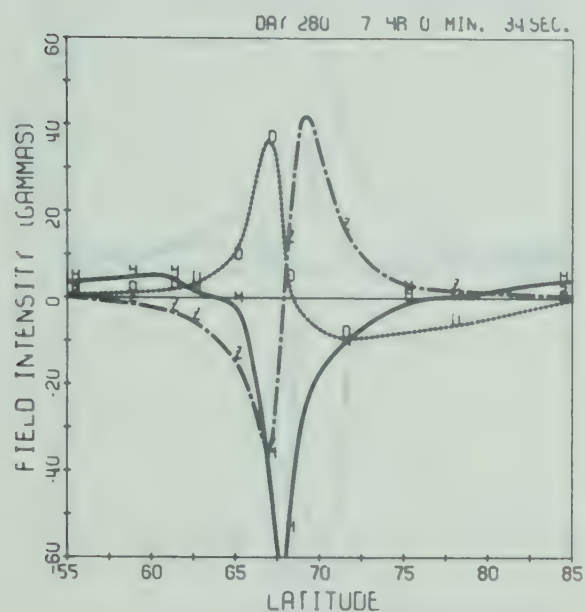
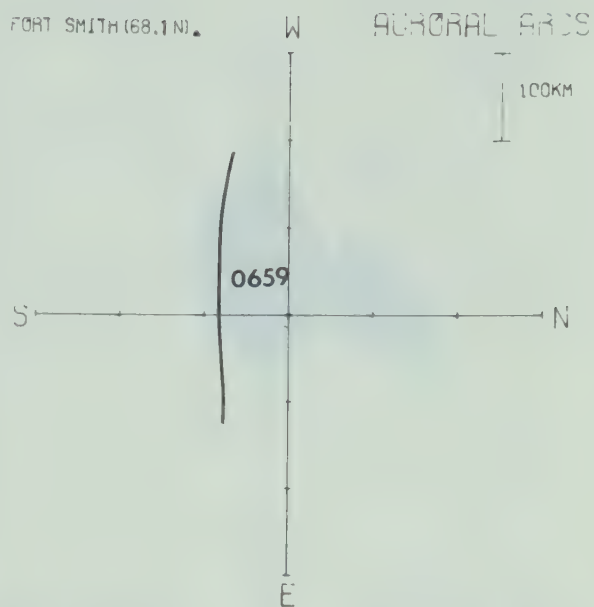
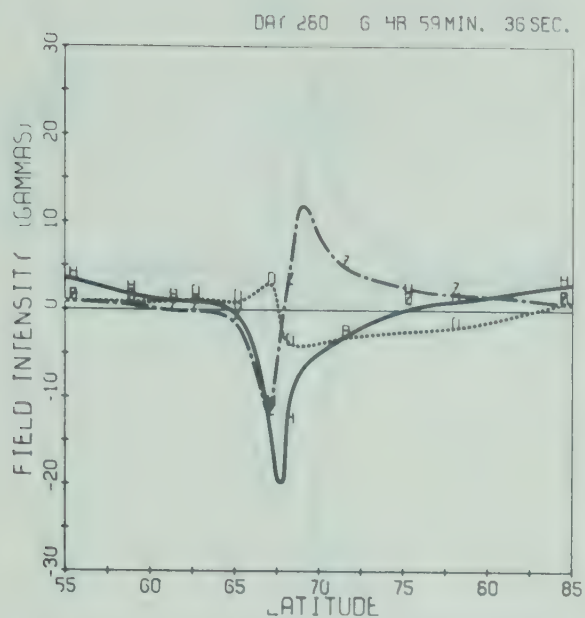
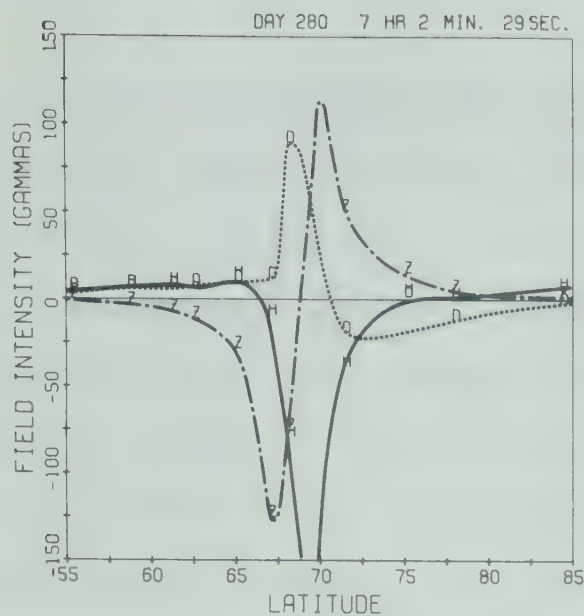
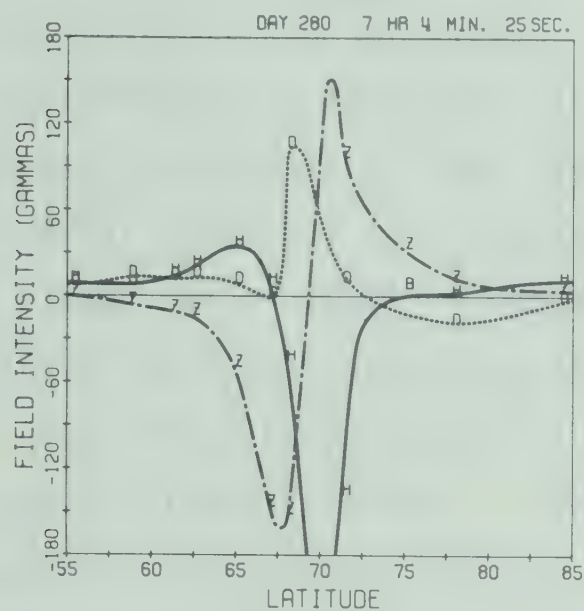
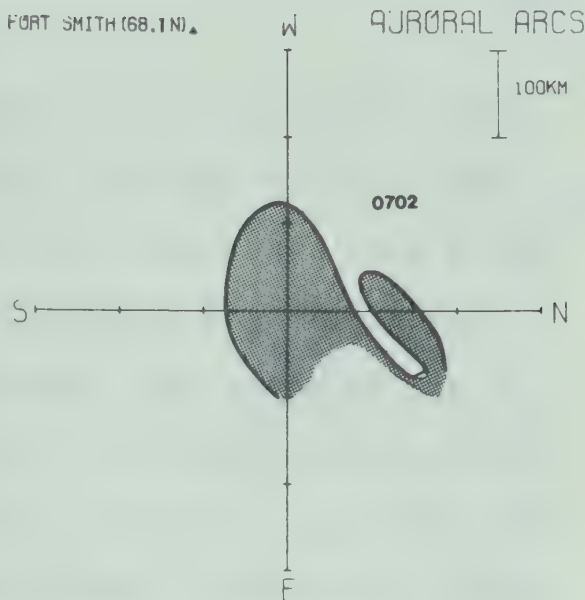


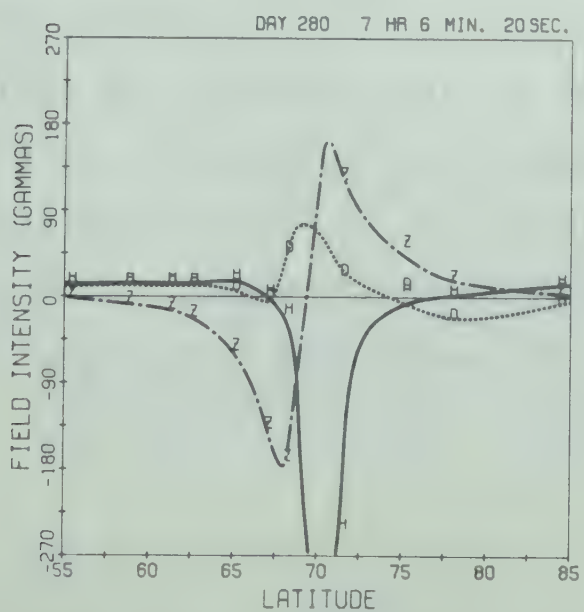
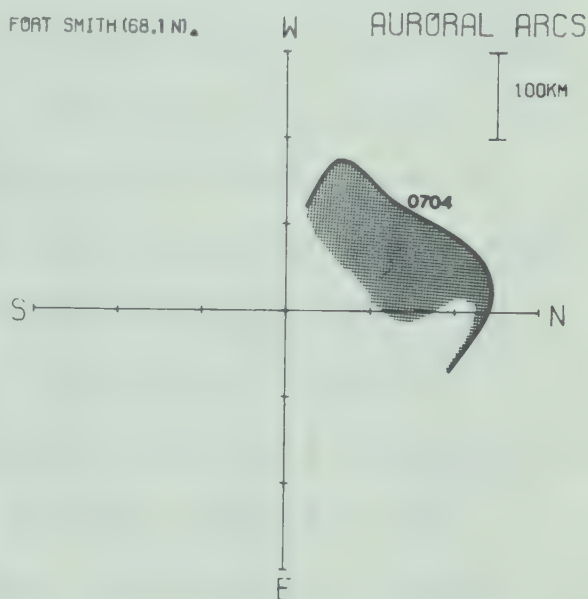
Fig. 5.4a Development of a westward travelling surge and the associated latitude profiles of stations.



FORT SMITH (68.1 N)▲



FORT SMITH (68.1 N)▲



FORT SMITH (68.1 N)▲

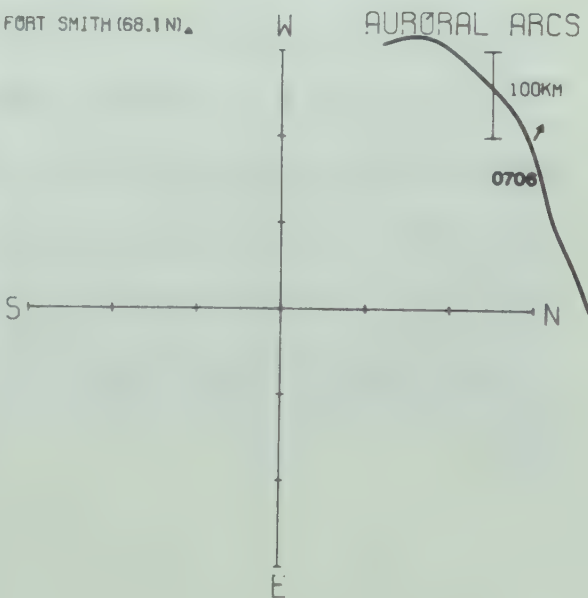


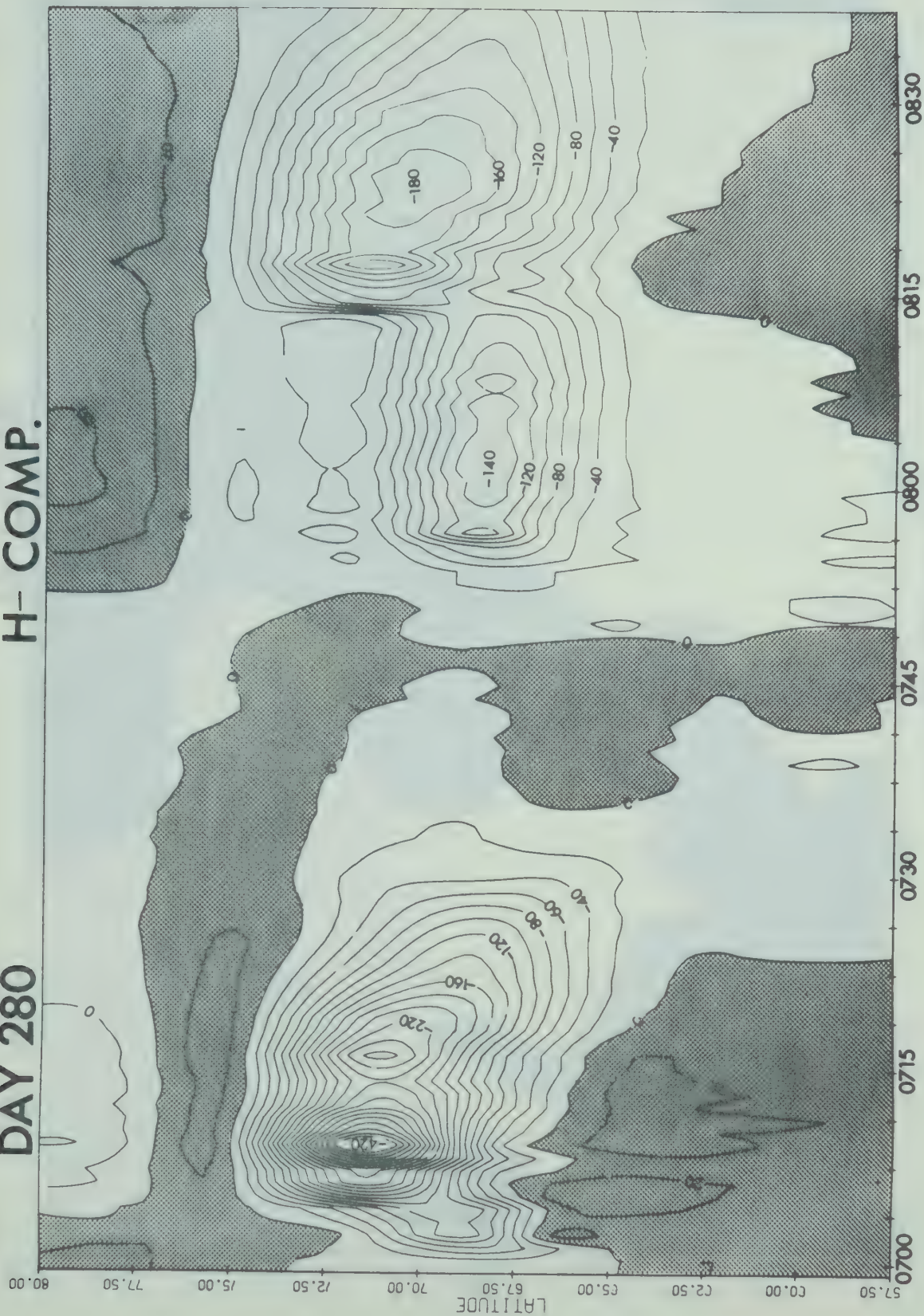
Fig. 5.4b Continuation of Fig. 5.4a.

of a bright E-W aligned arc located ~ 80 km south of FTSM. One minute later a westward travelling surge was recorded advancing from the east of our line of stations. The D profile became well deformed by the positive D perturbation associated with this advancing surge. The shape of the D profile at 0659 UT is indicative of a current system with a central meridian east of our line of stations (possibly where the surge originated). At ~ 0701 UT the surge passed overhead moving to the northwest. Our prediction of the maximum H perturbation at this time is $\sim -200\gamma$ (note the change in the amplitude scale for each successive latitude profile). The surge continued in a northwesterly direction and by 0707 UT passed out of range of the all-sky camera at FTSM. By 0712 UT the moment of the current system was located at $\sim 73.0^\circ$, the maximum northward motion that could be determined with our line of stations. The northern portion of the current system rapidly decayed thus resulting in a fairly rapid southward motion of the moment of the current system. During the recovery phase the moment moved to a latitude of $\sim 70^\circ$ ($\sim 2^\circ$ north of the latitude at which the current system began) and by 0740 UT the substorm and hence the current system had almost completely disappeared. No more auroral activity was observed at FTSM after 0707 UT, therefore we could not

determine whether possible equatorward motions of auroral arcs were concurrent with the rapid southward motion of the current system during the recovery phase.

The dynamic development of this particular substorm and the two later ones can best be illustrated by component contour diagrams (see Fig. 5.5a,b and c). The H and Z components from BAKE were used in the respective diagrams. The H component diagram shows the northward and southward motions associated with the expansive and recovery phases. We also see the +H regimes north and south of the current system as expected for a three-dimensional E-W current system. These are also evident in the latitude profiles shown previously. In the region of CAMB the H component is slightly negative and may be due to the effects of polar cap currents as discussed in Chapter IV. Another interesting aspect of this diagram is the +H regime centered slightly south of FTCH occurring after the recovery phase. Associated with this positive regime is a +Z regime south of FTMU and -Z regime north of FTMU confirming the existence of an eastward electrojet. This is also apparent from latitude profiles and the component magnetograms (see Fig. 5.1). The buildup of an eastward electrojet following a substorm is not uncommon and may possibly explain the +H perturbations following -H bays

DAY 280 H- COMP.



UNIVERSAL TIME

Fig. 5.5a H component contour diagram for the series of substorms shown in Fig. 5.1.

DAY 280

D-COMP.

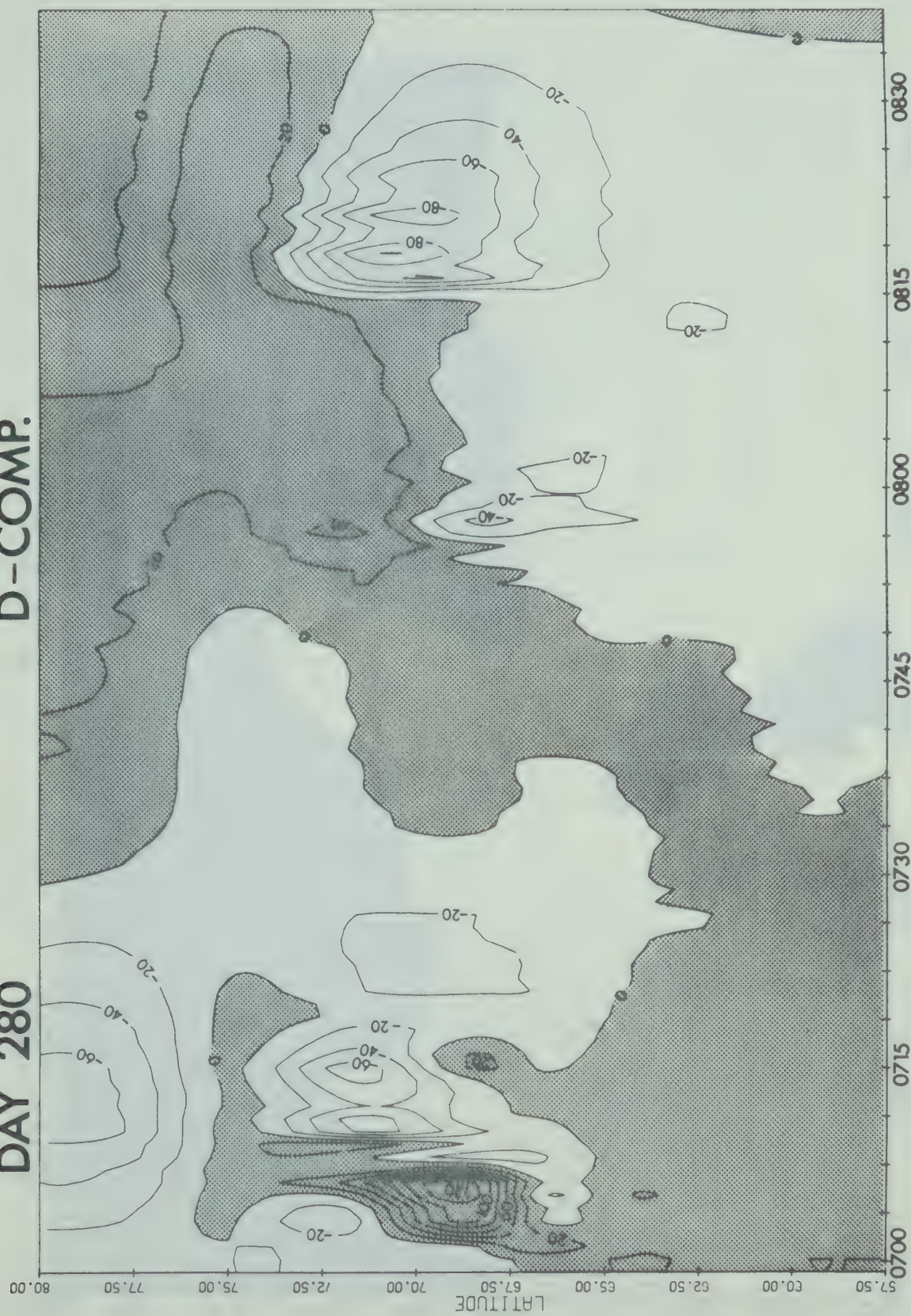


Fig. 5.5b Same as Fig. 5.5a but for the D component.

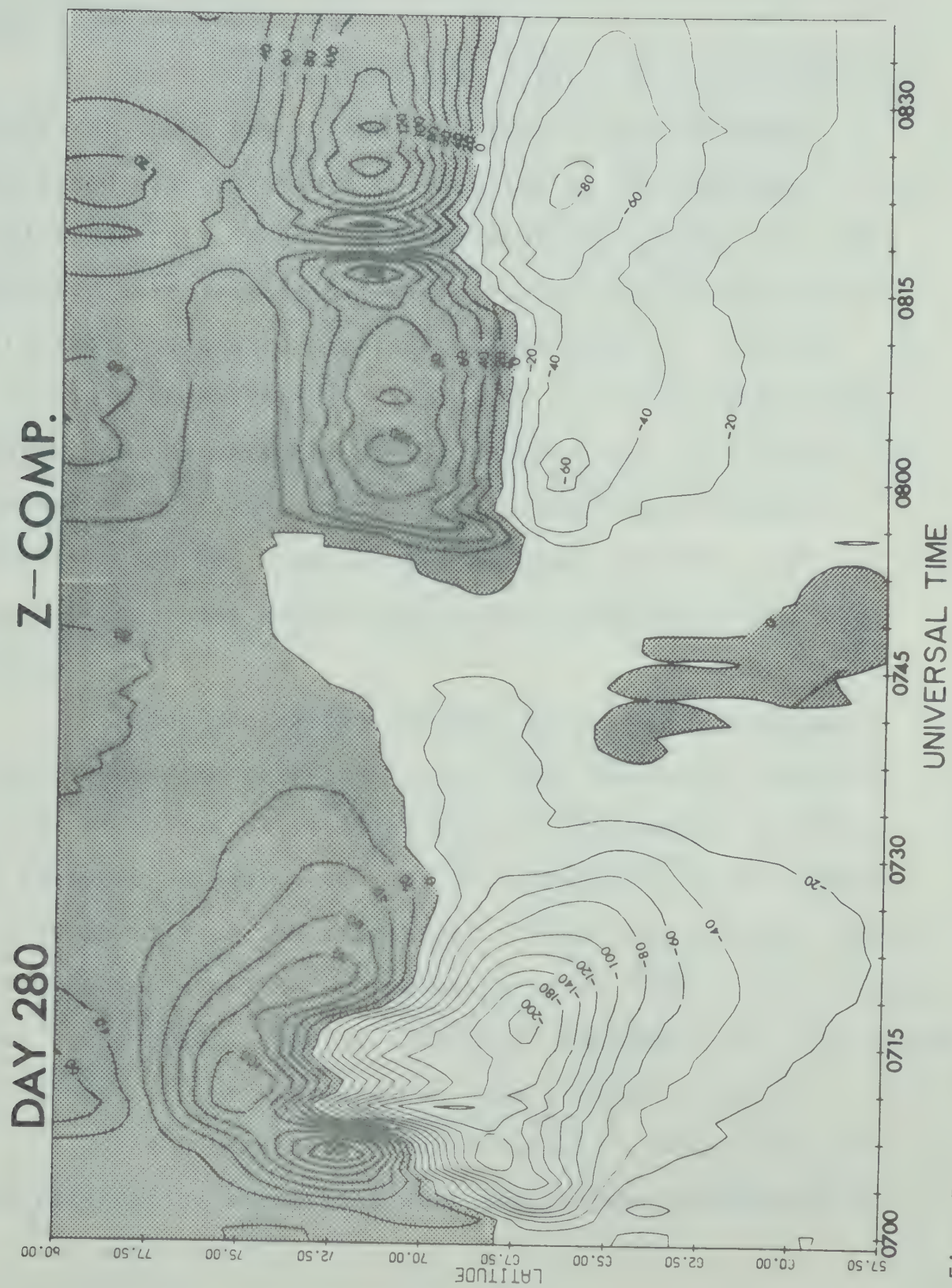


Fig. 5.5c Same as Fig. 5.5a but for the Z component.

reported by Heppner (1954).

The D component diagram (Fig. 5.5b) is interesting in that it shows the northward motion of the +D regime associated with the surge propagating to the northwest. This is also apparent in the latitude profiles in Fig. 5.4. The characteristic latitudinal width of this and other similar +D regimes associated with surges and loops is ~ 400 km. If we assume a characteristic time of ~ 6 min from the contour diagram and the velocity of the surge to be ~ 1.1 km/sec (as obtained from all-sky camera data), then the longitudinal width is ~ 400 km. Current systems that possibly explain these +D component perturbations are presented in the next chapter.

After the passage of the surge, the D component diagram shows the characteristics that one might expect to observe at a line of stations west of the central meridian. The enhanced -D regime at $\sim 71.0^\circ$ is believed to be caused by a NW-SE tilt of the electrojet. Polar cap currents appear to be the cause of the -D regime north of CAMB. In fact such polar cap currents usually affect all components in this region during most of the substorms we have analyzed thus far.

The Z component diagram reveals most of the pertinent information associated with the poleward expansion of

this current system. The average velocity for the northward motion of the moment of the current system for the first 9 min was ~ 0.8 km/sec. During this period, the width of the electrojet increased rapidly from ~ 1 at 0659 UT to ~ 5 to 6° at 0710 UT. Although the southern edge ($-Z$ peak) of the current system moved northward during the expansive phase the velocity was much less than that for the northern border. This would have to be the case since the width also developed rapidly during the same interval of time. In the next section we present an example of a poleward expansion with the southern border remaining almost stationary.

The development of the perturbation field as measured at 25 magnetic observatories is depicted by polar plots shown in Fig. 5.6 and 5.7. Fig. 5.7 shows the horizontal magnetic perturbation vectors observed at ~ 0703 UT. The open circle to the east of our line of stations represents the inferred location of the center (θ_c, ϕ_c) of the electrojet. This is easily verified by noting the distribution of perturbation vectors south of the auroral ($Q=1$) oval (see Fig. 3.4). The large perturbation vector at FTSM is still strongly influenced by the perturbation field associated with the westward travelling surge. The surge probably originated south of the open circle. Fig. 5.7 shows the

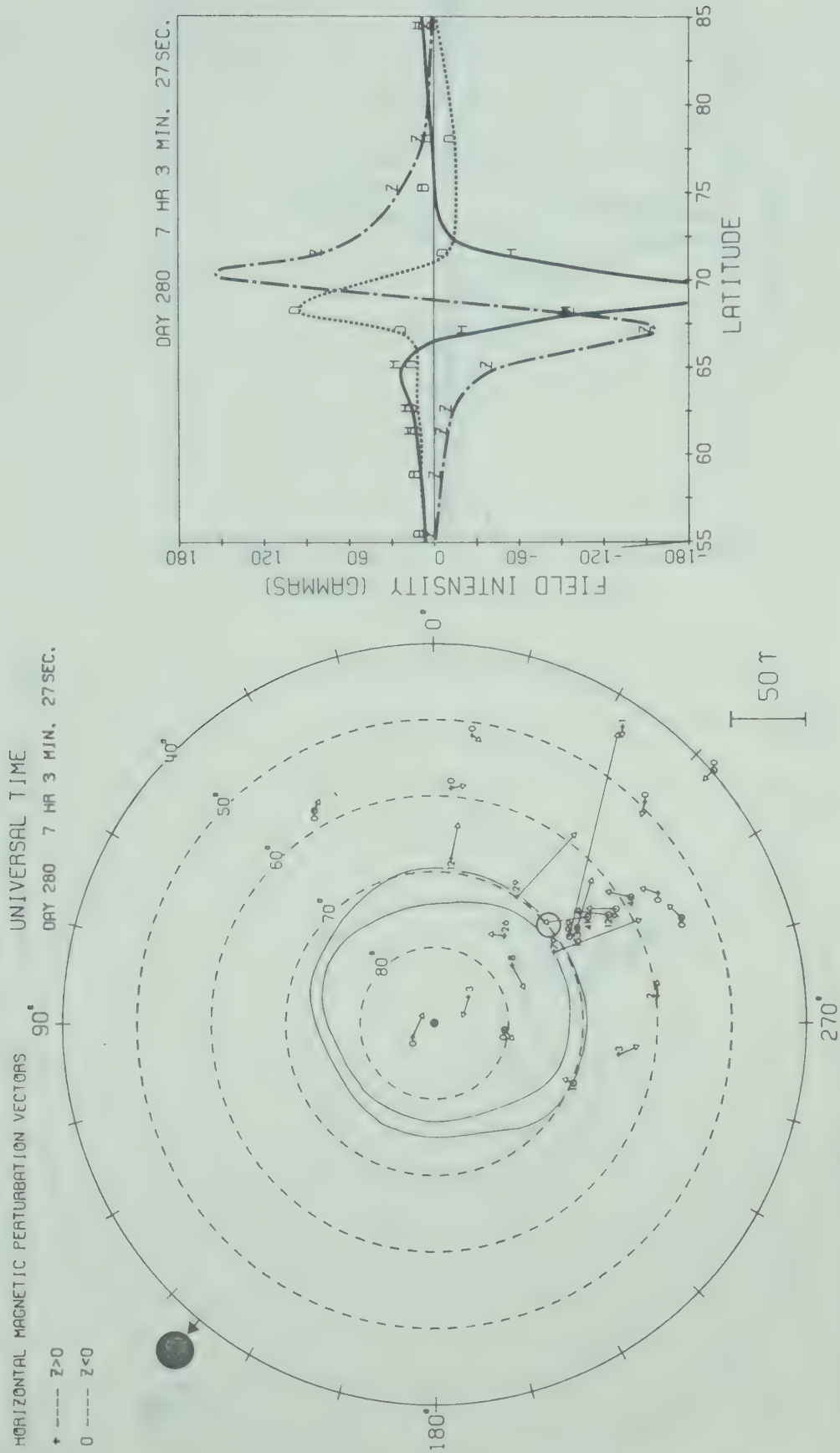


Fig. 5.6 Polar plot and latitude profile showing the distribution of perturbation vectors at ~ 0703 UT.

distribution of perturbation vectors 5 min later (~ 0708 UT). The D profile at this time had almost recovered from the distortion caused by the surge. Also at this time the -H perturbation reached its maximum value of $\sim -450\gamma$ as recorded with our line of stations. In both of these figures the perturbation vector at BARR is probably representative of a high latitude eastward electrojet associated with the substorm current system. Also the rapid reduction in the amplitude of the Z component away from the current system in both latitude and longitude is very pronounced in these polar plots.

Before the onset of the substorm there appears to be a slight depression of the H component at FRED, BOUL, DALL and TUCS (see Fig. 5.3). This could possibly be due to the asymmetric ring current associated with the eastward electrojet in the evening sector as discussed in Chapter IV.

5.2.2 Polar substorm (0748 UT)

The onset of the second substorm shown in Fig. 5.1 was difficult to determine since it occurred west of our line of stations and the perturbation was of relatively low magnitude. Even though the onset of Pi 2 micropulsation activity was ~ 0748 UT (see Fig. 5.2), the first indication

of a westward electrojet was not observed by our line of stations until 0752 UT. The all-sky camera at FTSM recorded only 2 min of auroral activity (0753 and 0754 UT) during this entire substorm. At \sim 0753 UT a quiet arc was evident \sim 100 km south of FTSM oriented from WNW to ESE. The arc also coincided with the moment of the electrojet evident at that time. At 0754 UT only a diffuse auroral patch was observed \sim 150 km west and 50 km north of FTSM.

The motion of the current system is clearly illustrated in Fig. 5.5C. The velocity of the poleward motion between 0753 and 0759 UT was \sim 0.3 km/sec with the moment reaching $\sim 68.3^0$ at 0759 UT. A very slow southward motion (probably associated with the recovery phase) started at \sim 0759 UT and continued until the onset of the third substorm at \sim 0814 UT.

Fig. 5.8 shows the distribution of the magnetic perturbation vectors observed in the northern hemisphere (see Fig. 5.3) along with the latitude profile for \sim 0800 UT. The D profile in this figure is an excellent example of a profile indicative of a current system with a central meridian west of our line of stations. This is clearly demonstrated in Fig. 5.5b also. The circle on the $Q = 1$ oval represents the inferred center of the current system ($\sim 20^0$ west of our

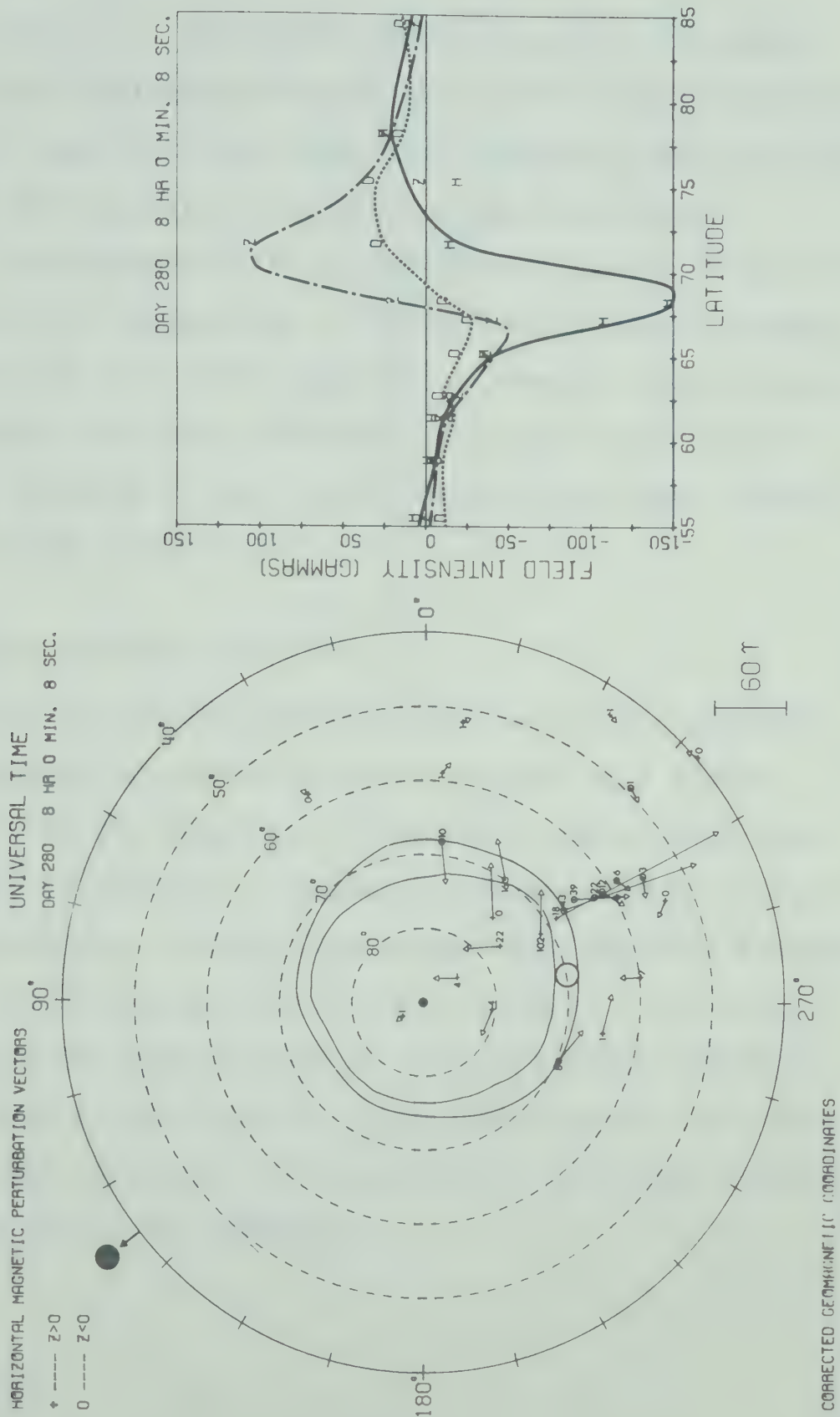


Fig. 5.8 Polar plot and latitude profile showing the distribution of perturbation vectors at ~ 0800 UT for the 0748 UT substorm.

line of stations). This could possibly explain the delay time (~ 4 min) between the onset of the Pi 2 micropulsations (~ 0648 UT) and the first sharp perturbation of the electrojet (0752 UT) as observed with our line of stations.

The maximum width of the current system as observed by our line of stations was $\sim 4.5\text{--}5.0^\circ$ along with a maximum H perturbation of $\sim -146\gamma$ (0800 UT). However, these values could possibly be quite different from those that would have been observed if our line of stations had been located farther to the west.

5.2.3 Polar substorm (0814 UT)

During the recovery phase of the second substorm, the development of a third substorm started at a higher latitude ($\sim 70.5^\circ$) (see Fig. 5.1 and 5.5) and slightly west of our line of stations. From both the onset of Pi 2 micropulsation activity and the development of a westward electrojet, the onset time was found to be ~ 0814 UT. The only auroral activity observed during this particular substorm was at ~ 0814 UT and 0815 UT. This took the form of a faint auroral surge located ~ 200 km north and 150 km west of FTSM moving rapidly to the northwest.

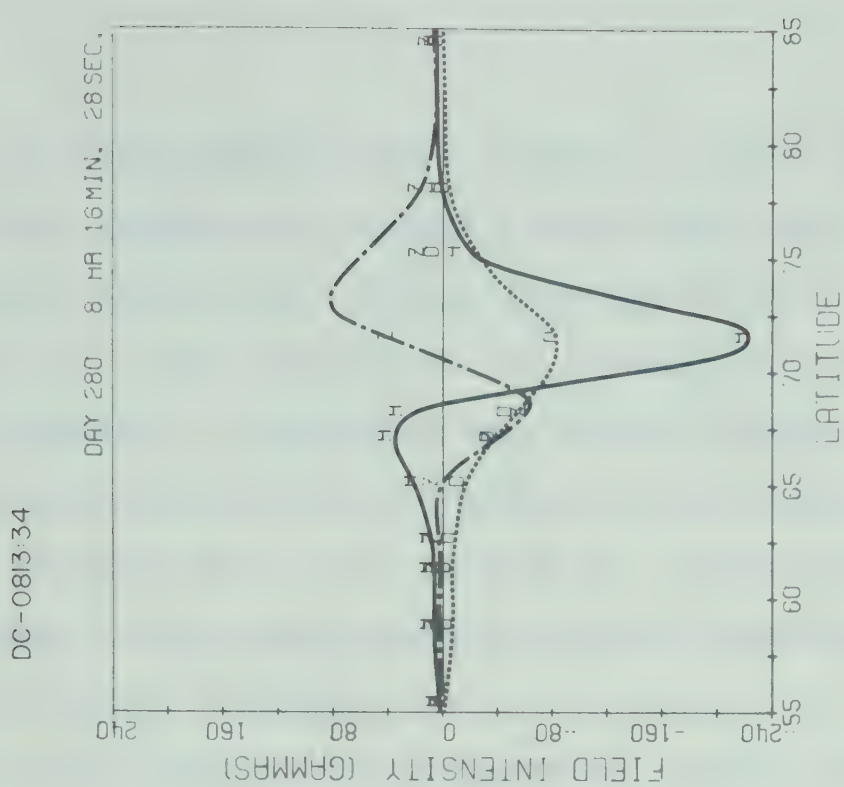
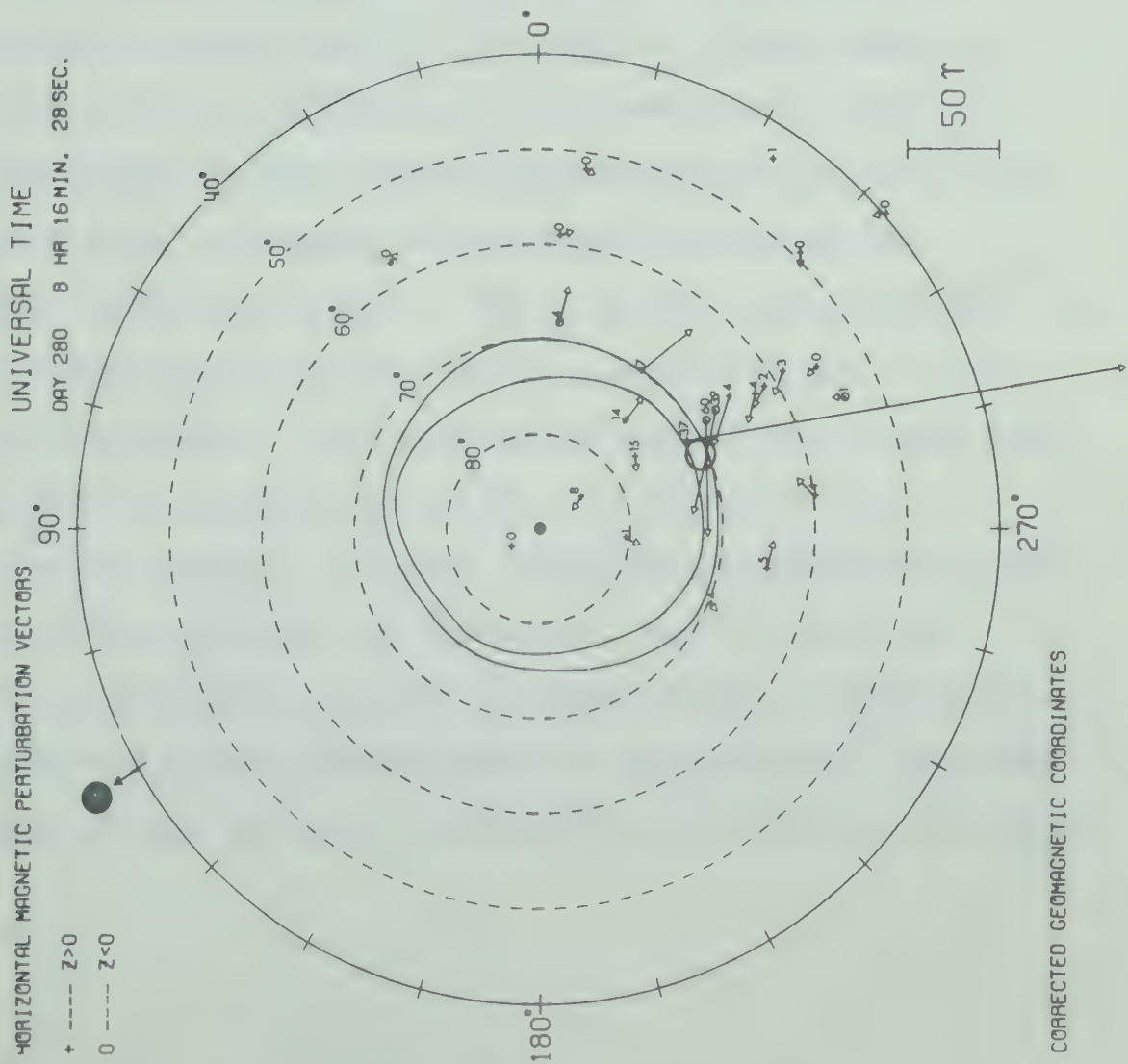


Fig. 5.9 Polar plot and latitude profile showing the distribution of perturbation vectors at ~ 0816 UT (DC-0813.34) for the 0814 UT substorm.

The development of this substorm is very similar to that of the previous one except for the fact that the electrojet was located at a higher latitude at the time of onset ($\sim 70.5^\circ$). The velocity of the poleward motion of the $Z = 0$ crossover is about the same as for the previous substorm (~ 0.3 km/sec) with the moment of the electrojet reaching a latitude of $\sim 71.5^\circ$ at 0820 UT. Commencing about the same time, a slow equatorward motion was observed for the duration of the substorm.

A polar plot of the perturbation vectors and associated latitude profile for 0816:26 UT are shown in Fig. 5.9. The D profile may be indicative of a tilt of the electrojet as was noted in our discussion of the first substorm (the -D regime following the passage of the westward travelling surge). The Z profile was difficult to interpret owing to the lack of stations in the vicinity of the electrojet. This particular profile could have been drawn with more pronounced peaks. Although there is a definite +H response at lower latitudes associated with the onset of the -H regime to the north, the +H regime can partly be explained in terms of the recovery of the electrojet from the second substorm due to the choice of baselines. However, we are not able to determine the relative magnitude

of each individual contribution.

Three-dimensional plots of the substorms presented in this section are presented in Appendix A6.

5.3 Substorm event of September 1, 1970 (Day 244)

On September 1, 1970 two large magnetic substorms were recorded with our line of stations. The H, D and Z component magnetograms and the associated Pi 2 micropulsations are shown in Fig. 5.10 and 5.11 respectively. The Kp indices for this day are (1-, 1o, 4o, 5o, 4+, 4-, 4o, 3+; $\Sigma Kp = 27$) and the Dst indices for the hours 5-12 consecutively are (3, 4, -2, -8, -19, -31, -27, -15) thus indicating an increase in the symmetric component of the ring current. Only an analysis of the first substorm is presented in this section since the center of the associated current system was only a few degrees east of our line of stations.

From the Pi 2 micropulsations and latitude profile analysis the onset of the first substorm was ~ 0655 UT. The gradual development of an eastward electrojet preceded the onset of the substorm by ~ 1.5 hours (see Fig. 5.10). From the available magnetic data no definite substorm activity was evident during this period prior to 0655 UT. Fig. 5.12 shows the approximate location of the eastward electrojet at ~ 0603 UT.

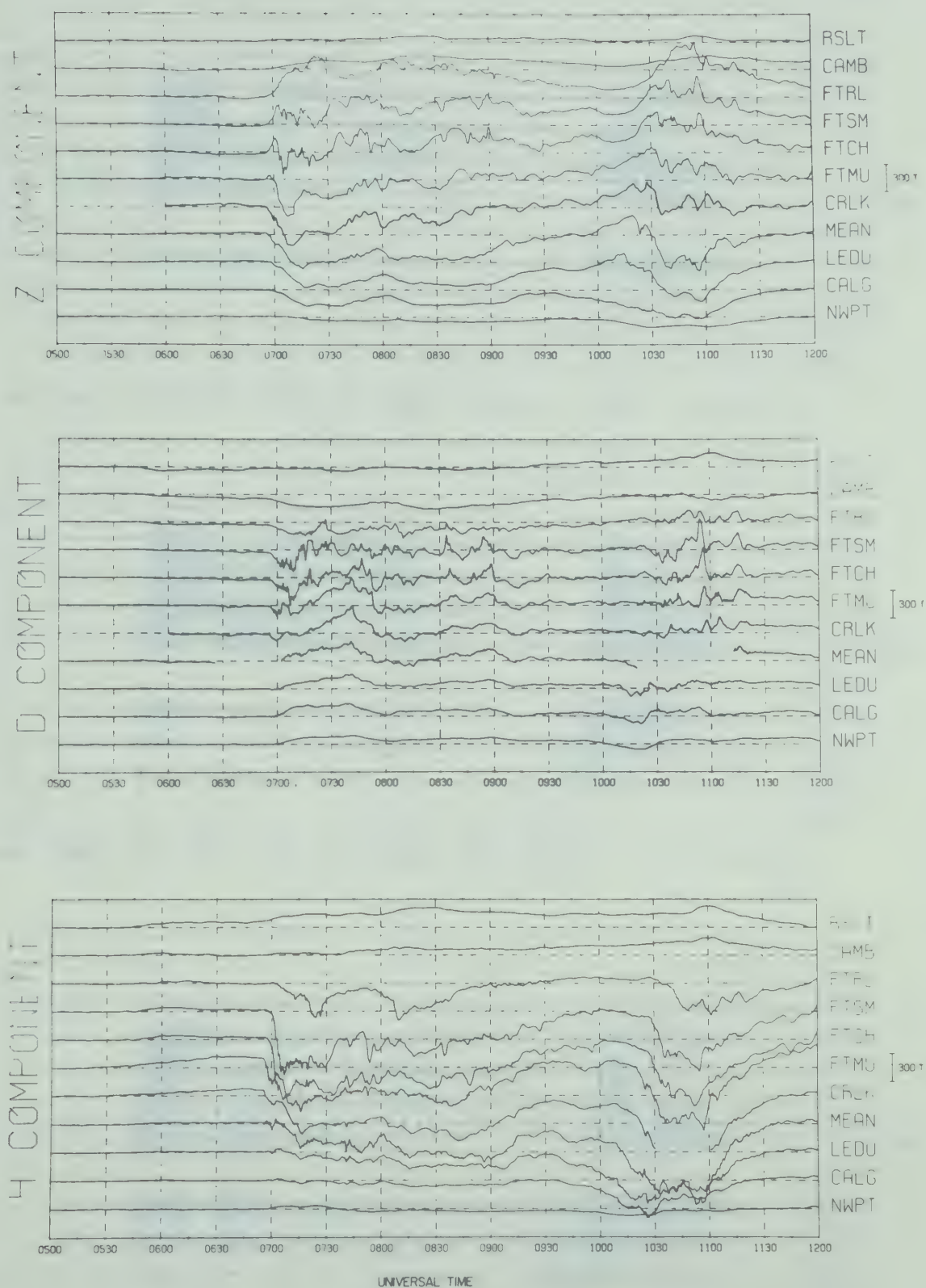


Fig. 5.10 Magnetograms for the substorm that occurred on September 1, 1970.

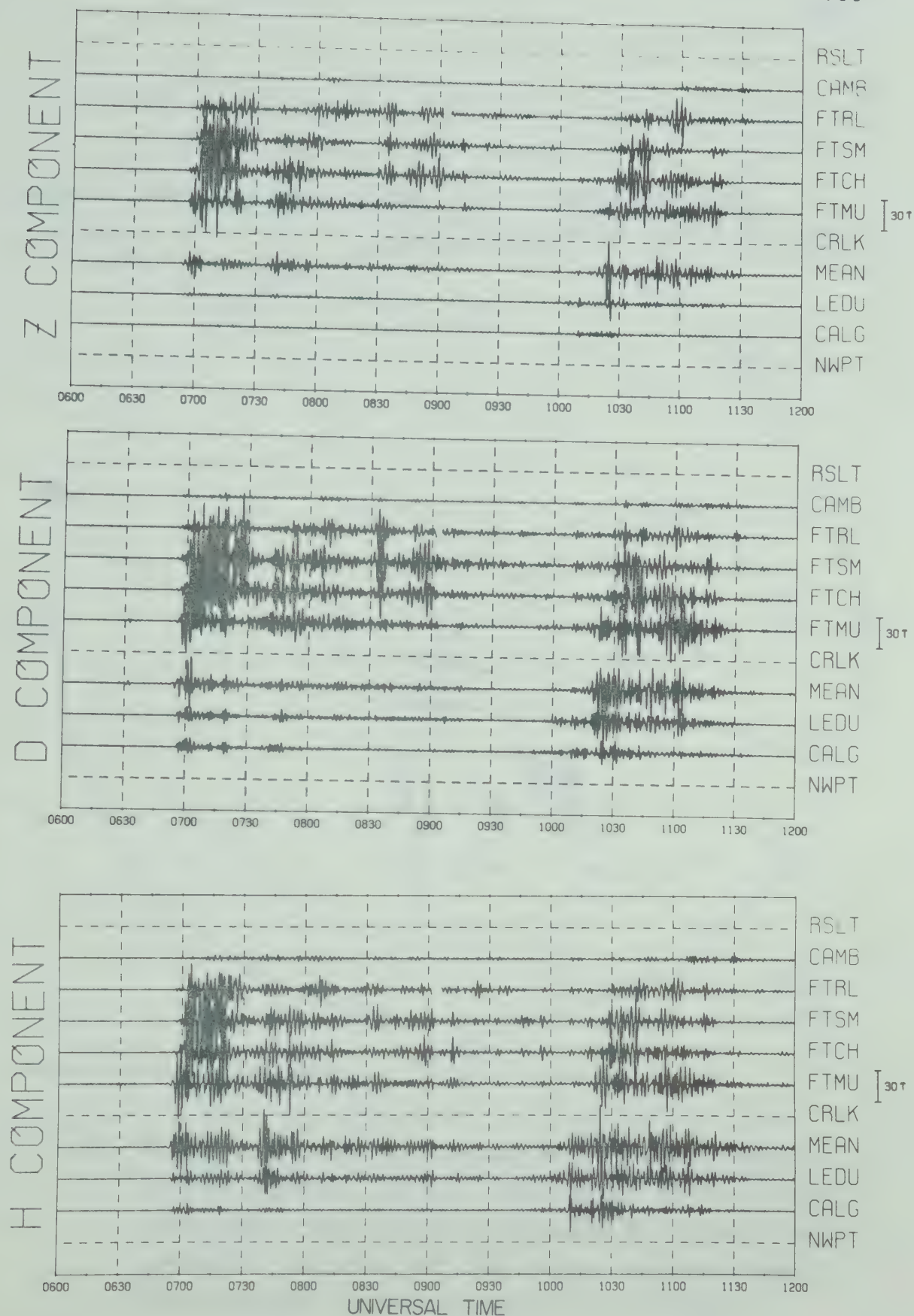


Fig. 5.11 Pi 2 micropulsation activity (40-150 sec) associated with the substorms shown in Fig. 5.10.

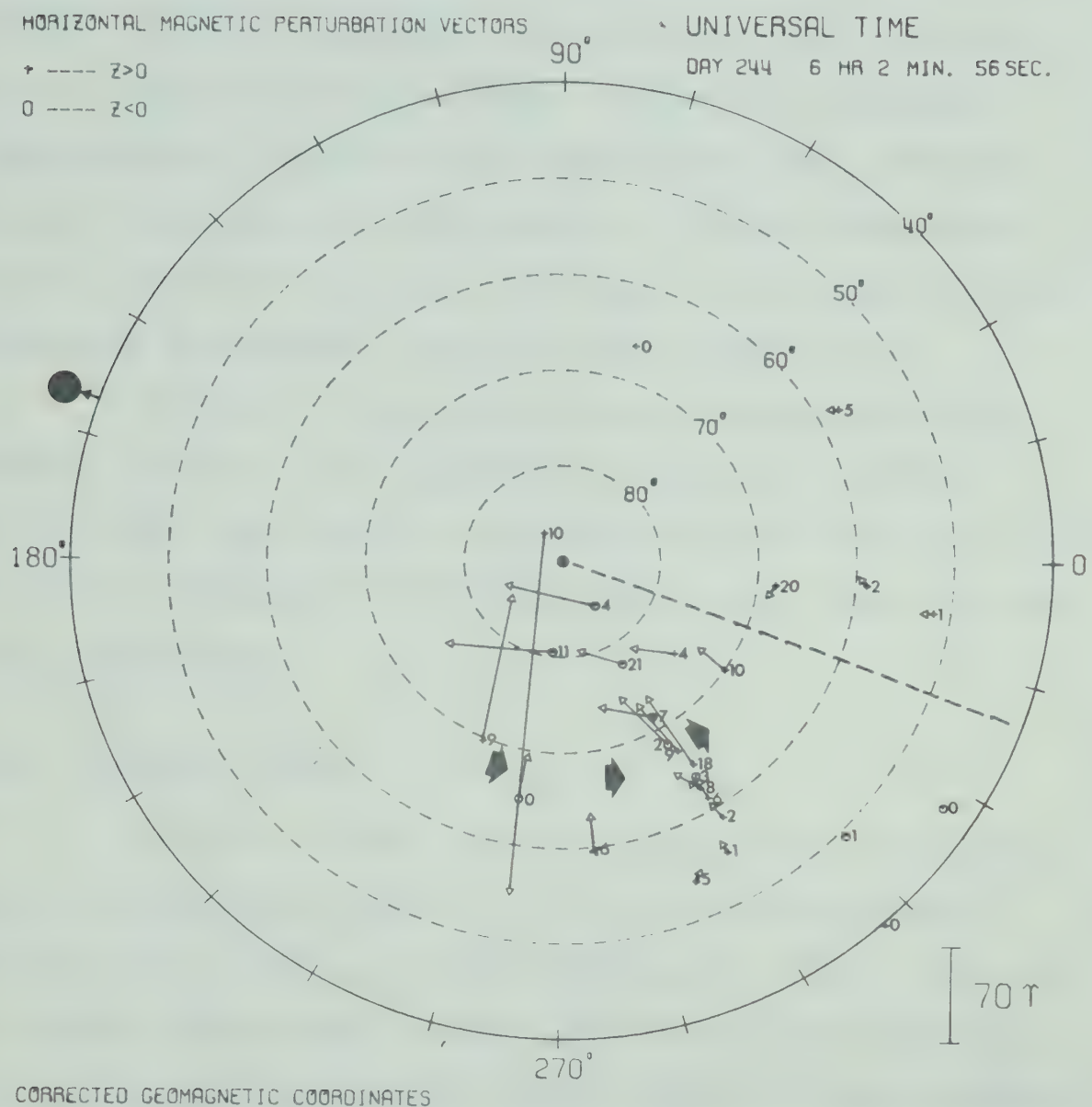


Fig. 5.12 Polar plot showing the distribution of perturbation vectors before the onset of the first substorm. The large arrowheads represent the probable location of the eastward electrojet. The dashed line represents C.G. midnight.

Note the lack of horizontal perturbation vectors in the post midnight sector (the dashed line represents C.G. local midnight). This could possibly be due to the sparse distribution of stations in this sector. In fact WHAL observed a Z perturbation of $\sim 20\gamma$ at this particular time. At the present time we do not know whether or not the development of this particular eastward electrojet in the evening sector represents the magnetic signature of a growth phase.

Similar to the substorm event presented in the previous section, the H component is depressed at BOUL, DALL and TUCS just prior to the substorm onset (see Fig. 5.13). The diurnal component at HOLU and GUAM is too large to infer such a depression.

5.3.1 Expansive phase

In this section a detailed analysis of the development of the current system associated with the expansive phase of the auroral substorm is presented. First, the overall dynamic development of the current system is discussed and secondly the very rapid intensifications of the northern border that produced the poleward expansion are examined.

The expansive phase of the auroral substorm first became evident at 0656 UT when a bright arc appeared ~ 400 -

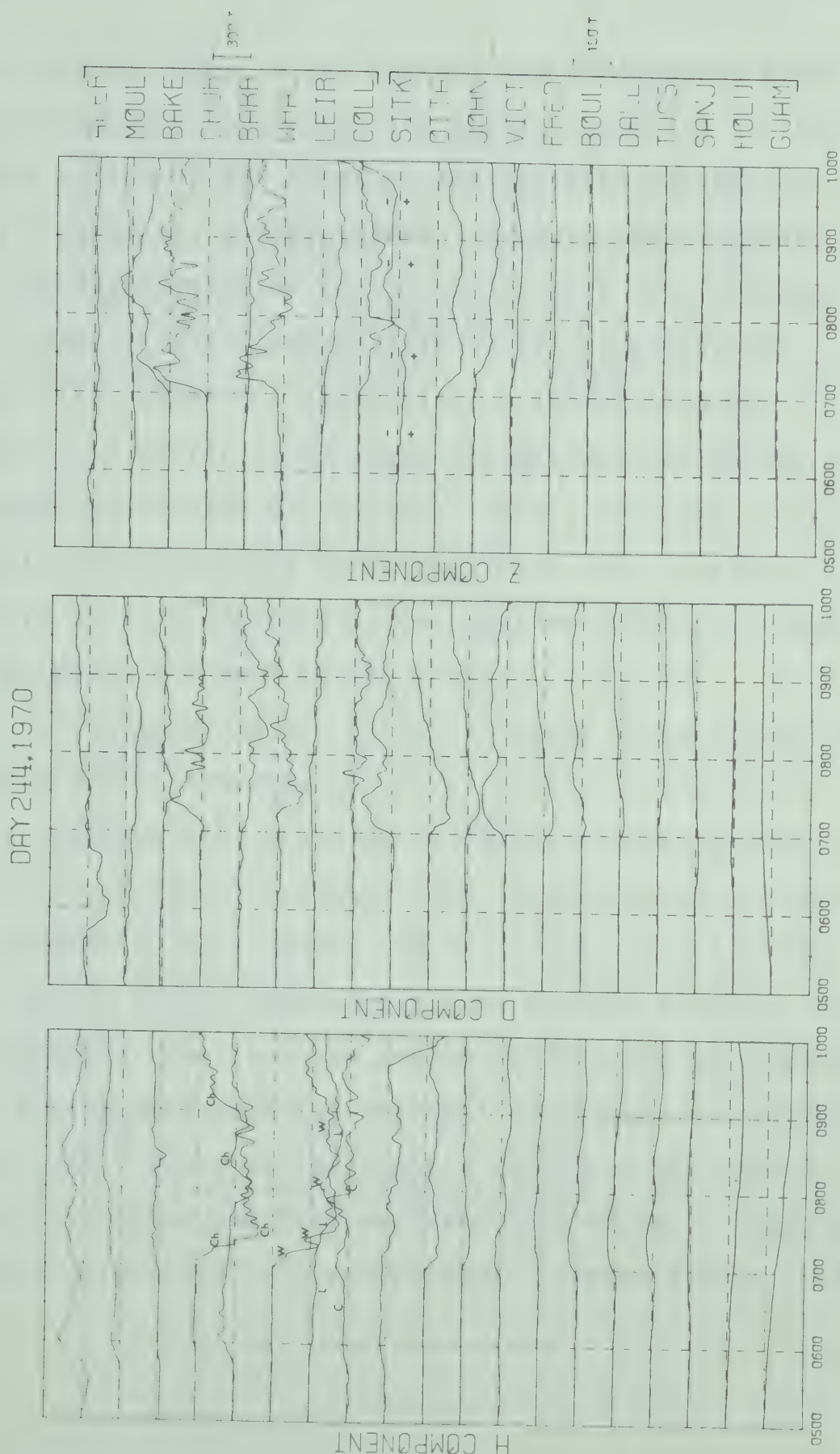


Fig. 5.13 Magnetograms from nineteen observatories in the northern hemisphere for September 1, 1970. The letters on the H component magnetogram allow the traces from each station to be followed.

500 km south of FTSM. Since the all-sky photographs from MEAN were obscured by clouds the auroral activity in the immediate region of the onset of the westward electrojet ($\sim 64.3^{\circ}$) could not be determined. The ensuing northward motion and development of the system of arcs was very rapid and at ~ 0706 UT the northern edge of the bulge passed overhead FTSM reaching a latitude of $\sim 70^{\circ}$ by 0710 UT. Although it is difficult to study the poleward expansion of the auroral bulge with one all-sky camera, from the analysis of magnetic perturbations associated with this expansion we believe that 70° represents the maximum latitude reached by the poleward boundary of the bulge.

To illustrate the rapid northward expansion of the westward electrojet during the first 15 min following the onset of the substorm, a series of latitude profiles are shown in Fig. 5.14. The dashed line in each column of profiles represents the location (64.3°) of the moment of the current system at the beginning of the expansive phase. The rapid northward expansion can easily be inferred by comparing the $Z = 0$ crossover with the dashed line in each successive profile. The D profiles immediately following the onset were very irregular and differed from that which is expected for an E-W orientated three-dimensional current system. We

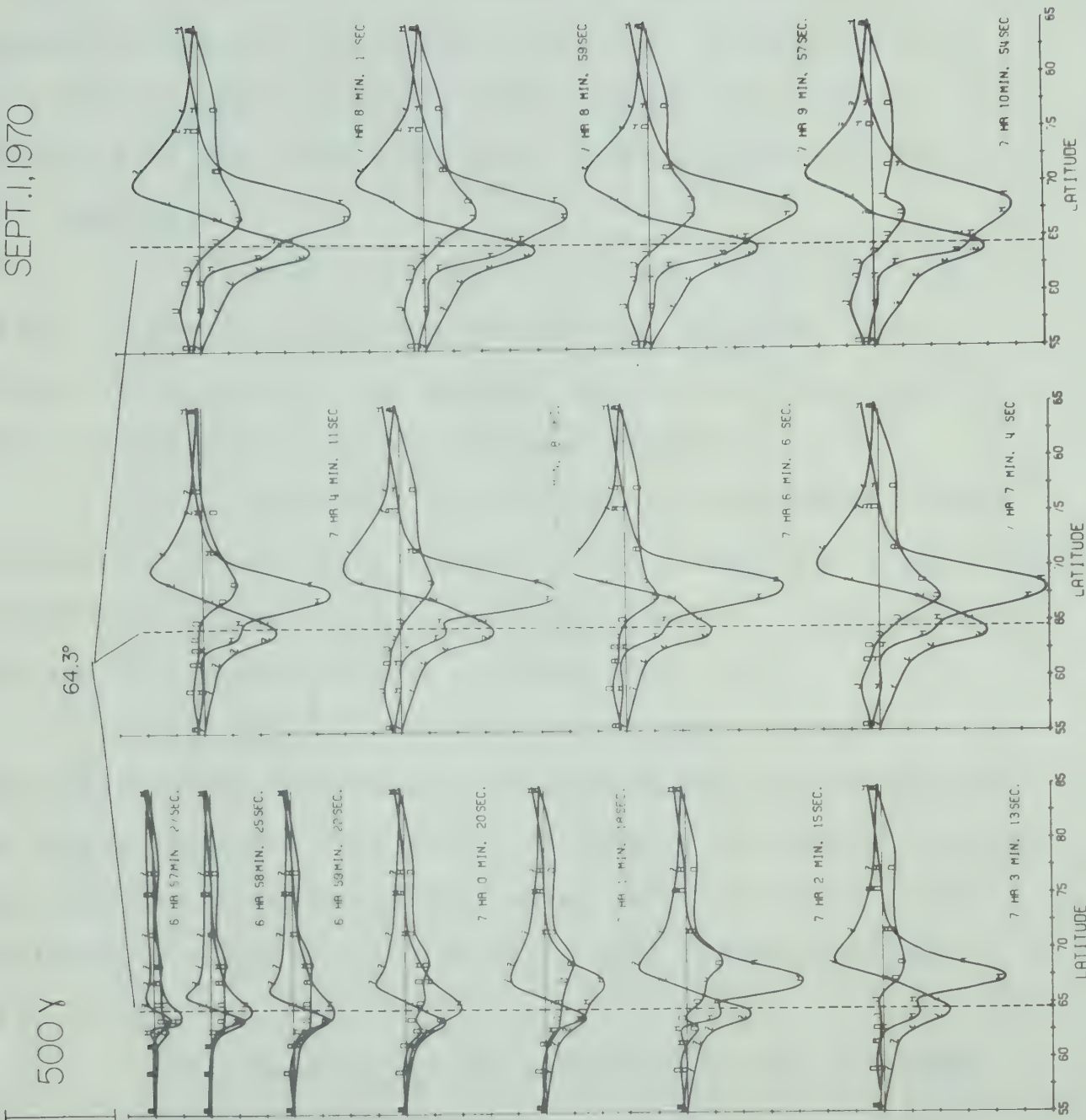


Fig. 5.14 Series of latitude profiles (~ 1 min intervals) showing the development and poleward expansion of the current system associated with the expansive phase of the auroral substorm.

believe that the deformations of these D profiles were caused by irregular auroral forms associated with the expansive phase of the auroral substorm. By 0702 UT the D profile began to resemble that expected for a current system with its central meridian to the east of our line of stations.

Fig. 5.15 shows the Z component diagram for the first 16 min following the onset of the substorm. Three important aspects of the poleward expansion of the electrojet are illustrated by this contour diagram:

(1) The moment of the current system moved rapidly poleward. The velocity of this motion varied from ~ 280 m/sec (0656-0702 UT) to ~ 1.6 km/sec (0702-0704 UT). The southward motion of the moment began at about 0708 UT.

(2) The southern boundary of the electrojet (represented by the dashed line through the maximum negative Z regime) remained very stable throughout the expansive phase, whereas the northern boundary moved poleward with a nearly uniform velocity of ~ 1.1 km/sec. This is also apparent in Fig. 5.14.

(3) The width of the electrojet rapidly expanded in a very short period of time reaching a value of ~ 900 -1000 km by 0709 UT.

Z - COMPONENT

SEPT. 1, 1970

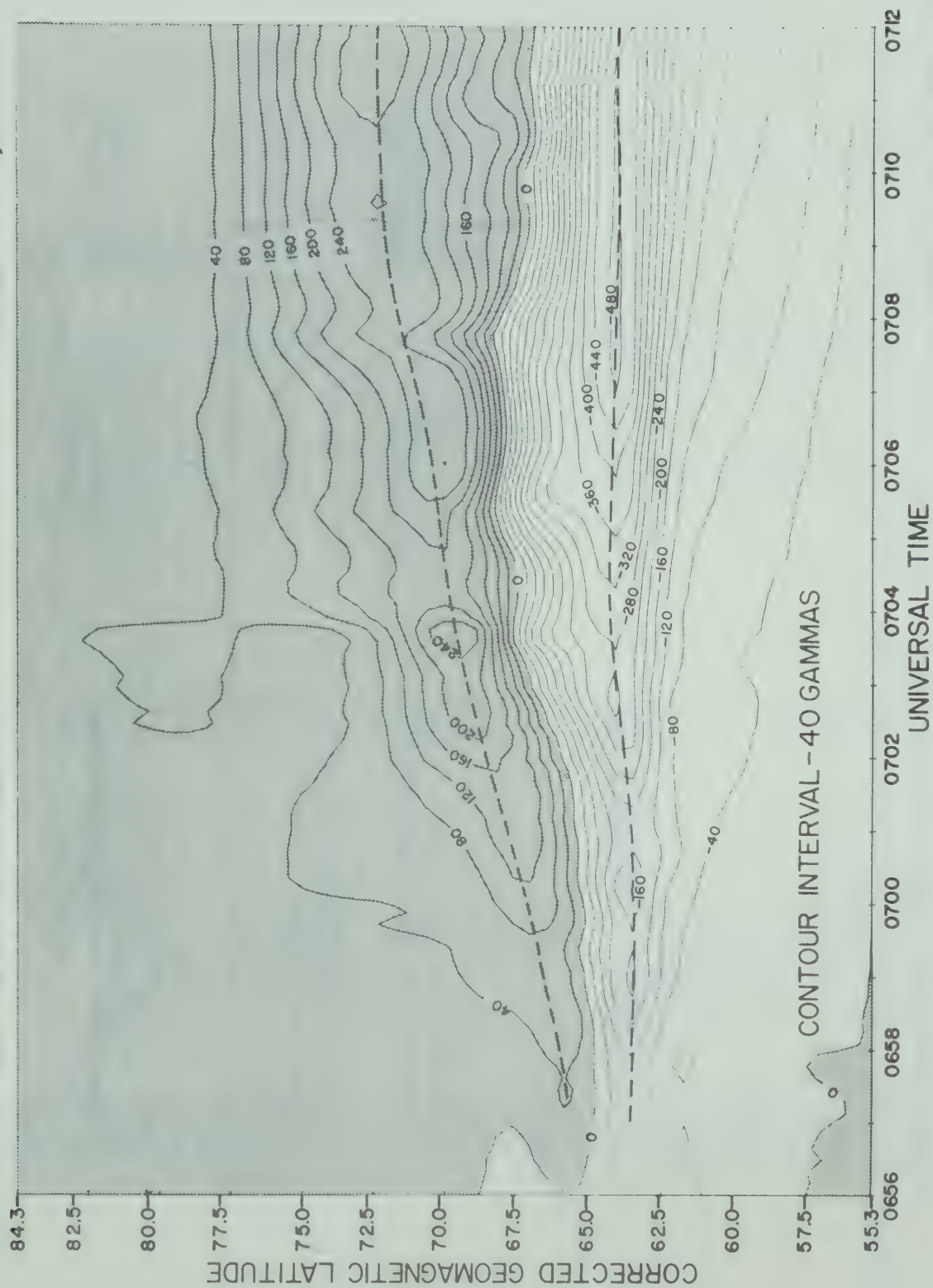


Fig. 5.15 The Z component contour diagram during the first 16 min of the substorm. The dashed line represents the approximate location of the borders of the electrojet.

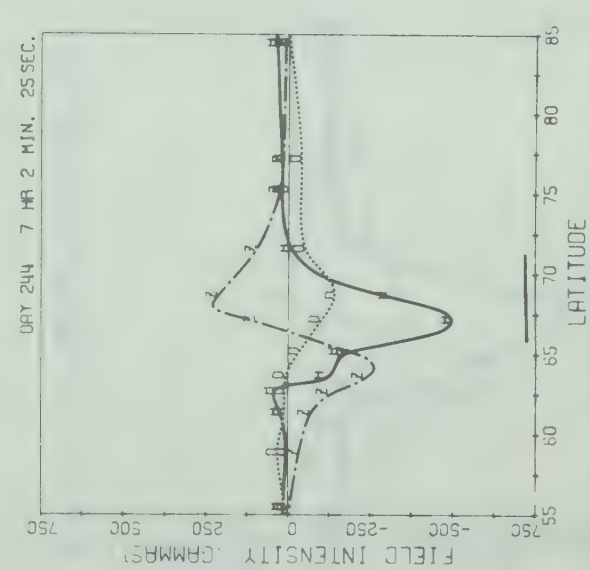
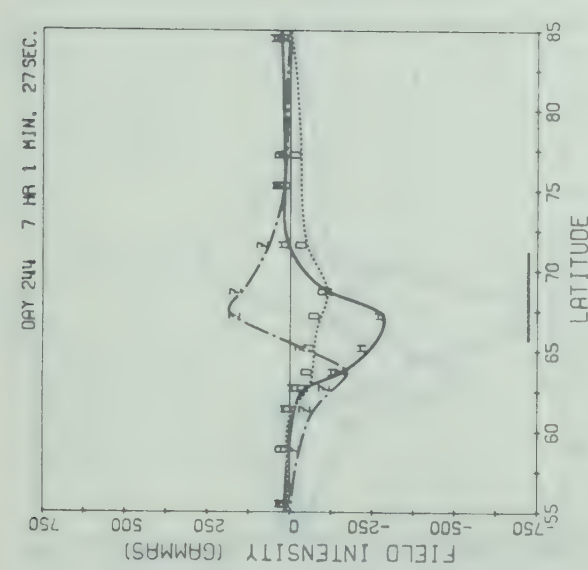
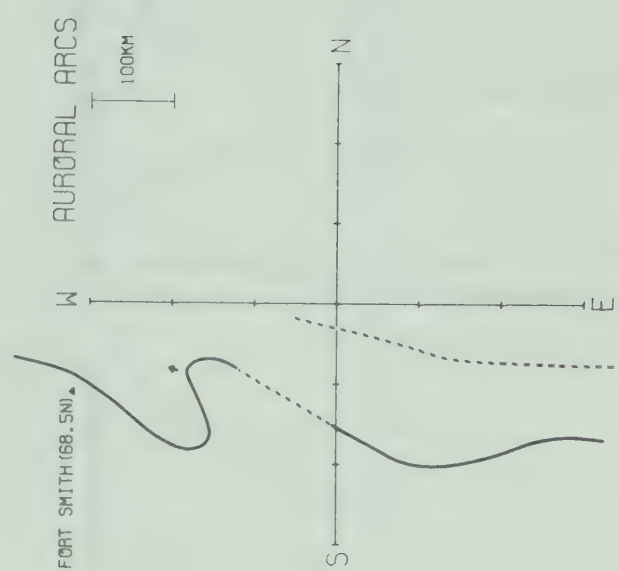
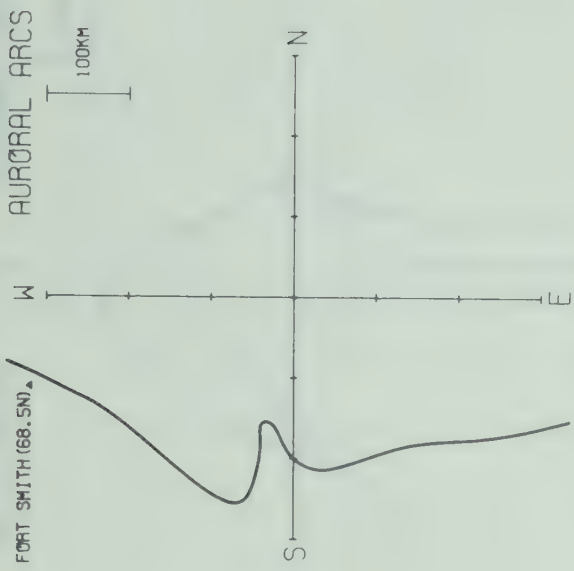


Fig. 5.16 Latitude profiles and the associated auroral diagrams associated with a westward travelling loop. The dashed lines represent diffuse auroral arcs and the solid lines represent intense arcs. The solid line beneath each latitude profile represents the extent of the NS axis in the auroral diagrams (600 km centered at 68.1°).

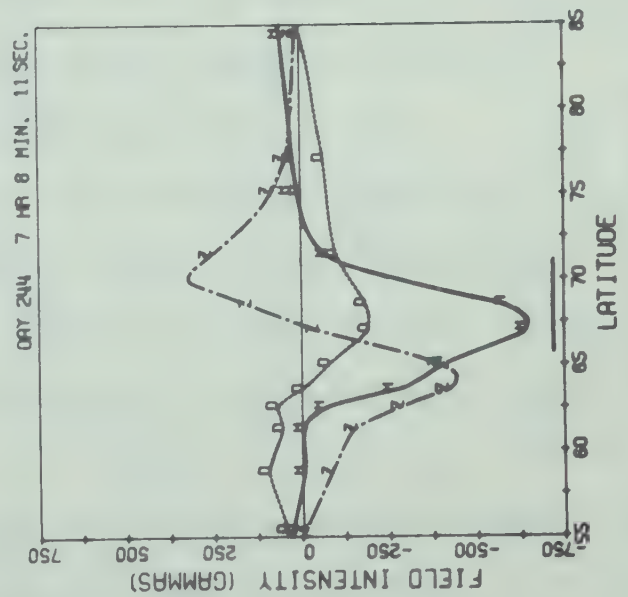
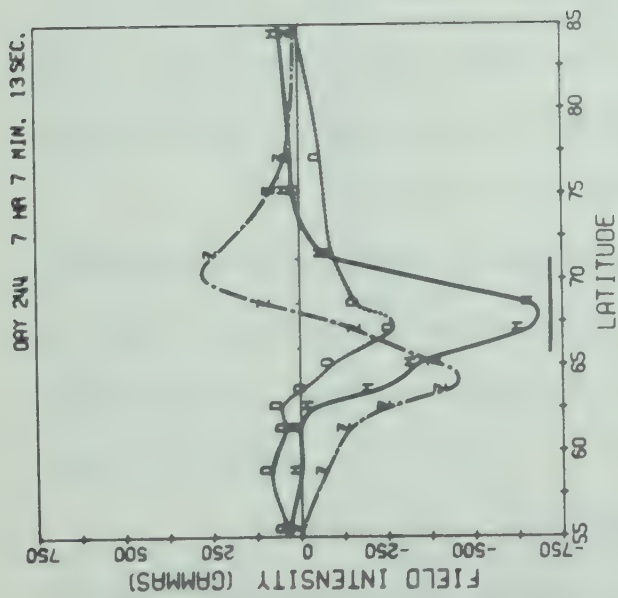
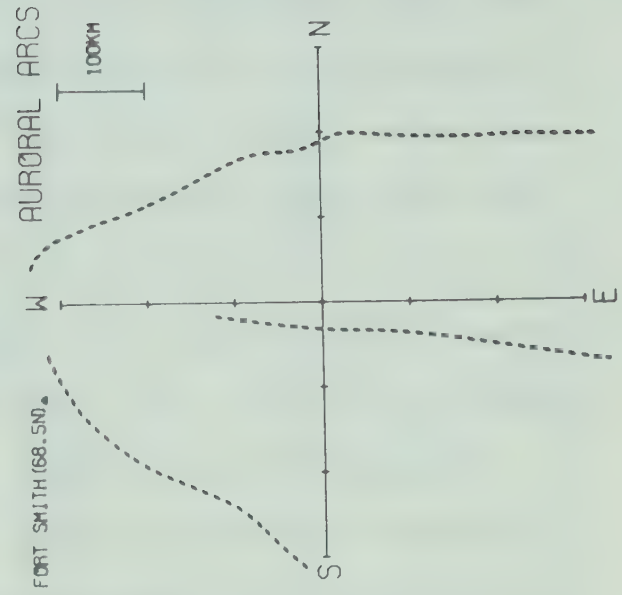
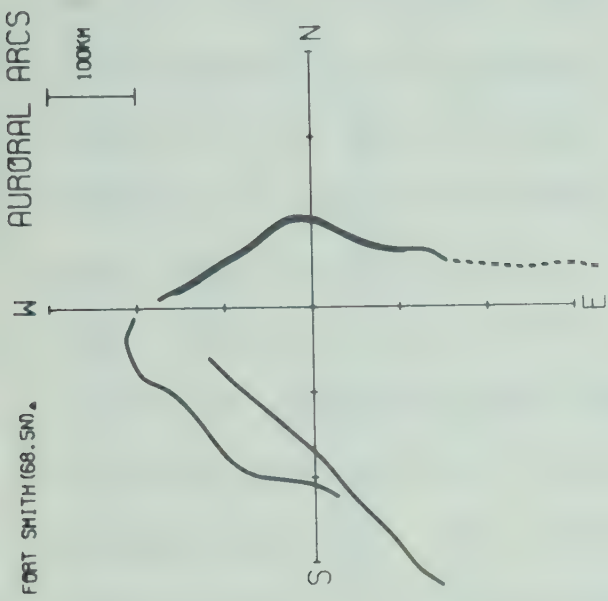


Fig. 5.17 Latitude profiles and the associated auroral diagrams showing the orientation of the auroral arcs and the -D regime (see Fig. 5.16).

Even though the all-sky photographs associated with the expansive phase were very difficult to interpret, we were able to extract what we think represents the important morphological features associated with the poleward motion of the auroral bulge. Fig. 5.16 and 5.17 show some examples of the interpreted arc structures along with the pertinent latitude profiles. Fig. 5.16 shows an intensified arc ~ 200 km south of FTSM along with the subsequent formation of a westward travelling loop. At ~ 0702 UT a diffuse arc developed north of the arc containing the westward propagating loop. One minute later (~ 0703 UT) the whole region south of FTSM was overexposed due to an activation of the existing auroral arcs. By 0705 UT a well formed arc was observed overhead FTSM moving to the northwest. At 0707 UT this particular arc (now north of FTSM) intensified while continuing to move to the northwest (see Fig. 5.17).

The tilt of the auroral arcs south of FTSM is interesting in that it may explain the large -D regime (due to the orientation with respect to our line of stations of the ionospheric current flow within the arc) also located slightly south of FTSM.

To study the perturbations of the current system during the expansive phase, we used 10 sec resolution latitude profiles. Such an analysis revealed a very inter-

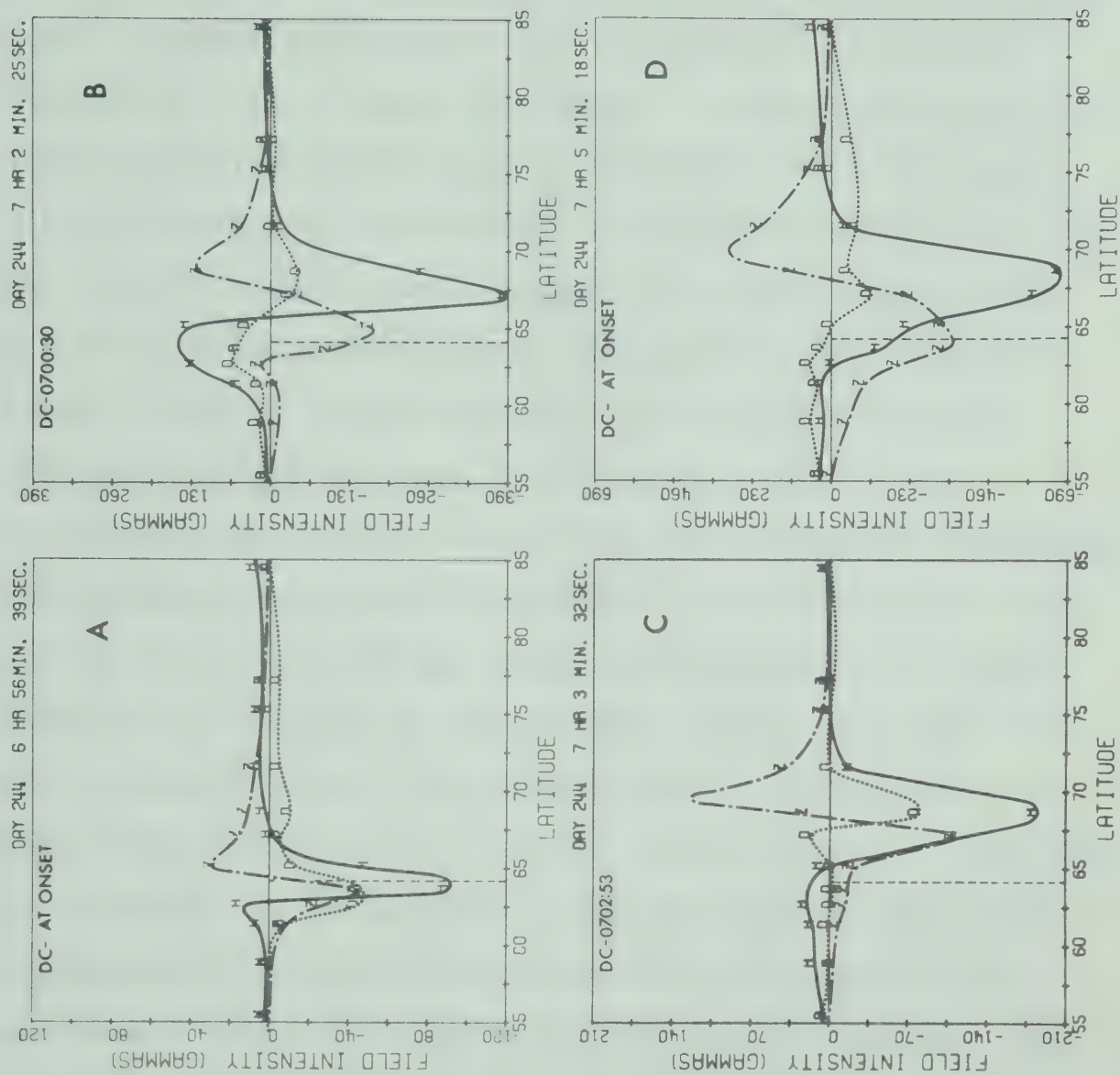


Fig. 5.18 Latitude profiles showing the initial current system (profile A) and the differential profiles (profiles B and C) showing perturbation current systems at the northern border. Profile D represents the resultant current system at ~ 0705 UT.

esting effect taking place during the northward expansion. Fig. 5.18A shows the initial development of the current system ~ 1 min after the onset. The current system at this time is probably less than 1.5° in width with a moment located at $\sim 64.5^\circ$ (note the change in the amplitude scale). This particular current system intensified over the next 2 min, at which time the maximum H perturbation observed along our line of stations was $\sim -240\gamma$. The width increased to $\sim 2.5^\circ$ with the moment moving northward to just slightly south of FTMU. The current system remained relatively unchanged during the next 2 min and at ~ 0701 UT the northern border of the preexisting current system intensified in conjunction with the activation of the auroral arc shown in Fig. 5.16. Fig. 5.18B shows the differential profile showing the location of the current system associated with this intensification. The dashed line in each graph represents the location (64.3°) of the current system at the time of the onset of the substorm. The +H regime to the south represents an eastward electrojet (or a reduction of the westward flowing currents in this particular regime). The shape of the Z profile south of 64° rules out the possibility of explaining this +H regime totally by field aligned currents associated with an E-W three-dimensional current system (see

Chapter II, Fig. 2.4). This particular deformation of the Z profile can be caused only by an ionospheric current. The shape of the D profile is what we would expect for a current system with a central meridian east of our line of stations.

A second intensification of the northern border occurred at ~ 0703 UT (this intensification was probably associated with the intense activation of the auroral arc overhead FTSM at 0703 UT. The resulting differential profile depicting this enhancement is shown in Fig. 5.18C. Except for the slight deformation of the D profile at FTSM (probably due to a NW-SE orientation of the electrojet), this profile can easily be explained in terms of a three-dimensional current system. As a result of these successive enhancements of the northern border of pre-existing electrojets, the overall system expands rapidly northward as previously shown in Fig. 5.14, 5.15 and also in Fig. 5.17D.

It is interesting to note that from the polar plot (for ~ 0708 UT) shown in Fig. 3.3 (Chapter III), the central meridian of the current system was calculated to be $\sim 10-15^{\circ}$ east of our line of stations. The central meridians of the perturbation current systems associated with the enhancements of the northern border were also to the east of our line of stations.

5.3.2 Recovery phase

The beginning of the recovery phase for this particular substorm is not as clearly defined as that for the 0659 UT substorm (Day 280) discussed in the previous section. Even though the first equatorward motion of auroral arcs was observed at ~ 0710 UT, Snyder and Akasofu (1972) reported that such motion can occur while the auroral bulge is still expanding. We also noted previously (see Fig. 5.15) that the moment of the electrojet began to move southward beginning at ~ 0708 UT. To make the problem of choosing an onset time for the recovery phase even more difficult, the northern border of the electrojet experienced two major enhancements at ~ 0717 UT and at 0806 UT. In fact, quasi-periodic intensifications of the northern border were in progress throughout the entire substorm. Snyder and Akasofu (1972) also questioned the meaning of the recovery phase in terms of whether it represented the reappearance of a significant equatorward component of motion within the bulge, or the recovery of the poleward boundary of the bulge. For the purpose of the following discussion we set the beginning of the recovery phase at the time of the first southward motion of the moment of the electrojet (~ 0708 UT).

The overall dynamic development of the H component of this particular substorm is shown in Fig. 5.19 (3-D diagrams for the D and Z components are included in Appendix A6). A 'double' current system, represented by the two 'mountain ranges' (centered about $\sim 64^{\circ}$ and 68°) in the 3-D diagram, existed throughout the entire substorm. In fact a triple peaked current distribution was evident at ~ 0717 and 0809 UT following northern border enhancements. The northern border enhancement at 0717 UT can not be seen in this particular perspective view of the H component array due to the strength of the second maximum at $\sim 68^{\circ}$.

The two polar plots shown in Fig. 5.20 show the distribution of the magnetic perturbation vectors at ~ 0730 UT and 0809 UT during the recovery phase. It is interesting to note the similarities between these two distributions even though they are separated in time by ~ 40 min. The longitudinal expansion of the electrojet can be seen by comparing these polar plots with that shown in Chapter III, Fig. 3.3 for ~ 0708 UT.

During the recovery phase, most of the auroral activity and perturbations of the current system were centered about FTSM. In fact, quasi-periodic intensifications of the northern border of the current system were in progress much

H-COMP.

SEPT. 1, 1970

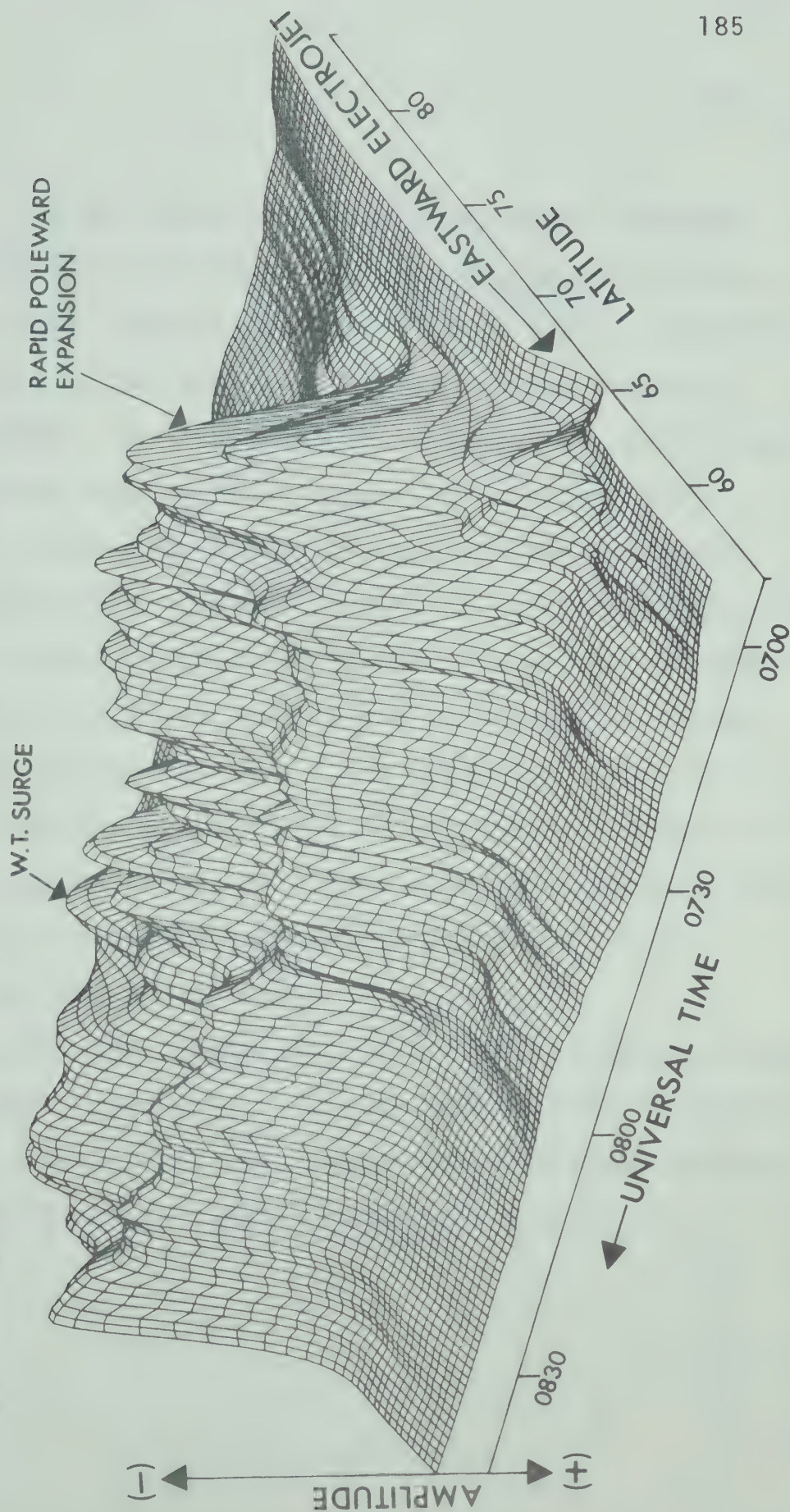


Fig. 5.19 Three-dimensional plot showing the dynamic development of the substorm for the first two hours. Note the stability of the southern border of the electrojet as compared to the northern border.

of the time. It was found that the D component responded to all the eastward and westward propagating auroral forms. These D component responses were similar to the +D perturbations discussed in the previous section for the westward travelling surge. To illustrate these responses, a filtered version (60-1000 sec) of the D component magnetogram is shown in Fig. 5.21. The dotted and solid lines represent westward and eastward propagating auroral forms respectively, that could be easily identified in the all-sky camera photographs. During the first hour of the recovery phase these +D perturbations occurred at ~ 7 min intervals. The lines were drawn along the peaks of the +D perturbation maxima (in latitude) to emphasize the fact that such perturbation fields may have their lines of N-S maxima slightly tilted with respect to our line of stations.

Upon closer examination of the Pi 2 micropulsations for this substorm (see Fig. 5.12), we noticed that an enhancement of Pi 2 activity was also associated with these eastward and westward motions of auroral forms. An example of a

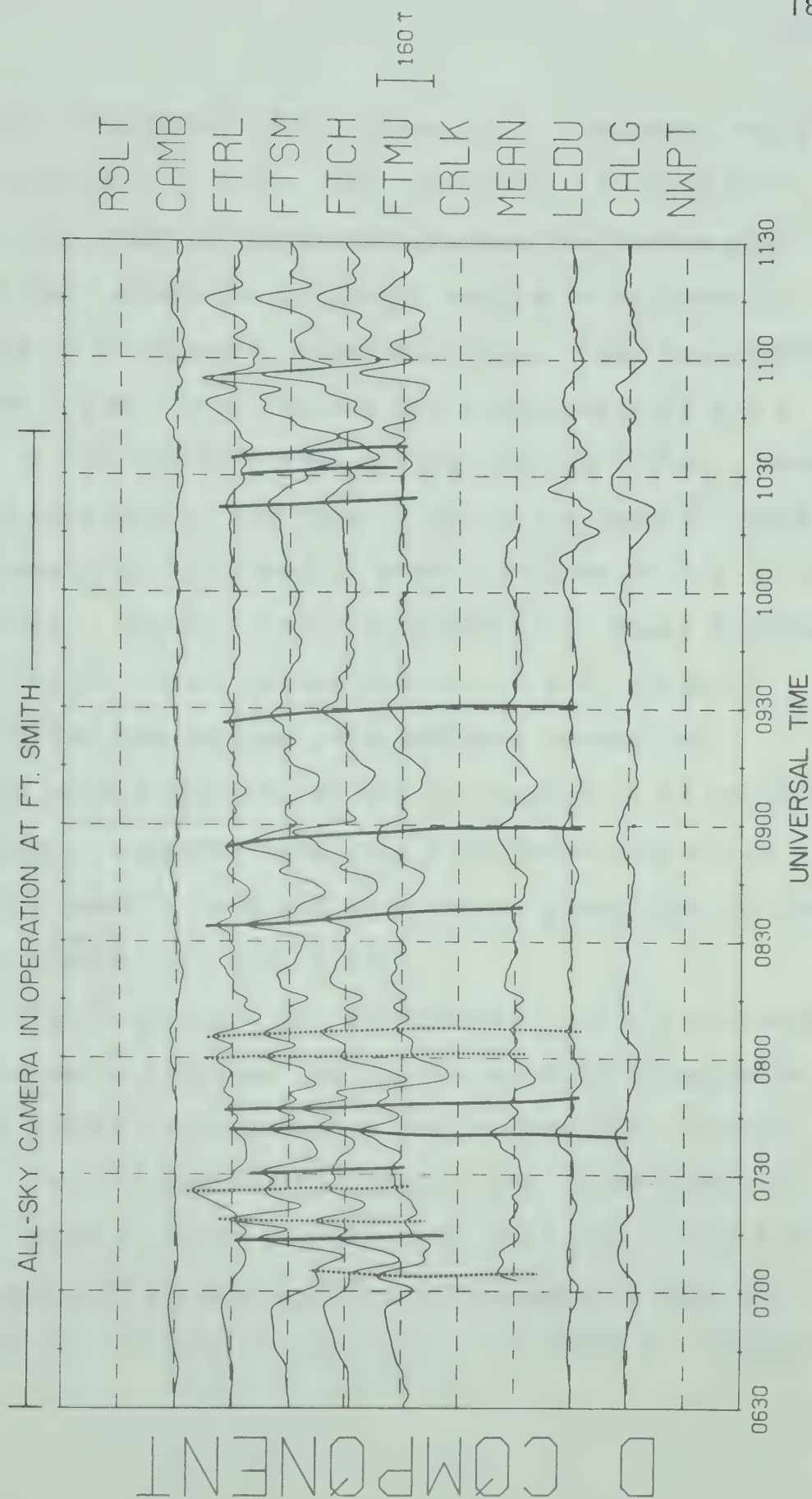


Fig. 5.21 The D component magnetogram band pass filtered (60-1000 sec). Note the correlation with observed eastward (solid line) and westward (dashed line) propagating auroral forms.

perturbation attributed to the passage of a westward travelling loop is shown in Fig. 5.22. The top profile (~ 0716 UT) represents the unperturbed system whereas the bottom profile (~ 1 min later) shows the perturbed system in response to the passage of a westward travelling loop. Note the deformation of the D and Z profiles and the enhancement of the H component at the northern edge of the current system. When we set the baseline at the time of the first profile (0715:51 UT), the resulting differential profiles shown in Fig. 5.23 were obtained. The most apparent property of these differential profiles is the +D regime similar to that normally observed during the passage of a westward travelling surge. The second property is the occurrence of an apparent shear system of currents involving a westward electrojet north of the auroral form and an eastward electrojet to the south (see Chapter II, Fig. 2.18C).

Fig. 5.24 shows the differential profile representing the magnetic perturbation associated with an eastward travelling auroral form (showing the accompanying auroral diagram). In this particular example, the +D perturbation is not as large as those shown in Fig. 5.23 due to the fact that the main N-S aligned portion of the auroral form was to the east of our line of stations. At ~ 0833 UT, however,

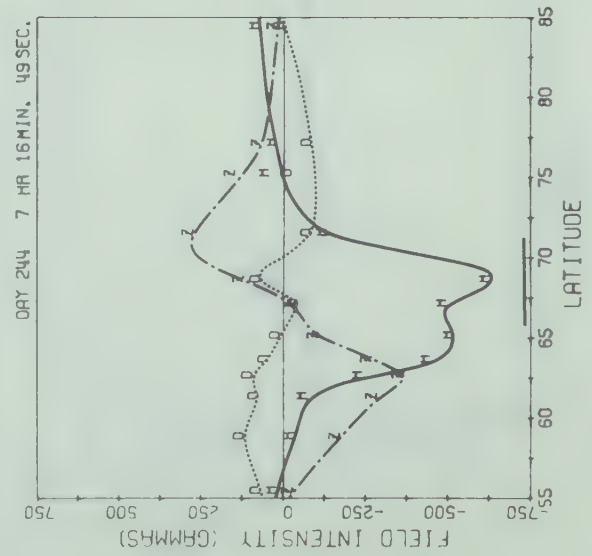
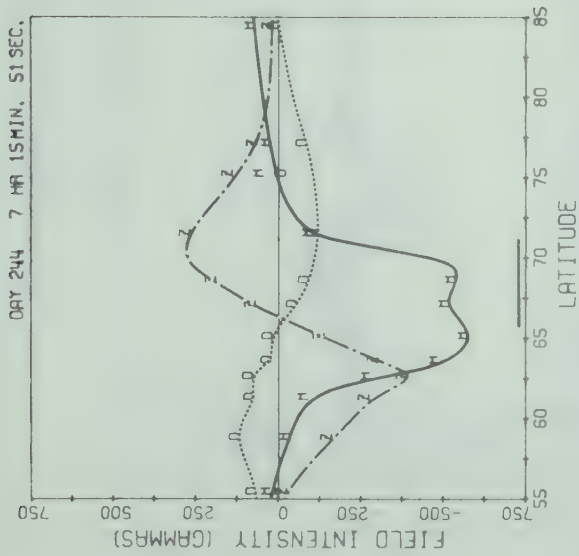
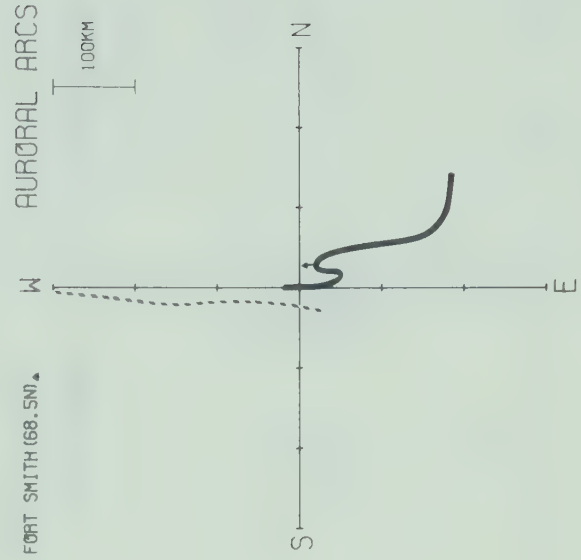
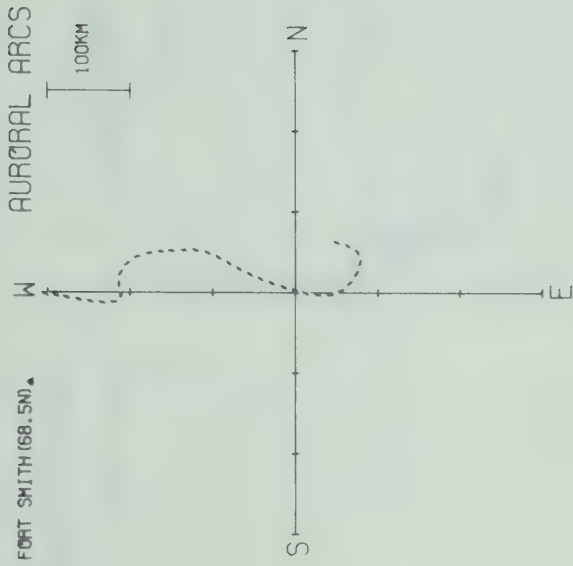


Fig. 5.22 Latitude profiles and associated auroral diagrams showing the enhancement of the northern border due to the westward propagating loop.

DIFFERENTIAL PROFILES (DC-0715:51)

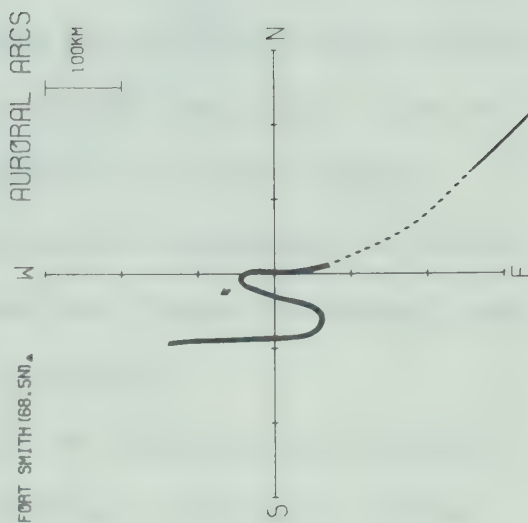
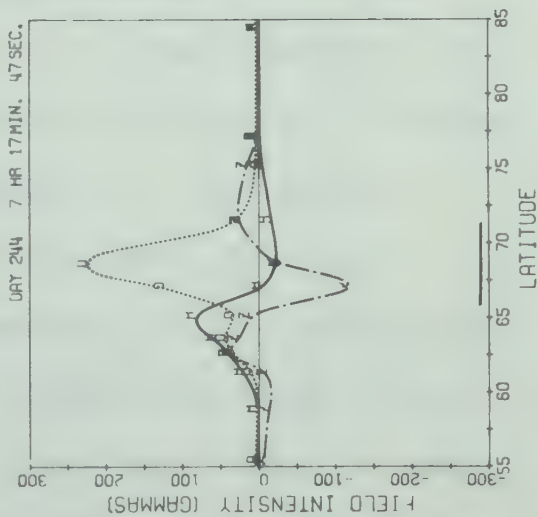
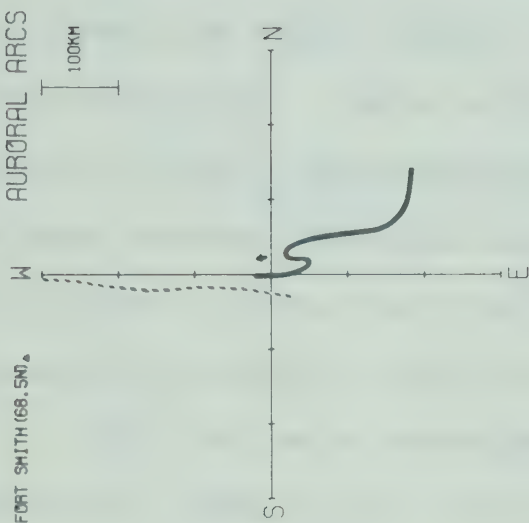
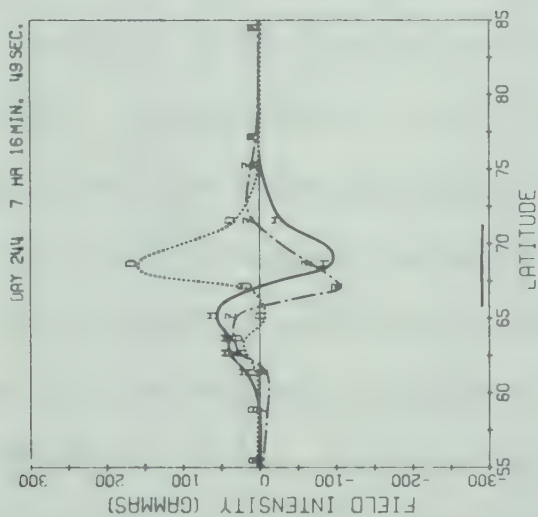


Fig. 5.23 Differential profiles depicting the magnetic perturbation associated with the westward propagating loop shown here and in Fig. 5.22.

the profile (not shown here) showed a much more enhanced D perturbation.

We analyzed several cases of E-W motions of isolated auroral forms and found similar magnetic perturbations along our line of stations. We also discovered that this form of differential profile was associated with a slowly moving N-S aligned auroral arc which occurred on September 19, 1970. A model current system that may explain these perturbations is discussed in detail in the next chapter.

The last major enhancement of the northern border commenced at ~ 0806 UT and the associated latitude profile (~ 0810 UT) is shown in Fig. 2.25. At 0800 and 0801 UT a well defined westward travelling loop was observed ~ 150 - 200 km north of FTSM (the +D response is clearly evident in Fig. 5.21). Approximately 5 min later a diffuse arc, located ~ 300 km north of FTSM developed (0806 UT). During the following 3 min a rapidly propagating auroral form was observed to develop while moving westward. It is not certain whether this represented a westward travelling surge (as we have indicated in Fig. 5.19) or a propagating loop. A westward propagating auroral form was also observed during the enhancement of the northern border at ~ 0717 UT.

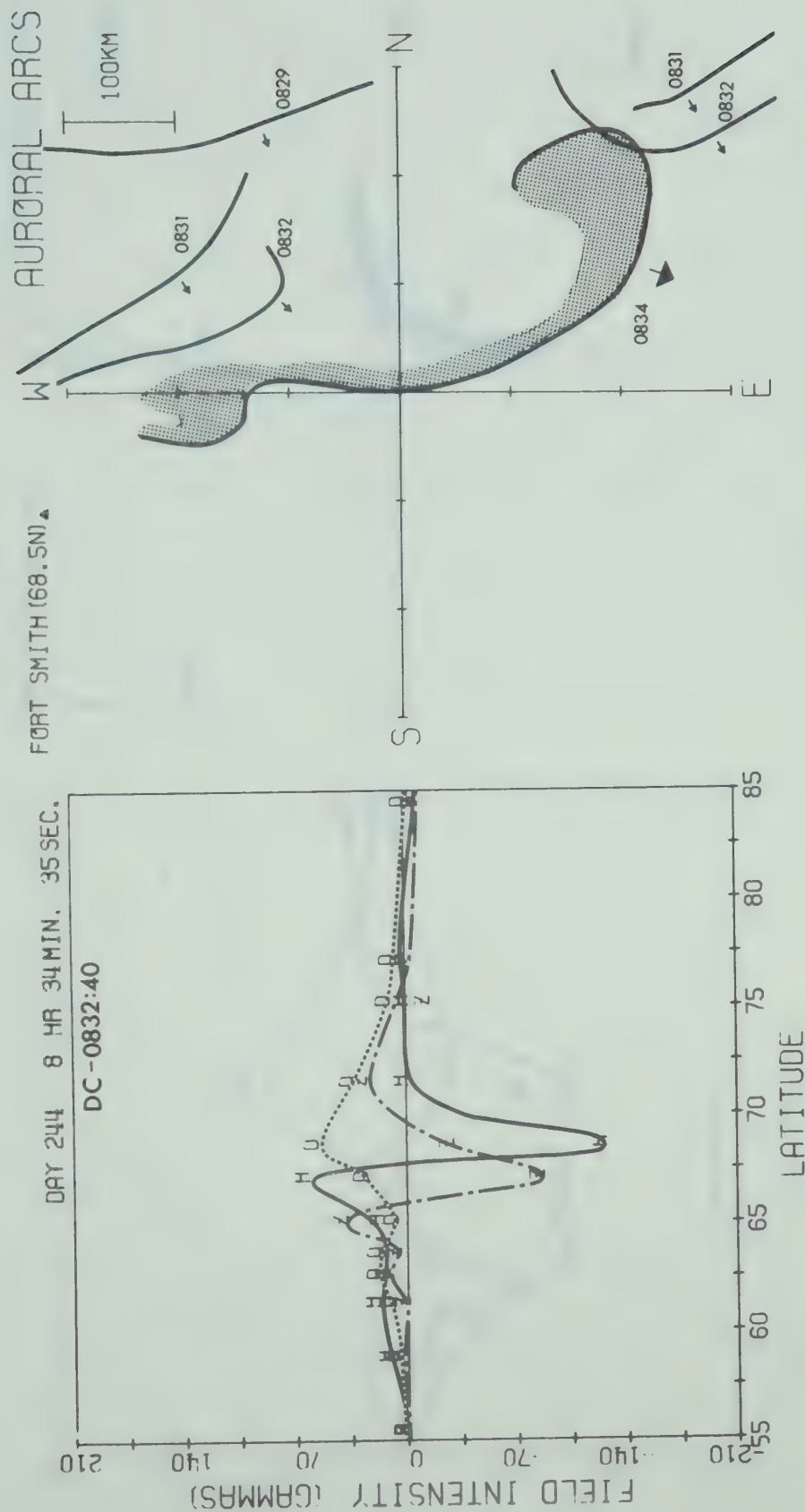


Fig. 5.24 Differential profile showing the magnetic perturbation associated with the eastward propagating auroral form also shown in this figure.

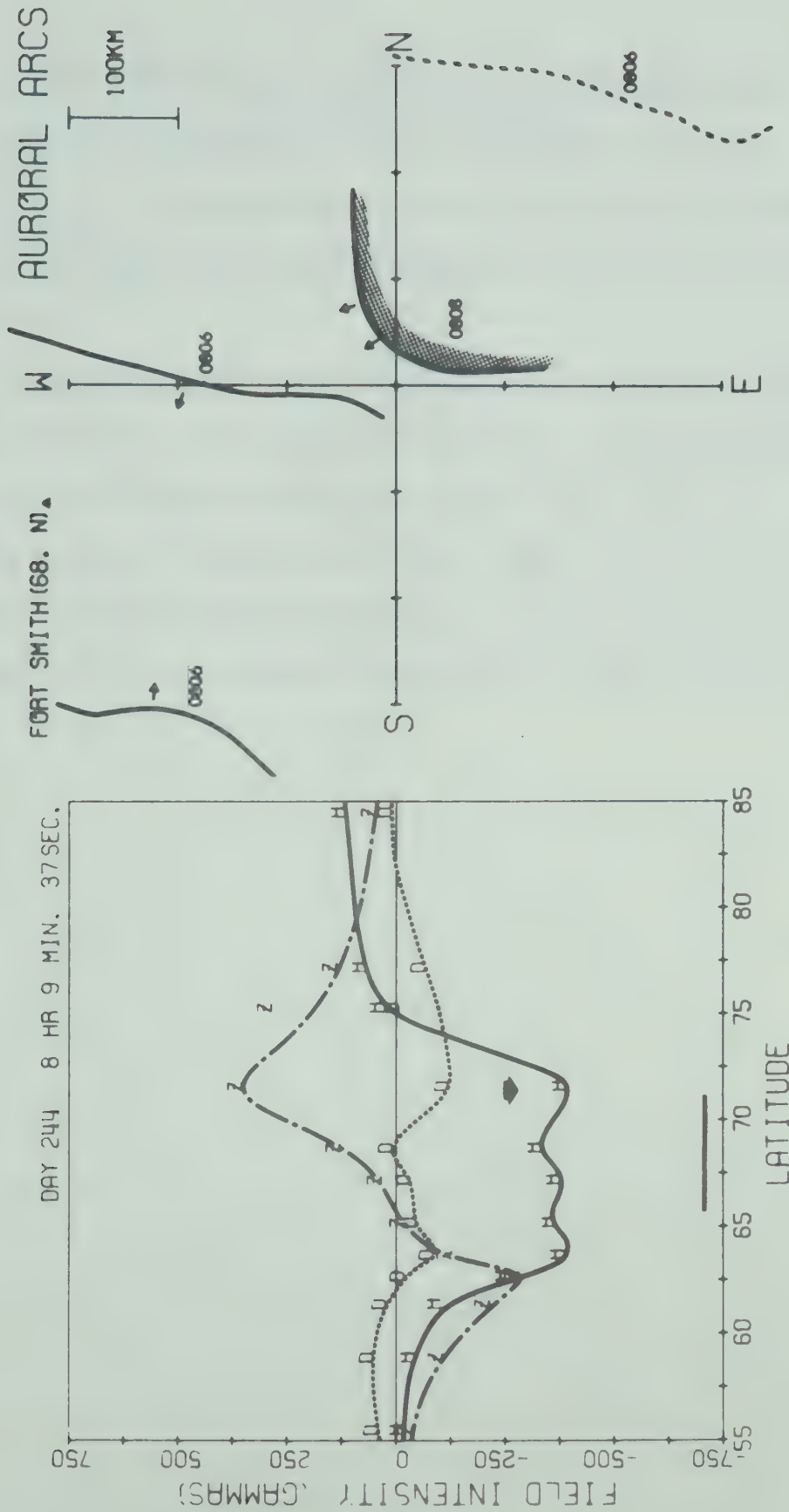


Fig. 5.25 Latitude profile depicting the last major enhancement of the northern border north of FTSM. This enhancement is associated with the westward travelling loop or surge.

At ~ 0810 UT the resulting current system was $\sim 10-11^\circ$ wide with both the Z and H component profiles shown in Fig. 5.25 indicative of complex structure in the latitudinal current distribution (possibly a triple peaked distribution).

Throughout the remaining portion of the recovery phase the northern border decayed while the southern border and the portion of the electrojet around FTCH (67.0°) experienced marked fluctuations. By ~ 0930 UT (the time of the onset of the second substorm), the maximum perturbation observed by our line of stations was approximately 150γ .

CHAPTER VI MODELLING OF THE CURRENT SYSTEM ASSOCIATED WITH THE POLAR MAGNETIC SUBSTORM

6.1 Introduction

In Chapter II and Appendices A1, A2 and A3 we presented the results of our study of magnetic field perturbations generated by three-dimensional current systems along with a convenient method of evaluating these fields.

In this chapter a comparison is made between the observed magnetic perturbations associated with polar magnetic substorms and the magnetic fields associated with three-dimensional current systems.

In section 6.2 we examine the best possible depth at which to place the superconductive layer below the surface of the Earth in order to compensate for induction effects. Section 6.3 contains a discussion of coordinate systems along with the presentation of the results of our modelling of the substorm associated current system. The modelling of magnetic field perturbations associated with eastward and westward propagating auroral forms is discussed in Section 6.4.

6.2 Depth of the superconductive layer used in our modelling

Since there are many parameters which affect the shape of the latitude profiles associated with model three-dimensional current systems, we decided to incorporate the results of previous research in order to remove one of these parameters, namely the depth of the superconductive layer.

McNish (1938) was the first researcher to examine the effects of induction on the magnetic field perturbations due to polar electrojets. In his model he ignored the curvature of the Earth and represented the electrojet by an infinitely long sheet current of finite latitudinal width, positioned at a given height above the surface of the Earth. To allow for the effect of induction he included a superconductive layer at some depth below the surface of the Earth. With this particular model McNish was able to obtain a fairly good approximation of the observed data for a particular event by assuming a sheet current of ~ 670 km wide positioned at a height of 100 km, and a superconductive layer 200 km below the Earth's surface. Forbush and Casaverde (1961), using a similar model, studied the magnetic field perturbations due to the equatorial electrojet. They found that a depth of 250 km for the position of the superconductive layer yielded the best re-

sults. They also applied the method of separating the external and internal fields used in their study of the equatorial electrojet, to the auroral zone magnetic data analyzed by McNish (1938). The depth they determined for the top of the superconducting layer was 250 km, in complete agreement with that obtained from the study of the equatorial electrojet. Czechowsky (1971), using the same model but allowing for various latitudinal distributions of current, obtained an average value for the depth of the superconductive layer of ~ 450 km. In his study, however, Czechowsky used magnetic data from only four stations, which as we have shown, may produce ambiguous results in terms of the causative current system.

Since the equatorial electrojet is probably more representative of a two-dimensional current system and also a more static system, we decided to use the value of 250 km for the depth of the superconductive layer as obtained by Forbush and Casaverde (1961).

6.3 Modelling of the polar electrojet

In Chapters IV and V we used the corrected geomagnetic (C.G.) coordinate system in our analysis of the dynamic development of polar magnetic substorms. Since

this particular coordinate system is non-orthogonal when transformed into geographic coordinates, distances measured in degrees of C.G. latitude and C.G. longitude are not the same as those in geographic or centered dipole (geomagnetic) coordinates. Therefore, since the model current systems are based on an orthogonal system of coordinates, we used the geomagnetic coordinate system for the presentation of the observed magnetic data. To do so the horizontal components of the magnetic perturbations were transformed from HDZ coordinates to H'D'Z (geomagnetic) coordinates using the following equation

$$\begin{bmatrix} H' \\ D' \end{bmatrix} = \begin{bmatrix} \cos \theta & -\sin \theta \\ \sin \theta & \cos \theta \end{bmatrix} \begin{bmatrix} H \\ D \end{bmatrix} \quad 6.1$$

where θ is defined as the difference between the magnetic declination (ϕ) and the dipole declination (ψ) as illustrated in Fig. 6.1 (X and H' being in the direction of geographic and dipole (geomagnetic) north respectively). Table 6.1 contains the values of θ , ϕ and ψ along with the geomagnetic coordinates for each observatory whose data were used in this thesis.

Table 6.1 Geomagnetic coordinates of observatories used in this thesis.

Observatory	Geomagnetic Latitude($^{\circ}$ W)	Geomagnetic Longitude($^{\circ}$ E)	Magnetic Declination $\phi(^{\circ}$ E)	Dipole Declination $\psi(^{\circ}$ E)	$\theta(^{\circ}$ E)
ALER*	85.8	168.2	-79.0	-17.6	17.6
RSLT*	83.0	289.3	-78.0	45.5	-45.5
MOUL*	79.1	283.6	62.5	54.3	-54.3
CAMB	76.7	294.7	33.0	30.5	2.5
BAKE*	73.7	315.3	5.0	18.9	-18.9
FTRL	70.2	299.6	29.8	22.2	7.6
CHUR*	68.7	322.6	4.0	13.5	-13.5
BARR	68.8	241.2	26.0	33.4	- 7.4
NARS	71.2	36.8	- 3.8	-14.4	10.6
WHAL	66.6	347.3	-22.0	4.4	-26.4
FTSM	67.2	298.6	28.0	20.5	7.5
LYNN	65.8	314.7	16.0	15.0	1.0
FTCH	66.2	300.7	27.0	14.3	7.7
LEIR	70.2	71.1	-24.8	-25.7	0.9
TIXI	60.4	191.4	10.0	7.1	2.9
FTMU	64.2	302.2	25.0	17.9	7.1
COLL	64.7	256.5	28.5	27.2	1.3
KIRU	65.2	115.6	2.0	-28.4	30.4
CRLK	62.7	301.5	25.0	17.8	7.2
MEAN	61.8	301.1	24.4	17.2	7.2
LEDU	60.5	301.6	23.6	16.5	7.1
SITK	60.0	275.4	28.5	21.4	7.1
OTTA	56.8	351.1	-13.3	2.5	-15.8
LERW	62.5	88.5	-10.0	-23.6	13.6
CALG	58.4	301.6	22.3	15.7	6.6
JOHN	58.5	21.2	-27.1	- 6.2	-20.9
LOVO	58.1	105.8	0.8	-22.1	22.9
NEWP	55.1	300.0	21.3	15.0	6.3
VICT	54.1	293.0	23.0	16.0	7.0
FRED	49.6	349.8	6.7	2.6	- 4.1
BOUL	49.0	316.5	13.5	10.3	3.2
DALL	43.0	327.7	10.0	7.3	2.7
TUCS	40.4	312.2	13.5	10.1	3.4

*We set θ equal to ψ since the magnetic data from these stations is measured in the XYZ coordinate system.

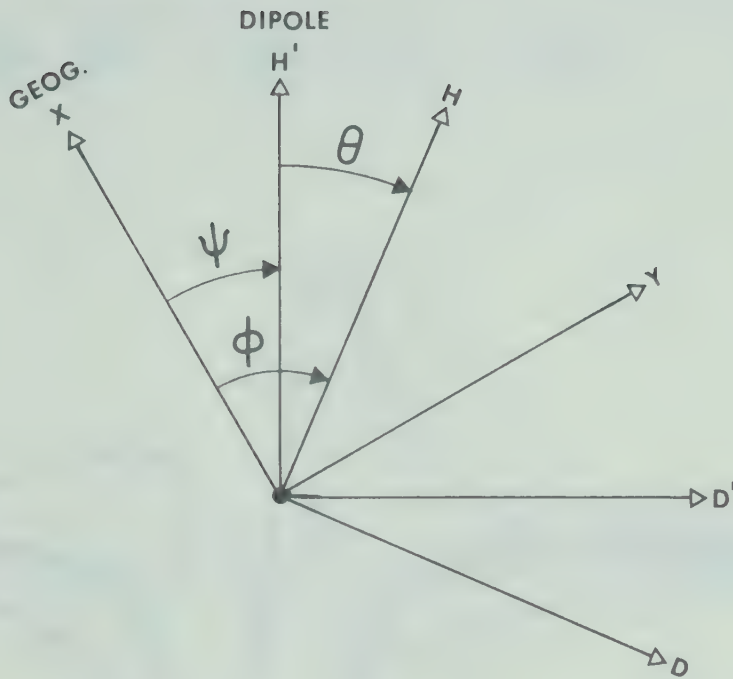


Fig. 6.1 The relationship between the coordinate systems defined within the text.

Three of the latitude profiles we have modelled thus far are presented in Fig. 6.2, 6.3 and 6.4. The first two profiles are for the substorm that occurred on June 15, 1970 (Day 166) and the remaining one is for the substorm that occurred on September 1, 1970 (Day 244). The parameters for the three model current systems we believe to be responsible for the observed magnetic perturbations are listed

THEORETICAL PROFILE

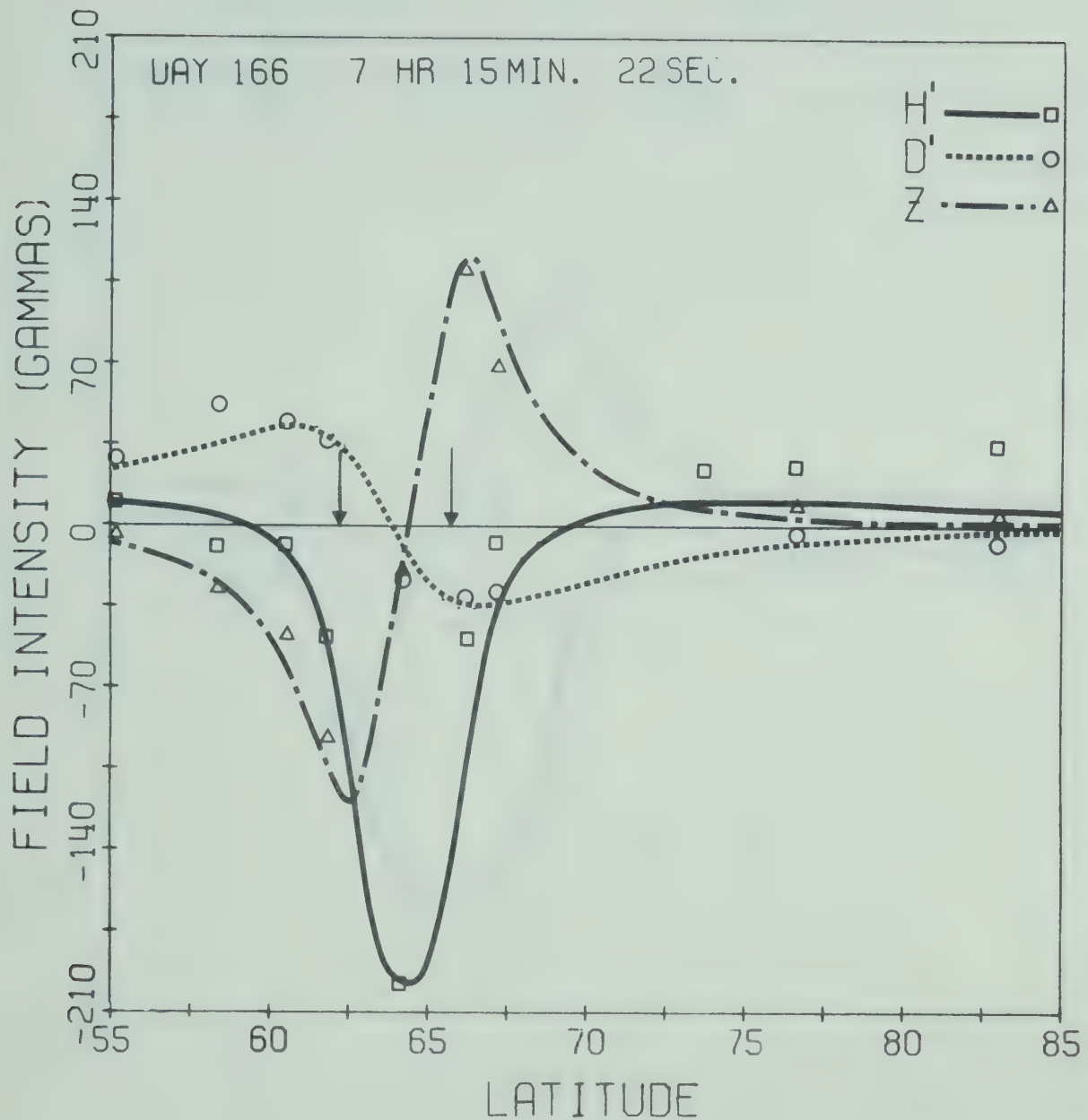


Fig. 6.2 Comparison of theoretical and observed profiles for Day 166 at ~ 0715 UT. The arrows represent the boundary of the oval along the central meridian.

THEORETICAL PROFILE

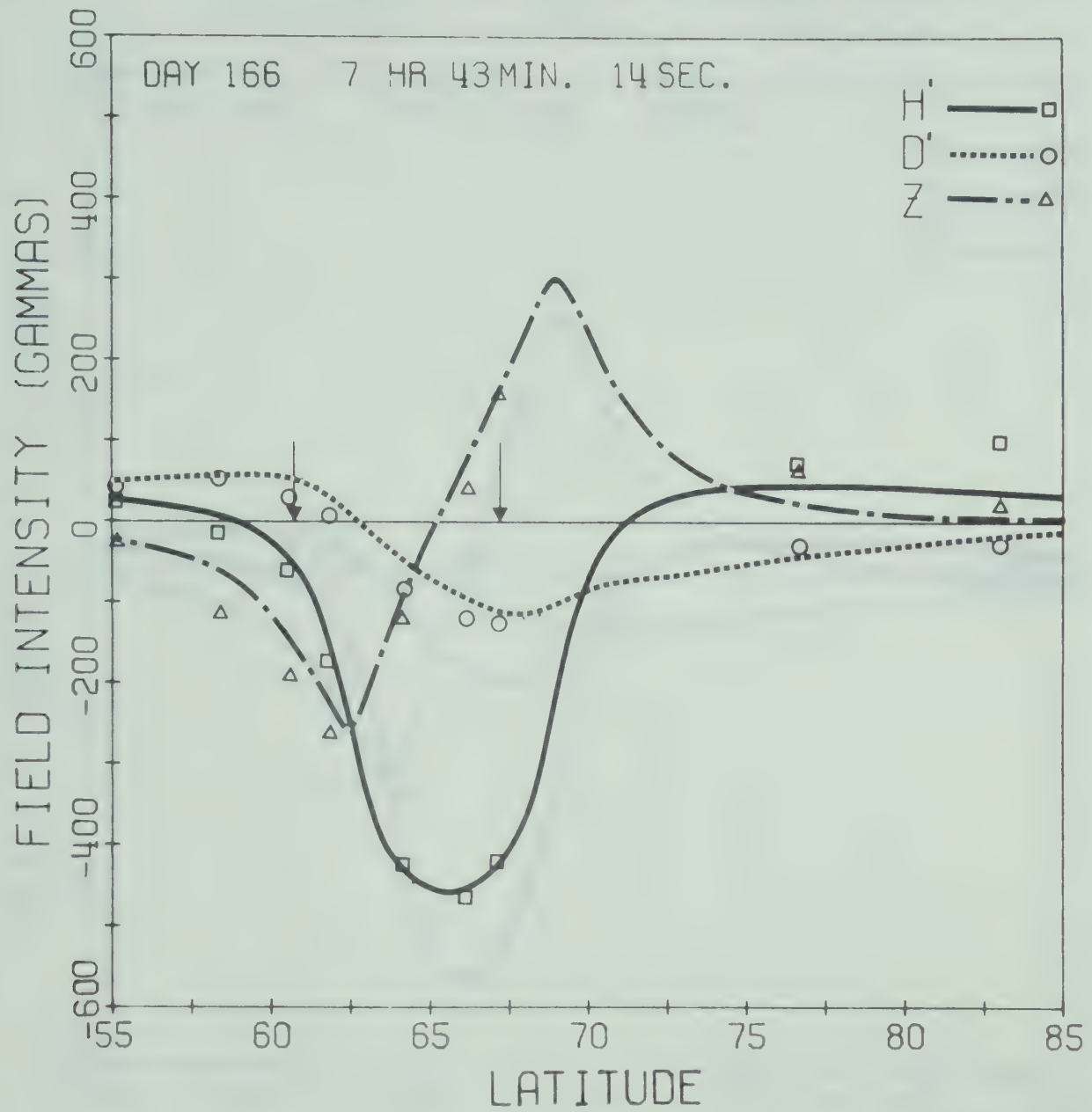


Fig. 6.3 Same as Fig. 6.2 but for Day 166 at ~ 0743 UT.

THEORETICAL PROFILE

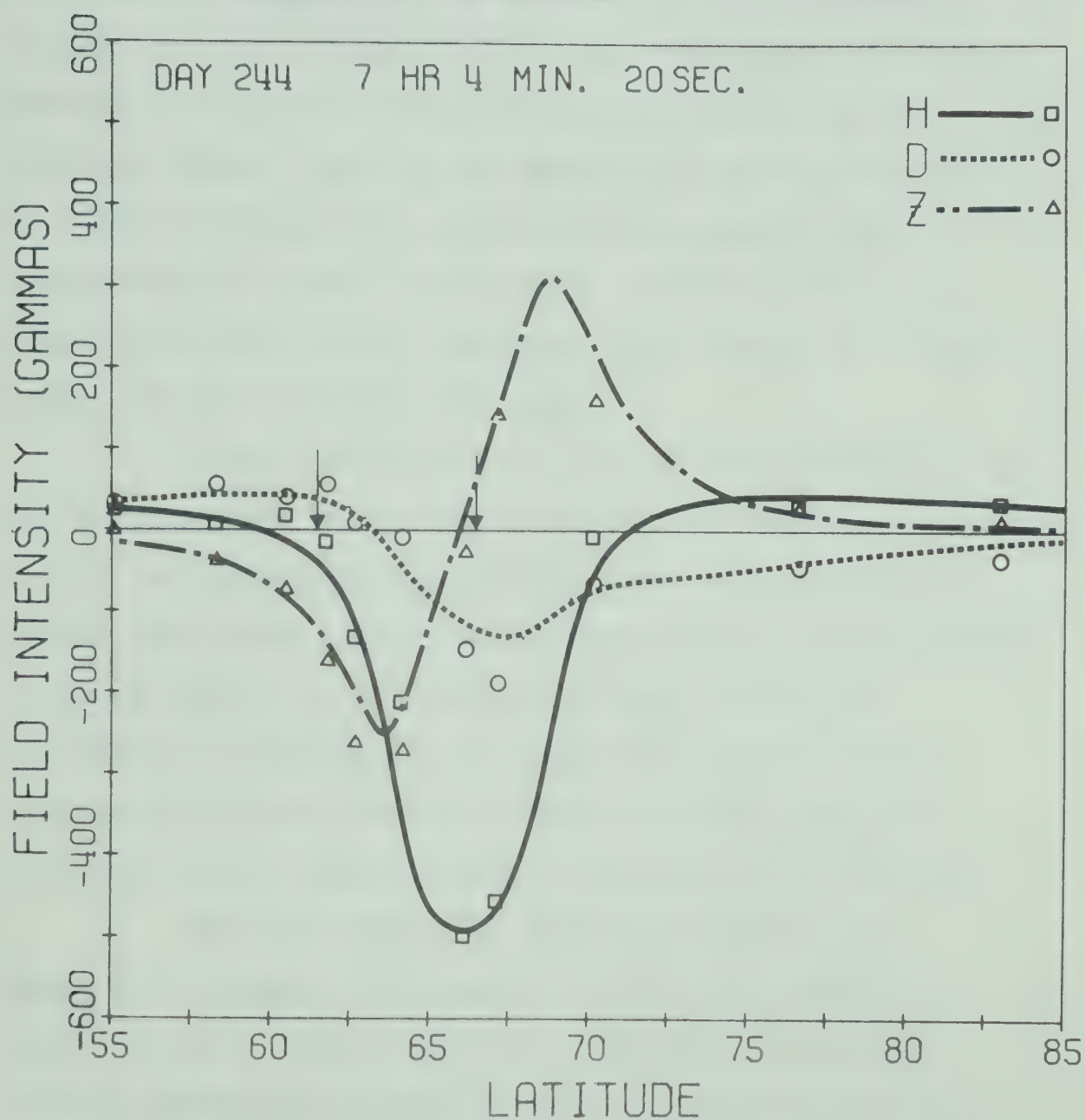


Fig. 6.4 Same as Fig. 6.2 but for Day 244 at ~ 0704 UT.

in Table 6.2. The oval parameters were discussed previously in Chapter II (see eq. 2.25 and Fig. 2.15). The model systems for 0715 UT and 0743 UT show the expansion of the current system associated with the development of the northern border. During the interval of time represented by these profiles, the current system expanded both in length (32.5° to 50°) and in width (3.5° to 6.5°). The total integrated current increased by a factor of 3, from 0.23×10^6 amp to 0.69×10^6 amp.

In all three profiles, we see the deformation of the D' component due to the fact that the ionospheric portion of the current system was flowing along the auroral oval rather than along a constant latitude circle. Also evident in these figures is the relatively good fit of the theoretical Z profiles to the observed Z perturbations. It appears that the choice of 250 km for the depth at which to put the superconductive layer was satisfactory.

The polar plots for both the observed and theoretical magnetic perturbations for these times are shown in Fig. 6.5, 6.6 and 6.7. The expansion of the current system for Day 166 is easily seen by comparing Fig. 6.5 and 6.6. The eastward electrojet in the evening sector and the currents in the polar cap region probably

Table 6.2 Parameters of model current systems.

Day	Time	Width	Length	Central Meridian	Oval Parameters (90°-a) (90°-b)	Total Integrated Current (10 ⁶ amp)
166	0715 UT	3.5°	32.5°	313°	64.0° 70.0°	0.23
166	0743 UT	6.5°	50.0°	315°	65.0° 72.5°	0.69
244	0704 UT	5.0°	50.0°	314°	64.5° 74.0°	0.59

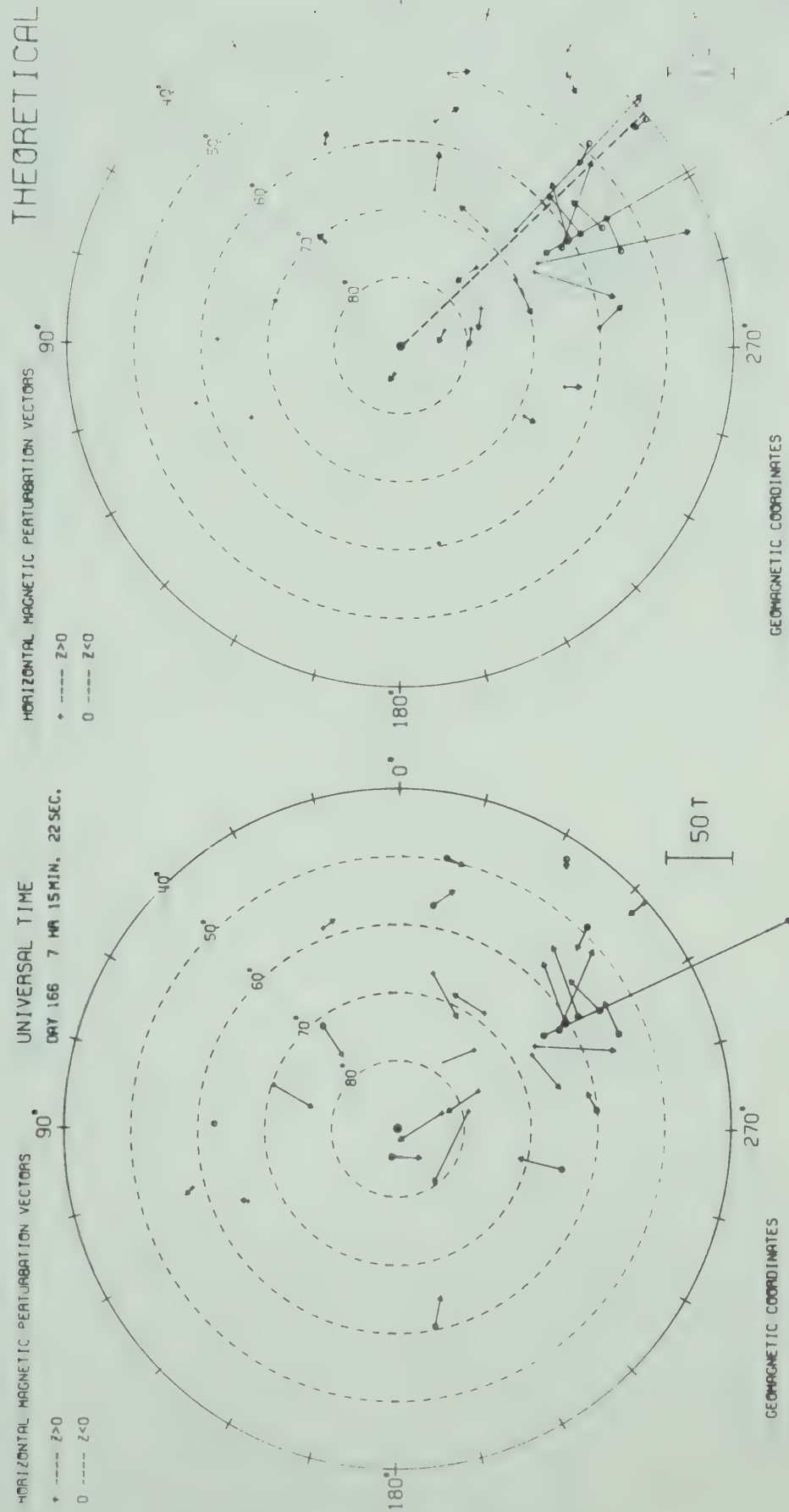


Fig. 6.5 Comparison of theoretical and observed horizontal magnetic perturbations in the northern hemisphere for Day 166 at ~ 0715 UT.

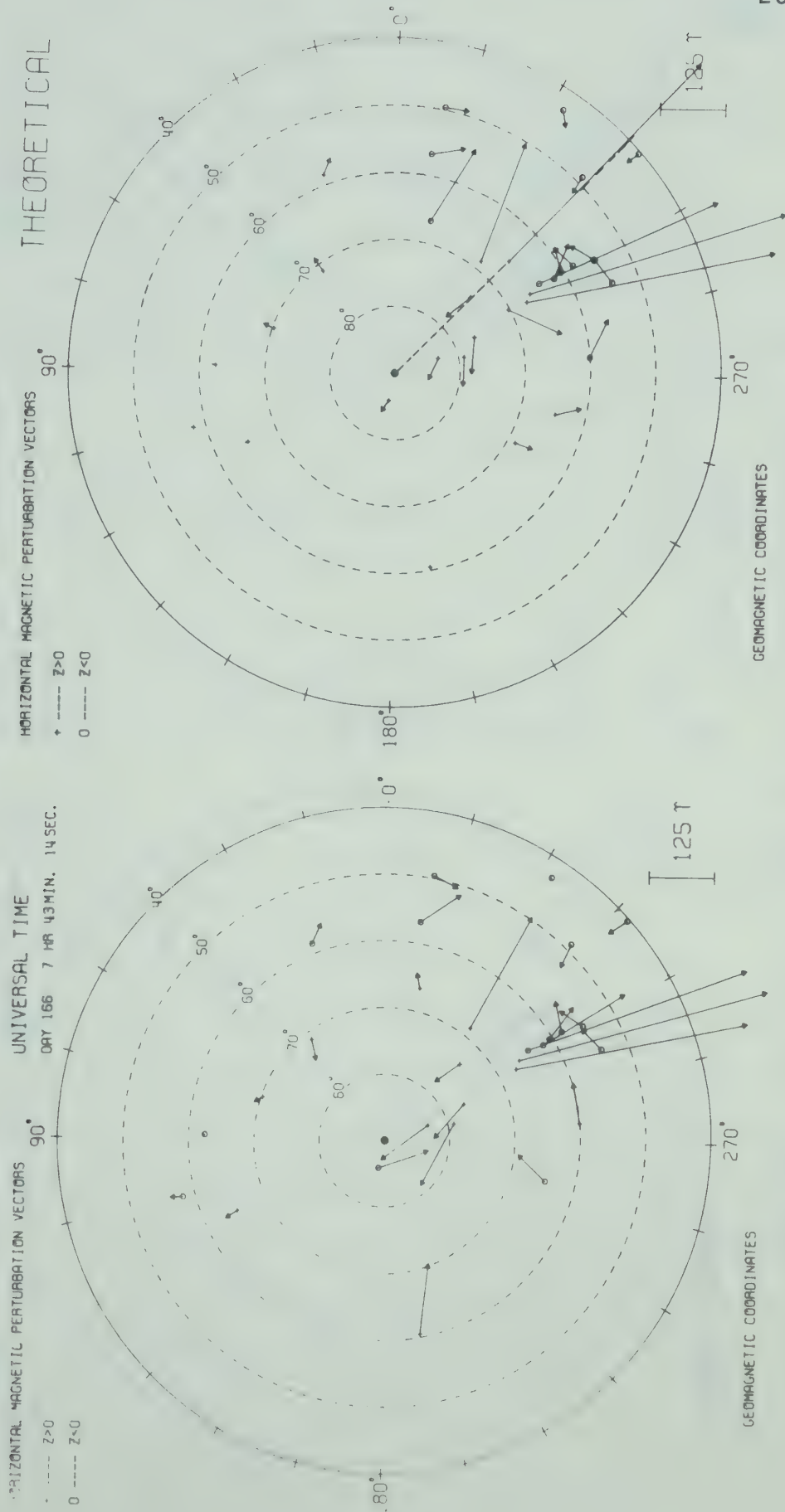


Fig. 6.6 Same as Fig. 6.5 but for Day 166 at ~ 0743 UT.

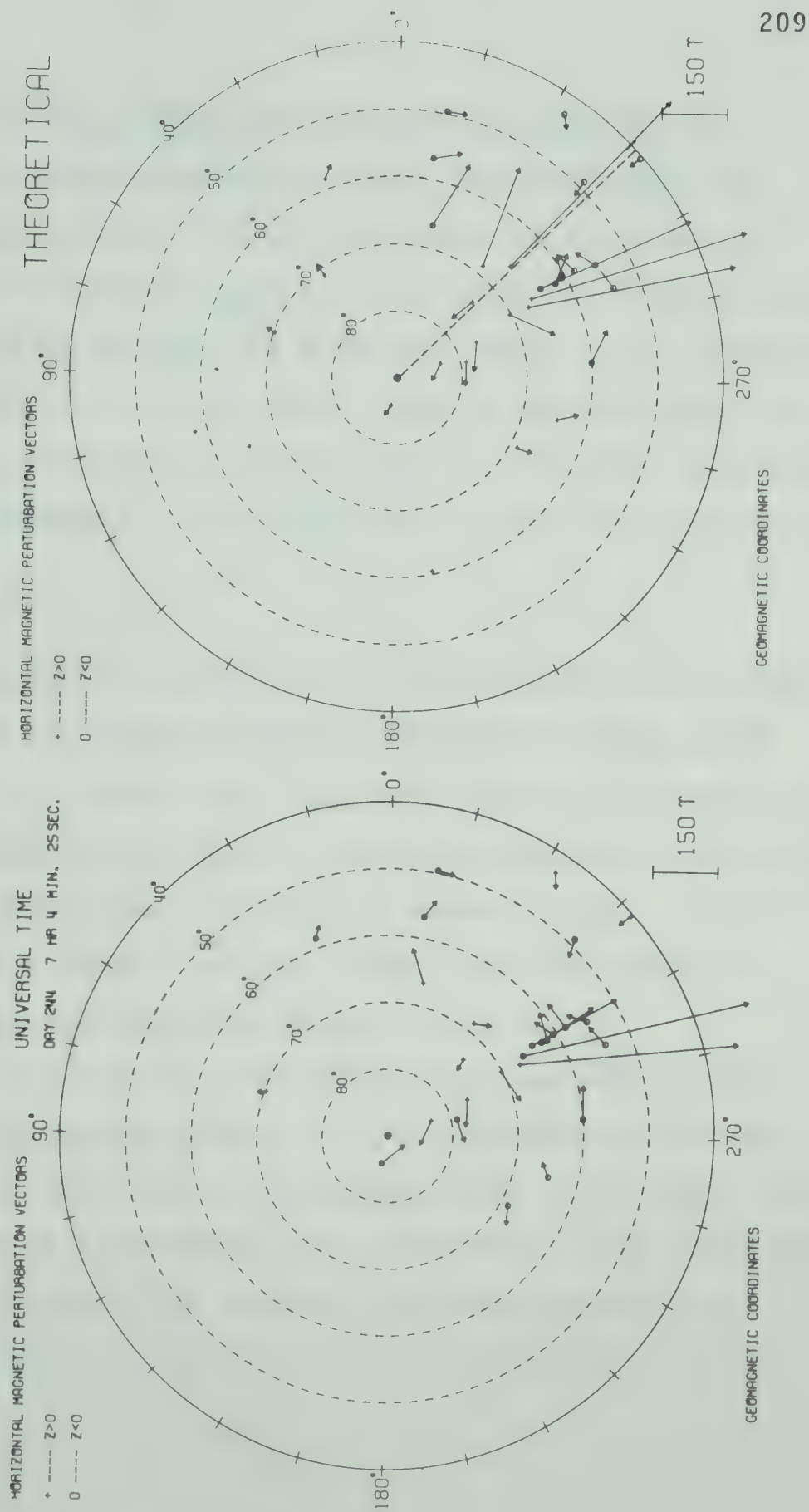


Fig. 6.7 Same as Fig. 6.6 but for Day 244 at \sim 0704 UT.

account for the disagreement between the observed and theoretical perturbation vectors in these regions. The polar plots shown in Fig. 6.7 are remarkably similar, even in the polar cap region (except ALER which is extremely anomalous (see Whitham and Andersen, 1962)). The substantial disagreement for some stations close to the electrojet can easily be reconciled by the fact that latitudinal gradients of the H component in this particular regime are extremely large.

6.4 Model current system to explain the magnetic perturbations associated with E-W propagating auroral forms

In Chapter V we presented examples of differential profiles showing the magnetic perturbations associated with eastward and westward propagating auroral forms. In this section we present a current system that could possibly explain the observed perturbation patterns.

A series of three-dimensional current configurations are presented in Fig. 6.8 to illustrate the changes that likely take place during the passage of an auroral form. Configuration A represents the unperturbed system and D the perturbed system. The southward directed current (i_2) indicates the location of the N-S aligned portion of the

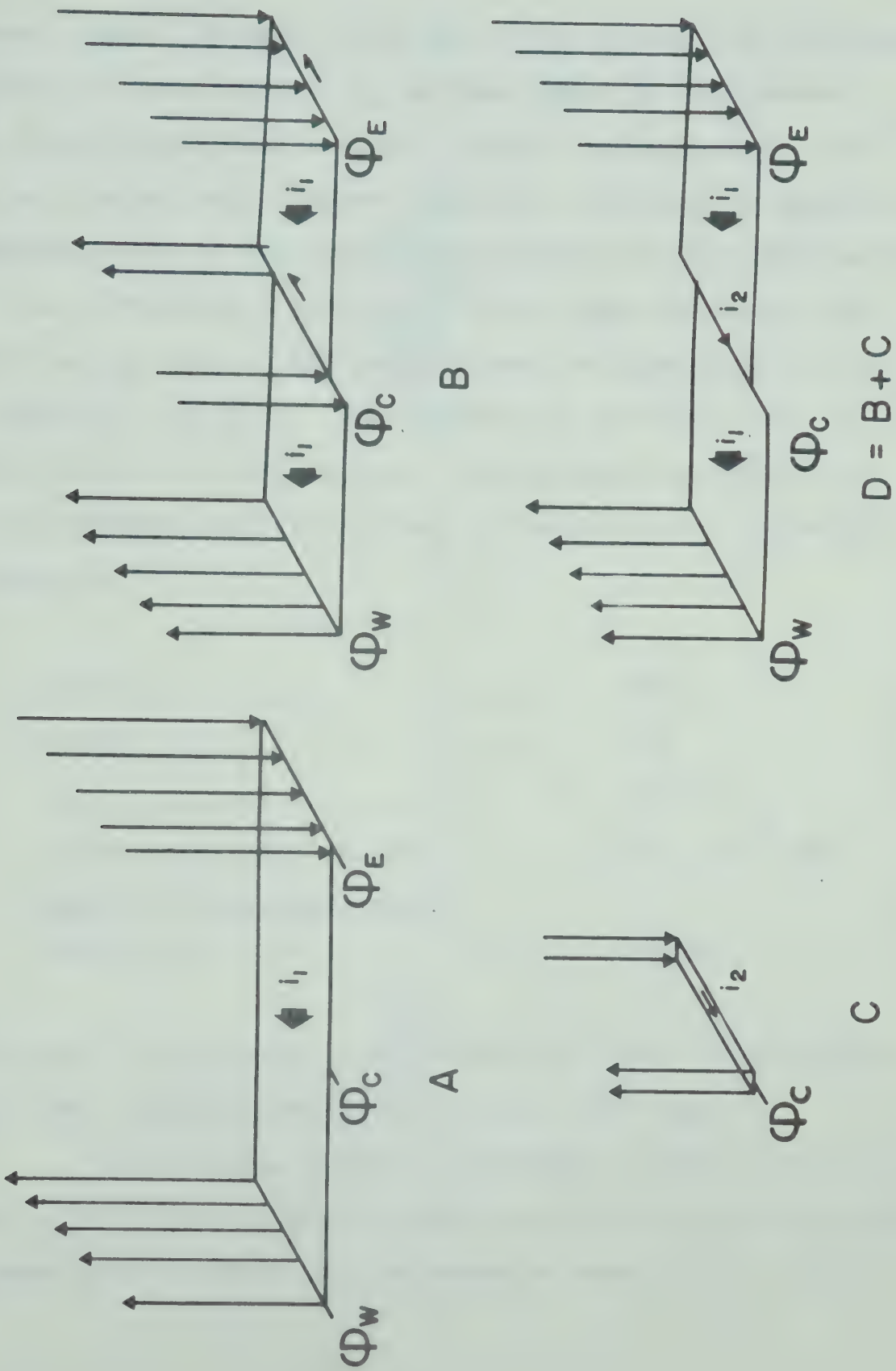


Fig. 6.8 Proposed model for the perturbation of the westward electrojet due to the passage of an auroral form.

auroral form. To model this particular system, we introduce a shear of A to produce B. We then add B to the narrow N-S three-dimensional current system C to produce D. We are not suggesting, however, that this sequence is necessarily representative of the dynamic development of the configuration D. The differential profile (D-A) as observed along the meridian ϕ_C due to the change from configuration A to D, is shown in Fig. 6.9. The differential profile (B-A) is also included in this figure. The original system (A) is a three-dimensional E-W current system with the following parameters:

Length	40°
Width	5°
θ_C	67.5°
Total integrated current	1.0×10^6 amp
Depth of superconductive layer	250 km

The shear is along the central meridian with a 1° displacement; thus the N-S current (C) is 0.2×10^6 amp.

Although we have not attempted to model a specific event, it is interesting to note the similarities that exist between profile (D-A) and the example shown in Fig. 5.23.

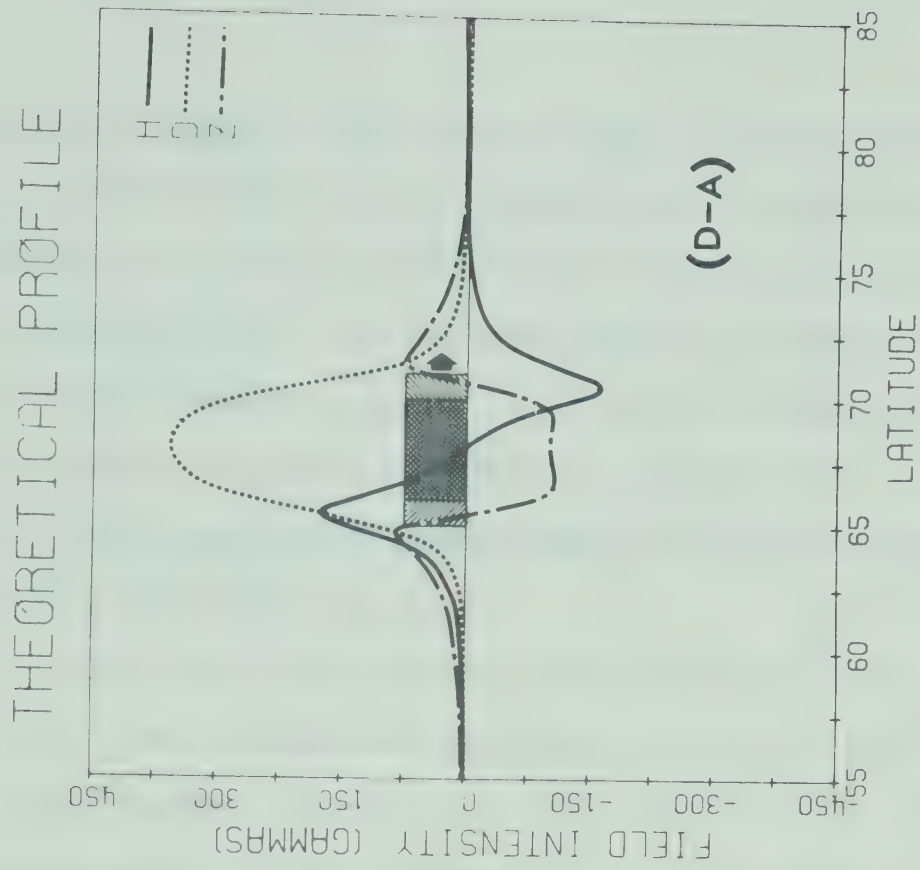
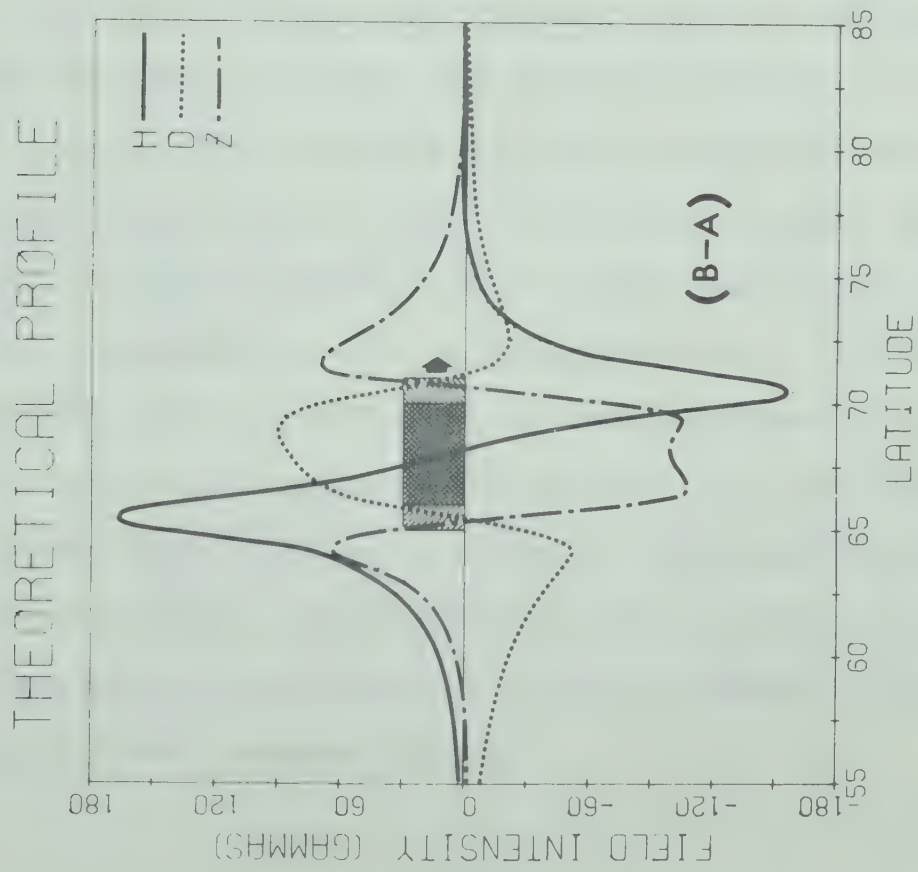


Fig. 6.9 Differential profiles for the system of currents shown in Fig. 6.8.

This particular model could also be used to explain the magnetic perturbations due to the westward travelling surge. For example the current configuration D may develop along with an enhancement of the northern border of the eastern portion of the sheared system. This could be associated with outward flowing Birkeland currents at the northern border near the shear zone (ϕ_C) and an enhancement of inward flowing currents near the meridian (ϕ_E).

Other possible current configurations which should be considered when modelling perturbations of current systems in the polar region are shown in Fig. 6.10. For a N-S three-dimensional current system 60° in length and 4° in width with a total integrated current of 2.0×10^6 amp, the observed perturbation along the central meridian is shown in Fig. 6.11 by the D profile in each latitude profile. The H and Z components of the field are zero along this meridian. If we introduce a shear along the central meridian, the H and Z components will no longer be zero. The latitude profiles for the four different current configurations in Fig. 6.10 are shown respectively in Fig. 6.11 (no induction field is included in these profiles). From these profiles we see that apparent enhancements of both eastward and westward electrojets could possibly be due to shears of N-S three-dimensional current systems.

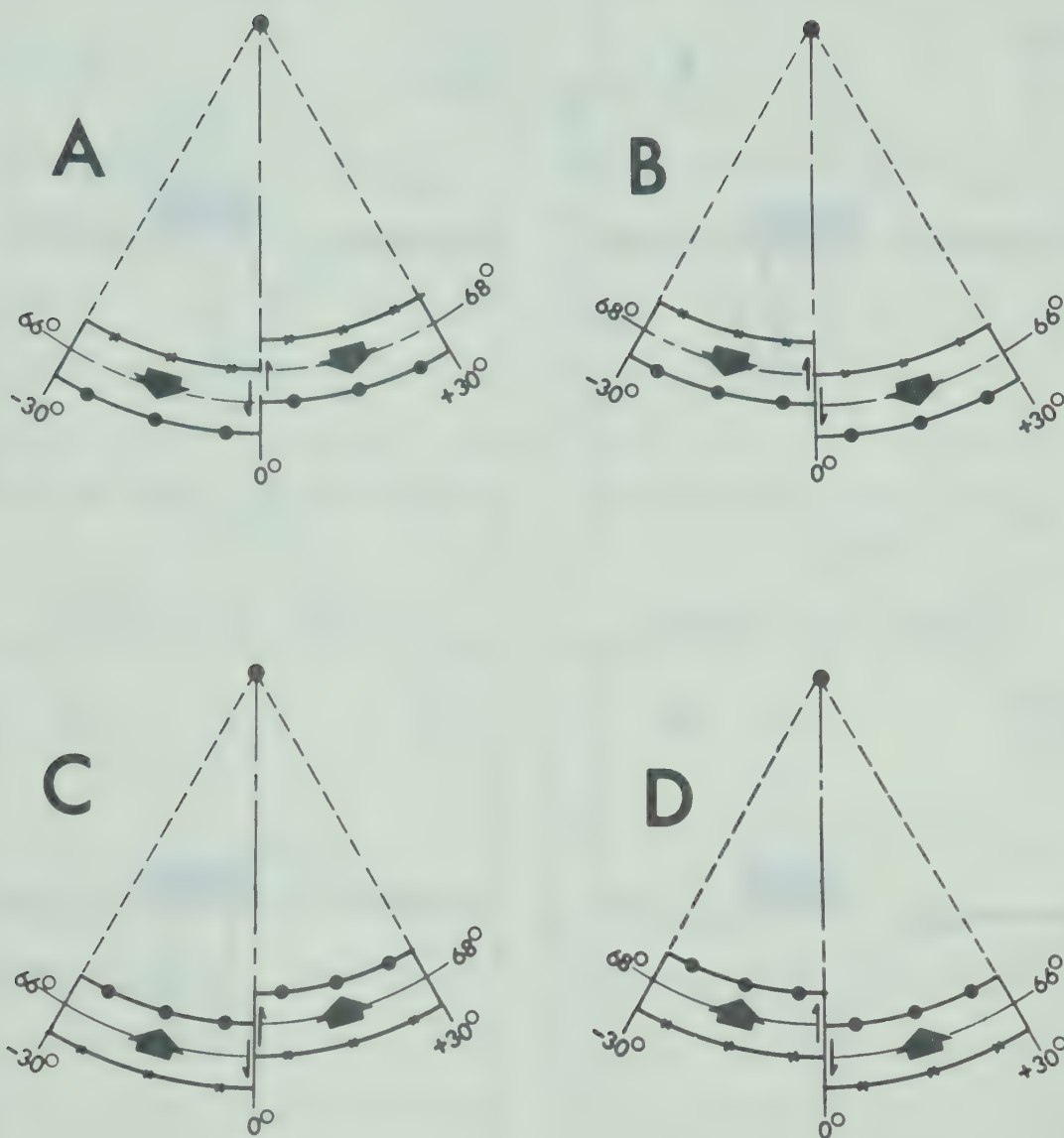


Fig. 6.10 Proposed shears of N-S three-dimensional current systems.

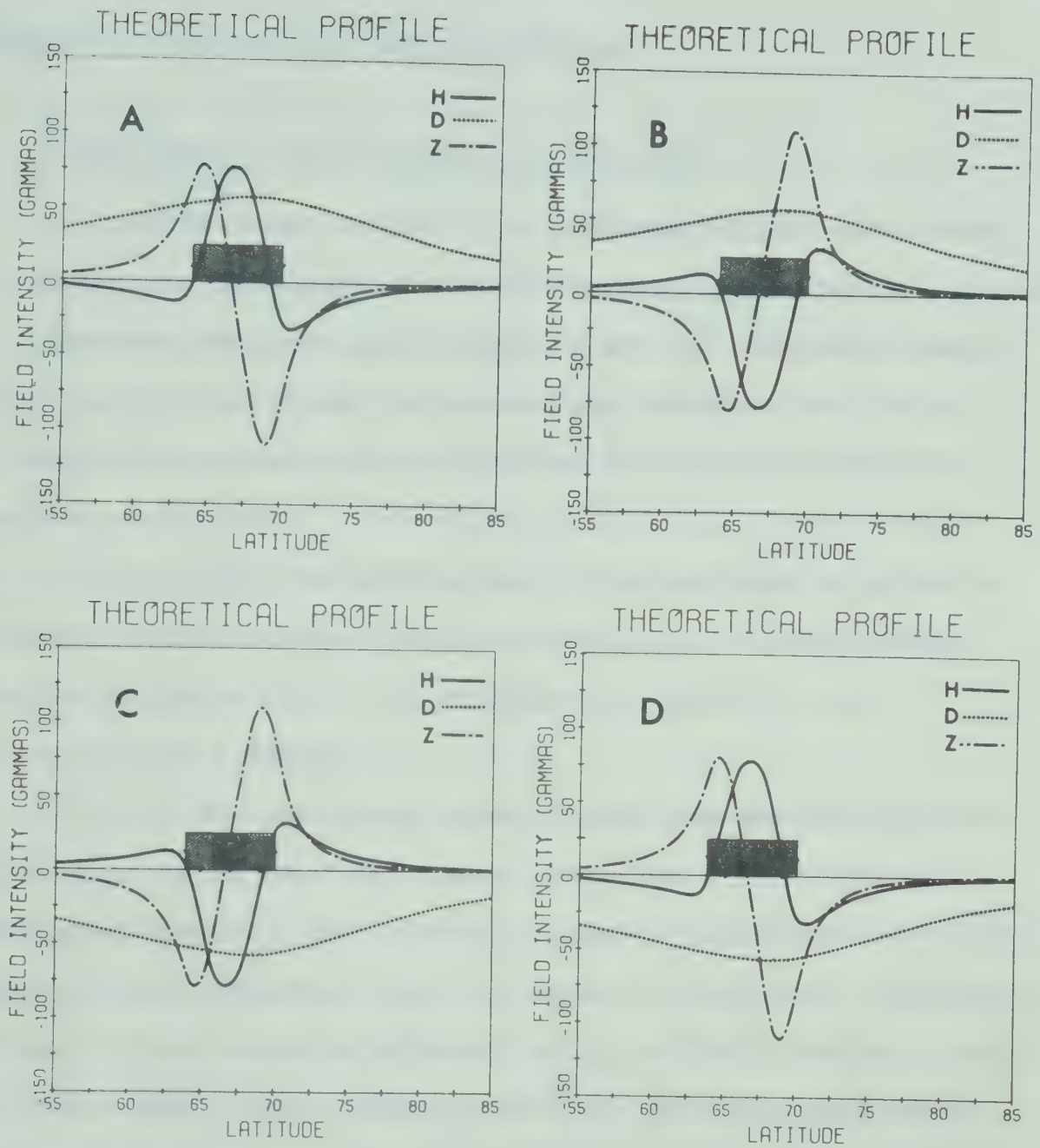


Fig. 6.11 Perturbations associated with the sheared current systems shown in Fig. 6.10. The D component profiles represent the field before introducing the shear.

CHAPTER VII DISCUSSION AND CONCLUSIONS

7.1 Morphology of polar magnetic substorms

In Chapters IV and V we presented a detailed study of the dynamic development of polar magnetic substorms. Using the framework proposed by Akasofu (1964) for the development of the auroral substorm, we now present what we feel to be the important morphological features of the polar magnetic substorm as follows:

(i) The intensification of the westward electrojet near the southern border of the auroral oval is coincident with the brightening of the southernmost auroral arcs (expansive phase Stage I).

(ii) The northward expansion of the northern border of the electrojet may take place in either a continuous or 'step-like' manner. During this poleward expansion the southern border of the electrojet usually remains relatively stationary although it may advance poleward with a velocity which is much less than that of the northern border. This development of the electrojet is associated with the expansive phase Stage II.

(iii) An intense enhancement of the current flow at the northern border of the electrojet along with the development of a +D component regime which is confined in both latitudinal and

longitudinal extent. This occurs in conjunction with the westward travelling surge during expansive phase Stage III. The +D component regime is believed to be caused by a north-to-south current flow in the region of the surge.

(iv) Associated with the recovery phase Stage I, minor quasi-periodic intensifications of the northern border of the electrojet occur in conjunction with eastward and westward propagating auroral forms such as loops and irregular folds. These intensifications can also occur at other latitudinal positions and are responsible for the variations in electrojet intensity pointed out by Kamide et al. (1969).

(v) Equatorward motion of the moment of the electrojet due for the most part to the decay of the current system at the northern border. This is associated with the equatorward drift of the auroral arcs during the recovery phase (Stages II and III).

The observed pattern of substorm development discussed above leads us to the following suggestions regarding the morphology of the polar magnetic substorm.

We first note that the poleward motion of the electrojet may occur in "discontinuous" steps. Such a pattern of development has recently

been suggested by Hones et al. (1972). That is, rather than having the main electrojet expand northward, new current elements may suddenly appear to the north of the moment of the main electrojet. Thus the description of poleward expansion by Akasofu et al. (1966b) must be treated with discretion in that it implies that the motion is continuous.

We have found that the first major enhancement of the northern border of the electrojet is associated with the generation of the westward travelling surge. The large positive D perturbation associated with this intensification is easily identifiable on normal magnetograms, and hence can be used to identify the presence of westward travelling surges.

The development of the westward surge (expansive phase Stage III) marks the onset of an interval of quasi-periodic intensifications of the northern border of the electrojet (recovery phase Stage I). The morphology of all these northern border disturbances seems very similar, so that we feel that expansive phase Stage III and recovery phase Stage I are part of the same process and should be combined under a common phase. We have suggested (Kisabeth and Rostoker, 1971) that this phase involves the direct input of energy from the magnetotail in impulsive bursts.

Finally we note that the main electrojet is often very stable during the period of northern border activity following the initial poleward expansion. Therefore we suggest that this electrojet is driven by a different source mechanism than the northern border activity.

It should be noted that this pattern of development of the westward electrojet is supported by the theoretical studies of Coroniti and Kennel (1972) who claimed that the onset of substorm activity was initiated through resistive instabilities at the inner edge of the plasma sheet which maps to the equatorward edge of the oval.

The development of magnetospheric substorm activity appears to be associated with the growth of an eastward electrojet in the post-noon and evening sector. This eastward electrojet can be very broad and stable, even during periods of substorm activity (see Rostoker, 1972). However, we have shown in Chapter IV that marked intensifications of the eastward electrojet may occur in conjunction with the onset of substorm activity. Therefore we feel that the eastward electrojet does respond to substorm fluctuations, although

it is not presently possible to evaluate quantitatively the level of response. We do feel, however, that this indicates that a single three-dimensional current system such as that proposed by Akasofu and Meng (1969) and Bonnevier et al. (1970) is insufficient to describe the overall substorm perturbation pattern. It is probable that the combination current system described in Chapter IV (see Fig. 4.1) coupled with a realistic polar cap current system (or equivalent field aligned current flow) will eventually be necessary to completely describe the observed perturbation pattern.

Finally we wish to point out that this study has emphasized how difficult it is to define the onset time of substorms from normal magnetograms only. In many cases, a strong perturbation associated with a northern border intensification in the middle of a substorm event, appeared as an "isolated" substorm onset at auroral zone stations far from the intensified portion of the auroral electrojet. The localized character of many of the substorm perturbations confirms the observation by Rostoker and Camidge (1972) that azimuthally confined sectors of the magnetotail may be sequentially activated thus generating the quasi-periodic activity at the northern border of the electrojet.

7.2 The modelling of polar magnetic substorm current systems

In modelling the polar electrojet, we have found it necessary to develop much more sophisticated models than have been presented by other workers (eg. Akasofu and Meng, 1969; Bonnevier et al., 1970; Kamide and Fukushima, 1971). In particular we have included the following variable parameters in our model current systems:

(i) A finite length and width of the ionospheric part of the current system.

(ii) Asymmetric flow of Birkeland currents along the length of the electrojet.

(iii) Combination current systems involving both eastward and westward electrojets.

(iv) Various latitudinal current distributions.

(v) Flow of current along the auroral oval.

(vi) The effects of induced currents in the Earth.

We have found that the variation of these parameters can significantly alter the computed perturbation pattern along a geomagnetic meridian for the three-dimensional system. To provide more information as to what these parameters should be, we used supporting data from the world wide network of observatories as well as all-sky camera data.

The examples of the modelling of substorm associated current systems given in Chapter VI clearly demonstrate the viability of our modelling techniques. It should be emphasized that the three-dimensional models we use represent only 'equivalent' current systems and should be treated as such.

Our study of induction effects substantiates the findings of Bonnevier et al. (1970) who concluded that the practice of correcting the observed components by constant factors ($2/3$ for H and 2 for Z) can not be used in studying localized currents such as the polar electrojets. Therefore, the importance of including the effects of induction in any model studies cannot be emphasized enough. For example Kamide (1970) presented variations of a model current system which included ionospheric return currents rather than field-aligned currents in order to explain the observations of Walker (1964) and Bonnevier et al. (1970). If the effects of induction had been included in this model system, the relative strengths of the H and Z components would have been unrealistic.

Finally, until now the expense of evaluating the magnetic effects associated with complex current systems has been insurmountable. Since the techniques developed in

this thesis allow such evaluations to be done with relatively small amounts of computer time, we feel that these techniques can be incorporated into any routine data analysis.

7.3 Techniques of presentation of polar magnetic substorm data

Throughout the course of this study, the various techniques of data analysis and presentation were utilized (see Chapter III, section 3.3). In this section we present a brief summary of the attributes of each method.

(i) Latitude profile: This method is very useful in providing a comprehensive picture of the distribution of the current in the westward electrojet at any instant during a substorm. A cursory examination of a profile can give considerable information about the position of the station line relative to the ionospheric portion of the current system, as well as a good quantitative estimate of the strength of the substorm. However all information about the temporal development of the substorm, as well as the longitudinal variation of the current system, is lost in this presentation.

(ii) **Polar Plots:** This commonly used technique was modified to incorporate some Z component information and the auroral oval contour as a reference frame in which to view the data. Polar plots are particularly useful to gain a semi-quantitative idea of the world wide character of the substorm perturbation pattern at a given instant in time, along with some indication of the azimuthal extent of the intensified portion of the electrojet. Quantitative information regarding the Z component perturbation is lost; however, our modification allowed changes in Z component polarity to be traced, yielding information on the position of the moment of the current system. As in the case of the latitude profile, information regarding the temporal development of the substorm current system is lost.

(iii) **Component Contour Diagrams:** This technique, developed by Zaitzev and Boström (1971), is very useful in tracing the temporal development of the substorm. Information is presented showing the motion of the moment of the current system, and its latitudinal expansion and contraction. Quantitative information regarding the strength of each component is readily available, and polarity changes are well portrayed. The information missing in this format is the instantaneous world wide character of the substorm current

system. The method is also cumbersome in that it requires three separate diagrams (one for each component) to transfer the information completely.

(iv) Three-dimensional diagrams: This technique is excellent in its ability to portray, using the technique of perspective viewing, the temporal development of a polar magnetic substorm. It is particularly useful in illustrating the changes in the latitudinal current distribution during the course of the substorm as well as effectively presenting qualitative information on the variations in the strength of the substorm current system. Once again, information is lost in the world wide character of the substorm current system, and the method is cumbersome in that it requires three separate diagrams to transfer the information completely.

From our study, we have concluded that no one method of data presentation adequately describes the character of the development of the polar magnetic substorm current system. Future studies should involve a combination of the techniques discussed above in order to yield complete information on the character of the substorms under study.

REFERENCES

- Abramowitz, M. and I. A. Stegun, *Handbook of Mathematical Functions*, Dover Publications, Inc., New York, 1965.
- Akasofu, S. -I., The development of the auroral substorm, *Planet. Space Sci.* 12, 273, 1964.
- Akasofu, S. -I., *Polar and Magnetospheric Substorms*, D. Reidel Publications Co., Dordrecht, Holland, 1968.
- Akasofu, S. -I., S. Chapman and C. -I. Meng, The polar electrojet, *J. Atmospheric Terrest. Phys.* 30, 227, 1965.
- Akasofu, S. -I., S. Chapman and A. B. Meinel, *The Aurora Handbuch der Physik* 49, p. 1, Springer-Verlag, New York, 1966.
- Akasofu, S. -I., D. S. Kimball and C. -I. Meng, Dynamics of the Aurora - V Poleward motions, *J. Atmospheric Terrest. Phys.* 28, 497, 1966a.
- Akasofu, S. -I., D. S. Kimball and C. -I. Meng, Dynamics of the Aurora - VII: Equatorward motions and the multiplicity of auroral arcs, *J. Atmospheric Terrest. Phys.* 28, 627, 1966b.
- Akasofu, S. -I. and C. -I. Meng, A study of polar magnetic substorms, *J. Geophys. Res.* 74, 293, 1969.
- Akasofu, S. -I., C. R. Wilson, A. L. Snyder and P. D. Perreault, Results from a meridian chain of observatories in the Alaskan sector, 1, *Planet. Space Sci.* 19, 477, 1971.
- Akasofu, S. -I. and A. L. Snyder, Comments on the growth phase of magnetospheric substorms, *J. Geophys. Res.* 77, in press, 1972.
- Alfvén, H. and C. -G. Fälthammar, *Cosmic Electrodynamics*, p. 161, Oxford University Press, 1963.

- Alpaslan, T., Spectral behavior of short period body waves and the synthesis of crustal structure in western Canada, M.Sc. Thesis, Edmonton, Department of Physics, University of Alberta, 1978.
- Armstrong, J. C. and A. J. Zmuda, Field-aligned current at 1100 km in the auroral region measured by satellite, *J. Geophys. Res.* 75, 7122, 1970.
- Ashour, A. A., The evaluation of the field of the currents induced in the Earth by an external field whose distribution is known numerically, *Radio Sci.* 6, 171, 1971.
- Atkinson, G., A theory of polar substorms, *J. Geophys. Res.* 71, 5157, 1966.
- Atkinson, G., The current system of geomagnetic bays, *J. Geophys. Res.* 72, 6063, 1967.
- Axford, W. I. and C. O. Hines, A unifying theory of high-latitude geophysical phenomena and geomagnetic storms, *Can. J. Phys.* 39, 1433, 1961.
- Birkeland, K., *The Norwegian Aurora Polaris Expedition 1902-1903*, vol. 1, 1st sec., Aschhoug and Co., Christiania, 1908.
- Birkeland, K., *The Norwegian Polaris Expedition 1902-1903*, vol. 1, 2nd sec., Aschhoug and Co., Christiania, 1913.
- Block, L. P., Coupling between the outer magnetosphere and the high-latitude ionosphere, *Space Sci. Rev.* 7, 198, 1967.
- Bonnevier, B., R. Boström and G. Rostoker, A three-dimensional model current system for polar magnetic substorms, *J. Geophys. Res.* 75, 107, 1970.
- Boström, R., A model of the auroral electrojets, *J. Geophys. Res.* 69, 4983, 1964.
- Boström, R., Currents in the ionosphere and magnetosphere, *Ann. Geophys.* 24, 681, 1968.

- Boström, R., The magnetic field of three-dimensional magnetospheric model current systems and currents induced in the ground, *Acta Poly. Scand.* 77, 1, 1971.
- Chapman, S., The electric current systems of magnetic storms, *Terrest. Magnetism and Atmospheric Elec.* 40, 349, 1935.
- Chapman, S., Historical introduction to aurora and magnetic storms, *Ann. Géophys.* 24, 21, 1968.
- Cloutier, P. A., Ionospheric effects of Birkeland currents, *Rev. Geophys. & Space Phys.* 9, 987, 1971.
- Comfort, R. H., Empirical analytic transformations between geographic and corrected geomagnetic coordinates, *NASA George C. Marshall Space Flight Center Rept. M-793-765*, July, 1970.
- Coroniti, F. V. and C. F. Kennel, Polarization of the auroral electrojet, *J. Geophys. Res.* 77, 2835, 1972.
- Cummings, W. D., Asymmetric ring currents and the low latitude disturbance daily variation, *J. Geophys. Res.* 71, 4495, 1966.
- Cummings, W. D. and A. J. Dessler, Field-aligned currents in the magnetosphere, *J. Geophys. Res.* 72, 1007, 1967.
- Czechowsky, P., Calculation of an equivalent current system in the polar E-region, *Radio Sci.* 6, 247, 1971.
- Dessler, A. J., Magnetic merging in the magnetospheric tail, *J. Geophys. Res.* 73, 209, 1968.
- Dungey, J. W., Interplanetary magnetic field and the auroral zones, *Phys. Rev. Letters* 6, 47, 1961.
- Feldstein, Y. I., Some problems concerning the morphology of auroras and magnetic disturbances at high latitudes, *Geomagnetizm i Aeronomiya* 3, 183, 1963.

- Feldstein, Y. I., Auroras and associated phenomena, *Solar-Terrestrial Physics 1970: Part III*, p. 152, ed. E. R. Dyer, D. Reidel Publications Co., Dordrecht, Holland, 1972.
- Feldstein, Y. I. and A. N. Zaitzev, Quiet and disturbed solar-daily variations of magnetic field at high latitudes during the IGY, *Tellus* 20, 338, 1968.
- Forbush, S. E. and M. Casaverde, *Equatorial Electrojet in Peru*, Dept. of Terres. Magn., Carnegie Inst. Washington Publication 620, 1961.
- Frank, L. A., Comments on a proposed magnetospheric model, *J. Geophys. Res.* 76, 2512, 1971.
- Fukushima, N., Polar magnetic storms and geomagnetic bays, *J. Fac. Sci., Tokyo Univ.*, 8, 293, 1953.
- Hakura, Y., Tables and maps of geomagnetic coordinates corrected by the higher order spherical harmonic terms, *Rep. Ionos. Space Res., Japan*, 19, 121, 1965.
- Heppner, J. P., Time sequences and spatial relations in auroral activity during magnetic bays at College, Alaska, *J. Geophys. Res.* 59, 329, 1954.
- Hones, E. W., Jr., J. R. Asbridge, S. J. Bame and S. Singer, Substorm variations of the magnetotail plasma sheet from $X_{SM} \approx -6 R_E$ to $X_{SM} \approx -60 R_E$, *J. Geophys. Res.*, in press, 1972.
- Kamide, Y., Spatial extent of the return current of the auroral zone electrojet, Part III, *Rep. Ionos. Space Res., Japan*, 24, 347, 1970.
- Kamide, Y., T. Iijima and N. Fukushima, Microstructure of auroral-zone electrojet, *Rep. Ionos. Space Res., Japan*, 23, 185, 1969.
- Kamide, Y. and N. Fukushima, Spatial extent of the return current of the auroral-zone electrojet, Part II, *Rep. Ionos. Space Res., Japan*, 24, 115, 1970.

- Kamide, Y. and N. Fukushima, Analysis of magnetic storms with DR-indices for equatorial ring current field, *Rep. Ionos. Space Res., Japan*, 25, 125, 1971.
- Kawasaki, K. and S. -I. Akasofu, The computed distribution of geomagnetic disturbance vectors for model three-dimensional current systems, *J. Atmospheric Terrest. Phys.* 19, 543, 1971.
- Kirkpatrick, C. B., On current system proposed for S_p in the theory of magnetic storms, *J. Geophys. Res.* 57, 511, 1952.
- Kisabeth, J. L. and G. Rostoker, Development of the polar electrojet during polar magnetic substorms, *J. Geophys. Res.* 76, 6815, 1971.
- Langel, R. A. and J. C. Cain,OGO-2 magnetic field observations during the magnetic storm of March 13-15, 1966, 2, The polar electrojet, *Rep. X-612-67-473, Goddard Space Flight Center, Greenbelt, Maryland*, 1967.
- McNish, A. G., Heights of electric currents near the auroral zone, *Terrest. Magnetism and Atmospheric Elec.* 43, 67, 1938.
- McPherron, R. L., Growth phase of magnetospheric substorms, *J. Geophys. Res.* 75, 5592, 1970.
- Maggs, J. E. and T. N. Davis, Measurements of the thicknesses of auroral structures, *Planet. Space Sci.* 16, 205, 1968.
- Meng, C. -I. and S. -I. Akasofu, A study of polar magnetic substorms, 2, three-dimensional current system, *J. Geophys. Res.* 74, 4035, 1969.
- Mozer, F. S., Origin and effects of electric fields during isolated magnetospheric substorms, *J. Geophys. Res.* 76, 7595, 1971.

- Nishida, A. and S. Kokubun, New polar magnetic disturbances: S_q^P , SP, DPC and DP2, *Rev. Geophys. & Space Phys.* **9**, 417, 1971.
- Park, R. J. and P. A. Cloutier, Rocket-based measurements of Birkeland currents related to an auroral arc and electrojet, *J. Geophys. Res.* **76**, 7714, 1971.
- Silsbee, H. C. and E. H. Vestine, Geomagnetic bays, their occurrence frequency and current systems, *Terrest. Magnetism Atmospheric Elec.* **47**, 195, 1942.
- Ralston, A., *A First Course in Numerical Analysis*, p. 76, McGraw-Hill Book Company, New York, 1965.
- Rikitake, T., *Electromagnetism and the Earth's Interior*, Elsevier Publication Co., New York, 1966.
- Rostoker, G., Polar magnetic substorms, *Rev. Geophys. & Space Phys.* **10**, 157, 1972.
- Rostoker, G. and F. P. Camidge, The localized character of magnetotail magnetic fluctuations during polar magnetic substorms, *J. Geophys. Res.* **76**, 6944, 1971.
- Snyder, A. L. and S. -I. Akasofu, Observations of the auroral oval by the Alaskan meridian chain of stations, *J. Geophys. Res.* **77**, 3419, 1972.
- Stratton, J. A., *Electromagnetic Theory*, p. 486, McGraw-Hill Book Company, New York, 1941.
- Subbarao, S. and G. Rostoker, The relationships of southward drifting auroral arcs to the magnetospheric electric field and substorm activity, *J. Geophys. Res.*, submitted for publication, 1972.
- Trigg, D. F., P. H. Serson and P. A. Camfield, A solid-state electrical recording magnetometer, Preprint, Earth Physics Branch, Dept. Energy, Mines and Resources, Ottawa, Canada, 1970.

- Vestine, E. H. and S. Chapman, The electric current system of geomagnetic disturbance, *Terrest. Magnetism Atmospheric Elec.* 43, 351, 1938.
- Vondrak, R. R., H. R. Anderson and R. J. Spiger, Rocket-based measurement of particle fluxes and current in an auroral arc, *J. Geophys. Res.* 76, 7701, 1971.
- Walker, J. K. Space-time associations of the aurora and magnetic disturbance, *J. Atmospheric Terrest. Phys.* 26, 951, 1964.
- Whalen, J. A., Auroral oval plotter and nomograph for determining corrected geomagnetic local time, latitude and longitude for high latitudes in the northern hemisphere, *Air Force Cambridge Research Laboratories*, Bedford, Massachusetts, 1970.
- Whitham, K. and F. Anderson, The anomaly in geomagnetic variations at Alert in the Arctic Archipelago of Canada, *Geophys. J.* 7, 220, 1963.
- Zaitzev, A. N. and R. Boström, On methods of graphical displaying of polar magnetic disturbances, *Planet. Space Sci.* 19, 643, 1971.

APPENDIX A1 METHODS OF EVALUATING THE MAGNETIC FIELD PERTURBATIONS OF MODEL CURRENT SYSTEMS

A1.1 Method using Biot-Savart's law

In this section we apply Biot-Savart's law in spherical coordinates to an arbitrary current loop c external to the Earth's surface (See Fig. A1.1). The result of this application is in the form of an integral of a simple third order matrix which is easily applied to an arbitrary three-dimensional current system in the magnetosphere.

The differential magnetic field vector $d\vec{B}$ at the observation position (r_o, θ_o, ϕ_o) due to an elemental current vector $Jd\vec{s}$ is given by Biot-Savart's law

$$d\vec{B} = k J \frac{d\vec{s} \times \vec{R}}{|\vec{R}|^3} \quad (A1.1)$$

where

$$\vec{R} = \vec{r}_o - \vec{r} \quad (A1.2)$$

and k is the proportionality factor dependent upon the system of units used. The field vector $d\vec{B}$ can be

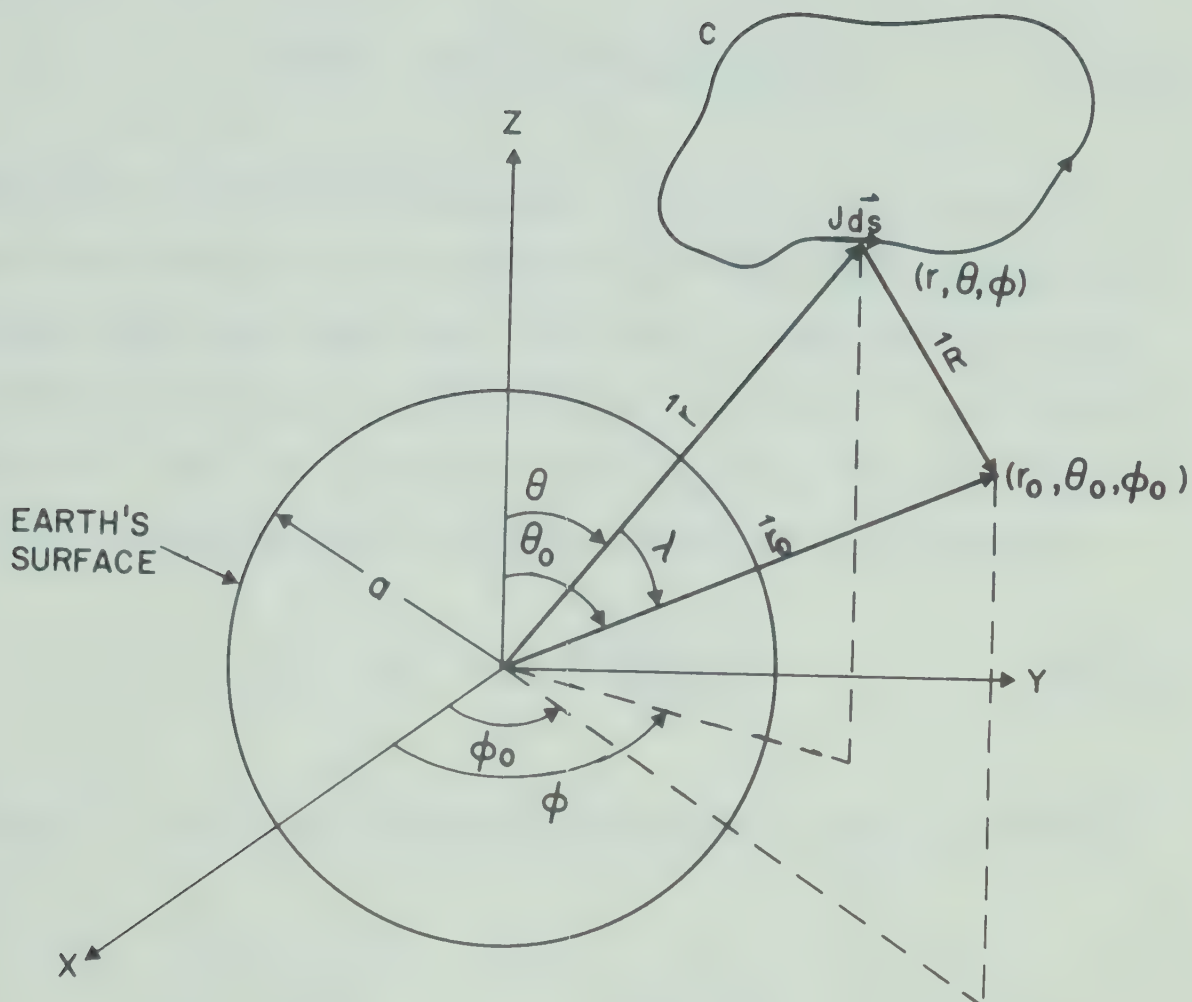


Fig. A1.1 Diagram defining vectors in spherical coordinates for magnetic field calculations.

written in component form as

$$d\vec{B} = dB_1 \hat{r}_0 + dB_2 \hat{\theta}_0 + dB_3 \hat{\phi}_0 \quad (A1.3)$$

Since the coordinate directions $(\hat{r}, \hat{\theta}, \hat{\phi})$ at the source position differ from the coordinate directions $(\hat{r}_0, \hat{\theta}_0, \hat{\phi}_0)$ at the observing position, $d\vec{s}$ and \vec{R} must be expressed in terms of $(\hat{r}_0, \hat{\theta}_0, \hat{\phi}_0)$ for A1.3 to be valid. If we express both $d\vec{s}$ and \vec{R} in terms of $(\hat{r}, \hat{\theta}, \hat{\phi})$ then the right hand side of equation (A1.1) must be transformed as follows:

$$d\vec{B} = k \tilde{A} \frac{\vec{J} d\vec{s} \times \vec{R}}{|\vec{R}|^3} \quad (A1.4)$$

where \tilde{A} is the orthogonal transformation matrix defined by

$$\begin{bmatrix} \hat{r}_0 \\ \hat{\theta}_0 \\ \hat{\phi}_0 \end{bmatrix} = \tilde{A} \begin{bmatrix} \hat{r} \\ \hat{\theta} \\ \hat{\phi} \end{bmatrix} \quad (A1.5)$$

In the present derivation we express $d\vec{s}$ and \vec{R} in terms of

$(\hat{r}_0, \hat{\theta}_0, \hat{\phi}_0)$ rather than transforming the resultant cross-product as illustrated in A1.4. To accomplish this we must still make use of the transformation matrix \tilde{A} .

We can derive \tilde{A} by making a series of two coordinate transformations; a transformation from (r, θ, ϕ) coordinates to (x, y, z) coordinates followed by a transformation from (x, y, z) coordinates to (r_0, θ_0, ϕ_0) coordinates. The first transformation is given by

$$\begin{bmatrix} \hat{x} \\ \hat{y} \\ \hat{z} \end{bmatrix} = \tilde{S}_1 \begin{bmatrix} \hat{r} \\ \hat{\theta} \\ \hat{\phi} \end{bmatrix} \quad (\text{A1.6})$$

where

$$S_1 = \begin{bmatrix} \sin \theta \cos \phi & \cos \theta \cos \phi & -\sin \phi \\ \sin \theta \sin \phi & \cos \theta \sin \phi & \cos \phi \\ \cos \theta & -\sin \theta & 0 \end{bmatrix} \quad (\text{A1.7})$$

and the second transformation by

$$\begin{bmatrix} \hat{r}_0 \\ \hat{\theta}_0 \\ \hat{\phi}_0 \end{bmatrix} = \tilde{S}_2 \begin{bmatrix} \hat{x} \\ \hat{y} \\ \hat{z} \end{bmatrix} \quad (\text{A1.8})$$

where

$$S_2 = \begin{bmatrix} \sin \theta_0 \cos \phi_0 & \sin \theta_0 \sin \phi_0 & \cos \theta_0 \\ \cos \theta_0 \cos \phi_0 & \cos \theta_0 \sin \phi_0 & -\sin \theta_0 \\ -\sin \phi_0 & \cos \phi_0 & 0 \end{bmatrix} \quad (\text{A1.9})$$

From A1.5, A1.6 and A1.8 we obtain

$$\begin{bmatrix} \hat{r}_0 \\ \hat{\theta}_0 \\ \hat{\phi}_0 \end{bmatrix} = \tilde{S}_2 \tilde{S}_1 \begin{bmatrix} \hat{r} \\ \hat{\theta} \\ \hat{\phi} \end{bmatrix} \quad (\text{A1.10})$$

$$= \tilde{A} \begin{bmatrix} \hat{r} \\ \hat{\theta} \\ \hat{\phi} \end{bmatrix}$$

Therefore \tilde{A} is given by

$$\tilde{A} = \begin{bmatrix} A_{11} & A_{12} & A_{13} \\ A_{21} & A_{22} & A_{23} \\ A_{31} & A_{32} & A_{33} \end{bmatrix} \quad (A1.11)$$

where

$$A_{11} = \sin \theta_0 \sin \theta \cos (\phi_0 - \phi) + \cos \theta_0 \cos \theta$$

$$A_{12} = \sin \theta_0 \cos \theta \cos (\phi_0 - \phi) - \cos \theta_0 \sin \theta$$

$$A_{13} = \sin \theta_0 \sin (\phi_0 - \phi)$$

$$A_{21} = \cos \theta_0 \sin \theta \cos (\phi_0 - \phi) - \sin \theta_0 \cos \theta$$

$$A_{22} = \cos \theta_0 \cos \theta \cos (\phi_0 - \phi) + \sin \theta_0 \sin \theta$$

$$A_{23} = \cos \theta_0 \sin (\phi_0 - \phi)$$

$$A_{31} = -\sin \theta \sin (\phi_0 - \phi)$$

$$A_{32} = -\cos \theta \sin (\phi_0 - \phi)$$

$$A_{33} = \cos (\phi_0 - \phi) \quad (A1.12)$$

The vector \vec{R} can be expressed as

$$\vec{R} = R_1 \hat{r}_0 + R_2 \hat{\theta}_0 + R_3 \hat{\phi}_0 \quad (A1.13)$$

whereas the vector $d\vec{s}$ is generally expressed in terms of the source coordinate directions as

$$d\vec{s} = ds_1 \hat{r} + ds_2 \hat{\theta} + ds_3 \hat{\phi} \quad (A1.14)$$

Therefore, before the cross-product $(d\vec{s} \times \vec{R})$ can be evaluated, we must transform $d\vec{s}$ to the (r_0, θ_0, ϕ_0) coordinate system by the equation

$$d\vec{s} = [ds_1 \quad ds_2 \quad ds_3] \tilde{A}^T \begin{bmatrix} \hat{r}_0 \\ \hat{\theta}_0 \\ \hat{\phi} \end{bmatrix} \quad (A1.15)$$

where \tilde{A}^T is the transpose of \tilde{A} . Thus

$$\begin{aligned}
d\vec{s} = & (ds_1 A_{11} + ds_2 A_{12} + ds_3 A_{13}) \hat{r}_0 + \\
& + (ds_1 A_{21} + ds_2 A_{22} + ds_3 A_{23}) \hat{\theta}_0 + \\
& + (ds_1 A_{31} + ds_2 A_{32} + ds_3 A_{33}) \hat{\phi}_0
\end{aligned} \tag{A1.16}$$

The components R_1 , R_2 and R_3 in A1.13 can be derived by making use of \tilde{A}^T as follows:

$$\begin{aligned}
\vec{R} &= \vec{r}_0 - \vec{r} \\
&= [r_0 \quad 0 \quad 0] \begin{bmatrix} \hat{r}_0 \\ \hat{\theta}_0 \\ \hat{\phi}_0 \end{bmatrix} - [r \quad 0 \quad 0] \begin{bmatrix} \hat{r} \\ \hat{\theta} \\ \hat{\phi} \end{bmatrix} \\
&= [r_0 \quad 0 \quad 0] \begin{bmatrix} \hat{r}_0 \\ \hat{\theta}_0 \\ \hat{\phi}_0 \end{bmatrix} - [r \quad 0 \quad 0] \tilde{A}^T \begin{bmatrix} \hat{r}_0 \\ \hat{\theta}_0 \\ \hat{\phi}_0 \end{bmatrix}
\end{aligned}$$

$$= (r_0 - rA_{11} \quad -rA_{21} \quad -rA_{31}) \begin{bmatrix} \hat{r}_0 \\ \hat{\theta}_0 \\ \hat{\phi}_0 \end{bmatrix} \quad (\text{A1.17})$$

Hence,

$$R_1 = r_0 - rA_{11}$$

$$R_2 = -rA_{21}$$

$$R_3 = -rA_{31}$$

$$\begin{aligned} R &= |\vec{R}| = (R_1^2 + R_2^2 + R_3^2)^{\frac{1}{2}} \\ &= (r^2 + r_0^2 - 2rr_0A_{11})^{\frac{1}{2}} \end{aligned}$$

(A1.18)

Therefore, substituting A1.16 and A1.18 into A1.1, $d\vec{B}$ can be written in matrix form

$$d\vec{B} = k J d\tilde{c} \begin{bmatrix} \hat{r}_0 \\ \hat{\theta}_0 \\ \hat{\phi}_0 \end{bmatrix} \quad (A1.19)$$

where

$$d\tilde{c} = \frac{1}{R^3} \begin{bmatrix} 0 & r_0 A_{31} ds_1 & -r_0 A_{21} ds_1 \\ rA_{13} ds_2 & (rA_{23} + r_0 A_{32}) ds_2 & (rA_{33} - r_0 A_{22}) ds_2 \\ -rA_{12} ds_3 & (r_0 A_{33} - rA_{22}) ds_3 & -(r_0 A_{23} + rA_{32}) ds_3 \end{bmatrix} \quad (A1.20)$$

Using A1.3 and A1.19, the total contribution to the j^{th} field component at the observation position (r_0, θ_0, ϕ_0) due to a current loop c is simply

$$B_j(r_0, \theta_0, \phi_0) = kJ \int_c \sum_i d\tilde{c}_{ij} \quad (j = 1, 2, 3)$$

$$(A1.21)$$

A1.2 Method using infinitesimal magnetic dipoles

The specific problem of evaluating the scalar magnetic potential and thus the magnetic field due to three-dimensional current systems which include dipole field-aligned currents has been solved using infinitesimal magnetic dipoles (Boström, 1968; Bonnevier et al., 1970). In this section we give only a brief summary of their solution to the problem.

Bonnevier et al. (1970) considered the two current loops shown in Fig. A1.2 where field-aligned currents in both loops have infinitesimally small separation at the base of the ionosphere. Hence the ionospheric portion of the E-W and N-S loops have lengths of $r_1 \sin \theta_1 d\phi_1$ and $r_1 d\theta_1$ respectively. ((r_1, θ_1, ϕ_1) is the coordinate position of the endpoints of both loops in the ionosphere).

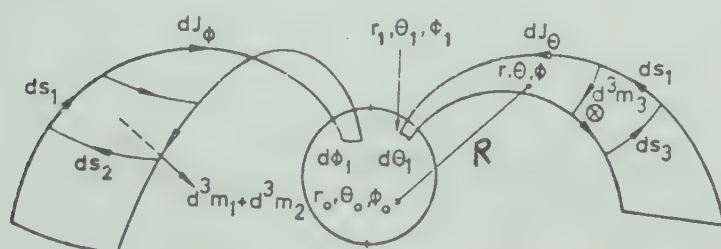


Fig. A1.2 E-W and N-S current loops with associated infinitesimal magnetic dipoles (after Bonnevier et al., 1970).

The current in each loop is defined as

$$\begin{aligned} dJ_{\phi} &= I_{\phi}(\theta_1, \phi_1) r_1 d\theta_1 \\ dJ_{\theta} &= I_{\theta}(\theta_1, \phi_1) r_1 \sin \theta_1 d\phi_1 \end{aligned} \quad (A1.22)$$

where I_{ϕ} and I_{θ} represent the eastward and southward component of the height-integrated ionospheric current density \vec{I} respectively. They have shown that the scalar magnetic potential due to these loops can be represented by an integration over elementary magnetic dipole moments, $\vec{d^3m}$, distributed along field lines as shown in Fig. A1.2. $\vec{d^3m}$ is defined by the equation

$$\vec{d^3m} = d^3m_1 \hat{r} + d^3m_2 \hat{\theta} + d^3m_3 \hat{\phi}$$

where

$$\begin{aligned} d^3m_1 &= -r^2 \sin \theta d\theta dJ_{\phi} d\phi_1 \\ d^3m_2 &= 2r^2 \cos \theta d\theta dJ_{\phi} d\phi_1 \\ d^3m_3 &= -2r^2 \cot \theta d\theta dJ_{\theta} d\theta_1 \end{aligned} \quad (A1.23)$$

The coordinate system used is the same as that shown in Fig. A1.1. The superscripts refer to the order of the differential.

Since the scalar magnetic potential at (r_0, θ_0, ϕ_0) due to moment $\vec{d^3m}$ at (r, θ, ϕ) is given by

$$d^3\psi = k \frac{\vec{R} \cdot \vec{d^3m}}{|\vec{R}|^3} \quad (\text{A1.24})$$

this expression can be integrated with respect to θ (integration along field lines) to obtain the total potential due to both loops

$$d^2\psi = k \int_{\theta=\theta_1}^{\pi/2} \frac{\vec{R} \cdot \vec{d^3m}}{|\vec{R}|^3} \quad (\text{A1.25})$$

The vector \vec{R} is the same as the one used in the previous section but is defined in terms of unit vectors $\hat{r}, \hat{\theta}, \hat{\phi}$ rather than $\hat{r}_0, \hat{\theta}_0, \hat{\phi}_0$. The components of \vec{R} defined by

$$\vec{R} = R_1 \hat{r} + R_2 \hat{\theta} + R_3 \hat{\phi} \quad (\text{A1.26})$$

can be derived using the same method as was used in A1.1.

Thus,

$$R_1 = -r + r_0 A_{11}$$

$$R_2 = r_0 A_{12}$$

$$R_3 = r_0 A_{13}$$

$$R = |\vec{R}|^{1/2} = (r^2 + r_0^2 - 2r r_0 A_{11})^{1/2} \quad (A1.27)$$

The magnetic field is obtained by taking the gradient of the potential, hence,

$$d^2 B_j = k \int_{\theta=\theta_1}^{\pi/2} \sum_i \left[(r_0 \delta_{1j} - r \frac{\partial R_1}{h_j \partial q_j}) \frac{3R_i d^3 m_i}{\ell^5} - \frac{\partial R_i}{h_j \partial q_j} \frac{d^3 m_i}{\ell^3} \right] \quad (j = 1, 2, 3) \quad (A1.28)$$

$$(q_1 = r_0, q_2 = \theta_0, q_3 = \phi_0, h_1 = 1, h_2 = r_0, h_3 = r_0 \sin \theta_0)$$

Therefore, for any distribution of current in the ionosphere, equation A1.28 can be integrated with respect to the ionospheric variables θ_1 and ϕ_1 to obtain the total contribution to the magnetic field at any observing position (r_o, θ_o, ϕ_o) . This three-dimensional integration represents a volume integration over a distribution of magnetic dipole moments $\overrightarrow{d^3m}$. It is interesting to note that a fourth integration can also be performed with respect to r_1 provided \vec{I} is expressed in the more general form $\vec{I}(r_1, \theta_1, \phi_1)$. Thus an arbitrary distribution of current with height can also be considered.

APPENDIX A2 EVALUATION OF THE MAGNETIC FIELD DUE TO CURRENTS INDUCED IN AN INFINITELY CONDUCTING EARTH

A2.1 Introduction

The derivation presented in the next section of this appendix is based on the results obtained by Ashour (1971) who calculated the magnetic field produced by currents induced in a uniformly finite conducting spherical shell where the field of external sources is known numerically. The present derivation is much simpler since we assume the Earth to be represented by a medium of infinite conductivity from the center out to a radial distance b (see Fig. A2.1) and a medium of zero conductivity from the radial distance b to the surface.

In the third section we apply the results of this induction problem to obtain the magnetic field due to currents induced in the Earth by the arbitrary three-dimensional current system studied in Appendix A1.1.

The fourth section summarizes the results obtained by Boström (1971) who used the image dipole method to obtain the field of currents induced by the three-dimensional current system discussed in Appendix A1.2.

A2.2 A simplification of Ashour's method

We assume the Earth to be composed of an infinitely conducting sphere of radius b surrounded by a shell with zero conductivity and thickness $a-b$ where a is the radius of the Earth (see Fig. A2.1). We also assume the external source to be a static current system external to the Earth such that the field can be calculated numerically everywhere inside and on the surface of the Earth. We can thus represent the scalar potential for the external field by a series of spherical harmonics as

$$\psi^e(r_o, \theta_o, \phi_o) = a \sum_{n,m} A_{nm} P_n^m(\cos \theta_o) \left(\frac{r_o}{a}\right)^n e^{im\phi}, (r_o < a)$$

(A2.1)

and the scalar potential for the field of the induced currents as

$$\psi^i(r_o, \theta_o, \phi_o) = b \sum_{n,m} B_{nm} P_n^m(\cos \theta_o) \left(\frac{r_o}{b}\right)^{-(n+1)} e^{im\phi}, (r_o > b)$$

(A2.2)

where

$$\sum_{n,m} \quad \text{represents} \quad \sum_{n=0}^{\infty} \sum_{m=0}^n$$

The three components of the inducing and induced fields in the directions $(\hat{r}_0, \hat{\theta}_0, \hat{\phi}_0)$ are obtained as follows:

$$\begin{aligned} B_1^e &= - \frac{\partial \psi^e}{\partial r_0} \\ &= - \sum_{n,m} n A_{nm} P_n^m(\cos \theta_0) \left(\frac{r_0}{a}\right)^{n-1} e^{im\phi} \end{aligned} \quad (A2.3)$$

$$\begin{aligned} B_2^e &= - \frac{1}{r_0} \frac{\partial \psi^e}{\partial \theta_0} \\ &= - \sum_{n,m} A_{nm} \frac{\partial}{\partial \theta_0} P_n^m(\cos \theta_0) \left(\frac{r_0}{a}\right)^{n-1} e^{im\phi} \end{aligned} \quad (A2.4)$$

$$\begin{aligned} B_3^e &= - \frac{1}{r_0 \sin \theta_0} \frac{\partial \psi^e}{\partial \phi_0} \\ &= - \frac{1}{\sin \theta_0} \sum_{n,m} im A_{nm} P_n^m(\cos \theta_0) \left(\frac{r_0}{a}\right)^{n-1} e^{im\phi} \end{aligned} \quad (A2.5)$$

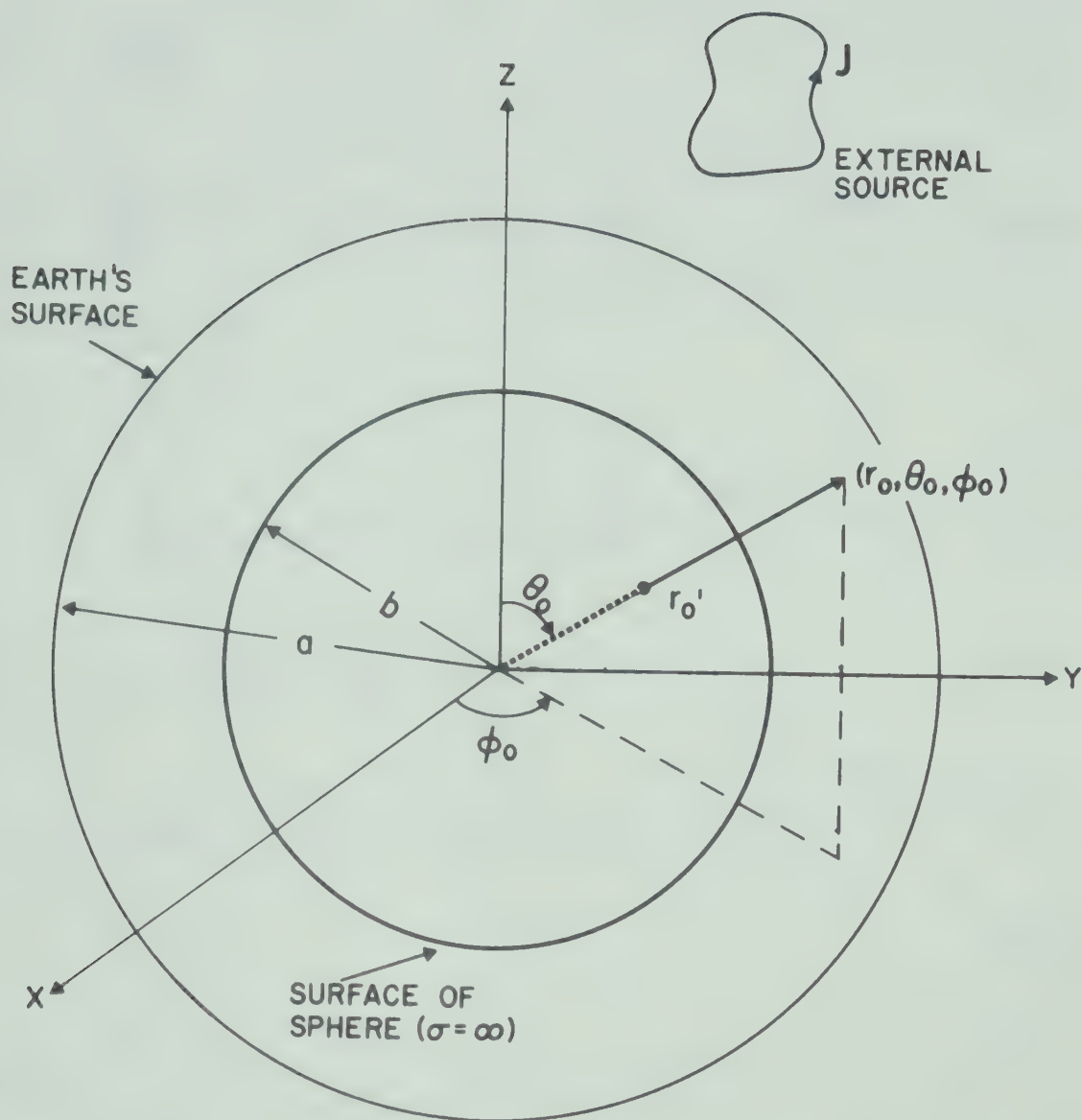


Fig. A2.1 Diagram showing the spherical conductor at depth $a-b$ and observation point (r_0, θ_0, ϕ_0) where the total field is calculated. The dashed line from the origin to r'_0 along the position vector \vec{r}_0 represents the path of integration for calculating the horizontal components of the induced field.

$$\begin{aligned}
B_1^i &= - \frac{\partial \psi^i}{\partial r_0} \\
&= \sum_{n,m} i(n+1) B_{nm} P_n^m(\cos \theta_0) \left(\frac{r_0}{b}\right)^{-(n+2)} e^{im\phi} \quad (A2.6)
\end{aligned}$$

$$\begin{aligned}
B_2^i &= - \frac{1}{r_0} \frac{\partial \psi^i}{\partial \theta_0} \\
&= - \sum_{n,m} B_{nm} \frac{\partial}{\partial \theta_0} P_n^m(\cos \theta_0) \left(\frac{r_0}{b}\right)^{-(n+2)} e^{im\phi} \quad (A2.7)
\end{aligned}$$

$$\begin{aligned}
B_3^i &= - \frac{1}{r_0 \sin \theta_0} \frac{\partial \psi^i}{\partial \phi_0} \\
&= - \frac{1}{\sin \theta_0} \sum_{n,m} im B_{nm} P_n^m(\cos \theta_0) \left(\frac{r_0}{b}\right)^{-(n+2)} e^{im\phi} \\
&\quad (A2.8)
\end{aligned}$$

where

$$\vec{B}^e(r_0, \theta_0, \phi_0) = B_1^e \hat{r}_0 + B_2^e \hat{\theta}_0 + B_3^e \hat{\phi}_0 \quad (A2.9)$$

and

$$\vec{B}^i(r_0, \theta_0, \phi_0) = B_1^i \hat{r}_0 + B_2^i \hat{\theta}_0 + B_3^i \hat{\phi}_0 \quad (A2.10)$$

Since we assume the coefficients A_{nm} are known for the external field, the coefficients B_{nm} for the induced field can be determined by applying the proper boundary conditions at the surface of the infinitely conducting sphere. We have a choice of using one of the three following boundary conditions,

$$\left[B_1^i(r_o, \theta_o, \phi_o) + B_1^e(r_o, \theta_o, \phi_o) \right]_{r_o=b} = 0 \quad (A2.11)$$

$$\left\{ \frac{\partial}{\partial r_o} \left[r_o (B_2^i(r_o, \theta_o, \phi_o) + B_2^e(r_o, \theta_o, \phi_o)) \right] \right\}_{r_o=b} = 0 \quad (A2.12)$$

$$\left\{ \frac{\partial}{\partial r_o} \left[r_o \sin \theta_o (B_3^i(r_o, \theta_o, \phi_o) + B_3^e(r_o, \theta_o, \phi_o)) \right] \right\}_{r_o=b} = 0 \quad (A2.13)$$

(see Stratton, 1941).

Applying boundary condition A2.11 for the vertical fields at $r_o=b$, we find

$$B_{nm} = \frac{n}{n+1} \left(\frac{b}{a} \right)^{n-1} A_{nm} \quad (A2.14)$$

Hence, A2.6, A2.7 and A2.8 become

$$B_1^i = \sum_{n,m} n \left(\frac{b}{a}\right)^{n-1} A_{nm} P_n^m(\cos \theta_0) \left(\frac{r_0}{b}\right)^{-(n+2)} e^{im\phi} \quad (A2.15)$$

$$B_2^i = - \sum_{n,m} \frac{n}{n+1} \left(\frac{b}{a}\right)^{n-1} A_{nm} \frac{\partial}{\partial \theta_0} P_n^m(\cos \theta_0) \left(\frac{r_0}{b}\right)^{-(n+2)} e^{im\phi} \quad (A2.16)$$

$$B_3^i = - \frac{1}{\sin \theta_0} \sum_{n,m} i m \frac{n}{n+1} \left(\frac{b}{a}\right)^{n-1} A_{nm} P_n^m(\cos \theta_0) \left(\frac{r_0}{b}\right)^{-(n+2)} e^{im\phi} \quad (A2.17)$$

respectively.

Expressions A2.15 through A2.17 for the components of the induced field are equivalent to those obtained by Ashour (1971) for the high frequency and infinite conductivity limit for a thin spherical shell of radius b . The following derivation of the relationships between the inducing and induced fields at the surface of the Earth is essentially the same as that presented by Ashour (1971).

Since we are interested in the value of the induced field at the surface of the Earth ($r_0 = a$), the components

of the induced field are represented in terms of components of the external field at $r_0 = a$. It can easily be shown from A2.3 and A2.15 that

$$B_1^i(a, \theta_0, \phi_0) = - \left(\frac{b}{a}\right)^3 B_1^e(r_0', \theta_0, \phi_0) \quad (\text{A2.18})$$

where

$$r_0' = \frac{b^2}{a}$$

To obtain similar relationships between the horizontal components of \vec{B}^e and \vec{B}^i is made more difficult due to the factor $\frac{n}{n+1}$ in A2.16 and A2.17. Since this factor can be written as

$$\frac{n}{n+1} = 1 - \frac{1}{n+1} \quad (\text{A2.19})$$

B_2^i and B_3^i can be represented by

$$B_2^i = C_2^i + D_2^i \quad (\text{A2.20})$$

and $B_3^i = C_3^i + D_3^i \quad (\text{A2.21})$

where

$$C_2^i = - \sum_{n,m} \left(\frac{b}{a}\right)^{n-1} A_{nm} \frac{\partial}{\partial \theta_0} P_n^m(\cos \theta_0) \left(\frac{r_0}{b}\right)^{-(n+2)} e^{im\phi} \quad (\text{A2.22})$$

$$D_2^i = \sum_{n,m} \frac{1}{n+1} \left(\frac{b}{a}\right)^{n-1} A_{nm} \frac{\partial}{\partial \theta_0} P_n^m(\cos \theta_0) \left(\frac{r_0}{b}\right)^{-(n+2)} e^{im\phi} \quad (\text{A2.23})$$

$$C_3^i = - \sum_{n,m} i m \left(\frac{b}{a}\right)^{n-1} A_{nm} P_n^m(\cos \theta_0) \left(\frac{r_0}{b}\right)^{-(n+2)} e^{im\phi} \quad (\text{A2.24})$$

and

$$D_3^i = \sum_{n,m} i m \frac{1}{n+1} \left(\frac{b}{a}\right)^{n-1} A_{nm} P_n^m(\cos \theta_0) \left(\frac{r_0}{b}\right)^{-(n+2)} e^{im\phi} \quad (\text{A2.25})$$

The terms C_2^i and C_3^i can be related to the external fields B_2^e and B_3^e in the same manner as for the vertical field B_1^i to give

$$C_2^i(a, \theta_o, \phi_o) = \left(\frac{b}{a}\right)^3 B_2^e(r_o', \theta_o, \phi_o) \quad (A2.26)$$

and

$$C_3^i(a, \theta_o, \phi_o) = \left(\frac{b}{a}\right)^3 B_3^e(r_o', \theta_o, \phi_o) \quad (A2.27)$$

The terms D_2^i and D_3^i can be represented by an integration of $r_o B_2^e$ and $r_o B_3^e$ along the position vector of the observing coordinates (r_o, θ_o, ϕ_o) from the origin to r_o' (see Fig. A2.1) as follows:

$$D_2^i(a, \theta_o, \phi_o) = -\frac{1}{ab} \int_0^{r_o'} r_o B_2^e(r_o, \theta_o, \phi_o) dr_o \quad (A2.28)$$

and

$$D_3^i(a, \theta_o, \phi_o) = -\frac{1}{ab} \int_0^{r_o'} r_o B_3^e(r_o, \theta_o, \phi_o) dr_o \quad (A2.29)$$

Therefore, since the external field can be evaluated numerically along this path of integration, the total induced field at $r_o = a$ can be evaluated numerically using

(A2.18) and

$$B_2^i(a, \theta_0, \phi_0) = \left(\frac{b}{a}\right)^3 B_2^e(r_0', \theta_0, \phi_0) - \frac{1}{ab} \int_0^{r_0'} r_0 B_2^e(r_0, \theta_0, \phi_0) dr_0$$

(A2.30)

$$B_3^i(a, \theta_0, \phi_0) = \left(\frac{b}{a}\right)^3 B_3^e(r_0', \theta_0, \phi_0) - \frac{1}{ab} \int_0^{r_0'} r_0 B_3^e(r_0, \theta_0, \phi_0) dr_0$$

(A2.31)

A2.3 Induction problem using Biot-Savart's law

In the previous section equations A2.18, A2.30 and A2.31 relating the induced and inducing fields on the surface of the Earth were derived. In this section we substitute into these equations the inducing field equations A1.21 to obtain a solution for the total field due to an arbitrary three-dimensional current system in the magnetosphere and induced currents in an infinitely conducting Earth.

We showed in appendix A1 that for any external current loop C (see Fig. A2.1) with $Jd\vec{s}$ representing an element of current along its path, the components of the field at (r_o, θ_o, ϕ_o) in the coordinate directions $(\hat{r}_o, \hat{\theta}_o, \hat{\phi}_o)$ are given by A1.21. For convenience, elements of $d\vec{c}$ are substituted in A1.21 to give three component equations

$$B_1^e(r_o, \theta_o, \phi_o) = k J \int_C \frac{r}{R^3} (A_{13} ds_2 - A_{12} ds_3) \quad (A2.32)$$

$$B_2^e(r_o, \theta_o, \phi_o) = k J \int_C \frac{1}{R^3} \left[r_o A_{31} ds_1 + (r A_{23} + r_o A_{32}) ds_2 + (r_o A_{33} - r A_{22}) ds_3 \right] \quad (A2.33)$$

and

$$B_3^e(r_o, \theta_o, \phi_o) = k J \int_C \frac{1}{R^3} \left[-r_o A_{21} ds_1 + (r A_{33} - r_o A_{22}) ds_2 - (r_o A_{23} + r A_{32}) ds_3 \right] \quad (A2.34)$$

We see from these equations that the vertical component and the first terms of the two horizontal components of the induced field can be obtained by substituting

$$r_o' = \frac{b^2}{a}$$

for r_o in A2.32 through A2.34 and multiplying by the constant factor $(\frac{b}{a})^3$ with the appropriate sign. The main difficulty that arises in calculating the induced field is the evaluation of the integral term in both horizontal component equations A2.30 and A2.31. This difficulty is partially overcome by the fact that the integration over the source (line integral along C) is independent of the variable r_o , thus enabling us to change the order of integration (i.e. for the B_2^i component) as follows,

$$\begin{aligned} \int_0^{r_o'} r_o B_2^e(r_o, \theta_o, \phi_o) dr_o &= k J \int_C \int_0^{r_o'} \frac{r_o}{R^3} \left[r_o A_{31} ds_1 + \right. \\ &\left. + (r A_{23} + r_o A_{32}) ds_2 + (r_o A_{33} - r A_{22}) ds_3 \right] dr_o \end{aligned} \quad (A2.35)$$

Since the matrix \tilde{A} and differential line element $d\vec{s}$ are independent of r_0 , we can integrate directly over terms such as r_0/R^3 and r_0^2/R^3 . Therefore, we have to find solutions to integrals of the form

$$I_1 = \int_0^r \frac{r_0 dr_0}{(r^2 + r_0^2 - 2r r_0 A_{11})^{3/2}} \quad (A2.36)$$

and

$$I_2 = \int_0^r \frac{r_0^2 dr_0}{(r^2 + r_0^2 - 2r r_0 A_{11})^{3/2}} \quad (A2.37)$$

The A_{11} element of matrix \tilde{A} represents the cosine of the angle λ between position vectors \vec{r} and \vec{r}_0 and hence, can range in value from -1 to $+1$. Thus, the integrals I_1 and I_2 must be solved separately for the two cases,

$$\text{Case I} \quad \cos \lambda \neq \pm 1$$

$$\text{Case II} \quad \cos \lambda = \pm 1$$

resulting in the following four integrals

$$\text{Case I} \quad I_{1,2} = \int_0^{r'_0} \frac{r_o^{1,2} dr_o}{(r^2 + r_o^2 - 2r r_o \cos \lambda)^{3/2}} \quad (\text{A2.38})$$

and

$$\text{Case II} \quad I_{1,2} = \int_0^{r'_0} \frac{r_o^{1,2} dr_o}{|r \mp r_o|^3} \quad (\text{A2.39})$$

The absolute value sign in A2.39 can be neglected since $r_o < r$ over the interval of integration. The solutions of these integrals are listed below:

Case I $(\cos \lambda \neq \pm 1)$

$$I_1 = \frac{R' - r + r_o \cos \lambda}{R' r \sin^2 \lambda} \quad (\text{A2.40})$$

$$I_2 = \frac{(2 \cos^2 \lambda - 1)r'_0 + (R' - r) \cos \lambda}{R' \sin^2 \lambda} + \log \left[\frac{R' + r'_0 - r \cos \lambda}{r(1 - \cos \lambda)} \right]$$

(A2.41)

Case II $(\cos \lambda = \pm 1)$

$$I_1 = \frac{(r'_0)^2}{2r(r \mp r'_0)^2} \quad (\text{A2.42})$$

$$I_2 = \frac{2r(r'_0 \mp \frac{3}{4}r)}{(r \mp r'_0)^2} \mp \log \left[\frac{r \mp r'_0}{r} \right] \mp \frac{3}{2} \quad (\text{A2.43})$$

where

$$R' = [r^2 + (r'_0)^2 - 2r r'_0 \cos \lambda]^{\frac{1}{2}}$$

and

$$r'_0 = \frac{b^2}{a}$$

Since we must integrate terms containing I_1 and I_2 over the entire current loop C (see equation A2.35), the task of switching between case I and case II depending upon the value of $\cos \lambda$ along the path of integration is very difficult due to the singularities in A2.40 and A2.41 at $\cos \lambda = \pm 1$. As a result of these singularities any numerical evaluation of the integral A2.35 is suspect

because of the change of solution for I_1 and I_2 from case I to case II as $\cos \lambda$ approaches ± 1 .

However, we can overcome this problem by noting that since $r > r_0$, solutions given by A2.40 and A2.41 can be rewritten to remove the singularities at $\cos \lambda = \pm 1$. The solution for I_1 (A2.40) can be rewritten as follows:

$$\begin{aligned}
 I_1 &= \frac{R' - r + r_0' \cos \lambda}{rR' \sin^2 \lambda} \\
 &= \frac{(r_0')^2}{rR'} \frac{R' - r + r_0' \cos \lambda}{(r_0')^2 \sin^2 \lambda} \\
 &= \frac{(r_0')^2}{rR'} \frac{1}{R' + r - r_0' \cos \lambda} \quad (A2.44)
 \end{aligned}$$

It can be shown that A2.44 is valid for all values of $\cos \lambda$ and, for $\cos \lambda = \pm 1$, reduces to the solution A2.42. The first term of the solution for I_2 (A2.41) can be rewritten in a similar manner,

$$\begin{aligned}
 I_2^a &= \frac{(2 \cos^2 \lambda - 1) r_o' + (R' - r) \cos \lambda}{R' \sin^2 \lambda} \\
 &= \frac{(r_o')^2 \cos \lambda}{R'} \left[\frac{R' - r + r_o' \cos \lambda}{(r_o')^2 \sin^2 \lambda} \right] - \frac{r_o'}{R'} \\
 &= r I_1 \cos \lambda - \frac{r_o'}{R'} \quad (A2.45)
 \end{aligned}$$

We must, however, consider two separate solutions in place of the second term because both numerator and denominator contain singularities. Since our main concern is to obtain proper solutions in the neighborhood of $\cos \lambda = \pm 1$, we choose two regions, namely $\cos \lambda \leq 0$ and $\cos \lambda > 0$ for the determination of these separate solutions. For $\cos \lambda \leq 0$ the second term

$$I_2^{b-} = \log \left[\frac{R' + r_o' - r \cos \lambda}{r(1 - \cos \lambda)} \right] \quad (A2.46)$$

remains unchanged. For $\cos \lambda > 0$

$$\begin{aligned}
I_2^{b+} &= \log \left[\frac{R + r_0' - r \cos \lambda}{r(1 - \cos \lambda)} \right] \\
&= \log \left[\frac{(1 + \cos \lambda)(R' + r_0 - r \cos \lambda)}{r \sin^2 \lambda} \right] \\
&= \log \left[\frac{r(1 + \cos \lambda)}{R' - r_0 + r \cos \lambda} \right] \tag{A2.47}
\end{aligned}$$

Therefore,

$$I_2 (\cos \lambda \leq 0) = I_2^a + I_2^{b-} \tag{A2.48}$$

and

$$I_2 (\cos \lambda > 0) = I_2^a + I_2^{b+} \tag{A2.49}$$

Equation A2.48 and A2.49 reduce to A2.43 for $\cos \lambda = -1$ and $\cos \lambda = 1$ respectively. We now have a set of solutions for integrals I_1 and I_2 valid for all values of $\cos \lambda$ provided $r_0' < r_0$. Hence, A2.35 becomes

$$\int_0^{r_0'} r_0 B_2^e(r_0, \theta_0, \phi_0) dr_0 = k J \int_C \left[I_2 A_{31} ds_1 + (r I_1 A_{23} + I_2 A_{32}) ds_2 + (I_2 A_{33} - r I_1 A_{22}) ds_3 \right] \quad (A2.50a)$$

and similarly for the other horizontal component

$$\int_0^{r_0'} r_0 B_3^e(r_0, \theta_0, \phi_0) dr_0 = k J \int_C \left[-I_2 A_{21} ds_1 + (r I_1 A_{33} - I_2 A_{22}) ds_2 - (I_2 A_{23} + r I_1 A_{32}) ds_3 \right] \quad (A2.50b)$$

By substituting A2.50a and A2.50b into A2.30 and A2.31 respectively we obtain a complete solution for the induced field due to an arbitrary current loop evaluated by Biot-Savart's law. Using A1.20 and A2.18 we can represent this complete solution by the following equation:

$$B_j^i(a, \theta_0, \psi_0) = kJ \int_C \sum_i \left[\epsilon_j \left(\frac{b}{a}\right)^3 dc_{ij}' - \left(\frac{1}{ab}\right) dc_{ij}'' \right]$$

$$(\epsilon_1 = -1, \epsilon_{2,3} = 1) \quad (A2.51)$$

where \tilde{dc}' is obtained merely by substituting r_0' for r_0 in the matrix \tilde{dc} and dc_{ij}'' are the elements of the matrix

$$\tilde{dc}'' = \begin{bmatrix} 0 & I_2 A_{31} ds_1 & -I_2 A_{21} ds_1 \\ 0 & (rI_1 A_{23} + I_2 A_{32}) ds_2 & (rI_1 A_{33} - I_2 A_{22}) ds_2 \\ 0 & (I_2 A_{33} - rI_1 A_{22}) ds_3 & -(I_2 A_{23} + rI_1 A_{32}) ds_3 \end{bmatrix}$$

A2.4 Induction problem using the image dipole method

Boström (1971) expanded equation A1.25 (see Appendix A1) in spherical harmonics in order to obtain a solution for the induced field associated with the current loops shown in Fig. A1.2 external to a spherical conductor of infinite conductivity (see Fig. A2.1). By satisfying the boundary condition for the vertical field (see eq. A2.11) he was able to show that the scalar magnetic potential due to the induced currents on the surface of the spherical conductor of radius b is given by the equation

$$d^2 \psi^i = k \int_{\theta=\theta_1}^{\pi/2} \sum_i \frac{R_i' d^3 m_i'}{(R')^3} \quad (\text{A2.52})$$

where

$$d^3 m_1' = - \left(\frac{b^3}{r^3} \right) d^3 m_1$$

$$d^3 m_{2,3}' = \left(\frac{b^3}{r^3} \right) d^3 m_{2,3}$$

$$R_1' = -r' + r_0 \cos \lambda$$

$$R_{2,3}' = R_{2,3} \left[1 - \frac{(R')^2}{r_0 (R' + r_0 - r' A_{11})} \right]$$

$$R' = [(r')^2 + r_0^2 - 2r'r_0 A_{11}]^{1/2}$$

$$(r' = b^2/r)$$

The expression for the magnetic field due to the induced currents is obtained by replacing d^3m_1 , R_i and R by $d^3m'_i$, R'_i and R' in eq. A1.28. The evaluation of the partial derivatives is much more complicated than for the external field due to the added term in both R'_2 and R'_3 . To remove some of the difficulties with evaluating these partial derivatives, Boström derived the following expressions:

$$\frac{\partial R'_1}{\partial q_j} = \frac{\partial R_1}{\partial q_j} \quad (j = 1, 2, 3)$$

and

$$\frac{\partial R'_i}{\partial q_j} = \frac{R'_i}{R_i} \frac{\partial R_i}{\partial q_j} + \frac{R_i}{r_0^2 (R' + r_0 - r' A_{11})^2} \times$$

$$\begin{aligned}
& \times \left[(r_0^2 - (r')^2 + R' r_0) r' \frac{\partial R_1}{\partial q_j} + \right. \\
& \left. + (R' - r_0)(R' + r_0)^2 + r_0 (r')^2 \delta_{1j} \right] \\
& (i = 2, 3; j = 1, 2, 3) \qquad (A2.53)
\end{aligned}$$

APPENDIX A3 THE METHOD OF GAUSSIAN INTEGRATION

Since the integrals presented in Chapter II and Appendices A1 and A2 cannot be integrated analytically we must resort to numerical methods for evaluating such integrals. The method of numerical integration we found to be the most suitable in terms of accuracy and efficiency is the Gaussian method. Gauss' formula for integration is given as follows:

$$\int_{-1}^1 f(x) dx = \sum_{i=1}^n w_i f(x_i) + E_n \quad (\text{A3.1})$$

where x_i is the i^{th} zero of the Legendre polynomial $P_n(x)$ and

$$w_i = \frac{2}{(1-x_i)^2 [P'_n(x_i)]^2}$$

Numerous tables of x_i and w_i for various n are readily available (see Abramowitz and Stegun (1965)). The error term E_n given by

$$E_n = \frac{2^{2n+1} (n!)^4}{(2n+1)[(2n)!]} f^{(2n)}(n) \quad (-1 < n < 1) \quad (A3.2)$$

can be approximated provided the $2n^{\text{th}}$ derivative of $f(x)$ can be evaluated. This is, however, not possible for the functions we must integrate. The determination of the error is made even more difficult due to the fact that we have to evaluate double and triple integrals. A discussion of E_n for double integrals is given by Ralston (1965). Another factor affecting the error term E_n is the change of variable necessary to make the interval of integration $-1 \leq x \leq 1$. For example if we have an integral with an interval of integration $a \leq \tau \leq b$, a change of variable can be made to give

$$\int_a^b f(t) dt = \frac{b-a}{2} \int_{-1}^1 f\left[a + \frac{b-a}{2} (x+1)\right] dx \quad (A3.3)$$

The effect of this change of variable on the error term is a multiplication factor $[(b-a)/2]^{2n+1}$ (Ralston, 1965). Thus, as long as the interval $b-a$ is less than 2, the error will be reduced. If not it may increase significantly.

Since the error term E_n could not be evaluated for the integrals discussed in Chapter II and Appendices A1 and A2, we subjected them to various degrees of Gaussian integration until convergence of the numerical results for each integral was obtained. As a further test for convergence we subdivided the intervals of integration, thus being assured of accurate numerical results.

The final and most significant test was performed by integrating over model current systems using both methods (see Appendices A1 and A2) of evaluating the associated magnetic fields. We found that the numerical results using these two methods were surprisingly similar for all model current systems integrated. Table A3.1 illustrates this similarity for an E-W current system. The induced field is also included in these results. It is interesting to note that the method derived in this thesis (Biot-Savart method) requires much less computer time (a factor of 6 to 10) than the magnetic dipole method as derived by Bonnevier et al. (1970) and Boström (1971). This fact is highly significant when considering large current systems or comparison of model field calculations with a large number of magnetic observations.

Table A3.1

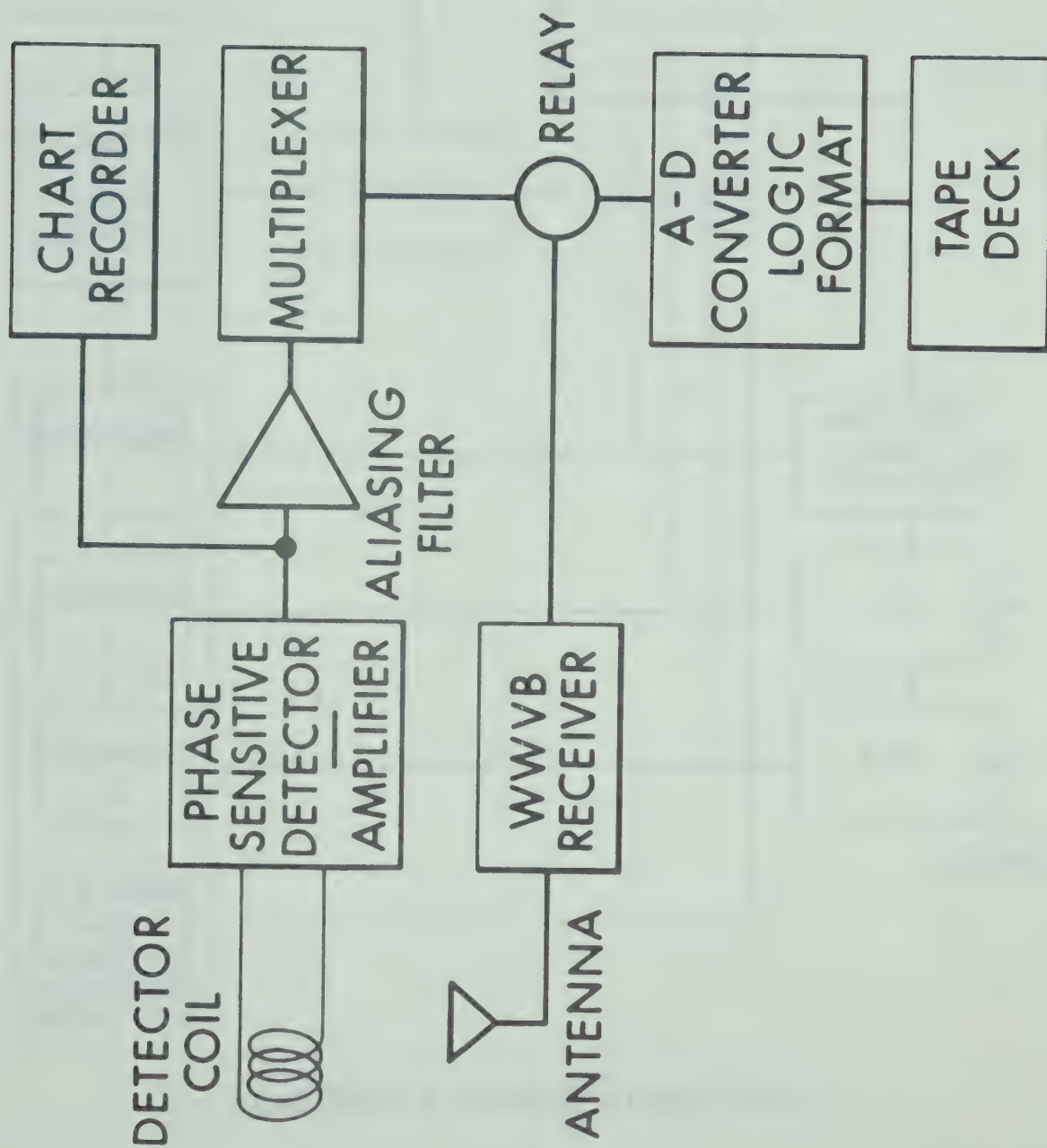
Comparison of the total field intensities obtained by using the method developed in this thesis with that developed by Bonnevier et al. (1970) and Boström (1971). The current system is an E-W system 20° long, 5° wide, height of 115 km located at latitude 67.5° . The depth of the superconductive layer is 200 km. Total integrated current is 10^6 AMPS.

Latitude (longitude is 5° east of central meridian)	Present Method Intensity($(H^2+D^2+Z^2)^{\frac{1}{2}}$)	Bonnevier et al. (1970) Method	% Difference
55°	59.64γ	58.51γ	1.89%
60°	111.80	110.76	0.93
65°	497.50	497.64	0.03
67.5°	584.56	583.96	0.10
70°	471.57	474.25	0.57
75°	71.74	71.43	0.42
80°	36.55	36.25	0.82
84.5°	23.19	23.09	0.43

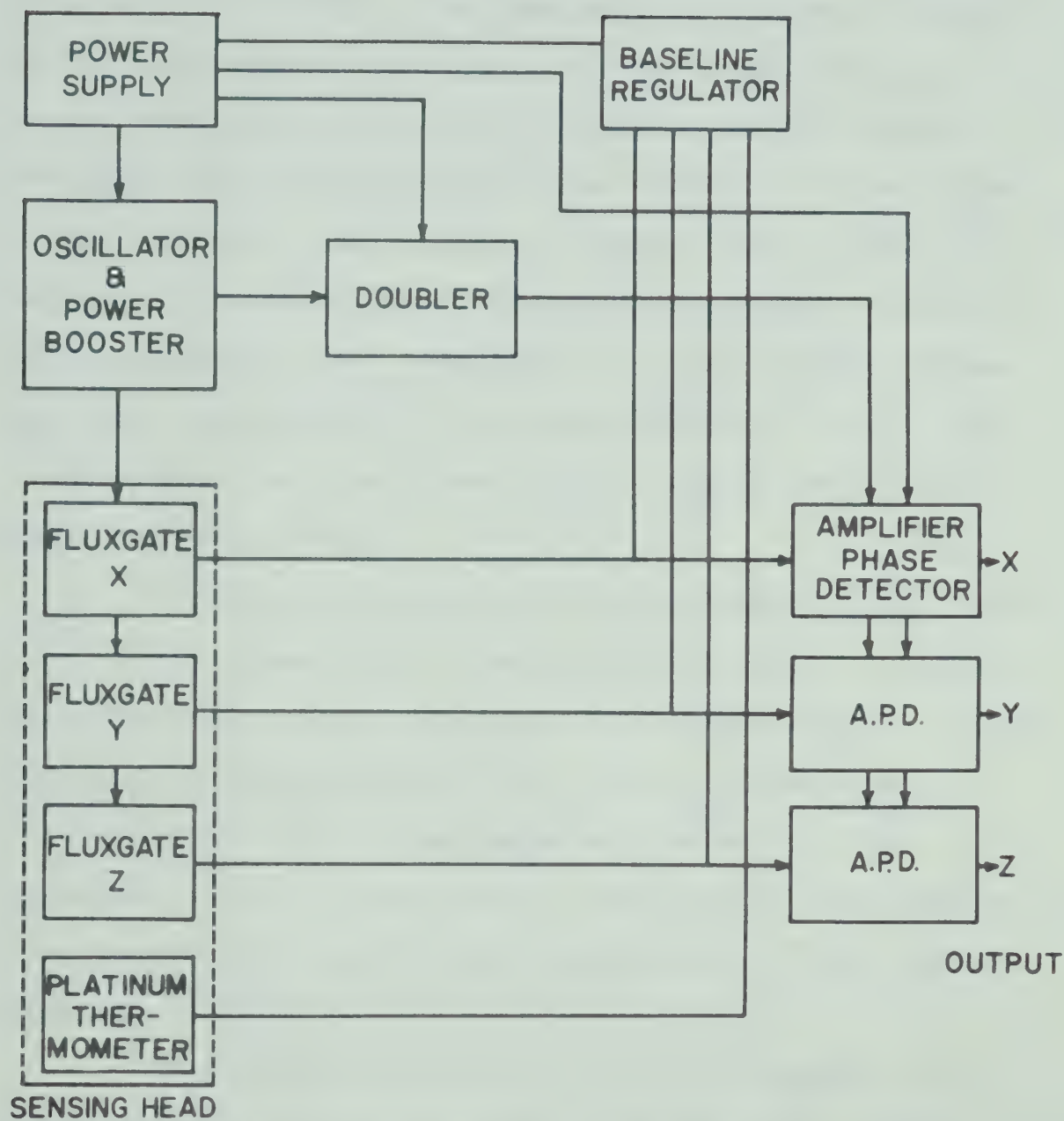
APPENDIX A4 INSTRUMENTATION

The basic system used to measure and record variations of the Earth's magnetic field at each field station is shown in Fig. A4.1. Each system included a three-component fluxgate magnetometer, analogue-to-digital converter, digital tape recorder, WWVB radio receiver and the necessary external power supplies and regulators. Since geomagnetic storms and related ionospheric disturbances have little or no effect on the reception of WWVB time transmissions (60 kHz carrier frequency), the recording of the WWVB signal for two minutes at 7.5 hr intervals provided excellent timing for the magnetic records.

All except one of the magnetometers used in this experiment were of the type designed by Dr. P. H. Serson of the Geomagnetic Division of the Department of Energy, Mines and Resources (see Fig. A4.2). The design specifications and results of tests performed on the magnetometer under normal field conditions have been presented in detail by Trigg et al. (1970). The Sharpe (MF0-3) fluxgate magnetometer used at Leduc has similar specifications except for better long term stability ($\pm 1\gamma/24$ hrs at constant temperature), a smaller temperature coefficient ($\pm 0.5\gamma/^{\circ}\text{C}$) and a broader frequency response



A4.1 Block diagram of the basic magnetic recording system at each station.



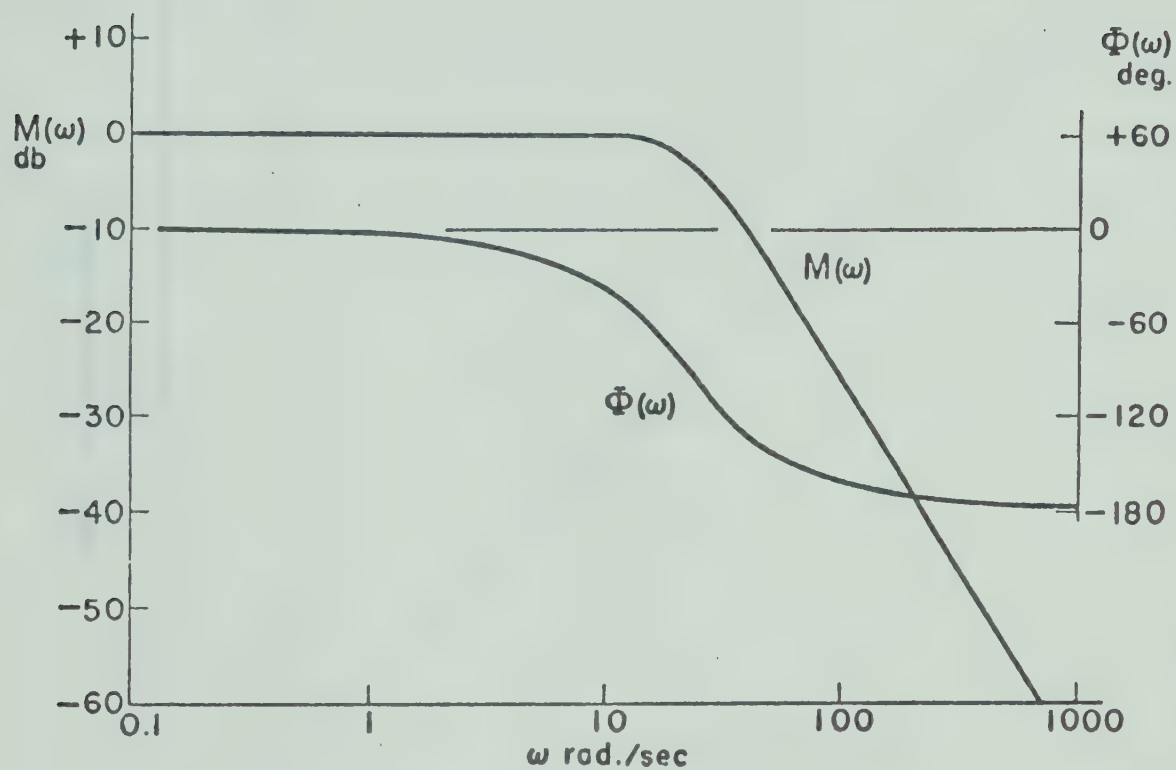
FLUXGATE MAGNETOMETER

A4.2 Block diagram of the fluxgate magnetometer.

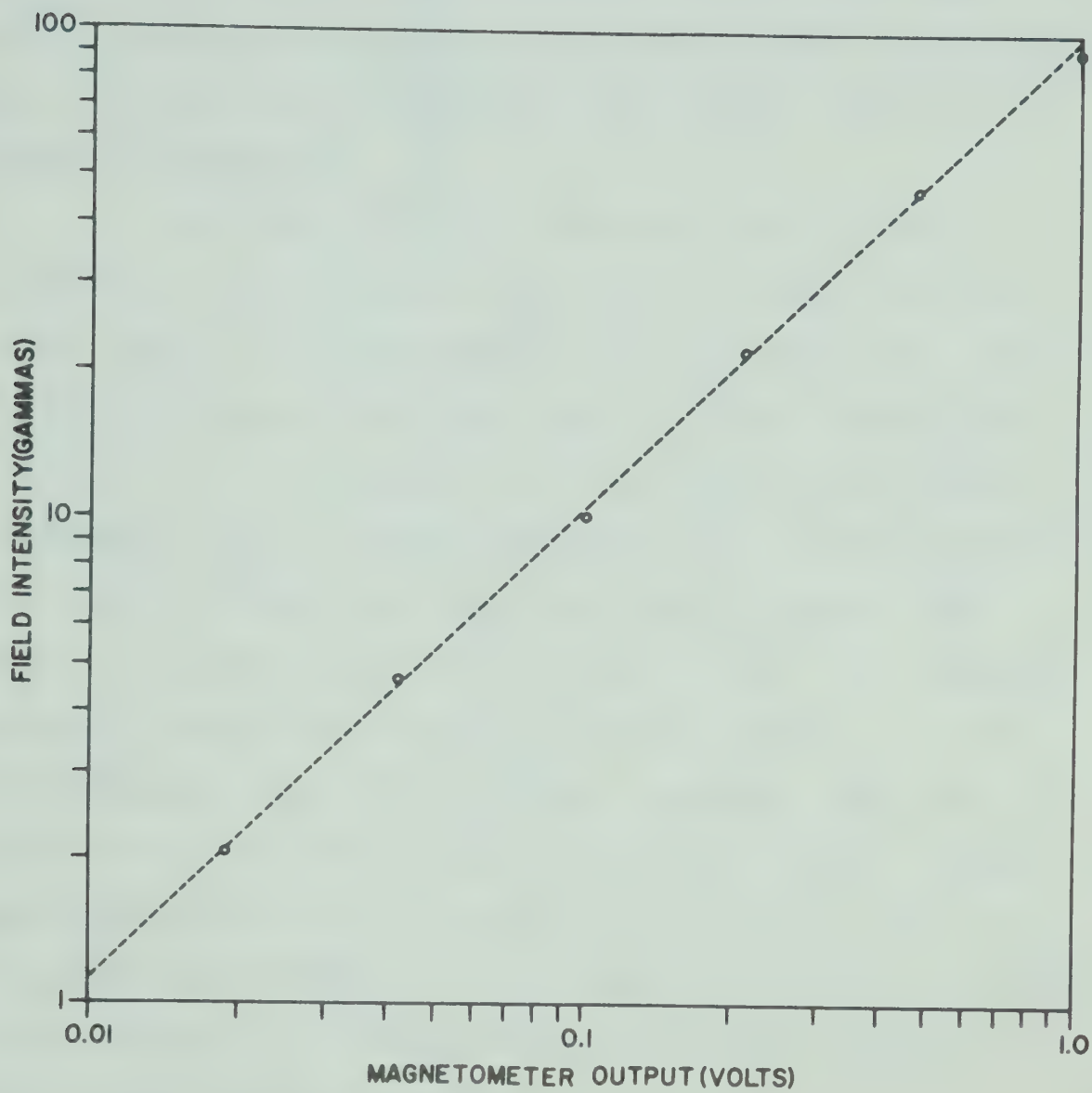
(D.C. to 55 Hz, -3db). The theoretical frequency response for the magnetometer is shown in Fig. A4.3. It can be seen from this figure that the phase and gain curves are essentially flat with the phase shift being zero from 0 to 0.025 Hz, the frequency interval used in this thesis. The sensitivity, resolution and dynamic range of the magnetometer are 1 volt/100 γ , 1 γ and $\pm 1000\gamma$ (from baseline) respectively. The outputs from the X, Y and Z amplifiers are linear over most of the dynamic range ($\pm 10\text{v}$) (see Fig. A4.4).

The stability and drift tests completed by Trigg et al. (1970) showed that fluctuations of the Y baseline (up to 20 γ) were much larger than expected and could not be explained by temperature drifts. Also a temperature coefficient of 10 $\gamma/^{\circ}\text{C}$ was necessary to explain the variations of the Z baseline. The value of the temperature coefficient given by the manufacturer of the magnetometers is $< 1\gamma/^{\circ}\text{C}$.

The sensing head (Fig. A4.3) was mounted on an aluminum pole set in concrete at the bottom of a plastic container (waste receptable). To reduce diurnal temperature variations the container was buried in the ground, the top being ~ 6 to 10 in. below the surface. Although



A4.3 Theoretical frequency response curves for the magnetometer (after Trigg et al. (1970)).

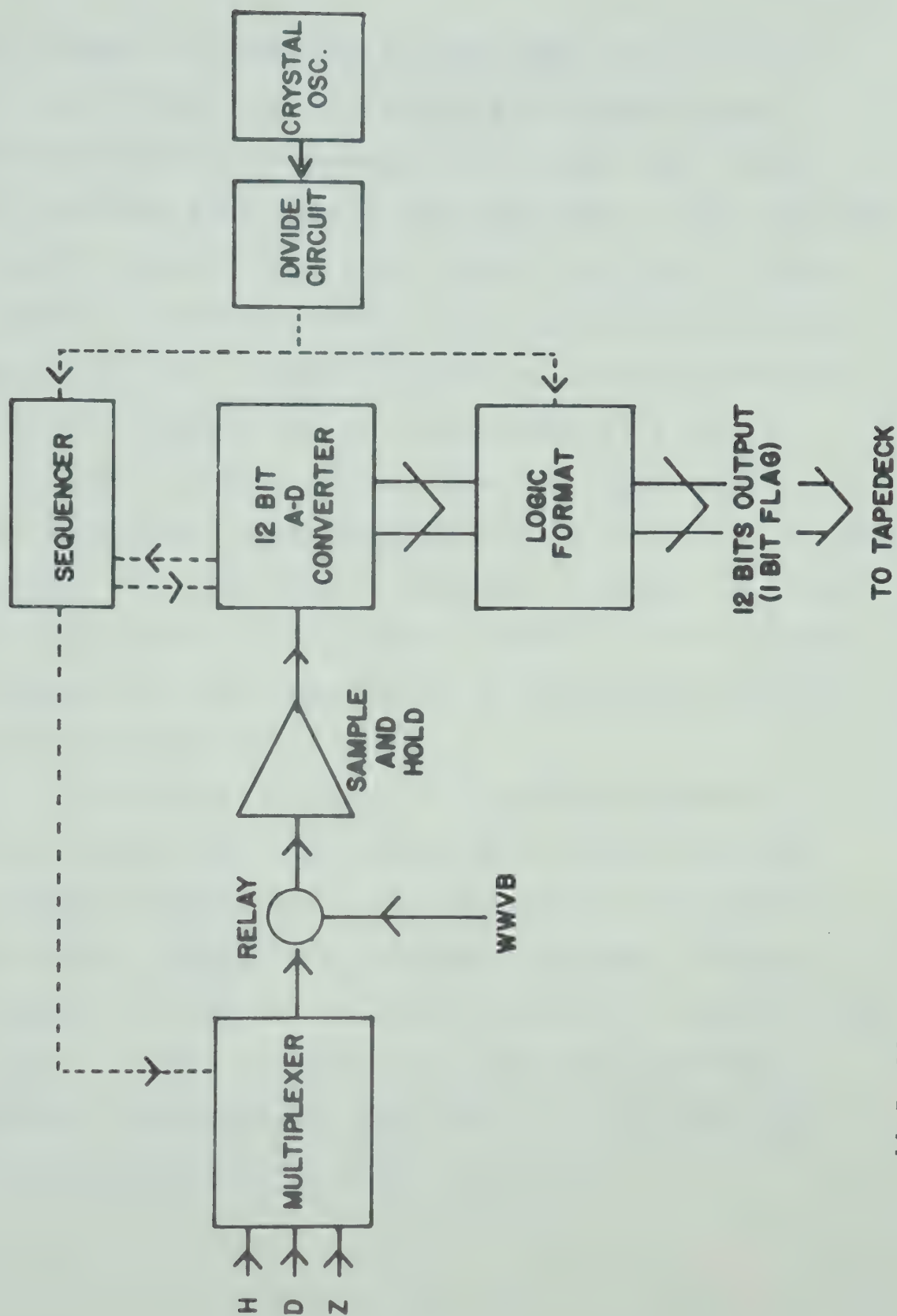


A4.4 Gain curve of the magnetometer for the lower portion of the dynamic range.

fluctuations in temperature were not determined, Trigg et al. (1970) suggested that burying the sensing head in the ground can reduce the daily temperature variations to one or two degrees centigrade.

The Redcor 720 A-D converters used in this experiment were modified to operate at various stepping rates, thereby allowing magnetic data and WWVB time signals to be recorded with the same digital system. After each series of 7 blocks of data (~ 65.5 min/block) the output of magnetic data from the multiplexer was interrupted for 123 sec while WWVB time signal was being recorded (Fig. A4.5). To permit accurate recording of WWVB the stepping rate was changed from 1.56/sec (sample interval of 1.92 sec/component) to 50.0/sec. These stepping rates were controlled by a 400 Hz crystal oscillator (with a maximum deviation from nominal frequency of ± 0.005 per cent) and an associated divider circuit. Hence the maximum variation in the nominal 7 hr 38 min interval between successive WWVB recordings was ~ 2 sec.

The cyclic sampling order (HDZHDZ...) of equal sample intervals in the multiplexer was controlled by the sequencer. The 12 bit A-D converter (the least significant bit was used as a flag to identify errors in the sampling

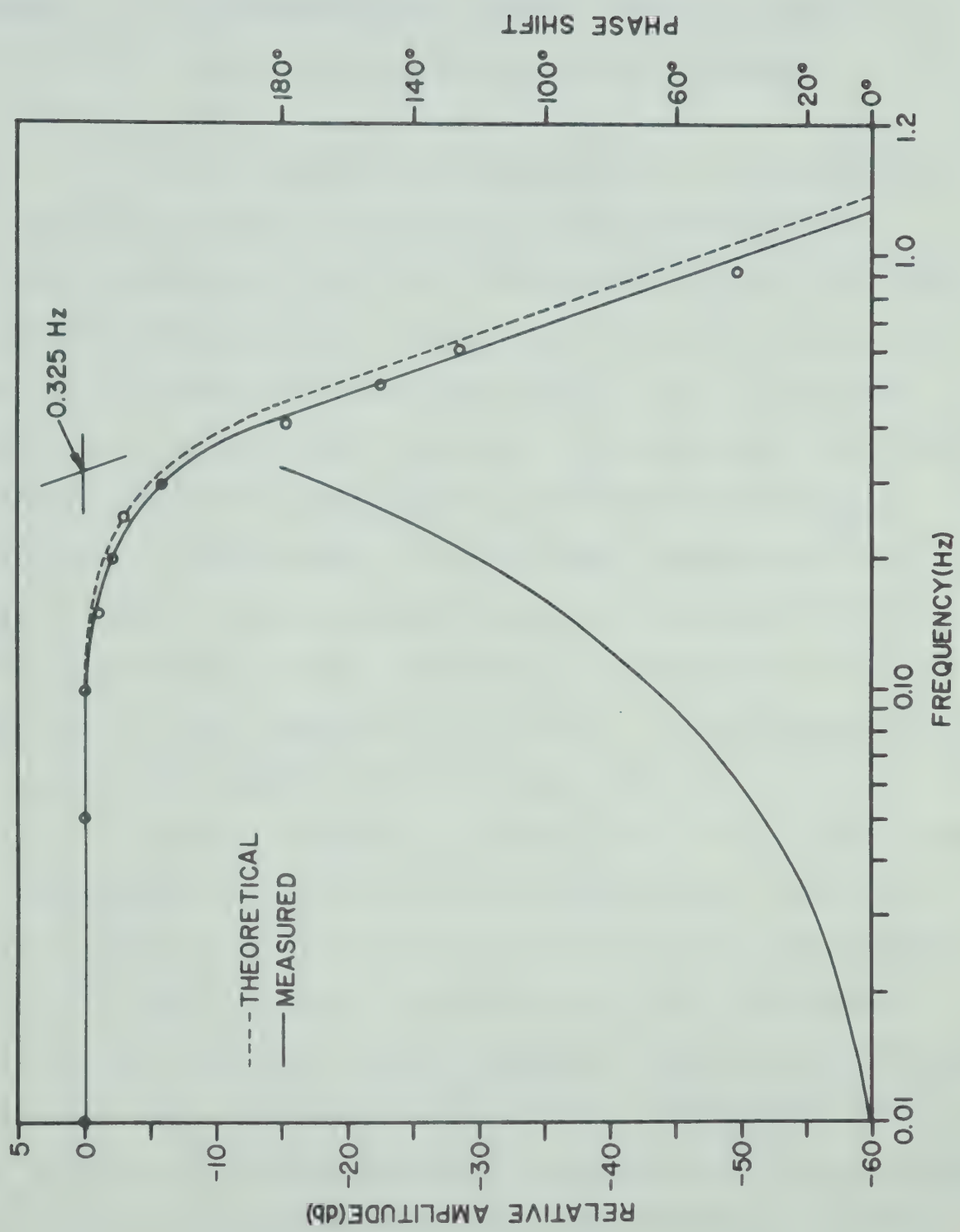


A4.5 Block diagram of the digital recording system.

order) output was formatted into two byte samples (each byte being 6 bits long) and recorded on a seven-track Peripheral Equipment incremental write tape deck. Each block contained 6144 samples and represented 65 min 32.2 sec of magnetic data or 122.8 sec of WWVB time signal. Since the dynamic range was $\pm 1000\gamma$, the least significant bit represented 0.976γ ($2000\gamma/2^{11}$) which is approximately the same as the resolution of the magnetometers ($\pm 1\gamma$).

The component outputs from the magnetometer were passed through two stage aliasing filters to remove frequency components above the Nyquist frequency (0.26 Hz) (see Fig. A4.6). The filters also served as buffers to isolate the multiplexer from the magnetometer by limiting the voltage input to less than 12 volts (\pm).

Because of the loss of significant amounts of data during the 1969 field season due to power failures, an automatic restart module was designed and installed at each station. Immediately following any power failures the restart process for the digital system was automatically carried out. Also the WWVB time signal was recorded immediately following the power failure to increase the timing reliability.



ALIASING FILTER RESPONSE

A4.6 Frequency response of the aliasing filters for the 1969 field season.
The cutoff frequency was changed to 0.17 Hz for the 1970 field season.

APPENDIX A5 INTERPRETATION OF MODEL CURRENT SYSTEMS WITH A HYPOTHETICAL LINE OF STATIONS

In this appendix we show examples of reproduction of theoretical profiles obtained by assuming that model current systems with different latitudinal current distributions were observed by a hypothetical line of stations with the same distribution in latitude as our line of stations. Latitude plots were made using the values obtained from three different current systems, each positioned at different latitudes. Latitude profiles were then interpreted from these plots in the same manner as the actual data from our line of stations, thereby, allowing a comparison to be made with the original theoretical profiles. For this exercise we assumed all stations to be in operation.

The first example is shown in Fig. A5.1. Profile A is the theoretical profile whereas profiles B, C and D are the interpreted profiles for the model current system located at 67.5° , 70.0° and 72.5° respectively. The interpreted profiles for the model current system at these three different latitudes agree reasonably well with the theoretical profile. The value of H at 70° in profile C was inferred from the value of H and Z at the southern and northern stations. For the

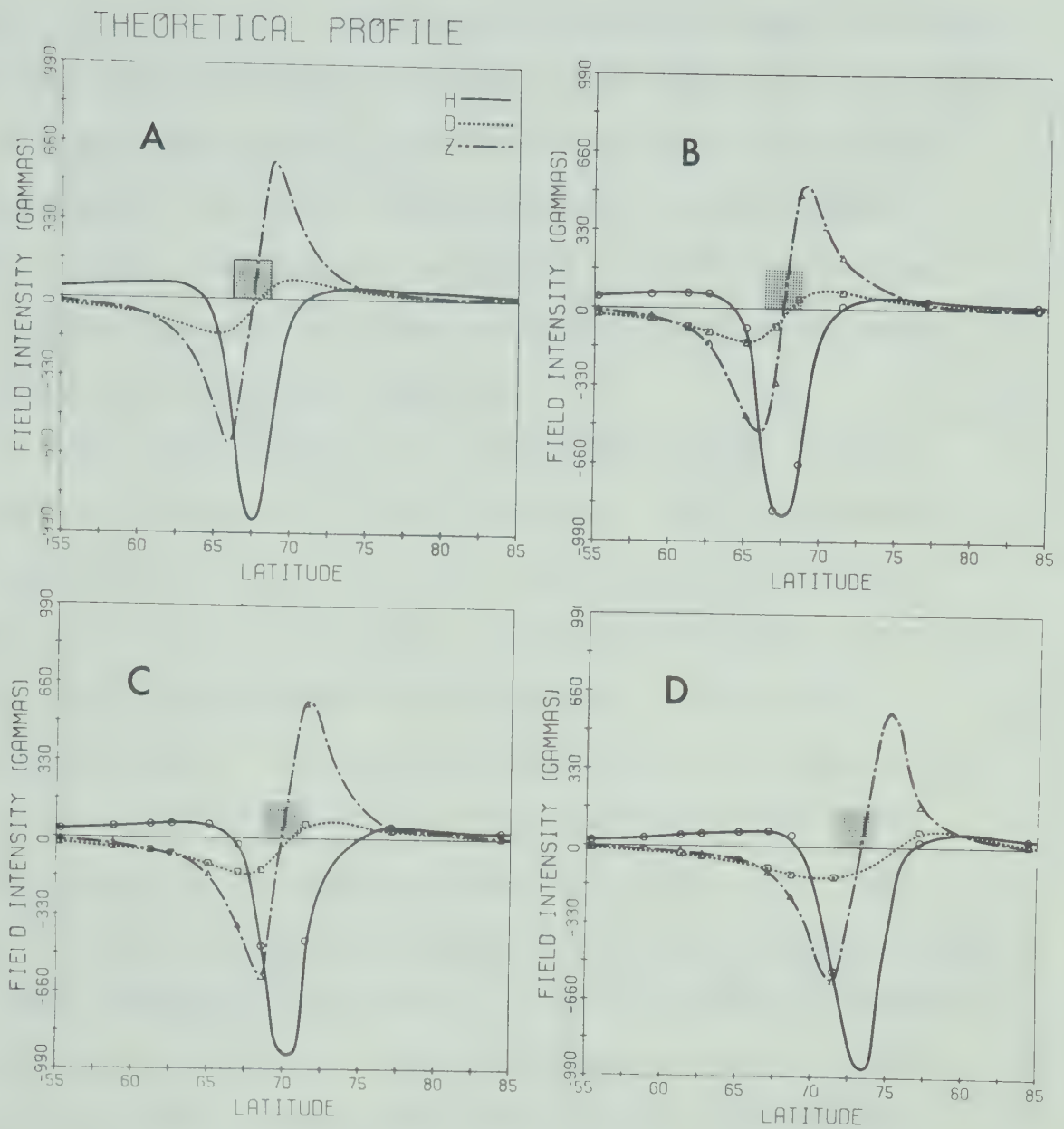


Fig. A5.1 Series of latitude profiles showing the theoretical profile followed by interpreted profiles using data from a hypothetical line of stations observing the same current system located at various latitudes.

current system at 72.5° the interpretation was more difficult due to the lack of stations between 71.4° and 77.0° . In the present study the magnetic data from Baker Lake has proved to be invaluable for the interpretation of high latitude current systems even though the station is 18° east of our line. Again for profile D the interpretation was based on the southern and northern stations.

Fig. A5.2 shows the results for a wide current system with an enhanced northern border. For this example the reproduction is very good for the current system being located at all latitudes shown. This is not however the case for the double current system shown in Fig. A5.3. Although profile B is in good agreement with the theoretical profile, the interpretation was more difficult when the current system was located at higher latitudes. In fact profile D completely misrepresents the actual current system. Thus, when the interpretation of a current system is dependent upon stations at lower or higher latitudes, such an interpretation may fail to show the more complex distributions in the current flow along the auroral oval (i.e. double current systems).

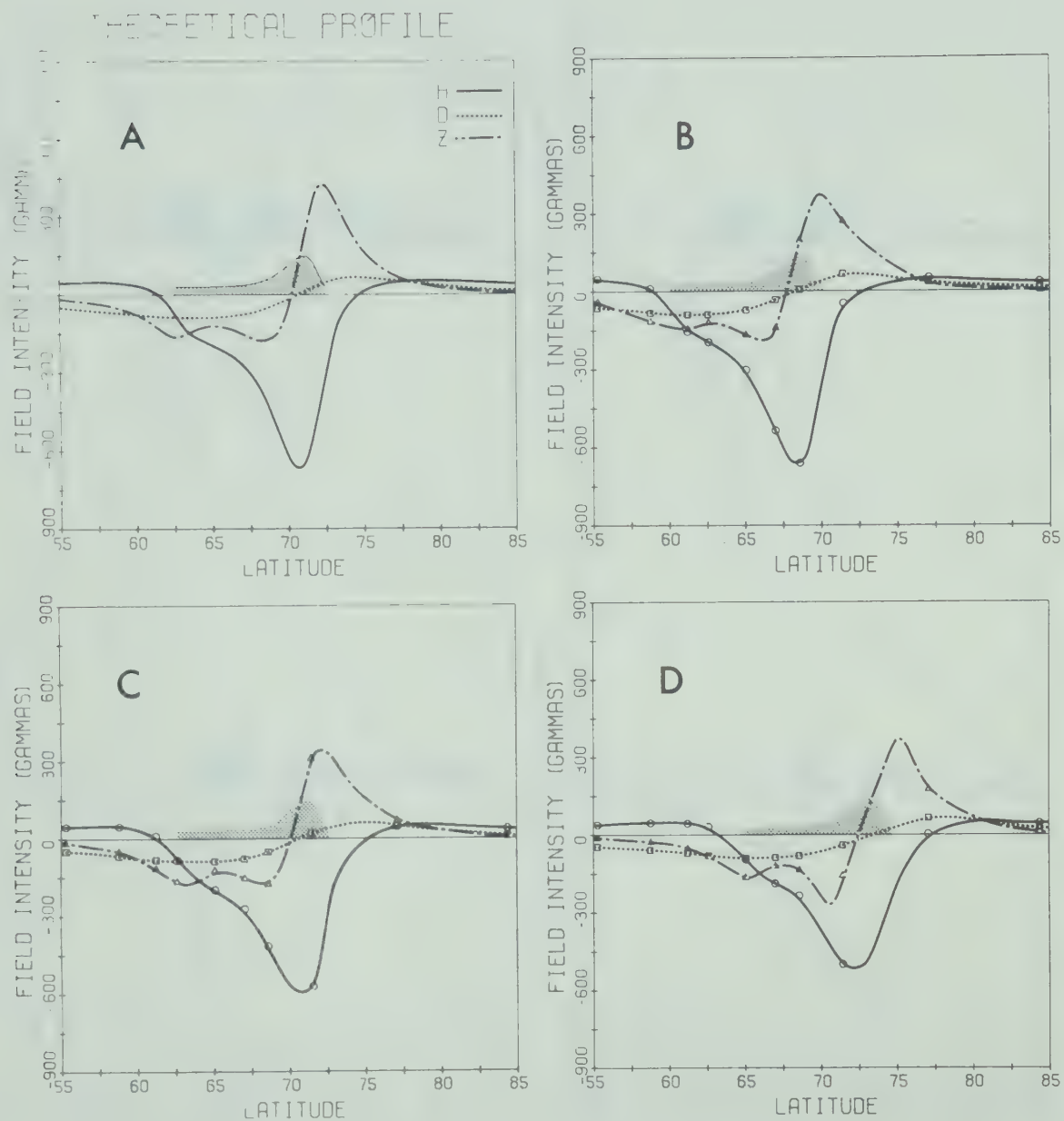


Fig. A5.2 Same as Fig.A5.1 but for a wide model current system with an enhanced northern border.

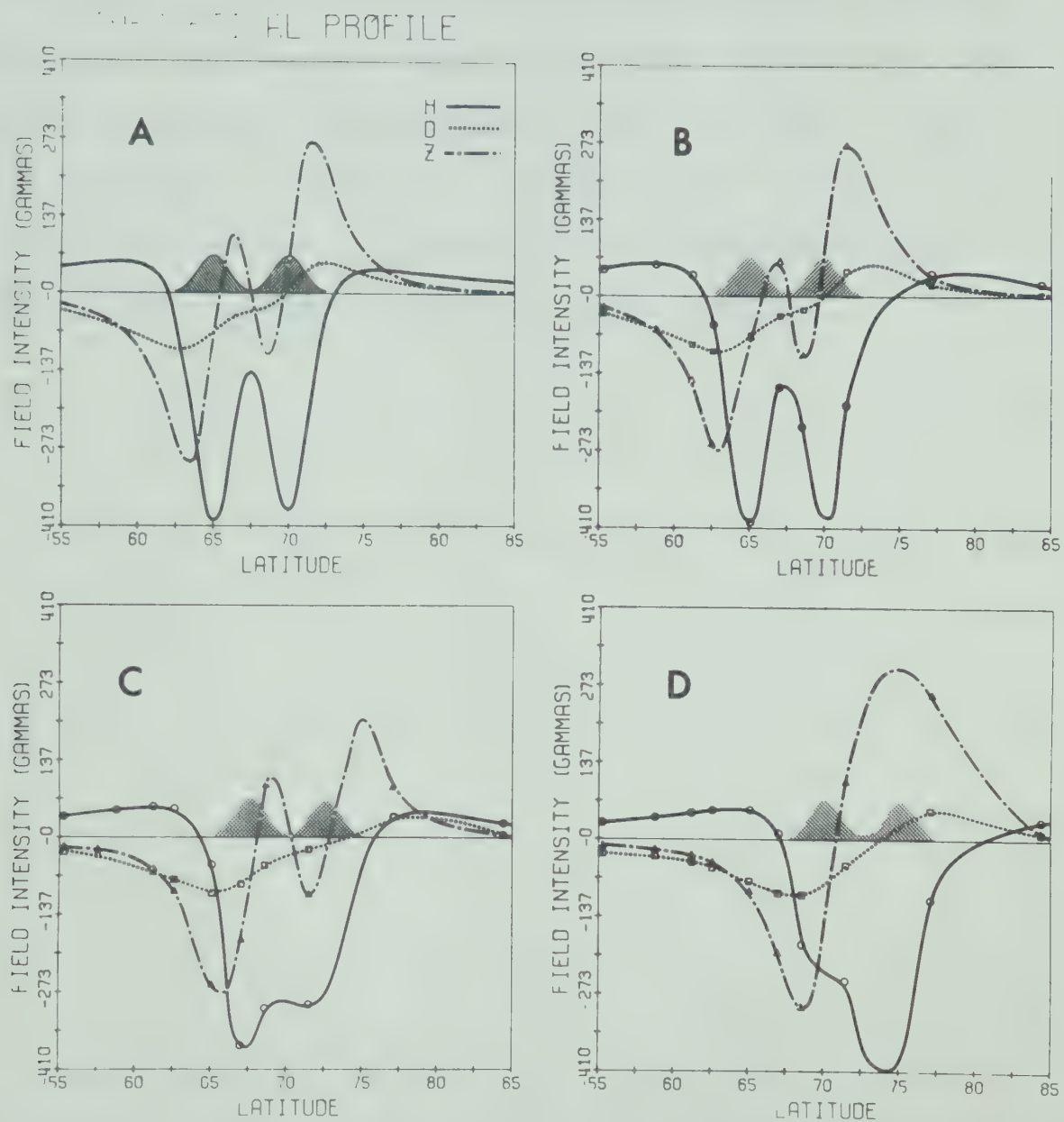


Fig. A5.3 Same as Fig. 5.1 but for a double current system.

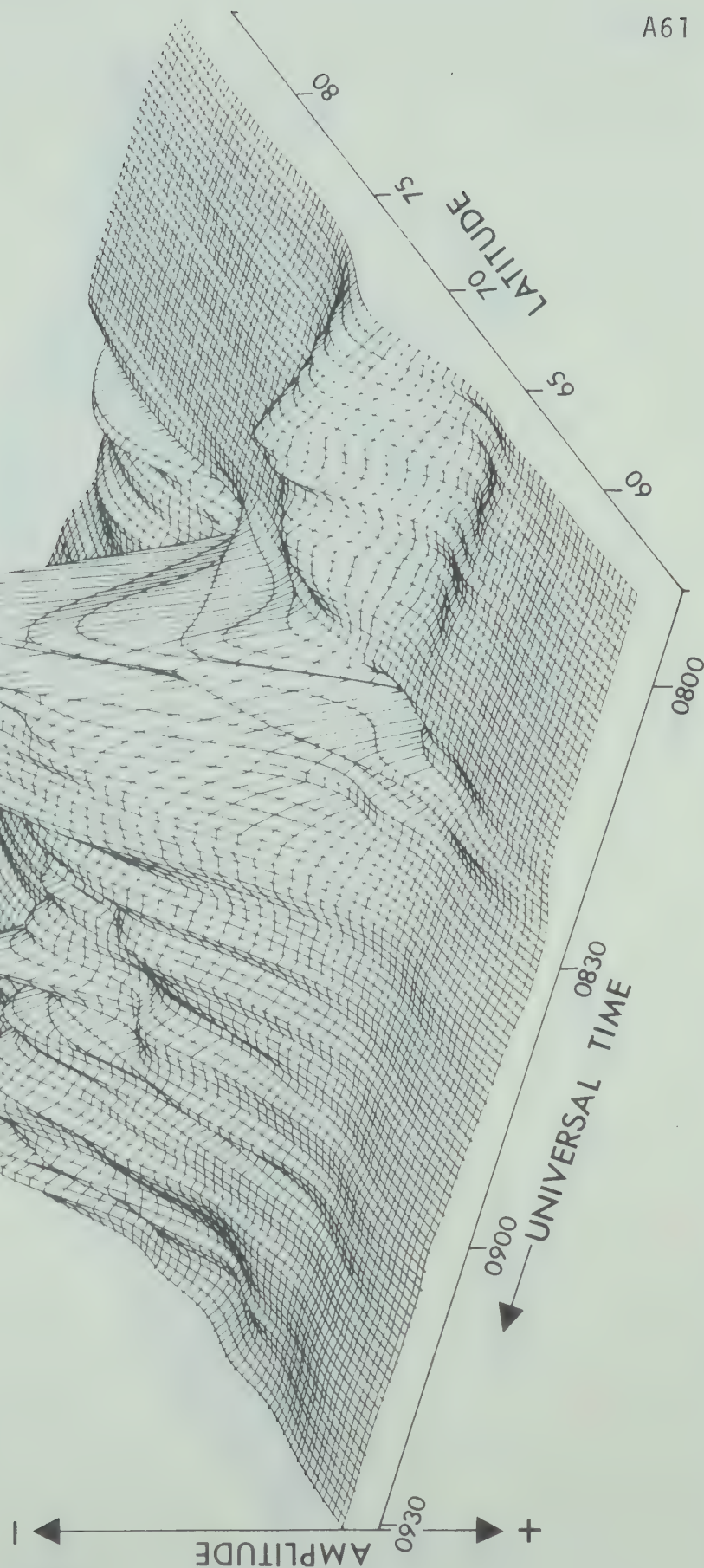
Even though the resolution of our line of stations is difficult to ascertain since the interpretation between stations for one component may be accomplished with the aid of other components either or both north and south of this particular regime, we feel the results of the foregoing exercise enhances our confidence in the interpretation of actual current systems presented in this thesis.

APPENDIX A6 THREE-DIMENSIONAL DIAGRAMS

In this appendix we present a selection of three-dimensional (3-D) diagrams of some of the polar magnetic substorms discussed in Chapters IV and V. It should be noted that the sign of the H component has been reversed. Hence a westward electrojet has the appearance of a mountain or mountain range while an eastward electrojet has the appearance of a valley. The amplitude scales on these plots are different for all components. Therefore a comparison between the relative amplitudes of different components can not be made with these particular diagrams.

H-COMP.

JULY 14, 1970

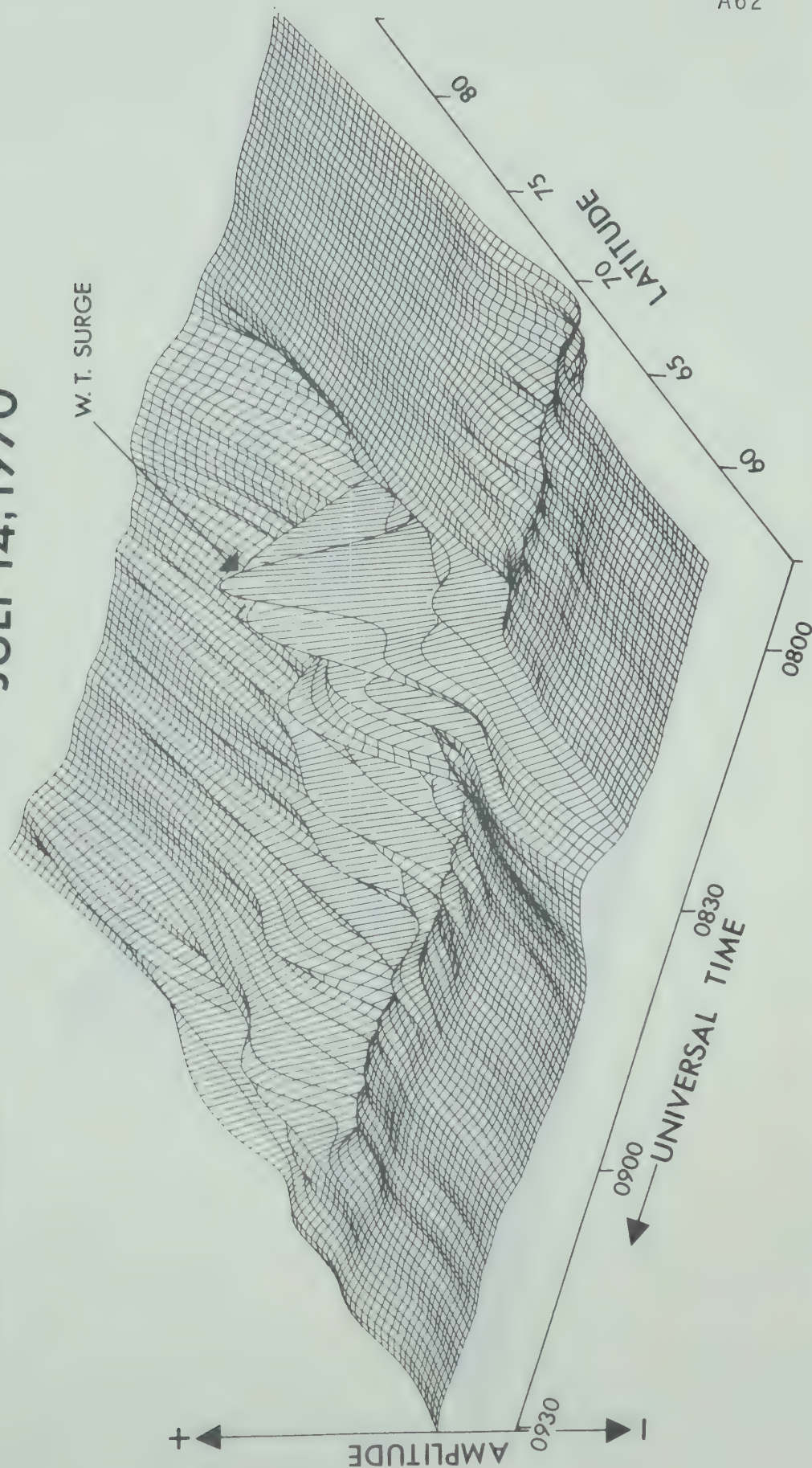


A61

Fig. A6.1 The H component 3-D diagram for the substorm that occurred on July 14, 1970 (Day 195).

D-COMP.

JULY 14, 1970

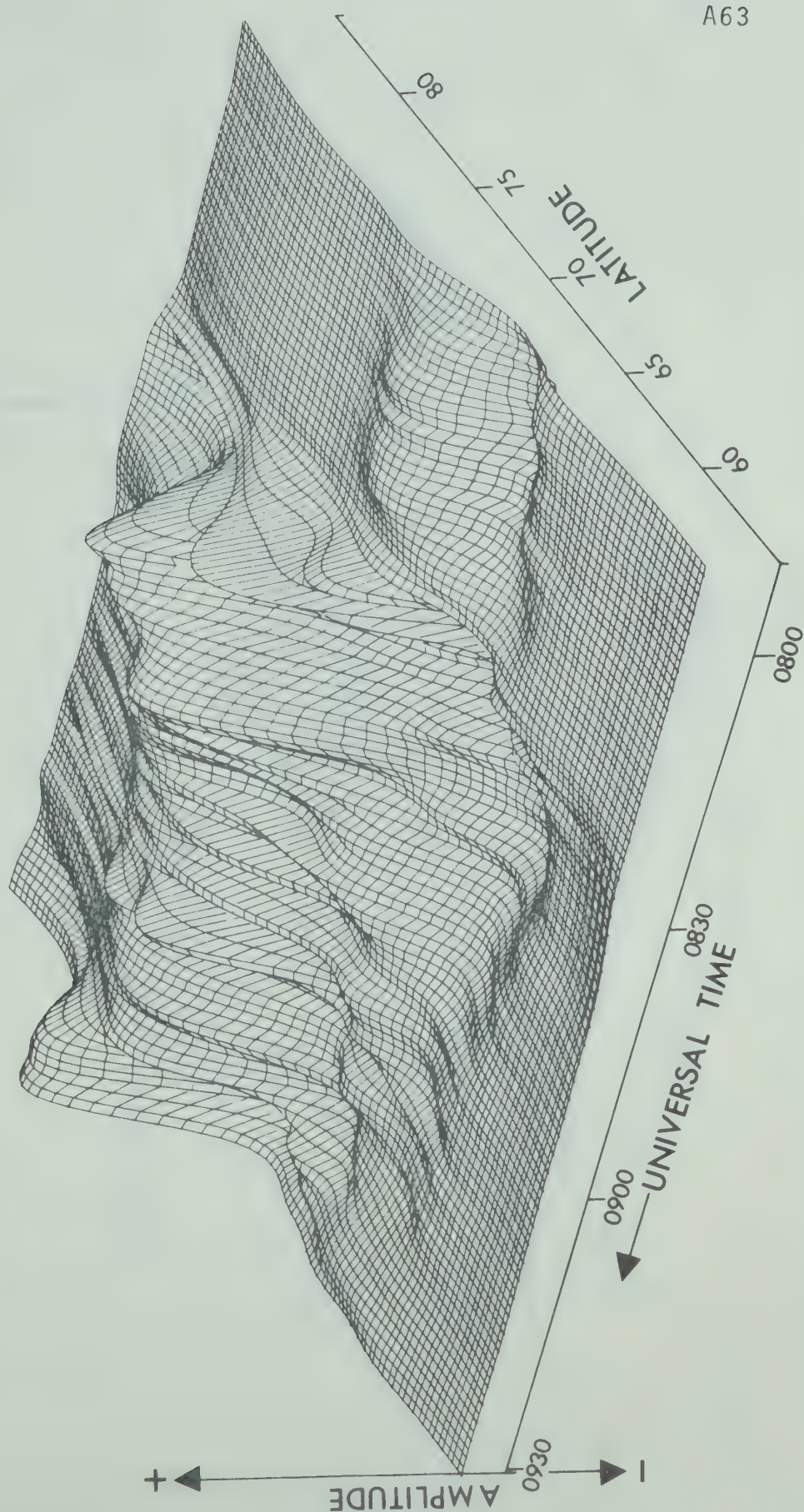


A62

Fig. A6.2 Same as Fig. A6.1 but for the D component. Note the +D perturbation due to an inferred westward travelling surge.

Z-COMP.

JULY 14, 1970



A63

Fig. A6.3 Same as Fig. A6.1 but for the Z component.

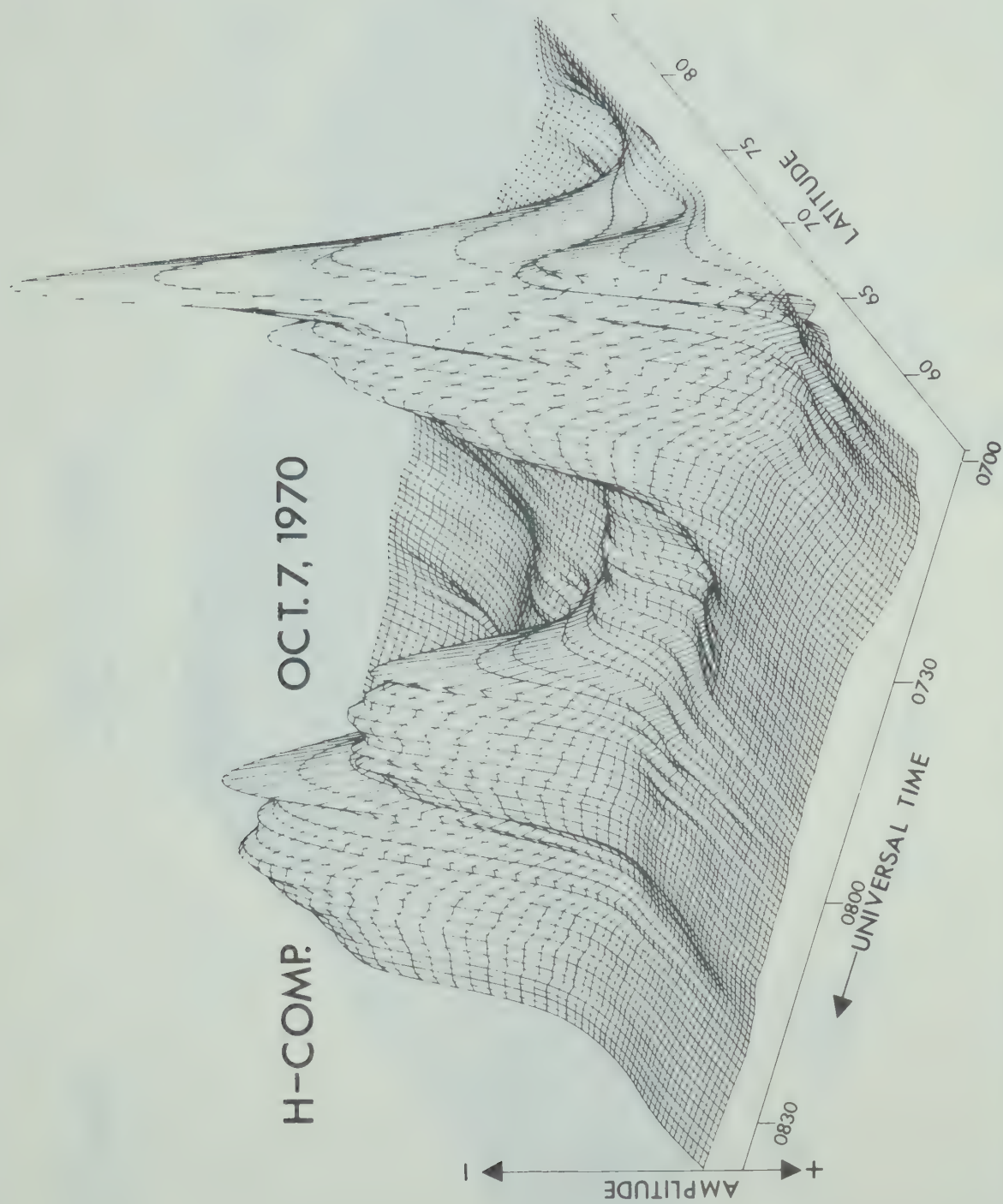
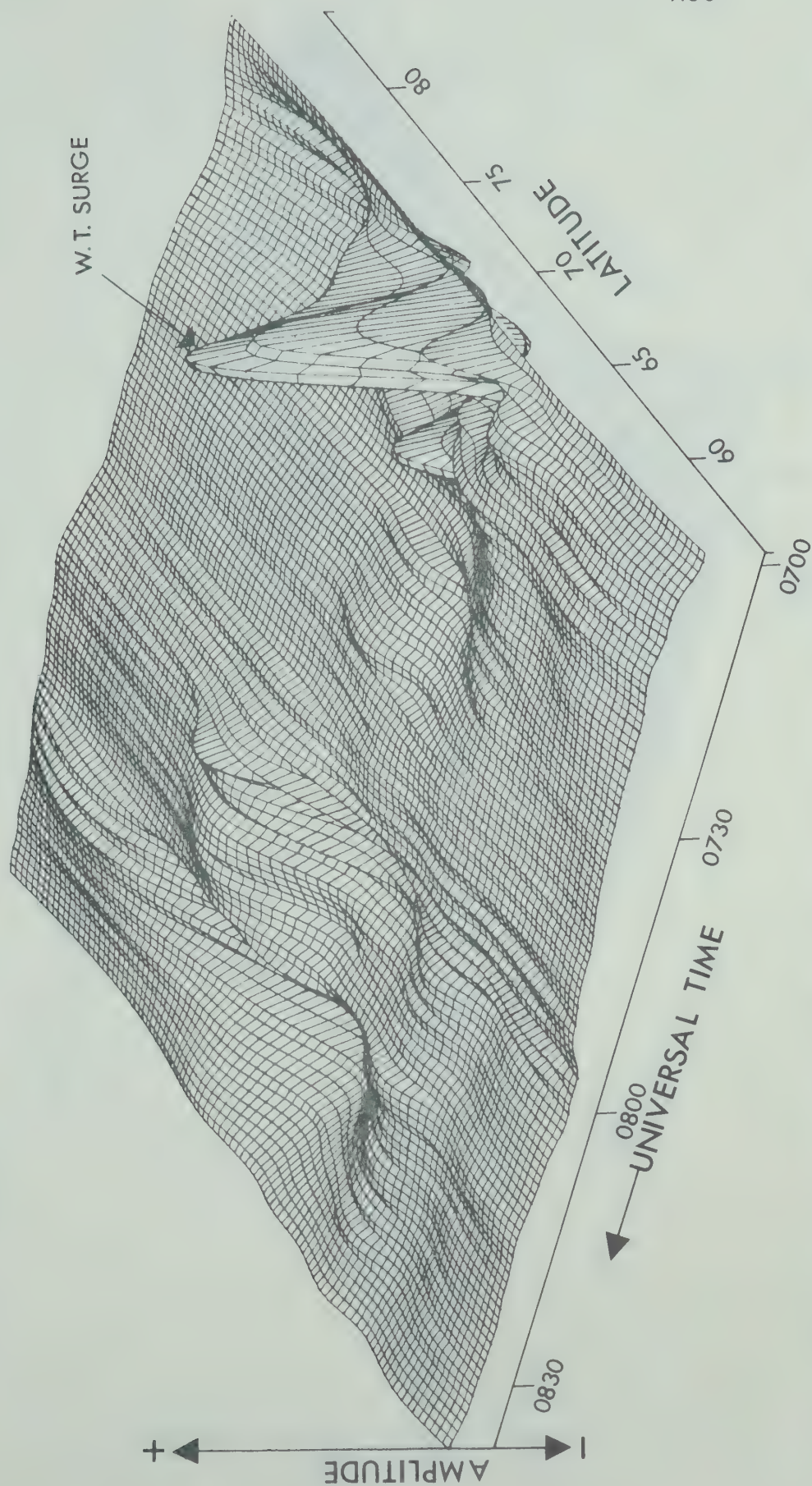


Fig. A6.4 The H component 3-D diagram for the series of substorms that occurred on October 7, 1970.

D-COMP.

OCT. 7, 1970

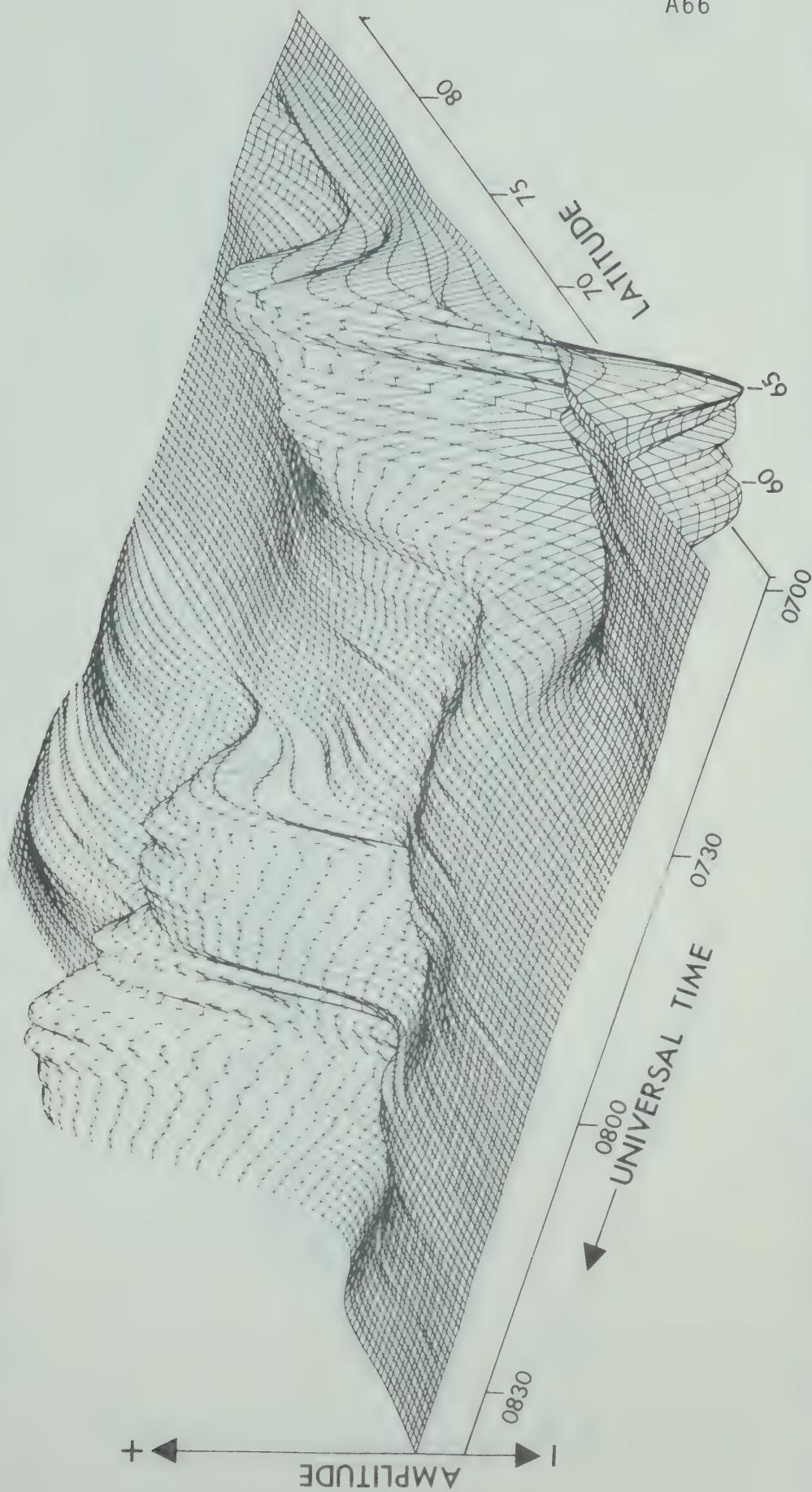


A65

Fig. A6.5 Same as Fig. A6.4 but for the D component. Note the +D perturbation associated with the westward travelling surge.

Z-COMP.

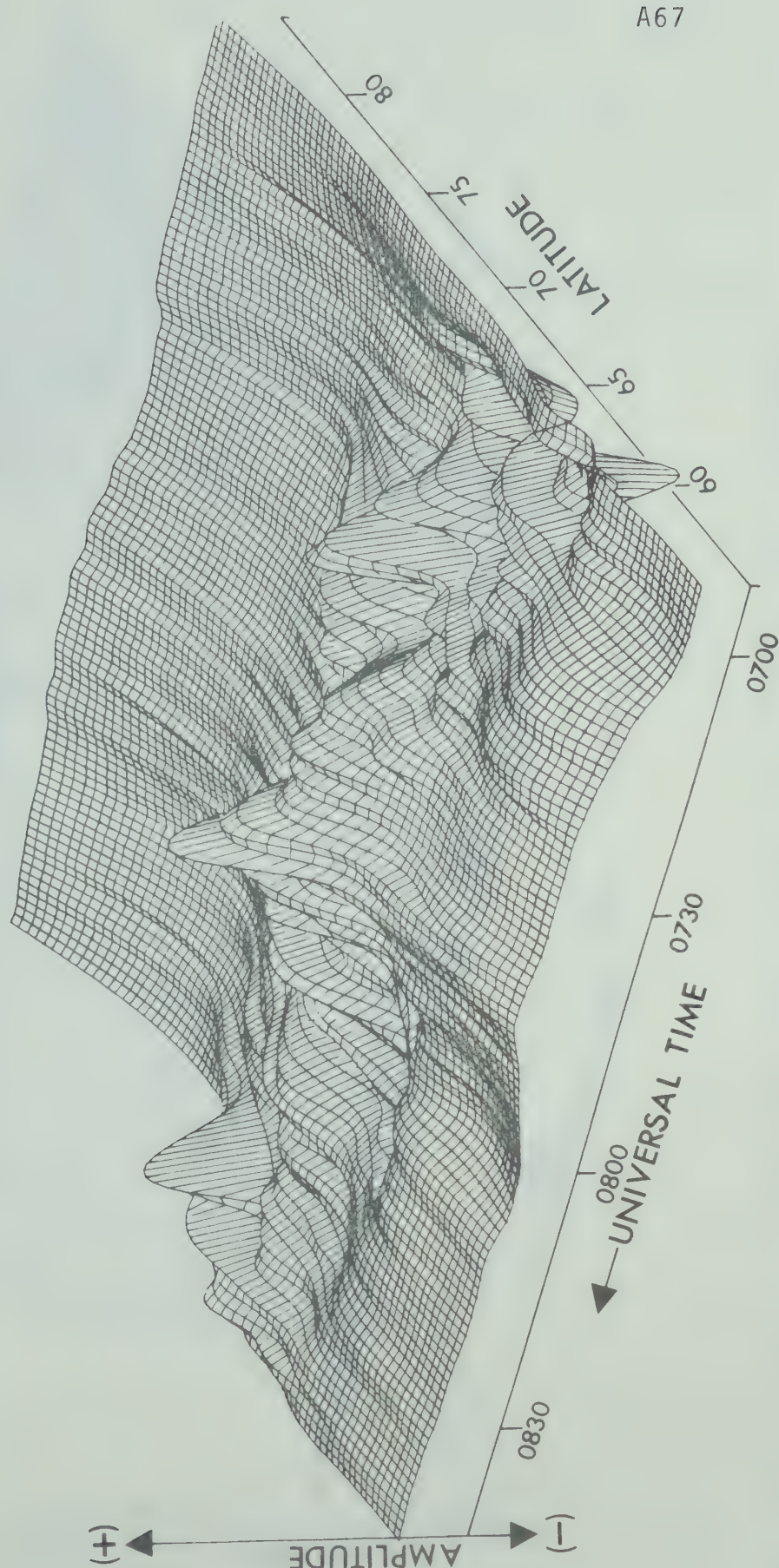
OCT. 7, 1970



A66

Fig. A6.6 Same as Fig. A6.4 but for the Z component.

D-COMP. SEPT. 1, 1970

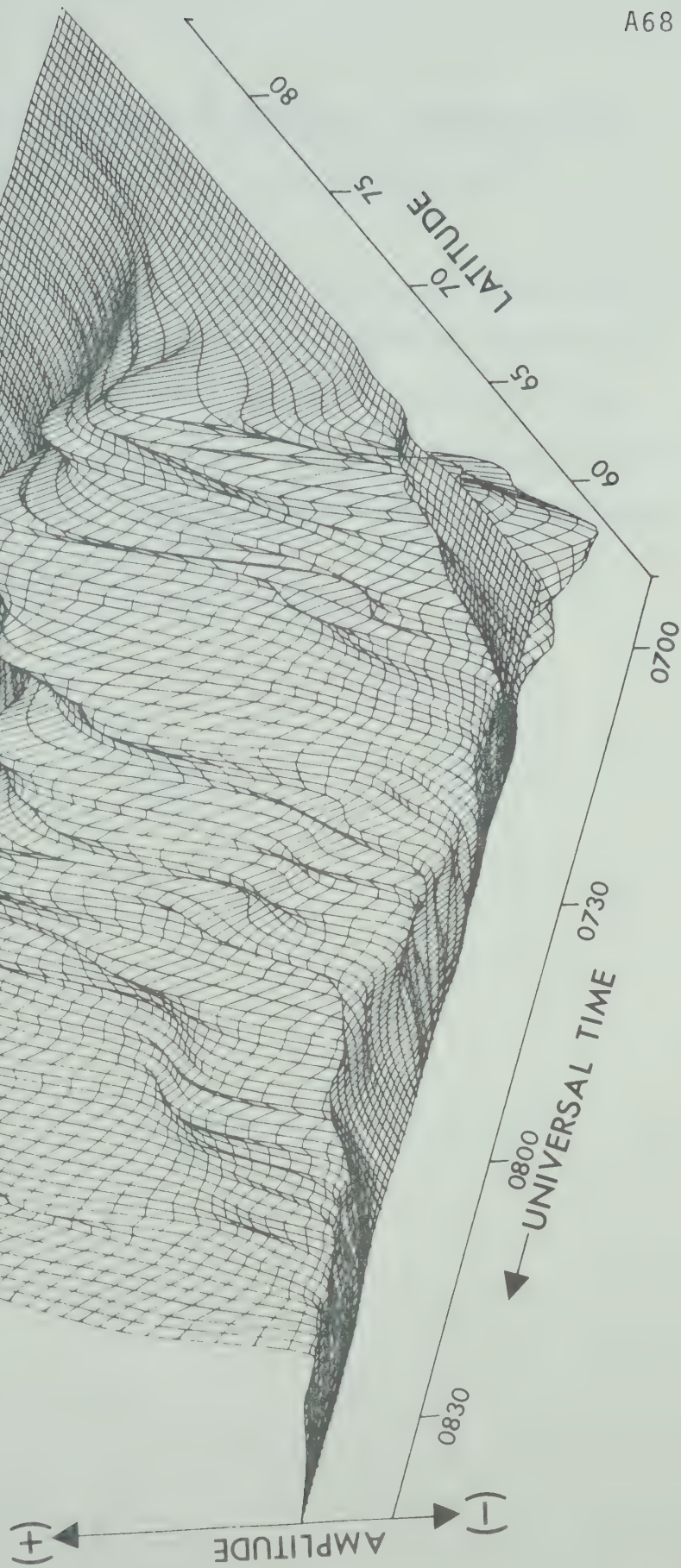


A67

Fig. A6.7 The D component 3-D diagram for the substorm that occurred on September 1, 1970. Note the +D perturbations associated with eastward and westward propagating auroral forms.

SEPT. 1, 1970

Z-COMP.



A68

Fig. A6.8 Same as Fig. A6.7 but for the Z component.

APPENDIX A7 MORE EXAMPLES OF MAGNETIC PERTURBATIONS
ASSOCIATED WITH POLAR ELECTROJETS

Several examples of polar magnetic substorm events and magnetic perturbations associated with eastward electrojets are presented in this appendix. Two latitude profiles for each event are also included. The Kp indices for the days represented in this appendix are listed in Table A7.1.

Table A7.1 Kp indices for the days represented in
this appendix

Day	Three-hour range indices Kp								Sum
	1	2	3	4	5	6	7	8	
170	2+	2+	2o	2-	1-	1+	2+	3	16
181	1o	1+	3-	1+	1o	1o	1-	1o	10
183	1+	2+	4+	3+	2+	2o	1-	1+	18-
189	1+	2-	1+	1o	2-	1+	1o	5	14+
190	4	7-	5+	5+	7+	6o	6o	7-	47+
193	3+	3+	2+	3-	2+	2+	4-	3+	23+
196	2-	2-	1o	2o	1+	1o	1o	2-	11+
261	3o	3o	3+	2-	2o	2+	2o	2-	19
262	1o	5-	4o	3+	2+	3	2+	3	25-

Fig. A7.1 Component magnetograms for June 19, 1970 (0430-0800 UT). The existence of a substantial $-Z$ perturbation at FTSM and FTCH and the $+Z$ perturbation at CAMB prior to 0445 UT are indicative of a westward electrojet between CAMB and FTSM. Note the large $+D$ perturbation at FTSM at ~ 0600 UT. This was probably associated with a westward travelling surge.

Fig. A7.2 Component magnetogram for June 19, 1970 (0830-1200 UT). This is an example of a large bay type event commonly seen in the post midnight sector.

Fig. A7.3 Latitude profiles for the events shown in Fig. A7.1 and A7.2. Note the similarity between the H and D profiles at 0610 UT. The electrojet was probably orientated in the NW-SE direction at this time. We have observed this effect several times, especially in the evening sector.

Fig. A7.4 Component magnetograms for June 30, 1970 (0500-1000 UT). Note the buildup of an eastward electrojet prior to the substorm. This event resembles the event (Day 195) discussed in Chapter IV.

DAY 170

A72

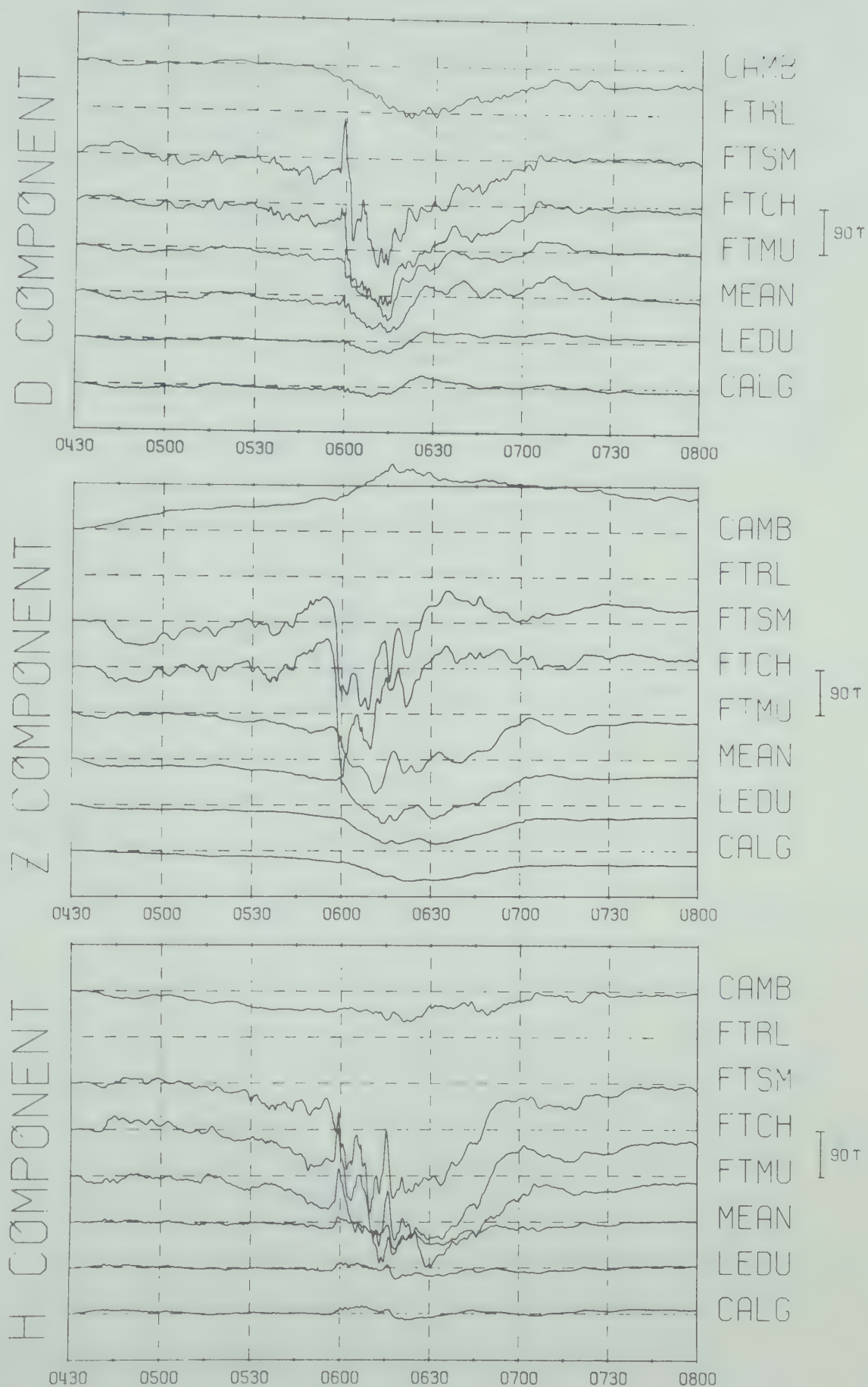


Fig. A7.1

DAY 170

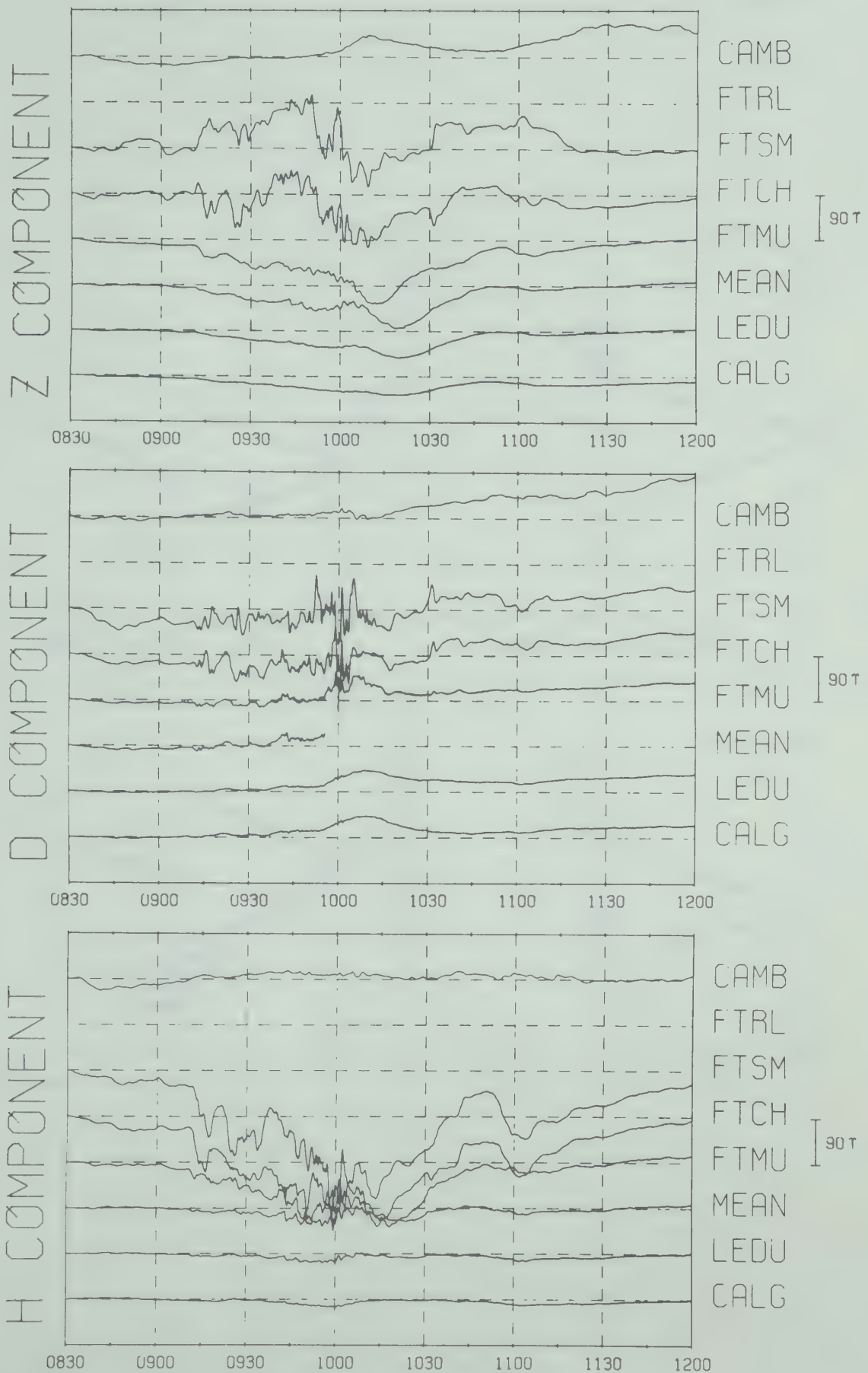


Fig. A7.2

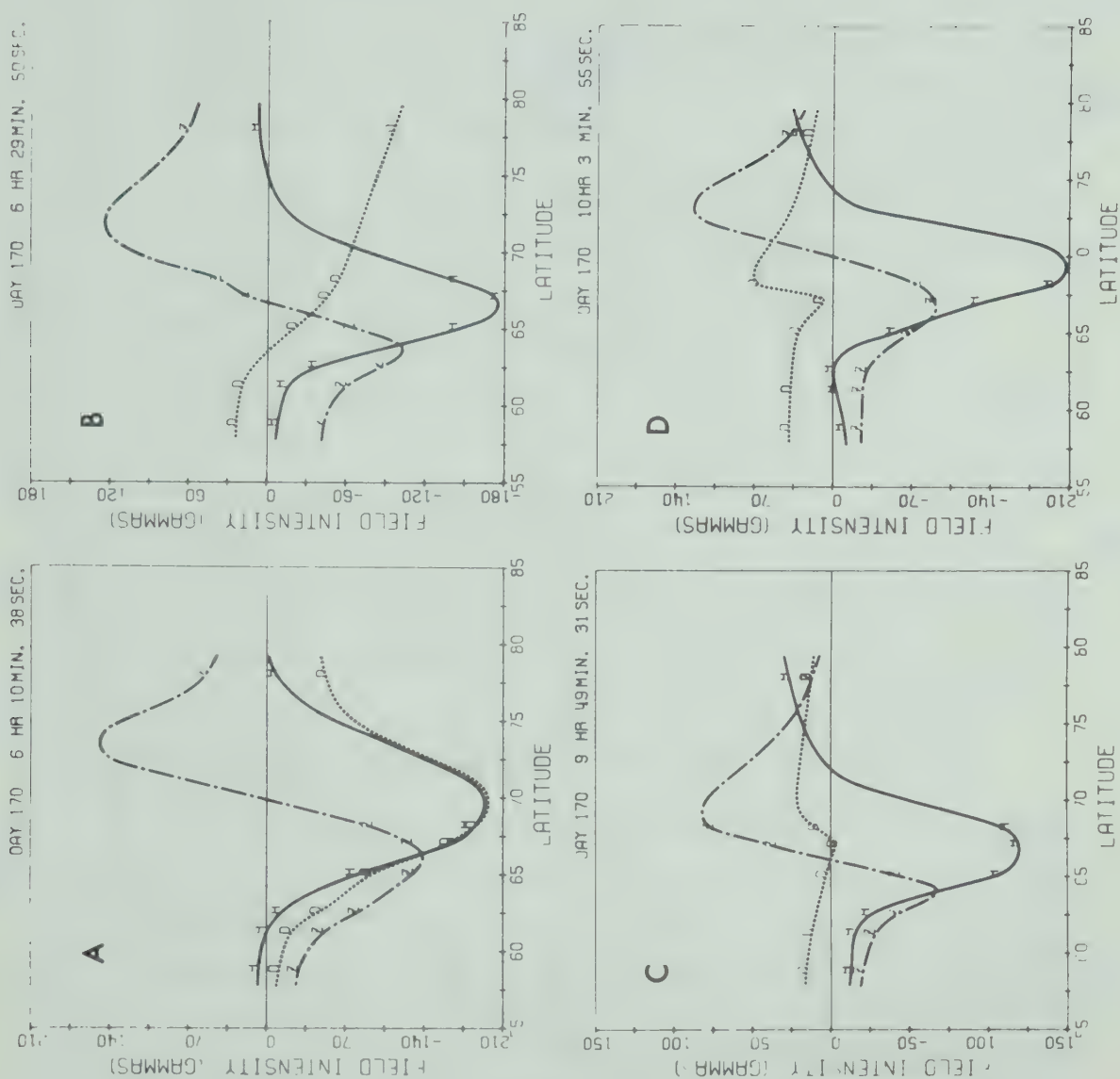


Fig. A7.3

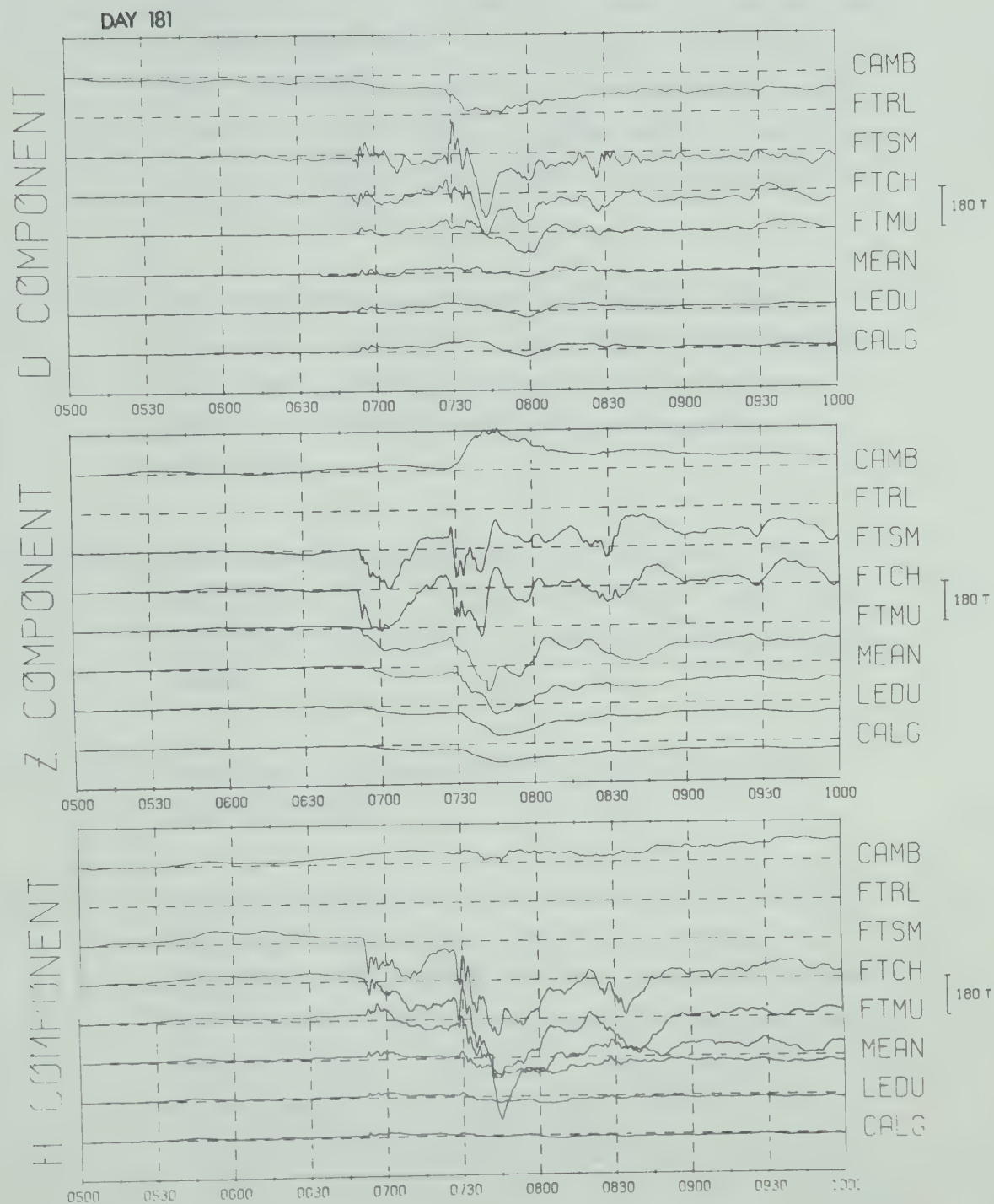


Fig. A7.4

Fig. A7.5 Component magnetograms for September 18, 1970 (0600-1000 UT). Note the transition of the D component from - to + at all latitudes. This particular event was associated with slowly drifting N-S aligned auroral arcs. This D component signature was observed on other occasions.

Fig. A7.6 Latitude profiles for the events shown in Fig. A7.4 and A7.5. Note the development of a new current system at the northern border of the pre-existing electrojet in each case.

Fig. A7.7 Component magnetograms for July 2, 1970 (0615-0915 UT). This particular event was discussed in detail by Kisabeth and Rostoker (1971).

Fig. A7.8 Component magnetogram for July 2, 1970 (0930-1300 UT).

Fig. A7.9 Latitude profiles for the events shown in Fig. A7.7 and A7.8. Profiles A and B illustrate the decay of the northern border leaving the stable portion of the electrojet to the south. Profiles C and D show the enhancement of the northern border of an electrojet in the post-midnight sector.

DAY 261

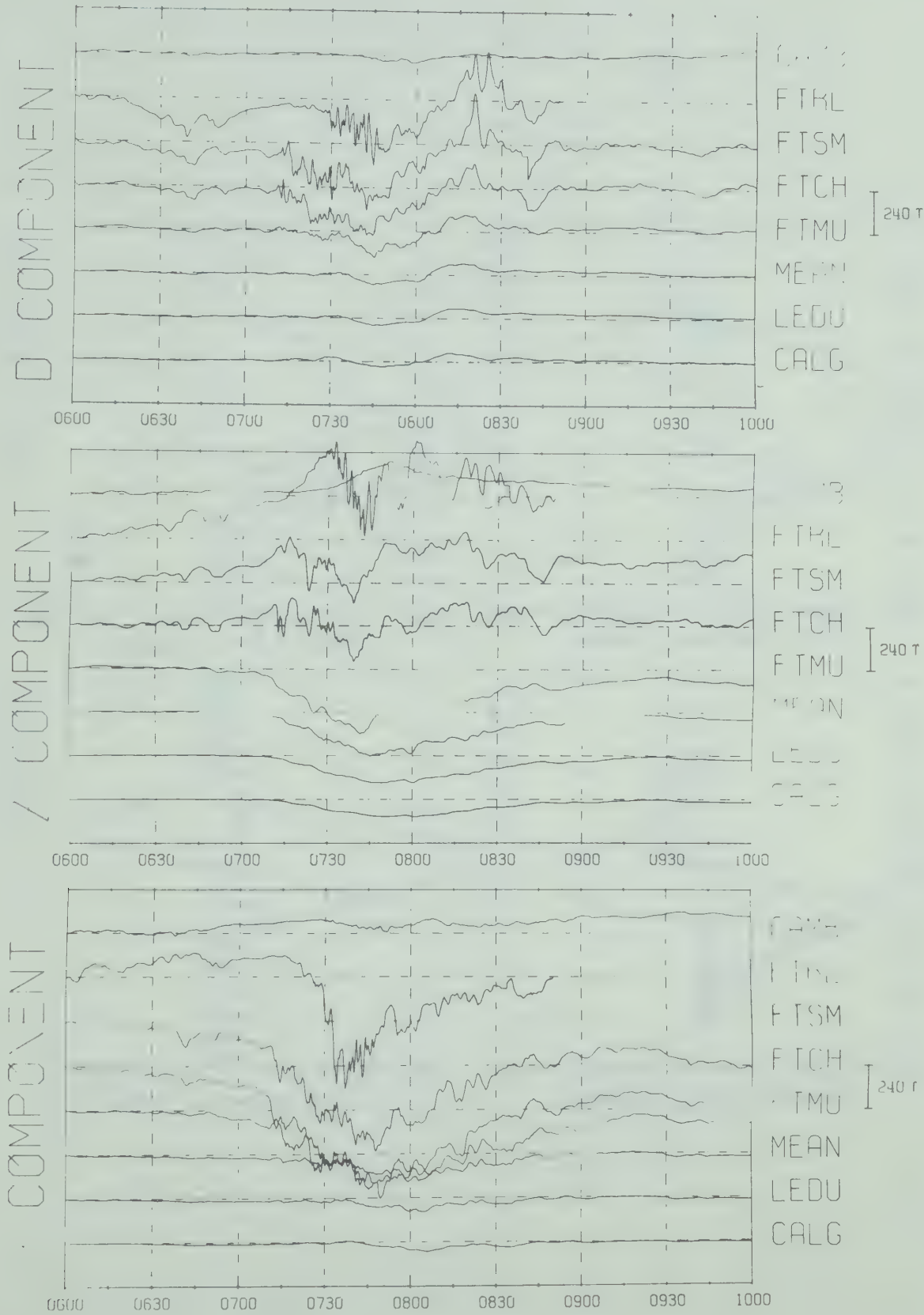


Fig. A7.5

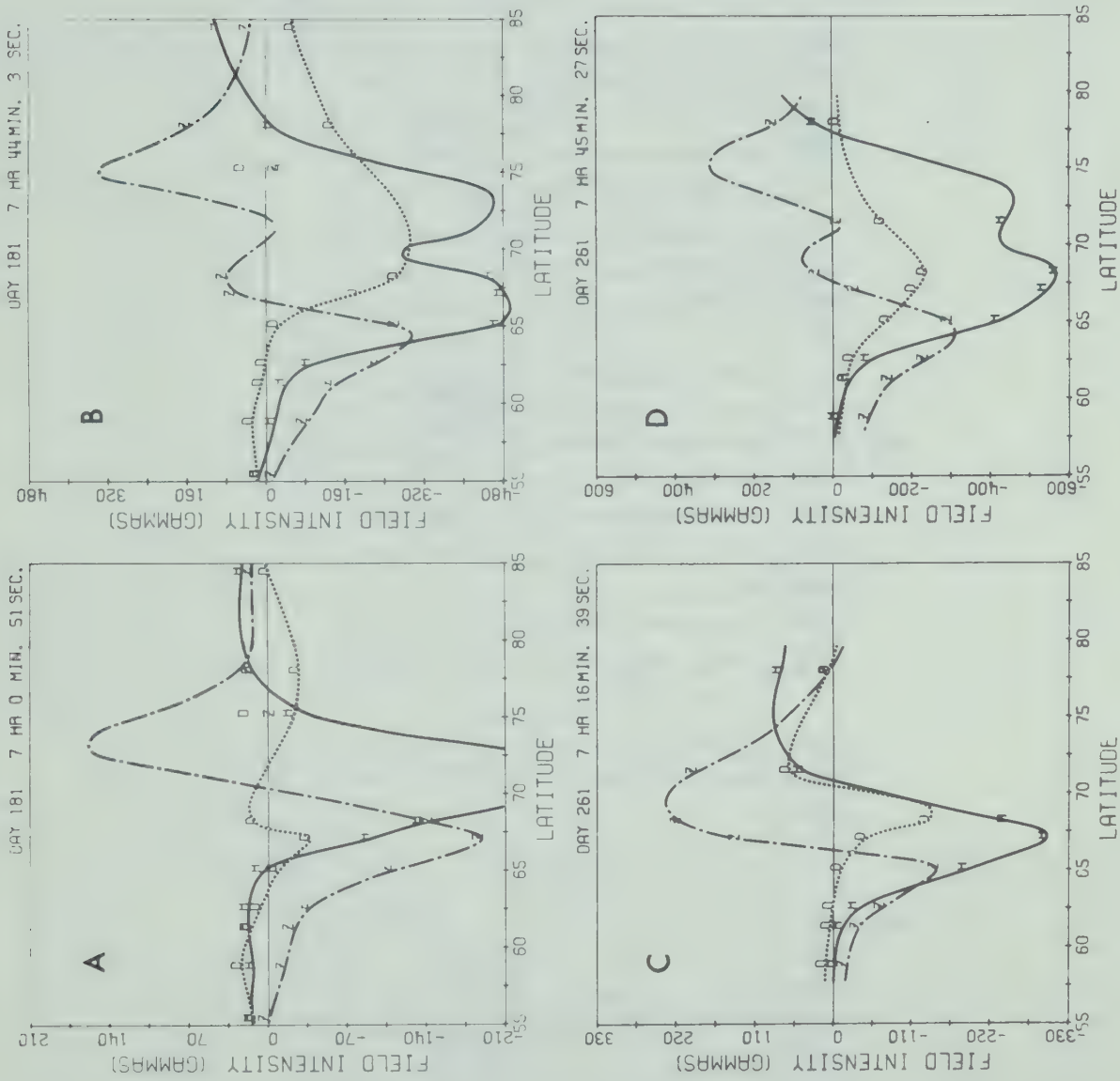


Fig. A7.6

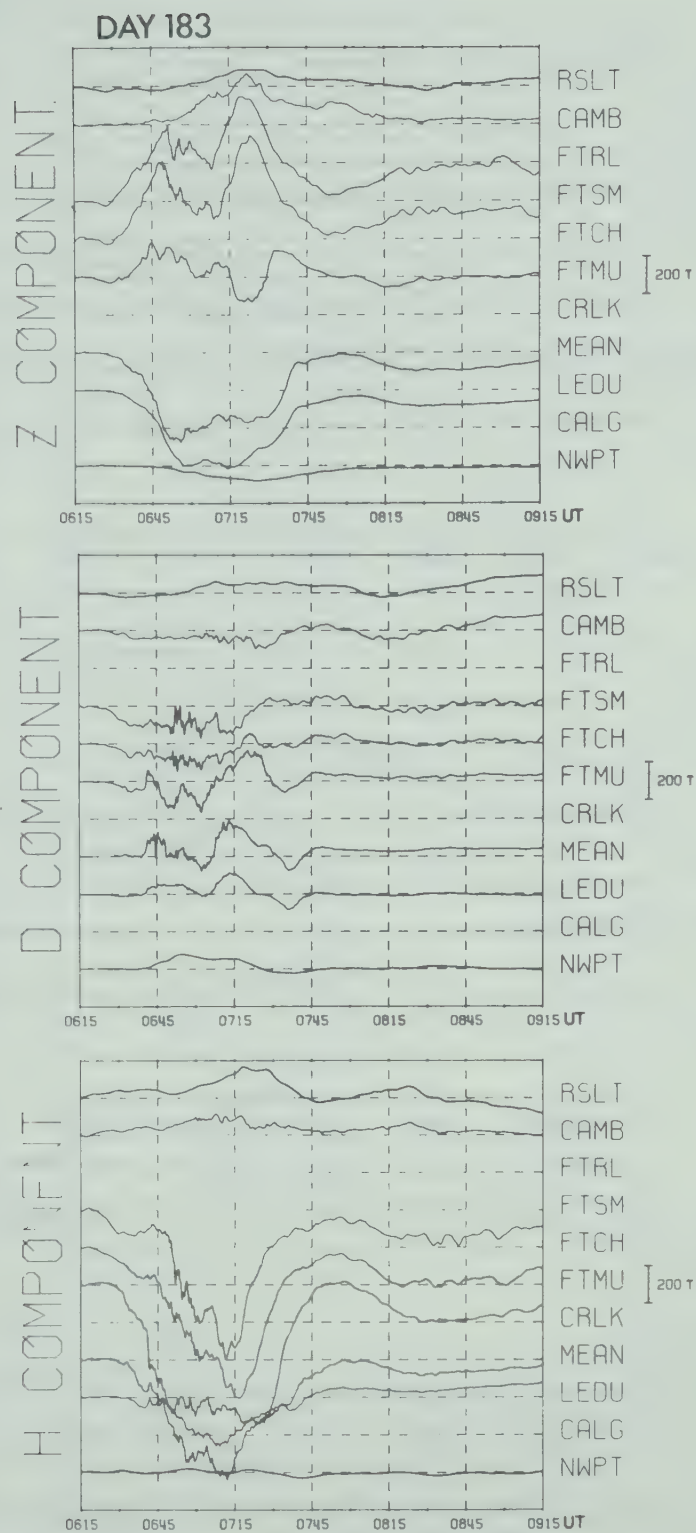
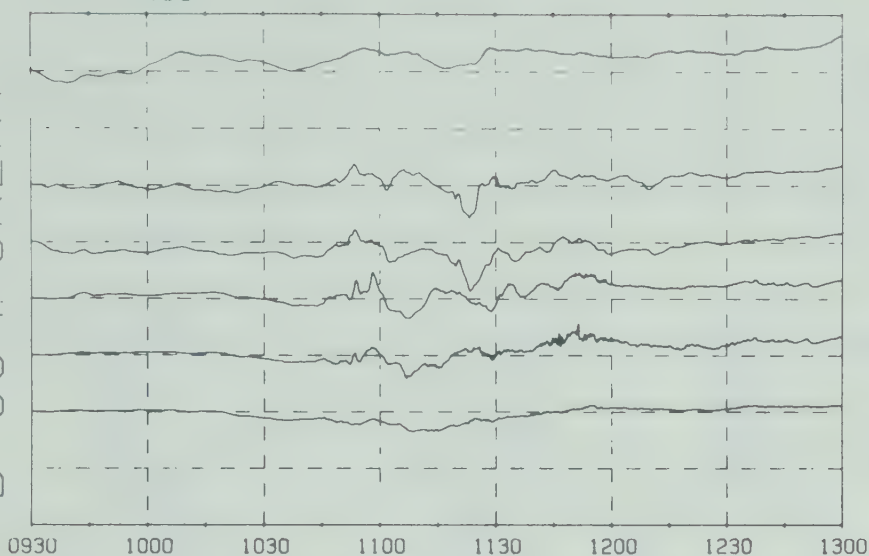


Fig. A7.7

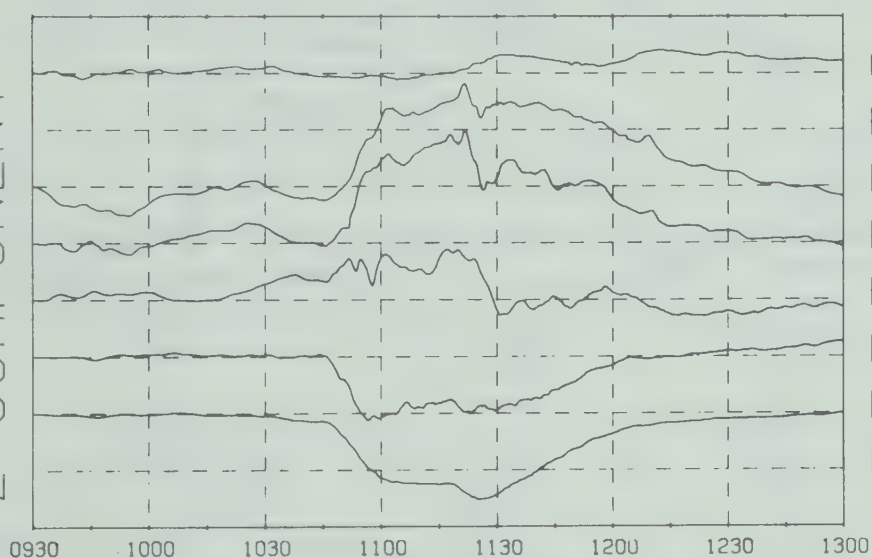
DAY 183

A80

D COMPONENT



Z COMPONENT



H COMPONENT

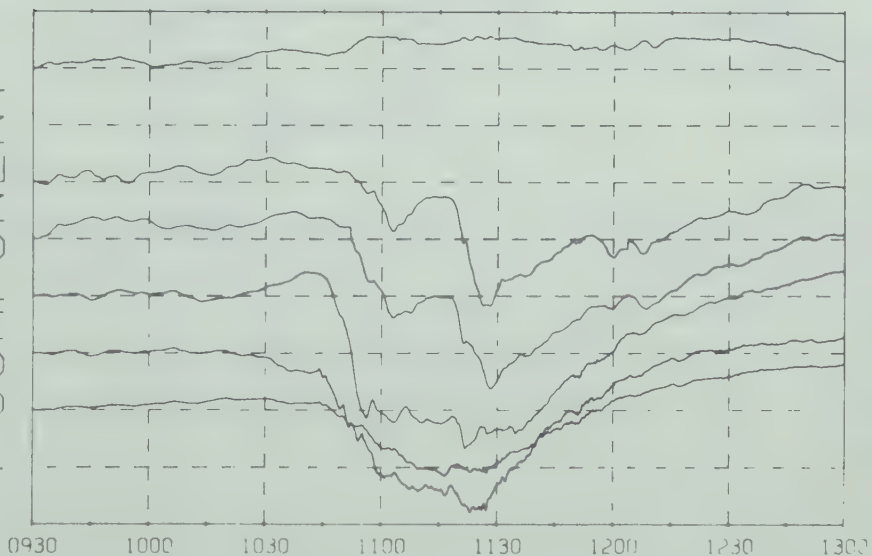


Fig. A7.8

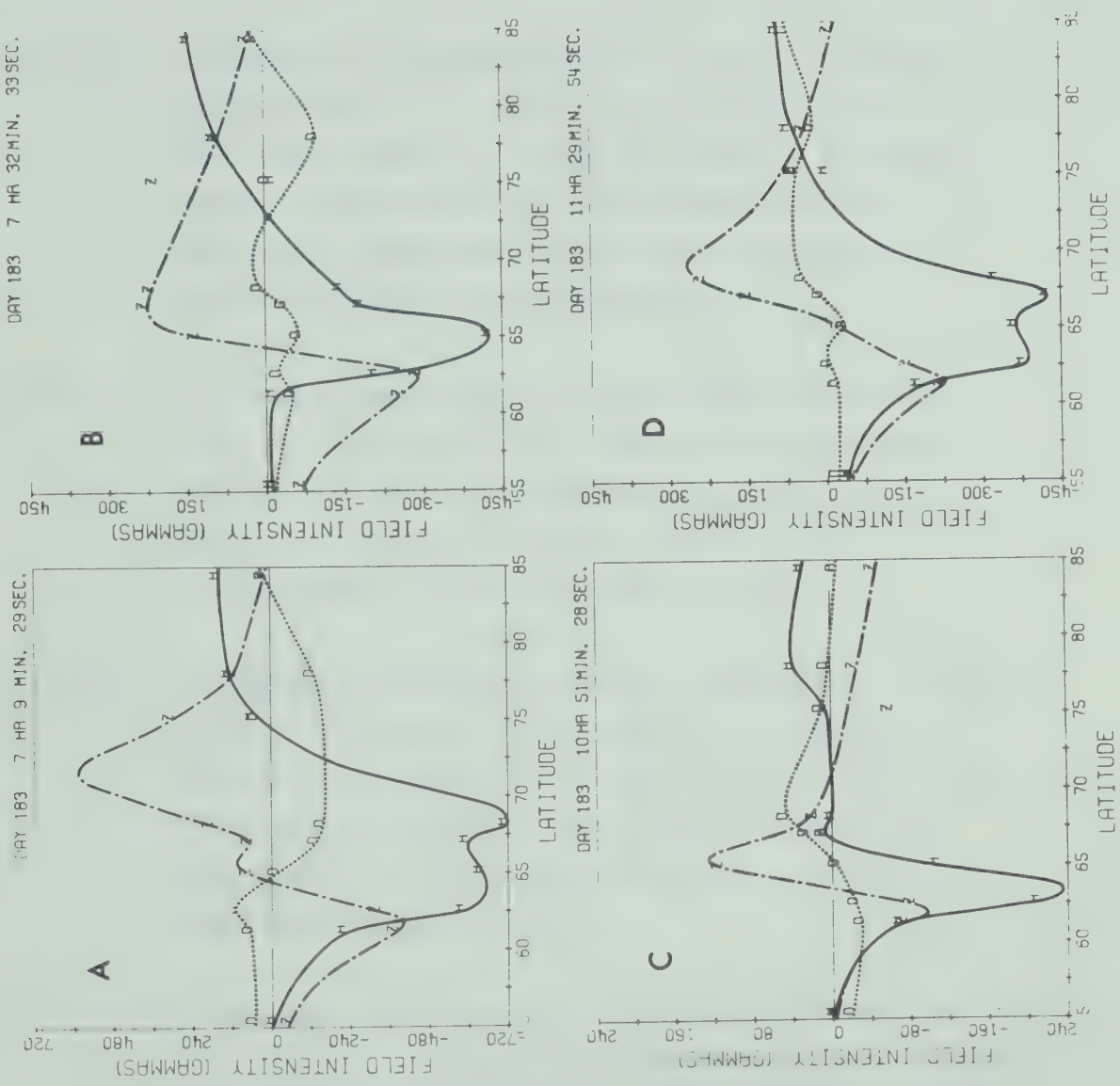


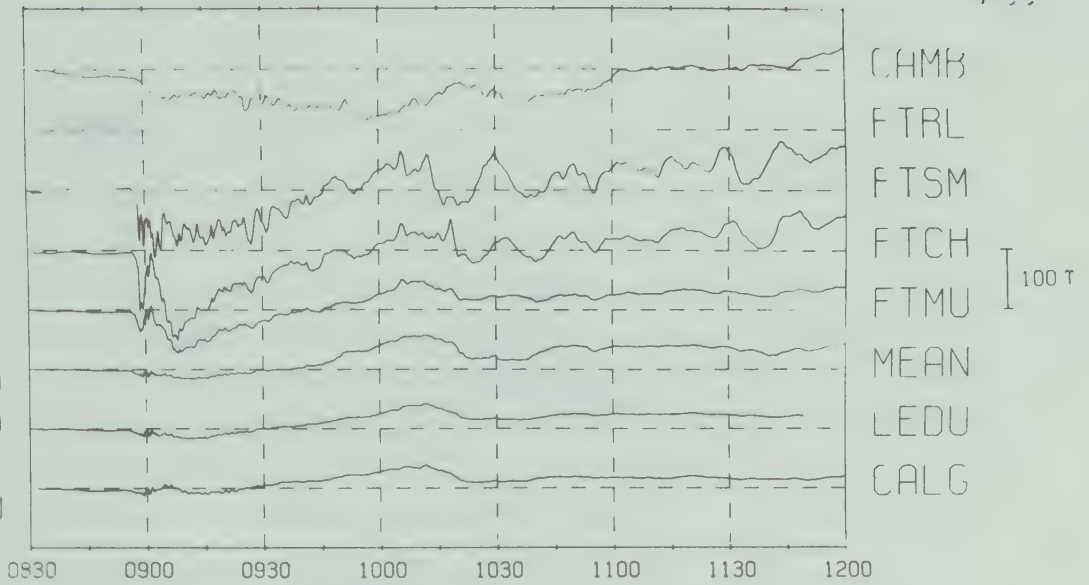
Fig. A7.9

- Fig. A7.10 Component magnetograms for July 15, 1970 (0830-1200 UT). Note the sharp onset and the associated +H perturbations at lower latitudes.
- Fig. A7.11 Component magnetograms for July 12, 1970 (0600-1100 UT). This is an example of a bay type event of long duration. The long period perturbations superimposed upon this bay represent variations in the westward electrojet intensity.
- Fig. A7.12 Latitude profiles for the events shown in Fig. A7.10 and A7.11. Note the northward motion of the Z crossover in profiles A and B. Profiles C and D depict the enhancement of the northern border.
- Fig. A7.13 Component magnetograms for September 19, 1970 (0440-1140 UT). Shown here are examples of substorms occurring in both the evening and midnight sectors. Note the long magnetic bay event (\sim 0630-1130 UT) with a substorm superimposed upon it.
- Fig. A7.14 Latitude profiles for the events shown in Fig. A7.13. Note the development of a double current system in the evening sector as well as in the midnight sector.

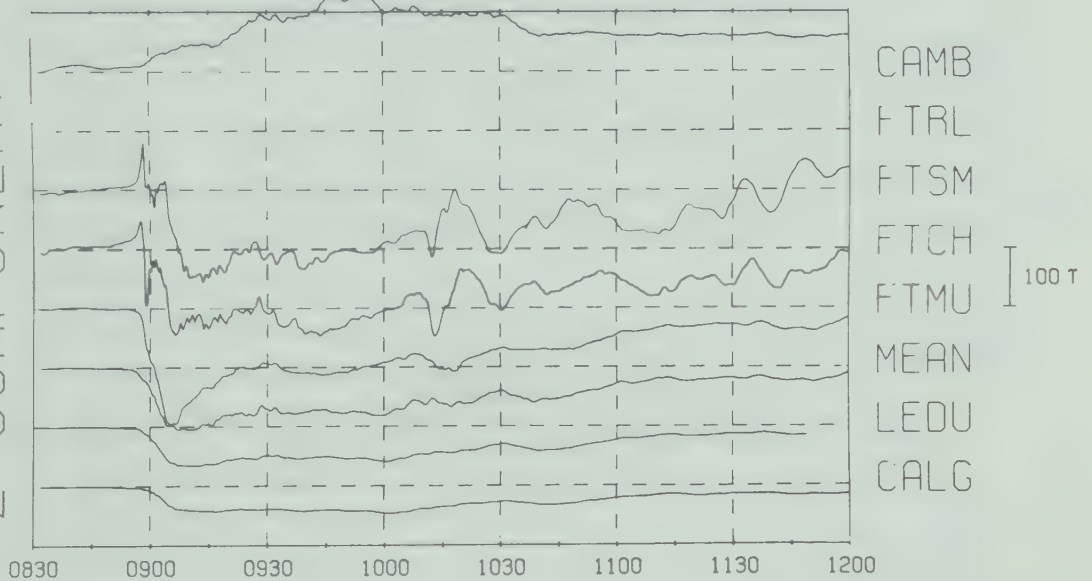
DAY 196

488

U COMPONENT



Z COMPONENT



H COMPONENT

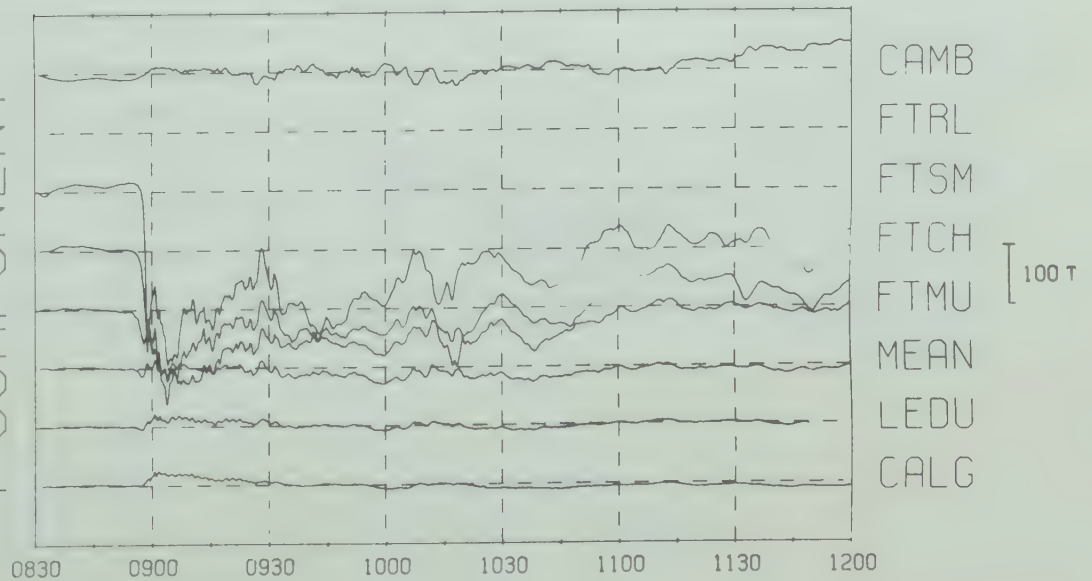


Fig. A7.10

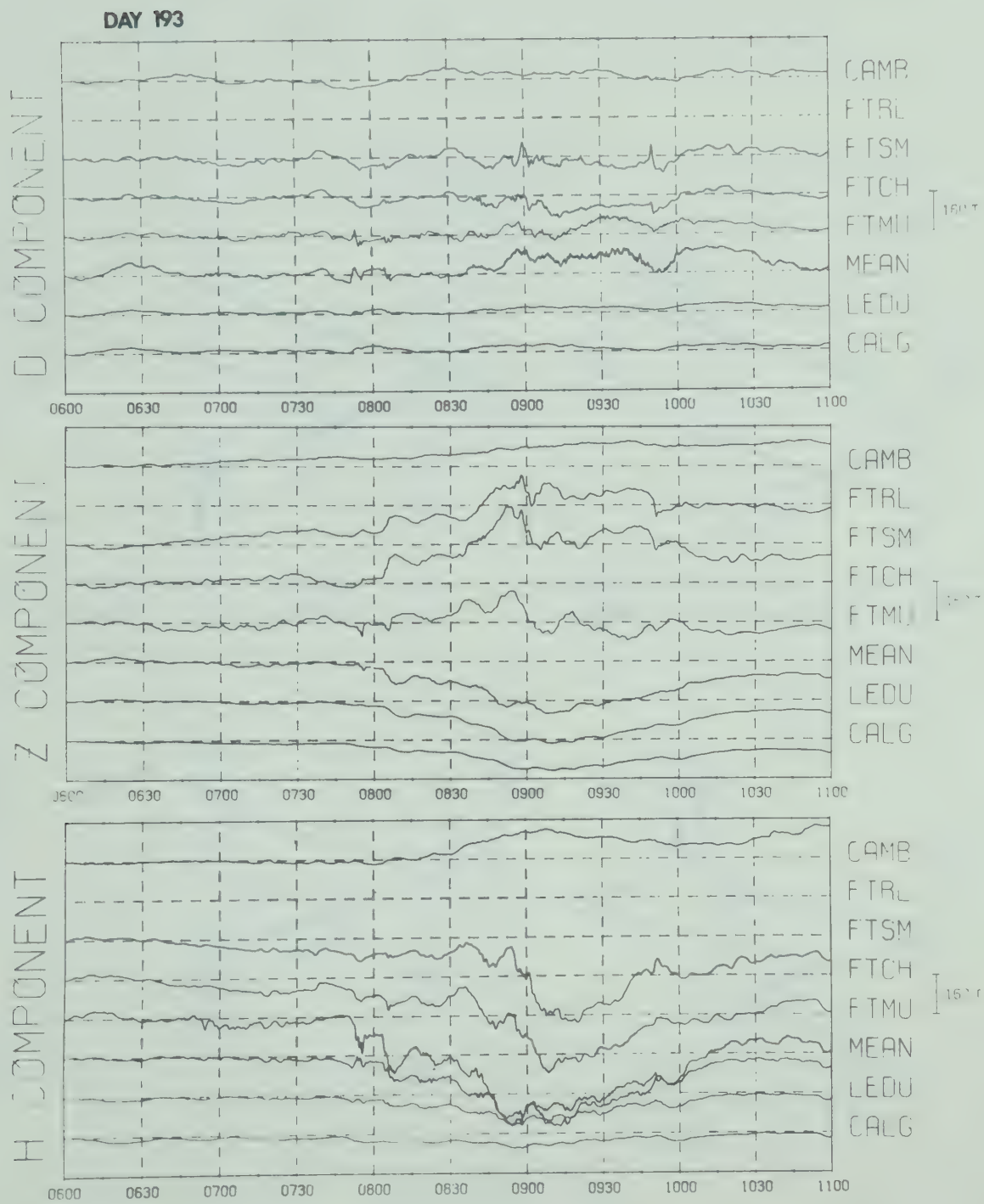


Fig. A7.11

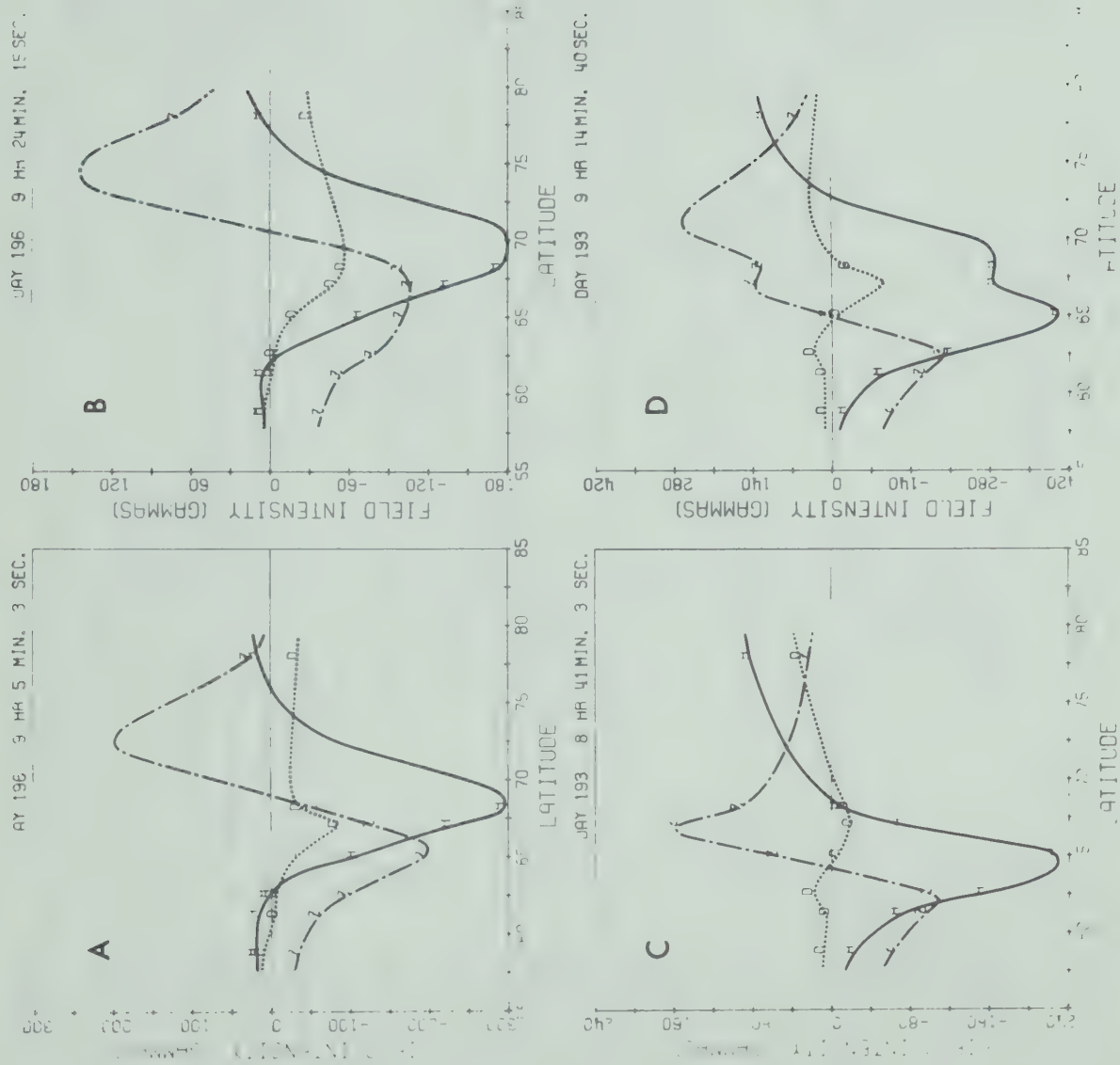


Fig. A7.12

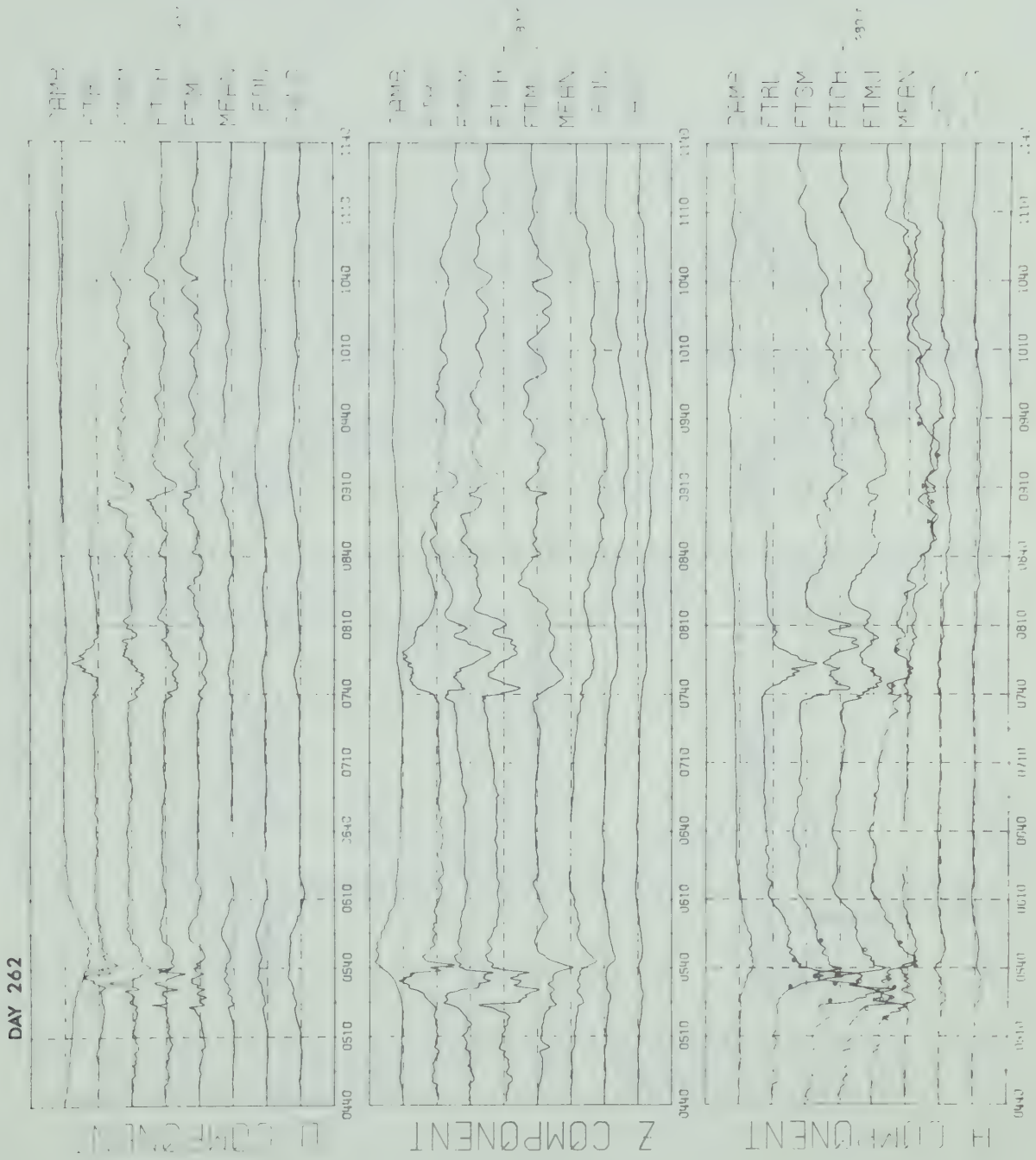


Fig. A7.13

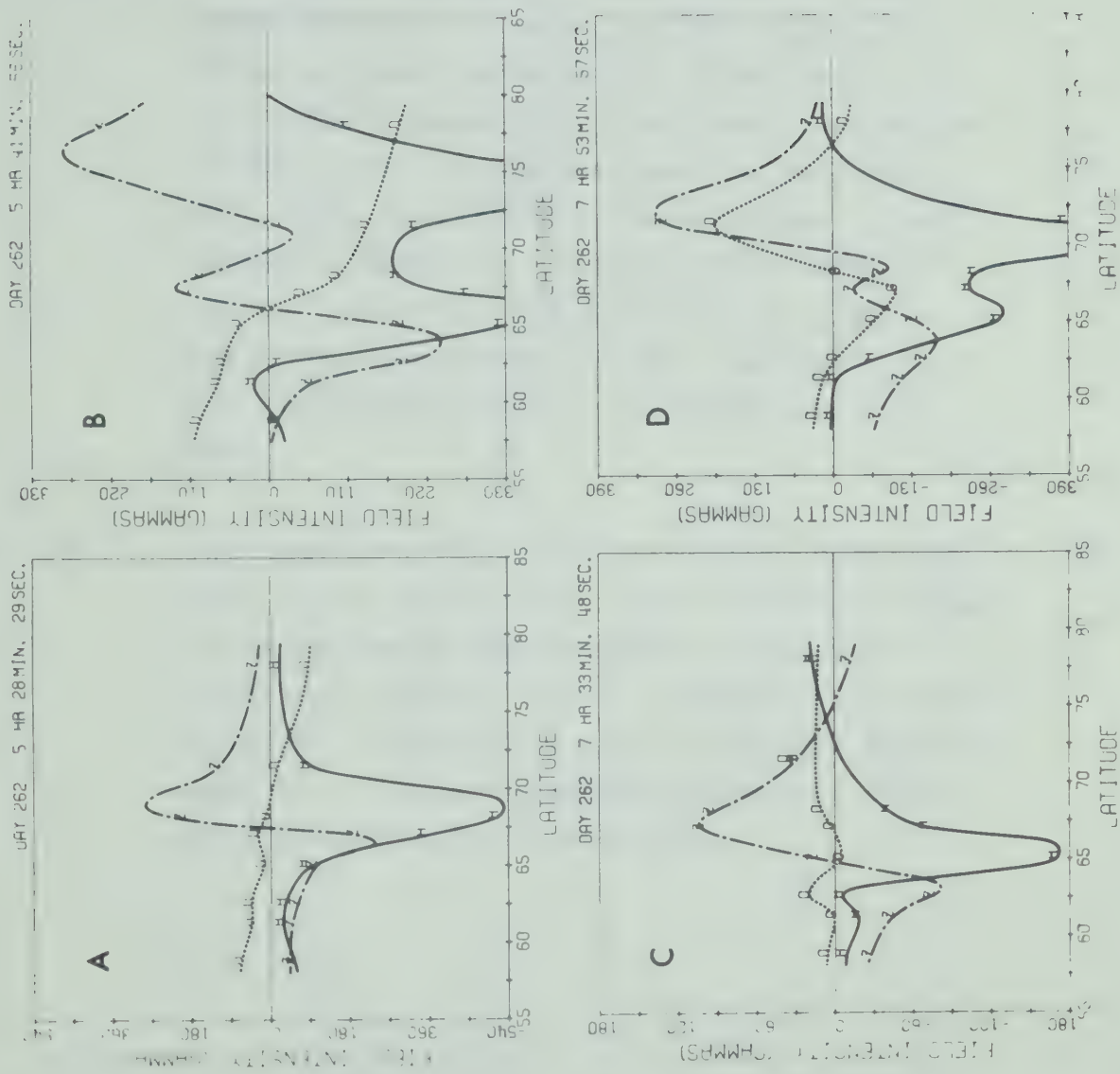


Fig. A7.14

- Fig. A7.15 Component magnetograms for July 8-9, 1970 (2300-0230 UT). This is an example of an SSC recorded with our line of stations.
- Fig. A7.16 Component magnetograms for July 9, 1970 (0230-0630 UT). Note the buildup of a large eastward electrojet along with a later development of a westward electrojet to the north of the eastward electrojet. Also note the intense low latitude ($\sim 62^{\circ}$) magnetic substorm onsetting at ~ 0545 UT. The Kp index for the interval of time including the onset of this substorm is 7-, thus indicating an expanded auroral oval.
- Fig. A7.17 Latitude profiles for the events shown in Fig. A7.15 and A7.16. Note the development of an eastward and westward electrojet following the SSC as illustrated in profiles A and B. Profiles C and D show the development of a large westward electrojet north of a pre-existing electrojet.

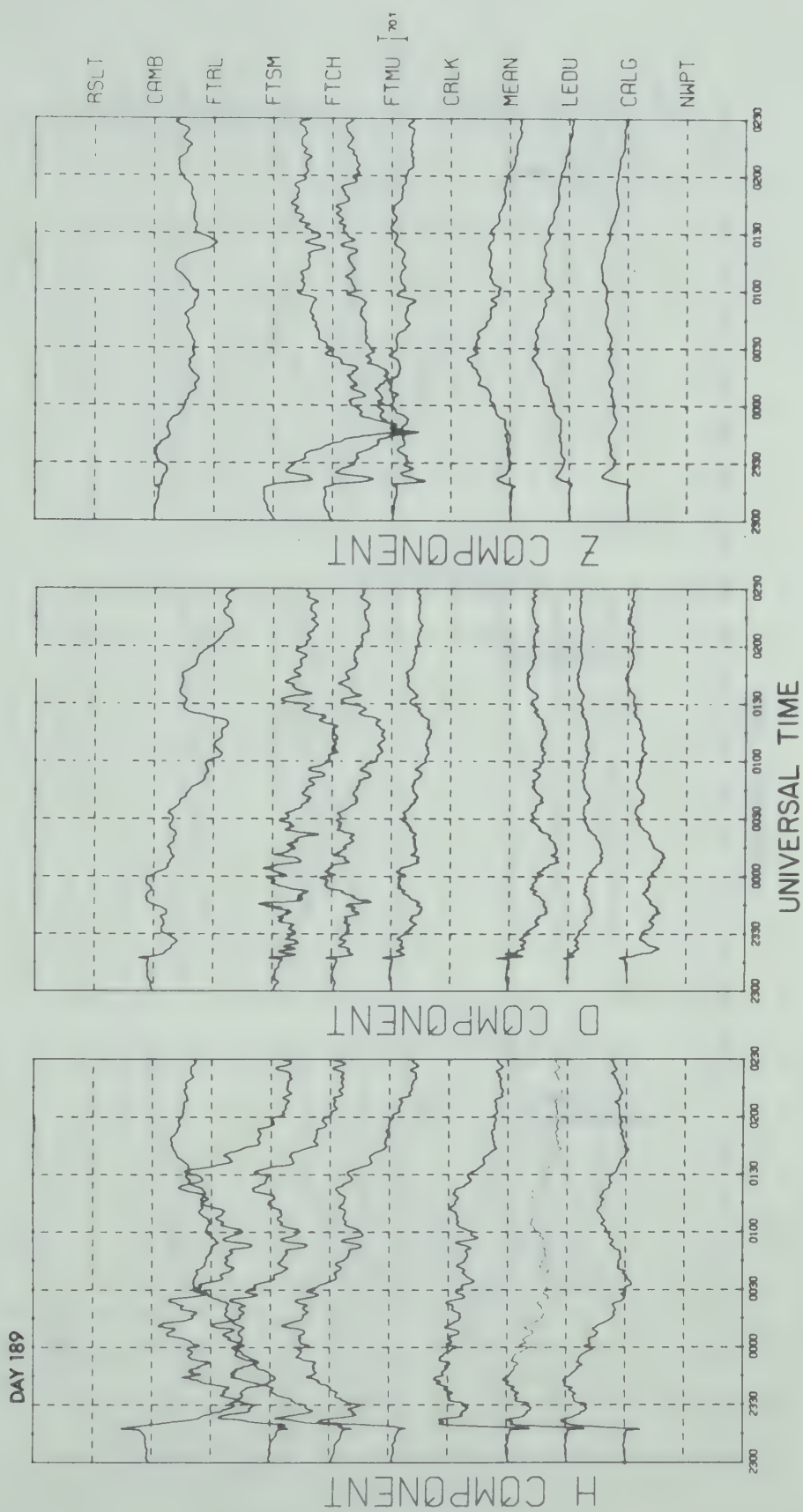


Fig. A7.15

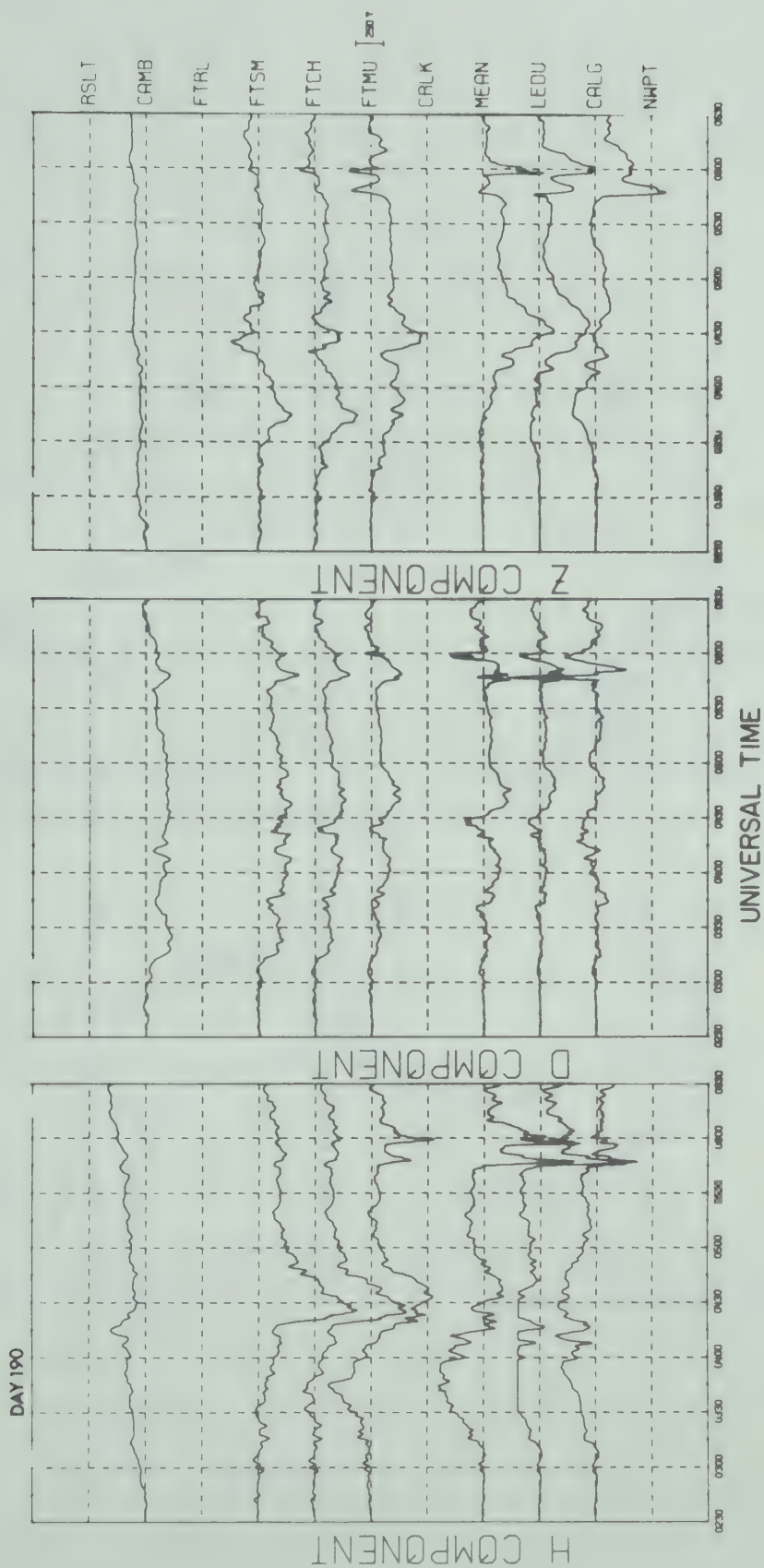


Fig. A7.16

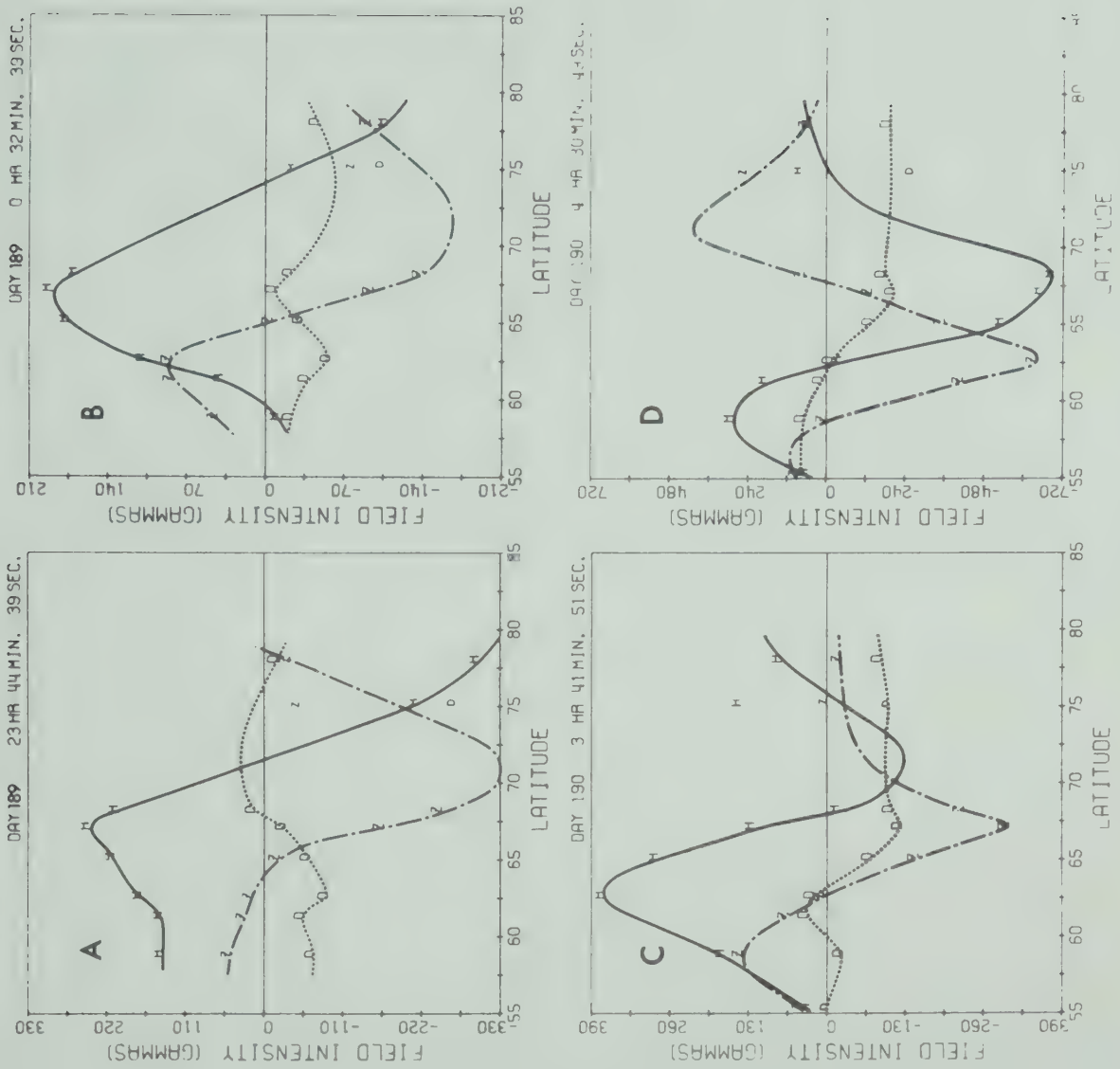


Fig. A7.17

B30040